

Inflight Microwave Drying Process of Micro-droplets for High Resolution 3D printing

Présentée le 3 novembre 2022

EDMX - Enseignement
Programme doctoral en physique

pour l'obtention du grade de Docteur ès Sciences

par

Kwanghoon CHOI

Acceptée sur proposition du jury

Prof. O. Yazyev, président du jury
Dr M. A. Pouchon, Dr S. Vaucher, directeurs de thèse
Prof. V. V. Yakovlev, rapporteur
Prof. P. Ganster, rapporteur
Dr M. Dehler, rapporteur

Acknowledgements

This research work and overall life at PSI / EPFL / EMPA have motivated me to enlarge my intellectual horizon and personally broaden the perspective that I have not imagined before.

First and foremost, I would like to express my gratitude to my supervisor Dr. Manuel .A. Pouchon who allowed me to explore the advanced research journey with physical thinking. This work could not be realized without his valuable guidance and encouragement.

I gratefully acknowledge the assistance of my co-supervisor, Dr. Sébastien Vaucher. His creative ideas based on various interdisciplinary experiences helped me figure proper solutions out once I was facing obstacles. In particular, his efforts to make me understand the concepts of microwave resonators and simulations have been challenging.

I deeply appreciate the committee members, Prof. Yakovlev, Dr. Dehler, and Prof. Ganster, for taking the time to provide valuable feedback and recommendations. I am sincerely thankful to Prof. Patrik Hoffman, who funded my research in the frame of the SFA-AM project, Powder Focusing for Beam-Induced Laser 3D Printing. Also, I am grateful to all collaborators who made an effort to finish our project in ETH Domain, Michael, Shahab, Patrik, and Briac.

Moreover, I would like to express my great appreciation to the Hochfrequenz group for the support relevant to the Microwave Studio simulation.

I am greatly indebted to all my lab members, Alina, Roger, Andrea, Anna, and Nathan, for giving me the courage and advice to complete my thesis. It would not have been possible without them.

Finally, I cannot forget to express my appreciation to my family who provided me the unconditional support during my Ph.D. work.

Abstract

A new Additive-Manufacturing (AM) or 3D printing concept is proposed to improve the printing resolution for metal additive manufacturing in the frame of the SFA-AM project, "Powder Focusing for Beam-Induced Laser 3D Printing". The project aims to transport small powder particles (largest diameter $< 10\text{ }\mu\text{m}$) at a high throughput to a spot smaller than $20\text{ }\mu\text{m}$. To realize the objective, a metal ion included liquid is suggested as source medium similar to the inkjet process, and the droplet is employed as a container for the metal ion transport. The key challenges of achieving this goal are 1) droplet size control and 2) efficient microwave heating that can dry the liquid portion of the dynamic droplet at high-speed ($\approx 3\text{ m}\cdot\text{s}^{-1}$). The most demanding part is the development of a miniaturized, very concentrated field density microwave resonator where the droplet is passing through. This follows from the extremely short interaction time between the microwave and the ejected droplets (research: $\approx 0.5\text{ ms}$) which results from the requirement for a small component size for its system integration. The primary medium examined for the experiment is water due to 1) a high dielectric loss proportional to the drying efficiency and 2) avoiding explosion risks at the laser sintering stage compared to organic solutions.

Various droplet generation conditions were investigated to determine the optimum conditions for the custom droplet generator, in particular, two key parameters were focused on: frequency and flow rate. The droplets obtained were analyzed with respect to size, gap distance, and linearity affecting the uniformity of the AM process. Moreover, Navier-Stokes-based fluid dynamics simulations enabled the understanding of the droplet behavior, especially the break-up formation. Eventually, the optimal condition for producing the smallest droplets with a diameter of $100\text{ }\mu\text{m}$ is determined to be 15 kHz and $0.5\text{ ml}\cdot\text{min}^{-1}$. Such droplets loaded with metallic particles could result in smaller than $20\text{ }\mu\text{m}$ of remaining metal powders aggregate after the drying process.

A new TEM (Transverse ElectroMagnetic) resonator has been developed for drying and sensing applications. The full-wave electromagnetic simulation software, CST Microwave Studio, supported the working mode of the device. Firstly, it is used for the dielectric characterizations of different water-ethanol mixtures contained in a microcapillary. The sensing relies on electric field perturbation due to the inserted sample, and is measured based on the change of both resonance frequency and Q-factor. These sample-dependent variations were analyzed to estimate the complex permittivity using different methods such as the Perturbation Method (PM), Least-Square Model (LSM), and Log-Linear Model (LLM). This work demonstrates that the proposed microwave module is capable of sensing nano-liter volume ranges even though the samples only partially influence the sensing area (error $< 13\text{ }\%$ in permittivity).

In microwave heating, the developed resonator achieved a temperature increase of 27 K in the microwave exposal time of 0.5 ms when the microwave power of 45 W was applied. Finally, numerical models have been proposed to estimate the maximum temperature of the initial droplet before cooling starts attributable to heat and mass transfer. This model well corresponds to the microwave electromagnetic simulation resulting in similar temperature deviations. It helps to determine the net heating efficiency of the microwave device.

Keywords

Additive Manufacturing, 3D Printing, Microwave Heating, Microwave Sensing, Droplet Generation, Droplet Evaporation, Inflight Drying, Heat Transfer, Mass Transfer, Microwave Internal Gelation (MIG), Fluid Dynamics, EletroMagnetism.

Résumé

Un concept de fabrication additive (AM) est proposé pour améliorer la résolution d'impression des métaux dans le projet SFA-AM, "Powder Focusing for Beam-Induced Laser 3D Printing". Le projet vise à transporter de petites particules (diamètre $< 10 \mu\text{m}$) à un débit élevé vers un point plus petit que $20 \mu\text{m}$. Pour atteindre l'objectif, un liquide contenant des ions métalliques est proposé comme milieu source similaire au jet d'encre, et la gouttelette est utilisée comme conteneur pour le transport des ions métalliques. Les principaux défis pour atteindre cet objectif sont 1) le contrôle de la taille des gouttelettes et 2) un chauffage par micro-ondes qui peut sécher la partie liquide de la gouttelette à grande vitesse ($3 \text{ m} \cdot \text{s}^{-1}$). La partie la plus exigeante est le développement d'un résonateur miniaturisé, à densité de champ très concentrée, où passe la gouttelette. Ceci découle du temps d'interaction extrêmement court (0.5 ms) qui résulte de l'exigence d'une petite taille de système pour son intégration. Le milieu examiné pour l'expérience est l'eau en raison d'une perte diélectrique élevée par rapport à l'efficacité du séchage et pour éviter les risques d'explosion au stade du frittage.

Diverses conditions de génération de gouttelettes ont été expérimentées afin de déterminer les conditions pour le générateur de gouttelettes, en particulier, deux paramètres ont été examinés: la fréquence et le débit. Les gouttelettes ont été analysées en fonction de leur taille, de leur distance et de la linéarité, ce qui affecte l'uniformité du AM. Des simulations de dynamique des fluides basées sur Navier-Stokes ont permis de comprendre le comportement des gouttelettes, en particulier leurs ruptures. Finalement, la condition pour produire les plus petites gouttelettes d'un diamètre de $100 \mu\text{m}$ est 15 kHz et $0,5 \text{ ml min}^{-1}$. De telles gouttelettes chargées de particules métalliques pourraient donner lieu à des agrégats de poudre métallique restants de moins de $20 \mu\text{m}$ après le séchage.

Un résonateur micro-ondes TEM a été développé pour le séchage et de détection. Le logiciel de simulation électromagnétique pleine onde, CST Microwave Studio, a pris en charge le mode de fonctionnement du dispositif. Il est utilisé pour les caractérisations diélectriques de mélanges eau-éthanol dans un micro-capillaire. La détection repose sur la perturbation du champ électrique due à l'échantillon inséré et est mesurée en fonction de la fréquence de résonance et du facteur de qualité. Ces variations dépendantes de l'échantillon ont été analysées pour estimer la permittivité complexe en utilisant différentes méthodes telles que la méthode de perturbation (PM), le modèle des moindres carrés (LSM) et le modèle log-linéaire (LLM). Le module micro-ondes proposé est capable de détecter des gammes de volumes du nanolitre même si les échantillons n'influencent que partiellement la zone de détection avec une erreur de 13% . En ce qui concerne le chauffage, le résonateur a atteint une augmentation de température de 28 K dans le temps d'exposition aux micro-ondes de 0.5 ms lorsqu'une puissance de 45 W a été appliquée. Des modèles ont été proposés pour estimer la température maximale de la gouttelette initiale avant que le refroidissement ne commence en raison du transfert de chaleur et de masse. Ce modèle correspond à la simulation électromagnétique, ce qui entraîne des écarts de température similaires. Il permet de déterminer l'efficacité de chauffage net du dispositif à micro-ondes.

Mots-clés

Fabrication additive, impression 3D, chauffage par micro-ondes, séchage en vol, détection par micro-ondes, génération de gouttelettes, évaporation de gouttelettes, transfert de chaleur, transfert de masse, gélification interne par micro-ondes (MIG), dynamique des fluides, électro-magnétisme.

Contents

| | |
|---|-------------|
| Acknowledgements..... | i |
| Abstract..... | ii |
| Keywords..... | iii |
| Résumé | iv |
| Mots-clés | iv |
| List of Figures..... | viii |
| List of Tables..... | xi |
| List of Abbreviation..... | xii |
| Chapter 1 Introduction..... | 1 |
| 1.1 Additive Manufacturing (AM) | 2 |
| 1.1.1 Classification of AM | 2 |
| 1.1.2 Feature size (resolution) and productivity of AM..... | 4 |
| 1.2 Research Framework | 6 |
| 1.2.1 Research Motivation..... | 6 |
| 1.2.2 Overview of SFA-AM Project “Powder Focusing” | 7 |
| 1.2.3 Research scope | 9 |
| 1.3 Organization of the Thesis | 10 |
| Chapter 2 Preliminaries and Benchmark | 11 |
| 2.1 Overview of Microwave Heating | 12 |
| 2.1.1 Energy Conversion | 12 |
| 2.2 Microwave Internal Gelation Process | 13 |
| 2.3 Candidate Materials..... | 15 |
| 2.3.1 Material Reaction of the Internal Gelation | 16 |
| 2.3.2 Material Reaction of the Thermal Decomposition | 17 |
| 2.4 Concept for New 3D Printing | 19 |
| Chapter 3 Droplet Generation | 22 |
| 3.1 Background | 23 |
| 3.1.1 Droplet Formation Mechanism | 23 |
| 3.1.2 Droplet Generation Method..... | 26 |
| 3.1.3 Droplet Generation Mode | 27 |
| 3.2 Experimental set-up..... | 28 |
| 3.3 Droplet Characterization..... | 29 |

| | | |
|------------------|---|-----------|
| 3.4 | Numerical Simulation for the Droplet Validation | 35 |
| Chapter 4 | Microwave Sensing | 40 |
| 4.1 | Background | 41 |
| 4.1.1 | Polarization Mechanism | 41 |
| 4.1.2 | Complex Dielectric Constant | 43 |
| 4.1.3 | Representative Microwave Sensor | 45 |
| 4.2 | TEM (Transverse Electro-Magnetic) Mode Resonator for Sensing..... | 51 |
| 4.2.1 | Design of a Microwave Resonator with the Experimental Equipment | 52 |
| 4.2.2 | Theoretical Background of New Microwave Resonator for Sensing | 53 |
| 4.2.3 | Validation of the MW Resonator (Experiment and numerical simulation)..... | 58 |
| 4.3 | Dielectric Property Sensing with TEM (Transverse Electro-Magnetic) Mode Resonator . | 62 |
| 4.3.1 | Experimental Measurement | 62 |
| 4.3.2 | Device Characterization..... | 63 |
| Chapter 5 | Microwave Heating | 69 |
| 5.1 | Background | 70 |
| 5.1.1 | Microwave Penetration Depth | 70 |
| 5.1.2 | Microwave Power Absorption | 72 |
| 5.2 | Microwave Feasibility Test..... | 72 |
| 5.3 | Microwave Cavity..... | 73 |
| 5.3.1 | Resonance Frequency..... | 74 |
| 5.3.2 | Cavity Coupling | 76 |
| 5.3.3 | Design of the Microwave Cavity | 79 |
| 5.3.4 | Numerical Simulation | 80 |
| 5.3.5 | Impedance Matching and Experimental Details..... | 82 |
| 5.3.6 | Experimental result..... | 84 |
| 5.4 | Modified Coaxial Resonator | 88 |
| 5.4.1 | Experimental Procedure | 88 |
| 5.4.2 | Experimental Result..... | 91 |
| 5.4.3 | Statistical Analysis..... | 95 |
| Chapter 6 | Heat and Mass Transfer Model | 98 |
| 6.1 | Heat Transfer | 99 |
| 6.1.1 | Mechanism | 99 |

| | | |
|-------------------------------|---|------------|
| 6.1.2 | Heat Equation | 102 |
| 6.1.3 | Boundary Conditions | 104 |
| 6.2 | Droplet Evaporation..... | 105 |
| 6.2.1 | Droplet evaporation in the quiescent air | 105 |
| 6.2.2 | Droplet evaporation in the convective air..... | 107 |
| 6.3 | Heat and Mass transfer-based Numerical models of the Falling droplet..... | 109 |
| 6.4 | Microwave validation..... | 114 |
| 6.4.1 | Numerical temperature estimation by the droplet cooling | 114 |
| 6.4.2 | Numerical temperature estimation by the droplet heating..... | 118 |
| Chapter 7 | Experimental equipment..... | 123 |
| 7.1 | Equipments | 123 |
| 7.2 | Impedance matching by Vector Network Analyzer | 133 |
| Chapter 8 | Conclusion and Outlook | 134 |
| 8.1 | Conclusion..... | 135 |
| 8.2 | Future work..... | 137 |
| Chapter 9 | Appendix | 139 |
| 9.1 | Cavity Perturbation | 139 |
| 9.1.1 | Material Perturbation..... | 139 |
| 9.1.2 | Shape Perturbation..... | 141 |
| 9.2 | Quality Factor..... | 143 |
| 9.3 | EM-Field Distribution of Microwave Cavity | 144 |
| 9.3.1 | Rectangular cavity [130] | 144 |
| 9.3.2 | Cylindrical cavity [130]..... | 149 |
| 9.3.3 | Bessel Function | 151 |
| 9.4 | Microwave Numerical Solution..... | 152 |
| 9.4.1 | FDTD (Finite Differential Time Domain)[31] | 152 |
| 9.4.2 | FEM (Finite Element Method)[31] | 153 |
| 9.4.3 | CST Simulation | 154 |
| References..... | | 157 |
| Curriculum Vitae | | 167 |

List of Figures

| | | |
|------------|--|----|
| Fig. 1.1: | Types of additive manufacturing. | 2 |
| Fig. 1.2: | Minimum feature size versus throughput for metal AM process [17–21] [Supplier’s website]..... | 4 |
| Fig. 1.3: | Metal AM classification with characteristics: powder bed (a), powder feed (b), and wire feed (c). 6 | |
| Fig. 1.4: | Schematic illustration for SFA-AM “Powder Focusing”. | 8 |
| Fig. 1.5: | Scope of research activities for “Powder Focusing”. | 9 |
| Fig. 2.1: | Microwave interaction depending on the materials [31]. | 13 |
| Fig. 2.2: | Comparison of sphere-pac production processes: conventional method (a), microwave internal gelation [MIG] (b), and the procedure comparison (c) [34]. | 14 |
| Fig. 2.3: | The chemical structure (a) and TGA data (b) of the copper-formate tetrahydrate [55]. | 18 |
| Fig. 2.4: | Scheme for new 3D printing. | 20 |
| Fig. 3.1: | The mechanisms of the droplet break-up in the quiescent air. Impact of outlet velocity on break-up length of injected liquid from a circular nozzle [70]. | 24 |
| Fig. 3.2: | The Ohnesorge diagram [74]. | 25 |
| Fig. 3.3: | Typical droplet generation methods [73]. | 27 |
| Fig. 3.4: | Equipment for the droplet generator with a nozzle. | 29 |
| Fig. 3.5: | Characterization factors of the droplet, size (a), gap distance (b) and linearity (c). | 30 |
| Fig. 3.6: | Droplet formation images under various vibrational frequencies with 0.5 ml·min ⁻¹ flow rate. | 30 |
| Fig. 3.7: | The flow chart of the image procedure (a) and processed image (b) by Mathematica®. | 31 |
| Fig. 3.8: | Characterization of the droplet behavior under the various flow rates and vibrational frequencies by comparing with theoretical values in terms of size (a), gap distance (b), and linearity (c). Dotted lines are calculated, and solid lines are experimental values. | 32 |
| Fig. 3.9: | Characterization of the droplet behavior under the fixed condition of 0.5 ml·min ⁻¹ flow rate: processed image (a), size (b), gap distance (c), and linearity (distance from the center line) (d) with various vibrational frequencies. | 33 |
| Fig. 3.10: | Characterization of the droplet behavior under the fixed condition of 15 kHz frequency: processed image (a), size (b), gap distance (c), and linearity (distance from the center line) (d) with various flow rates. | 34 |
| Fig. 3.11: | Images of simulations at 4 ms under various vibrational amplitudes: 12 μm (a), 10 μm (b), 8 μm (c), and 6 μm (d) with 0.5 ml·min ⁻¹ flow rate / 15 kHz vibrational frequency. | 37 |
| Fig. 4.1: | Frequency response of dielectric mechanisms [92]. | 41 |
| Fig. 4.2: | Complex permittivity of water (a), and ethanol (b). | 42 |
| Fig. 4.3: | Electric dipole moment [93]. | 43 |
| Fig. 4.4: | The geometry of the open-ended coaxial probe with E-field distribution (a), the capacitance model of open-ended coax sensor (b), and the probe tip geometry (c), see also [110, 111]. | 46 |
| Fig. 4.5: | Microstrip-coupled split ring resonator: diagram (a) and equivalent circuit (b) [129]. | 48 |
| Fig. 4.6: | Typical resonant cavities with inserted samples: rectangular cavity (a) and cylindrical cavity (b). 49 | |

| | |
|--|----|
| Fig. 4.7: Coaxial microwave resonator: drawing (a), simulation model (b), and photograph (c)..... | 52 |
| Fig. 4.8: Open-ended coaxial resonator and capacitance (a), with metal wall (b), plus material samples (c). | 55 |
| Fig. 4.9: Gap capacitance at the open-end of 50 Ω (a), and 75 Ω (b). | 57 |
| Fig. 4.10: Normalized gap capacitance at the open-end by the cross sectional area of 50 Ω (a) and 75 Ω (b). | 57 |
| Fig. 4.11: Resonance frequency as a function of the central conductor's length (a), the 3D relationship among the capacitance - C_p , resonance frequency - f_r , and gap distance (b), the Smith-chart (c) and S_{11} (d) as a function of gap distance. | 59 |
| Fig. 4.12: Schematics for the analytical method (a), simulation (b), and experiment (c). | 60 |
| Fig. 4.13: Electric field distribution (a) and intensity as a function of z-axis position (b) by CST. | 60 |
| Fig. 4.14: Resonance frequency changes when the water-filled \varnothing 100 μm capillary is loaded into the resonator with the various gap distances: ■ lines - without water & ■ dotted line - with water. | 61 |
| Fig. 4.15: S_{11} spectra for inserted capillaries of \varnothing 100 μm (a), \varnothing 200 μm (b), and resonance frequency & Q-factor (c). All as a function of ethanol contents in various water-ethanol mixtures. | 63 |
| Fig. 4.16: The mixture's complex permittivity with an estimated error at 10.413 GHz (f_r of the empty cavity) obtained from the open-ended coaxial dielectric probe kit (HP 85070B). | 64 |
| Fig. 4.17: The loaded Q-factor and un-loaded Q-factor with different size of the capillary (Number: capillary size, and U: un-loaded). | 65 |
| Fig. 4.18: The complex permittivity comparison obtained by Standard, PM, LSM, and LLM methods. ϵ' for 100 μm capillary (a), ϵ'' for 100 μm capillary (b), ϵ' for 200 μm capillary (c), and ϵ'' for 200 μm capillary (d)..... | 67 |
| Fig. 5.1: All resonators examined for their heating performance (O: Heating, \triangle : Partial heating, and X: No heating)..... | 73 |
| Fig. 5.2: Typical resonant cavity: rectangular cavity (a), and cylindrical cavity (b)..... | 74 |
| Fig. 5.3: Coaxial coupling using electric field (a), magnetic field (b), waveguide coupling using electric field (c), and magnetic field (d)..... | 77 |
| Fig. 5.4: Smith-chart expressing the reflection coefficient as a function of the coupling coefficient, β' , in the case of a parallel RLC circuit. | 78 |
| Fig. 5.5: Cylindrical microwave cavity: model (a) and real part (b). | 79 |
| Fig. 5.6: Resonant mode chart for a cylindrical cavity [172]. | 80 |
| Fig. 5.7: Simulation model for the software QWED. | 81 |
| Fig. 5.8: E-field distributions of the cylindrical cavity: x-y plane (a), y-z plane (b), and x-z plane (C)..... | 81 |
| Fig. 5.9: Normalized E-field distribution as a function of hole-sizes of the cavity without water..... | 82 |
| Fig. 5.10: A quartz capillary used for the impedance matching (a), S_{11} parameters as a function of various iris hole sizes without water b), with water (c), and Smith-chart with an \varnothing 8 mm iris (d)..... | 83 |
| Fig. 5.11: Microwave heating test for the static scheme (a), experimental setup (b), and temperature log (c). | 84 |
| Fig. 5.12: Sample preparation of Copperformate tetrahydrate. | 84 |
| Fig. 5.13: The deposited copper formate on the glass capillaries with microwave power values of 10 W (blue) and 40 W (brown). | 85 |
| Fig. 5.14: XRD pattern of the copper formate tetrahydrate deposited on the glass capillary. | 86 |

| | |
|---|-----|
| Fig. 5.15: Microwave heating test for the static scheme (a), experimental set up (b) and the introduced materials for preventing contamination during microwave test with a power of 20 W (c). | 86 |
| Fig. 5.16: Experimental setup (a), temperature logs obtained from a thermocouple (b) and IR camera (c), and images taken by the high-speed camera (IDY Y4) inside the cavity (d). | 87 |
| Fig. 5.17: Experimental procedure for the dynamic droplet heating. | 88 |
| Fig. 5.18: Experimental set up (a) and the temperature measurement (b). | 90 |
| Fig. 5.19: Image processing procedure for the droplet volume characterization. | 90 |
| Fig. 5.20: Heating performance as a function of the input power: temperature log (a), and overall result (b). | 91 |
| Fig. 5.21: A spherical droplet diameter corresponding to the irregular volume of droplets (no power). | 92 |
| Fig. 5.22: Image processing of the droplet trains as a function of input power. | 94 |
| Fig. 5.23: Images for the statistical analysis. | 96 |
| Fig. 5.24: Averaged volume of Fig. 5.23 as a function of height. | 97 |
| Fig. 6.1: Lifetime of the water droplets under different surrounding conditions: fixed relative humidity (40 %) with various temperatures (a) & fixed ambient temperature (20 °C) with various relative humidities (b) in the quiescent air. | 107 |
| Fig. 6.2: Lifetime of the water droplets under different surrounding conditions: fixed relative humidity (40 %) with various temperatures (a) & fixed ambient temperature (20 °C) with various relative humidities (b) in the convective air. | 108 |
| Fig. 6.3: Saturation humidity ratio with a polynomial curve fitting. | 113 |
| Fig. 6.4: Temperature profiles of a \varnothing 100 μ m falling water droplet with respect to different conditions: ambient temperature (°C) - Humidity (%) - Model (Mixing / NonMixing), with the initial temperatures of 343 K - 70 °C (a) and 323 K - 40 °C (b). | 114 |
| Fig. 6.5: Experimental configuration with the measured results. | 115 |
| Fig. 6.6: Size distribution (a) and temperature profiles of the droplets based on numerical models: \varnothing 100 μ m (b), \varnothing 90 μ m (c), and \varnothing 80 μ m (d) in diameter. | 116 |
| Fig. 6.7: Adaptive mesh refinement and S_{11} result of the model. | 118 |
| Fig. 6.8: Simulation results of E-field intensity (RMS), power loss density (a), and average power loss density normalized by the temperature-dependent ϵ'' (b) along the z-axis. | 119 |
| Fig. 6.9: Complex dielectric permittivity ϵ' (a) and ϵ'' (b): ■ black dash dot - CST simulation, ■ blue line - Fig. 4.2 (Debye model), and ■ red dot - polynomial curve fitting. | 120 |
| Fig. 6.10: Maximum temperature comparison by different numerical methods: ■ lines - only considering the main heating zone, and ■ dashed lines - additionally considering the extended heating zone. Both are calculated by the cylindrical coordinate model taking into account MW heating with cooling. ■ symbols - calculated by the spherical coordinate model considering only cooling. | 121 |
| Fig. 7.1: Experimental configuration. | 123 |
| Fig. 7.2: LSD v201 with dimensions - Brüel & Kjær. | 124 |
| Fig. 7.3: APSIN20G signal generator - Anapico AG (a) with maximal output power in frequency ranges (b). | 125 |
| Fig. 7.4: 250TR7z5g18 microwave amplifier - AR (a) with typical output power in frequency ranges (b). | 126 |
| Fig. 7.5: WRD750D24 isolator: termination combined circulator. | 128 |
| Fig. 7.6: WR90 waveguide directional coupler. | 129 |

| | |
|---|-----|
| Fig. 7.7: 779D directional coupler - HP (a) with the connected direction (Forward & Reverse) (b)..... | 129 |
| Fig. 7.8: WR 90 waveguide to coax adapter. | 130 |
| Fig. 7.9: Agilent 8720D Vector network analyzer. | 130 |
| Fig. 7.10: LS class HPCL pump - Teledyne SSI. | 131 |
| Fig. 7.11: Stroboscope 1531-A (a) and an extension lamp - IET Labs (b). | 132 |
| Fig. 8.1: Reflected signal changes as a function of various water flow rates. | 137 |
| Fig. 8.2: Possibility for the needle-free injection ($\Delta t = 0.4$ ms, total $t = 1.2$ ms). | 138 |
| Fig. 9.1: Material perturbation. | 139 |
| Fig. 9.2: Shape perturbation..... | 141 |
| Fig. 9.3: Bessel function of the first order $J_m(x)$, $m = 0, 1, 2, 3$ | 151 |
| Fig. 9.4: Leap-frog scheme of transient solver. | 154 |

List of Tables

| | |
|---|-----|
| Table 3.1: Simulation conditions for Fig. 3.11. | 37 |
| Table 3.2: Simulation results under various amplitudes with $0.5 \text{ ml}\cdot\text{min}^{-1}$ flow rate / 15 kHz frequency. | 37 |
| Table 3.3: Simulation results under various flow rates with a 15 kHz vibrational frequency. | 38 |
| Table 3.4: Simulation results under various vibrational frequencies with a $0.5 \text{ ml}\cdot\text{min}^{-1}$ flow rate..... | 38 |
| Table 4.1: Geometrical parameter of the coaxial microwave resonator. | 52 |
| Table 4.2: Resonance frequency corresponding to Fig. 4.14..... | 61 |
| Table 4.3: Complex permittivity corresponding to Fig. 4.16. | 64 |
| Table 5.1: Cavity dimensions and the operation mode..... | 81 |
| Table 6.1: Typical convective heat transfer coefficient. | 99 |
| Table 6.2: Variables for (6-32). | 110 |
| Table 6.3: Saturation humidity ratio (kg_w/kg_a) [184]. | 113 |
| Table 6.4: Values used for the calculation for (6-32) and (6-33). | 113 |
| Table 6.5: All temperature data in Celsius ($^{\circ}\text{C}$) for Fig. 6.6 (b). | 117 |
| Table 6.6: All temperature data in Celsius ($^{\circ}\text{C}$) for Fig. 6.6 (c). | 117 |
| Table 6.7: All temperature data in Celsius ($^{\circ}\text{C}$) for Fig. 6.6 (d). | 117 |
| Table 7.1: Specification of the stroboscope 1531-A. | 132 |
| Table 9.1: Bessel function of the first kind $J_m(x)$ and its derivative $J_m'(x)$ | 152 |

List of Abbreviation

| | | |
|-------------|---|---|
| 3DP | : | 3D printing |
| AF | : | Additive Fabrication |
| ACT | : | Advanced Compaction Technology |
| ALE | : | Arbitrary Lagrangian-Eulerian |
| ALM | : | Additive Layered Manufacturing |
| AM | : | Additive Manufacturing |
| Bi | : | Biot number |
| BJ | : | Binder jetting |
| CCD | : | Charge-Coupled Device |
| CFD | : | Computational fluid dynamics |
| CIJ | : | Continuous Inkjet Printing |
| CSRR | : | Complementary Split Ring Resonator |
| CST | : | Computer Simulation Technology (an electromagnetic field simulation software) |
| DED | : | Direct Energy Deposition |
| DMD | : | Direct Metal Deposition |
| DMLS | : | Direct Metal Laser Sintering |
| DMT | : | Direct Metal Tooling |
| DOD | : | Drop on Demand (Inkjet printing) |
| DSRR | : | Double Split Ring Resonator |
| DUT | : | Device under test |
| EBM | : | Electron Beam Melting |
| EBF3 | : | Electron Beam Free-Form Fabrication |
| EBM | : | Electron Beam Melting |
| EHD | : | Electrohydrodynamic Jet printing |
| EM | : | ElectroMagnetic |
| FIT | : | Finite Integration Technique |
| FDTD | : | Finite-Difference Time-Domain |
| FVM | : | Finite Volume Method |
| HMTA | : | HexaMethyleneTetrAmine (Methenamine) |
| HMUR | : | HexaMethylenetetramine and URea Mixture |
| HPLC | : | High Precision Liquid Chromatography |
| IG | : | Internal Gelation |
| IP | : | In-Plane |
| KEMA | : | Keuring van Elektrotechnische Materialente Arnhem (a nuclear fuel wet production route) |
| LENS | : | Laser Engineered Net Shaping |
| LIFT | : | Laser Induced Forward Transfer |
| LMF | : | Laser Metal Fusion |
| LMD | : | Laser Metal Deposition |
| LOC | : | Lab On Chip |
| LUT | : | Liquid Under Test |
| LWR | : | Light Water Reactor |
| MCED | : | Meniscus-Confined ElectroDeposition |
| ME | : | Material Extrusion |
| MIG | : | Microwave Internal Gelation |
| MJ | : | Materials jetting |
| MMA | : | Miniaturized Microwave Applicator |
| MSRR | : | Multi Split Ring Resonator |
| MUT | : | Material Under Test |
| MW | : | MicroWave |
| Nu | : | Nusselt number |
| NS | : | Naviers-Stoke |
| Oh | : | Ohnersorge number |
| OOP | : | Out-of-plane |

| | |
|---------------|---|
| Open- | : Open Field Operation and Manipulation (an open source CFD Software) |
| FOAM | |
| Oh | : Ohnesorge number |
| PBF | : Powder bed fusion |
| PDE | : Partial Differential Equation |
| Pr | : Prandtl number |
| QW | : Qwick-Wave (an electromagnetic field simulation software) |
| Radar | : Radio Detection And Ranging |
| Re | : Reynolds number |
| RF | : Radio Frequency |
| RM | : Rapid Manufacturing |
| RP | : Rapid Prototyping |
| RPD | : Rapid Plasma Deposition |
| RSD | : Relative Standard Deviation |
| SFA-AM | : Strategic Focus Area Advanced Manufacturing |
| SFF | : Solid Freeform Fabrication |
| SFR | : Sodium-cooled Fast Reactor |
| SL | : Sheet Lamination |
| SLM | : Selective Laser Melting |
| SPR | : Split Ring Resonator |
| Sc | : Schmidt number |
| Sh | : Sherwood number |
| TE | : Transverse Electric |
| TEM | : Transverse Electro-Magnetic |
| TM | : Transverse Magnetic |
| TWTA | : Traveling Wave Tube Amplifier |
| VNA | : Vector Network Analyzer |
| VOP | : Volume Of Fluid |
| VP | : Vat Photopolymerization |
| We | : Weber number |
| WLAM | : Wire and Laser Additive Manufacturing |

Chapter 1 Introduction

- A brief introduction of general research trends in Additive Manufacturing (AM).
- Thesis motivation in the framework of the SFA-AM (Strategic Focus Area Advanced Manufacturing) research project: increasing the resolution without degrading the AM functionality.
- The thesis organization with summarized contents by chapters.

1.1 Additive Manufacturing (AM)

Additive Manufacturing (AM) has been named by many synonymous terminologies such as 3D Printing (3DP), Solid Freeform Fabrication (SFF), Rapid Manufacturing (RM), Additive Layered Manufacturing (ALM), and Additive Fabrication (AF). According to ASTM, Additive manufacturing is defined as “the process of joining materials to make objects from 3D model data, usually layer upon layer, as opposed to subtractive manufacturing methodologies” [1]. This technology has become increasingly prominent over the last few decades, since it enables new manufacturing processes, not only for lab-scale fabrication, but also for industrial products with material classes such as ceramics [2, 3], polymers [4, 5], and metals [6]. In addition, the AM process can overcome the limitations of the conventional process, for instance, geometrical complexity, molds, fixtures of tools, and near-net shaping [7].

The first AM conception appeared in 1860 by a French artist, Francois Willem, based on the precursor technologies [8]. He proposed a ‘Photo-Sculpture’ method that involved 24 cameras arrayed at 15-degree increments around the subject and extracting the silhouettes from the images to construct the sculpture. Blather’s topography, which consists of adding contour cut papers on top of each other to form a stack, is one of the closest concepts to the modern AM process [9]. Baker suggested the moving weld head to create a 3D shaped-decorative part based on material deposition in 1925 [10]. This idea is used for the current metal AM process. A commercial AM product of SLA-1 was introduced in 1987 by 3D systems [11]. Since then, many modifications have been conducted to optimize the process for rapid prototyping, and advanced manufacturing approaches with various materials have emerged [2–6].

1.1.1 Classification of AM

The ISO/ ASTM [1] categorizes all AM processes into seven types as shown in Fig. 1.1

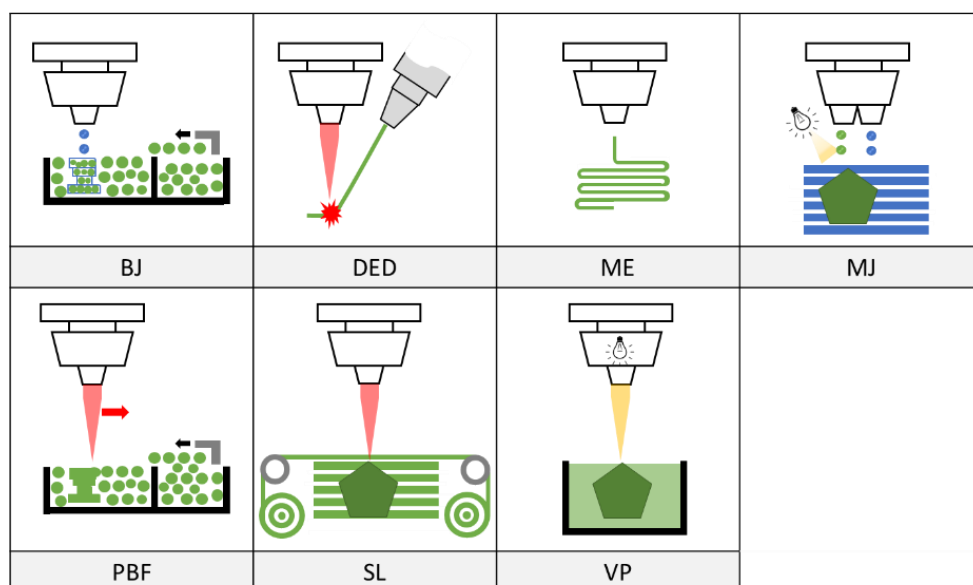


Fig. 1.1: Types of additive manufacturing.

Binder Jetting (BJ) is one of AM processes in which the building powders are selectively agglomerated by a liquid bonding agent resulting in 3D geometry by gluing the particles together. The design concept is similar to inkjet printing by dropping the bonding liquid from the printer head. The main benefits of this process type accompany a support-free structure, high productivity with cost-effectiveness, and large platform size. In addition, this method allows a wide range of materials such as metals, ceramics, glass, sand, etc.

Direct Energy Deposition (DED) is an AM method that uses concentrated energy to melt a material and a portion of the substrate for deposition. The laser, electron beam, or plasma arc can be employed as energy sources, and the resolution and speed vary depending on the source types. The main principle of operation is that concentrated energy meets coaxially with the powder stream at the substrate and pre-deposited layers. Therefore, it is advantageous in terms of productivity compared to the PBF (Powder Bed Fusion) method because it omits the need to supply powder layerwise, which means that a continuous process can be realized.

Material Extrusion (ME) can be described as the selective dispensing of material through a nozzle by a driving force (e.g., pressure). The extruded material solidifies on the build platform along with the previous deposition. A common terminology that indicates this method is FDM (Fused Deposition Modeling), which is more applicable for polymer-based materials. This methodology is effective because it can guarantee good mechanical properties and a high build-speed simultaneously, as well as a relatively low-cost extrusion machine.

Materials Jetting (MJ) is a droplet-based AM method, where the material is selectively deposited as opposed to a bonding agent in binder jetting. After completion of all layers, the support structure is eliminated by a water jet to obtain the final user-designed part. Photopolymers are commonly used materials. It has an advantage in terms of precision due to the stacking method based on inkjet technology.

Powder Bed Fusion (PBF) is one of the AM processes, in which a focused energy source selectively fuses the region where the powder is stacked on the build platform. After selectively applying the energy on the previous layer, a new powder layer is supplied by a recoater (blade) with a defined thickness. The main working principle is based on thermal heating using a laser- or E-beam. In the metal AM categories, this method offers comparably good mechanical properties of the products with high printing resolution [12].

Sheet Lamination (SL) is a process, in which material sheets are bonded layer by layer to create a 3D object. It is also called a stack and cut approach, wherein sheets of material are combined with the previous layer by an adhesive or ultrasound, and then a laser cutting is applied. It shows a substantial productivity.

Vat Photo-polymerization (VP) is a general term related to stereolithography. A photo-curable resin is selectively exposed to light resulting in a light-activated polymerization. This procedure is related to the chemical reaction among the photo-initiators, additives, and reactive monomers. Moreover, it offers a high resolution, a superb surface finish, and a high processing speed.

All the descriptions relevant to AM classification are in the references [13–15].

Nowadays, all the classified processes are able to build 3D metal structures depending on the requirement of the object, for example, process applicability, resolution, material, productivity, size, and mechanical/electrical property. However, commercial machines are still limited to the PBF, DED, and BJ categories.

1.1.2 Feature size (resolution) and productivity of AM

The critical aspect, not only for AM techniques but also for all micro-manufacturing technologies, is the areal fabrication or machining resolution that determines the dimensional accuracy and the surface roughness of a target structure, particularly once the geometric dimension is smaller than the targeted wavelength (e.g. optical metamaterials) [16, 17]. The dimensional resolution is determined by the in-plane (IP: x and y-axis) spot size, corresponding to the focus of the energy source, such as the laser-, plasma-, or E-beam, and the input material focus of liquid droplet or powder streams. A further factor is the out-of-plane (OOP: z-axis) resolution which can be maximized by a minimum layer thickness. The fabrication speed is a typical drawback of AM that increases the overall manufacturing cost. Therefore, it should be improved for mass production. Generally, it is defined as a volumetric throughput representing the deposition rate (mm^3/hr). However, there is a trade-off between the two variables, resolution and production rate. In other words, a more extensive input material results in higher throughput but less accuracy.

Fig. 1.2 shows the operational window of the reported metal AM technique with respect to the feature's size versus volumetric throughput. In short, It accounts for the relationship between size and productivity [17–21].

The micro-nanoscales methodology can accompany the high-resolution without offering a high throughput rate. On the other hand, the wire-based AM method can show a high deposition rate but less resolution.

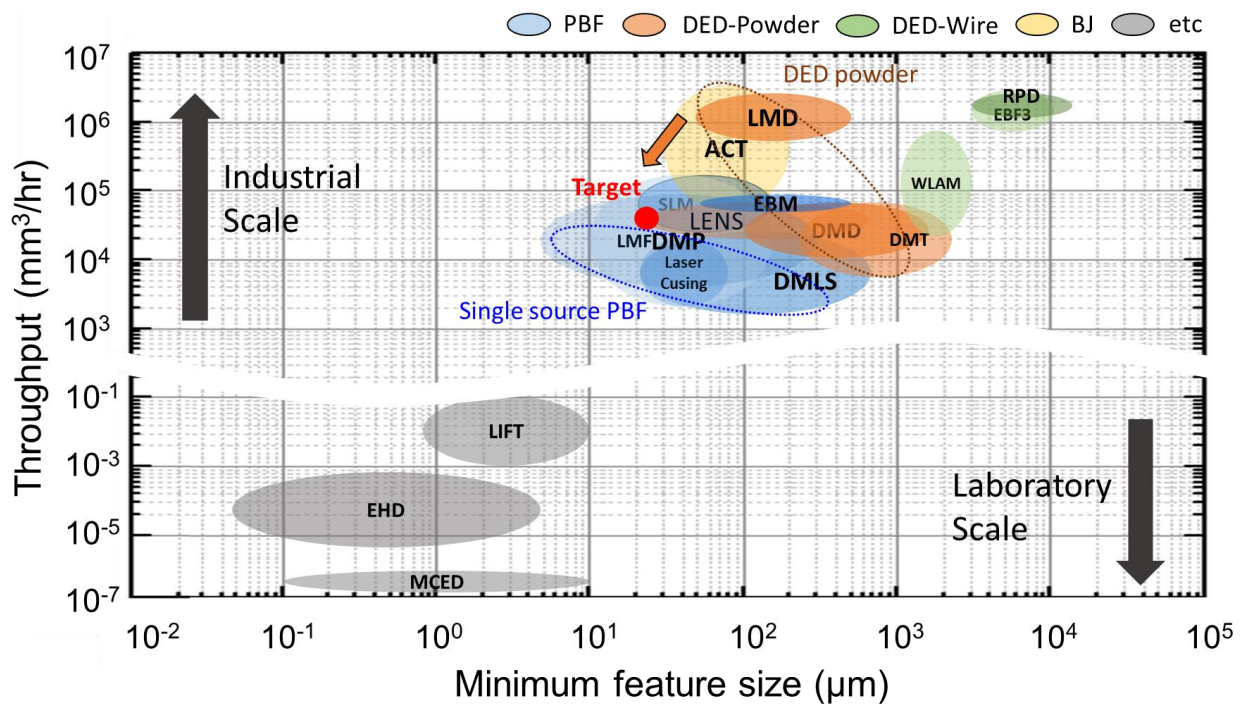


Fig. 1.2: Minimum feature size versus throughput for metal AM process [17–21] [Supplier's website].

DMLS: Direct Metal Laser Sintering, **EBM:** Electron Beam Melting, **SLM:** Selective Laser Melting, **LMF:** Laser Metal Fusion, **LMD:** Laser Metal Deposition, **DMT:** Direct Metal Tooling, **LENS:** Laser Engineered Net Shaping, **DMD:** Direct Metal Deposition, **RPD:** Rapid Plasma Deposition, **WLAM:** Wire and Laser Additive Manufacturing, **EBF3:** Electron Beam Free-Form Fabrication, **ACT:** Advanced Compaction Technology, **LIFT:** Laser Induced Forward Transfer, **EHD:** Electrohydrodynamic Jet Printing, and **MCED:** Meniscus-confined Electrodeposition

In the frame of commercial AM production, the PBF suppliers try to improve the production speed by introducing multiple laser sources for building several objects simultaneously. Consequently, this method already satisfies the accuracy as well as the surface roughness in the micrometer range. Most cases of the PBF processes, being located in the high-throughput region in the operation window, result from this approach of having several laser sources to enhance productivity, see Fig. 1.2. It is simple and effective to produce numerous independent parts, but complicated to create a single part using multiple laser beams. This is due to overlapping, especially for small samples.

The RPD (Rapid Plasma Deposition) is a wire-based AM technique based on conventional arc welding to increase the deposition rate. The millimeter-range metal wire is fed into a molten pool where an arc plasma is generated between the electrode and workpiece, and lamination proceeds. Argon is the usual inert gas introduced for plasma generation and oxidation shielding. The WLAM (Wire and Laser Additive Manufacturing) and EBF3 (Electron Beam Free-Form Fabrication) are similar to the RPD process. However, the energy source type applied to the object is different, being a laser or an electron beam respectively. The properties and dimensions of the resulting component produced by this way are strongly correlated to both the wire characteristic (e.g., size and chemical composition) and the process parameters such as feeding direction and angle, source power, wire feed rate, and the welding speed for all wire-based AM processes [20, 21]. Therefore, the classification of these techniques falls into the DED or ME process.

The powder-based DED method occupies the area between the wire AM and PBF. It means that the DED technique has many advantages to enable compromising the functionalities between the minimum feature size and the throughput. Hence, an exceptional laser-based DED process is proposed to increase the resolution without significant throughput deterioration in the frame of the SFA-AM project as marked "Target" in Fig. 1.2 by optimizing the material transport. The details of the project will be dealt with in Chapter 1.2.2.

Other unique printing techniques for fabricating tiny structures with high-resolution are additionally marked in Fig. 1.2, for example, LIFT (Laser-Induced Forward Transfer), EHD (Electro Hydro-Dynamic Jet Printing), and MCED (Meniscus-confined Electrodeposition). However, the productivity is extremely low compared to the commercial methods of PBF, DED, and RPD. Hence, these methods are more suitable for lab-scale research to produce 2D or 2.5D dimensional parts. All these methodologies are established based on the MJ process. The main principles of these methods are described below.

- **Laser Induced Forward Transfer (LIFT):** this technique is a direct writing method based on the laser reaction to transfer a tiny fraction of the sample from the thin donor layer to the substrate. It is beneficial to control the particle size decided by the laser characteristics and the material properties.
- **Electrohydrodynamic Jet Printing (EHD):** this method is a high-resolution printing where the electric field drives the liquid droplet. The E-field gives rise to the polarization of the dielectric liquid and the repulsive force of the ions causes the meniscus at the nozzle resulting in a Taylor cone shape. The droplet ejects when surface charge repulsion at the cone apex exceeds the surface tension.
- **Meniscus-Confined ElectroDeposition (MCED):** this way is a precise electrodeposition that uses the thermodynamic stability of a liquid meniscus. The electrical potential between the conductive substrate and electrolyte filled in the micropipette is the main driving force to form the meniscus at the nozzle and then initiates the detachment.

1.2 Research Framework

1.2.1 Research Motivation

The metal AM applicability has been emerging recently; corresponding definitions usually dealt with in industry are DED and PBF. William E. Frazier [6] classified the metal AM process depending on the material and the feeding method. These are 1) powder bed systems, 2) powder feed systems, and 3) wire feed systems, all shown in Fig. 1.3. This is similar to the above ASTM categorization but splits the DED methods based on the forms of the source material such as powder and wire.

Although this concept of building up parts from layers was first tested 30 years ago [22], the metal parts produced by AM-processes have only been applied in a few fields, like in aerospace industry [23] and for medical applications [24]. This is mainly due to several limitations such as the process feasibility for materials, price of both machine and powder, size, resolution, roughness, and productivity [25–28]. Atzeni et al. compared the cost for fabricating the same component by the PBF versus the high pressure die-casting and concluded that the AM method is only cost-effective when the product number is smaller than a specific limit. For example, the breakeven point is anticipated to be about 42 assembly components made out of aluminum alloy, since most of the cost is attributable to the die fabrication [29]. These limits must be overcome by optimizing both, the process and the topological design, thereby extending the field applicability [30].

This study focuses on the metal powder AM process using laser technology. In this frame, and to resolve the encountered difficulties mentioned above, an unconventional concept for the metal AM process is presented, where especially the resolution improvement is addressed.

Additional detailed comparisons for metal AM methods are shown in Fig. 1.3.

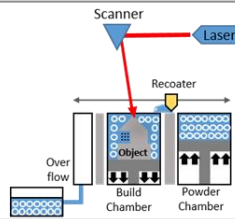
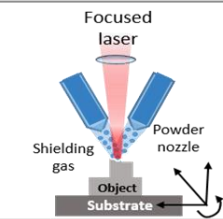
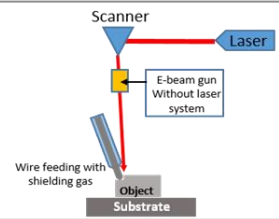
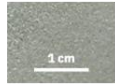
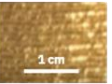
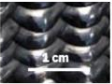
| | (a) Powder bed method | (b) Powder feeding method | (c) Wire feeding method |
|---|---|--|---|
| Description |  |  |  |
| Surface Roughness (um) |  Ra = 5~18 |  Ra = 15~60 |  Ra = 45~200 |
| Resolution(um) [layer thickness] | 20~200 Diameter of the Source | 100~1000 Width of the bead | 2000~50000 Width of the bead |
| Print speed (cc/hour) | 25~50 | 100~300 | 500~1000 |
| Unit cost (\$/cc) | \$2.50~4.00 | \$0.33~1.50 | \$0.25~0.60 |
| Usage (%) | 54 | 16 | |

Fig. 1.3: Metal AM classification with characteristics: powder bed (a), powder feed (b), and wire feed (c).

The powder bed method in Fig. 1.3 (a) has the upper hand in industry because of the dimensional precision, and a superior design flexibility among the metal AM processes, even though it is not appropriate for mass production due to the low production speed. In addition, the powder should be fully packed in the build chamber before processing, even though only small fractions might end up in the targeted object.

On the other hand, the powder feed & wire feed methods (Fig. 1.3 b, c), similar to a welding procedure, are more advantageous in terms of the mechanical properties, productivity, and the useability for variable materials. Moreover, these methods can partially recover/repair damaged parts, especially suitable for large components. One reason why these technologies are not used broadly as metal AM processes in industry is the need for additional machining of the built-up component parts, because of the low resolution and poor surface finish resulting in a dimensional accuracy problem. A key factor to increasing the resolution and precision using these methods is a size control of the material feed up to the laser irradiation and melting. Size control is an arduous task to deal with. Particularly in the case of the wire feed method (Fig. 1.3 c), it is hard to produce a thinner wire for a wide range of materials.

Moreover, the wire-feed method requires more post-processing than other techniques [12]. For this reason, this project's scope concentrates on the powder feed method (Fig. 1.3 b), and especially improving its resolution. This research proposes a novel concept of the feeding and synthesis of the printing material by online solution mixing and internal gelation based on previous research explained in the following chapter.

The droplet train, as a container of metal powder, is then dried in-flight by microwave heating, resulting in powder packages. The most important part is to generate heat inside the medium, driving chemical synthesis. This way, it will be possible to bring a focused powder stream into a laser melt, where the focus should be ten times smaller than today's power-feed methods ($200 \rightarrow 20 \mu\text{m}$). In addition, no hazardous and difficult-to-control powder preparation is necessary, unlike most existing metal AM technologies, since the materials are delivered in a gelled or suspension state. This new approach of powder focusing is researched in the frame of the ETH SFA-AM project "Powder Focusing for Beam-Induced Laser 3D Printing".

1.2.2 Overview of SFA-AM Project "Powder Focusing"

SFA-AM is the abbreviation for the project "Strategic Focus Area (SFA) Advanced Manufacturing (AM)" that aims to enable Switzerland's scientific and technical community to contribute at the most advanced level to these developments. The research has been conducted on "Powder Focusing" which can propose a novel AM methodology resulting in an improved resolution.

This method is based on the DED (Direct Energy Deposition) technique that focuses on a laser beam meeting the powder jet coaxially on the substrate to build a 3D object. The structure's dimensions obtained by this method today are usually in the range of millimeters up to several tens of millimeters. It is determined by parameters such as the laser spot size, the precision of the mechanical tables, the powder particle diameters ($> 50 \mu\text{m}$) of flowable powders, and the powder jet spot size. This project desires to overcome the size limit of the conventional powder-DED method by increasing the resolution. In particular, the project aims to find technical solutions for transporting small particle powders ($< 10 \mu\text{m}$ largest diameter) at a high throughput to a spot smaller than $20 \mu\text{m}$.

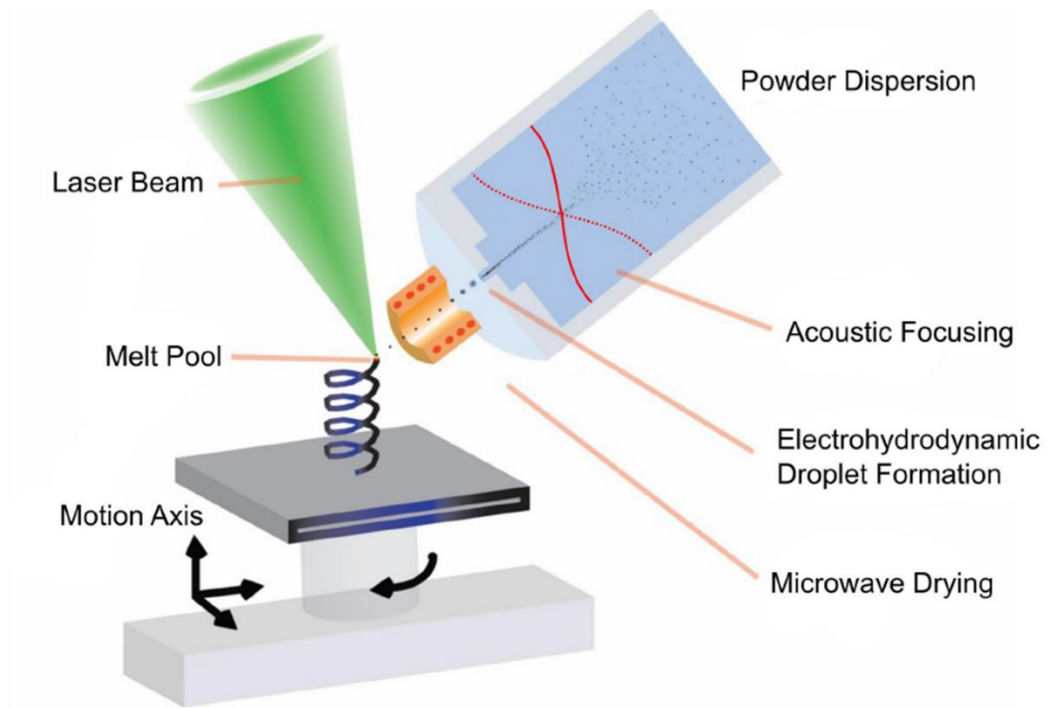


Fig. 1.4: Schematic illustration for SFA-AM "Powder Focusing".

This approach is concerned with a new powder focusing system in combination with other processing techniques, especially acoustic focusing, liquid jetting, and microwave drying. The system will be established in an existing powder-DED chamber with a laser focused to comparable spot dimensions ($< 25 \mu\text{m}$ diameter). The 3-axis system, which moves the substrate to build the designed part, can guarantee a precision of better than $5 \mu\text{m}$ in all three dimensions.

This extraordinary technique can contribute to Switzerland's industry, renowned for its expertise in high precision and the highest quality machining of any materials. It is capable of imparting in med-tech, watch industry as well as a multitude of related branches since its capability to open up alternatives to conventional, subtractive micro-manufacturing.

The final target in this project is the creation of a metal spring of $40 \mu\text{m}$ wire diameter, $200 \mu\text{m}$ spring diameter, and 2 mm height, as shown in Fig. 1.4.

1.2.3 Research scope

In order to achieve the goal, the project aims at decreasing the powder feed spot size, which is a prerequisite for the accuracy improvement of additive manufacturing before the laser melting process. Hence, the material supply process is studied in two tracks. The first approach is based on the preparation of the stable powder dispersed liquid, its acoustic focusing using the piezo device (by project partner ETHZ), transfer into the droplets ejection using EHD (ElectroHydroDynamic) process (by ETHZ), and drying by the microwave resonator or natural evaporation (by PSI). The second approach adopts the metal precursor dissolved in the solution to form size-controlled droplets or a laminar jet by a vibration-enabled generator with a micro-nozzle. Next, the material passes through a microwave resonator to dehydrate the liquid fraction in a concept similar to the previous approach and then is delivered into a laser beam (by PSI). Each procedure is compatible with different steps and assemblies. For example, the acoustic powder focusing technique can be combined with a droplet generator. In addition, the entire modeling and simulation concerning the particle behavior in liquids, droplet formation, jetting ejection, and drying process are carried out to support the experimental work (by EPFL). All of these approaches are tackled by the consortium consisting of the partners ETHZ, EPFL, EMPA, and PSI, and the obtained results are used to decide about the method integration into the printing system.

The research scope at each site is summarized in Fig. 1.5. At PSI, the main research focus lies in the droplet generation using kilohertz vibrations and the in-flight drying of the microscopic droplets using microwave heating, framed with a violet box in Fig. 1.5. It encompasses the development of the new experimental set-up and the corresponding validations. Hence, simulation studies are performed in parallel with experimental work in order to get a better understanding of the proposed process.

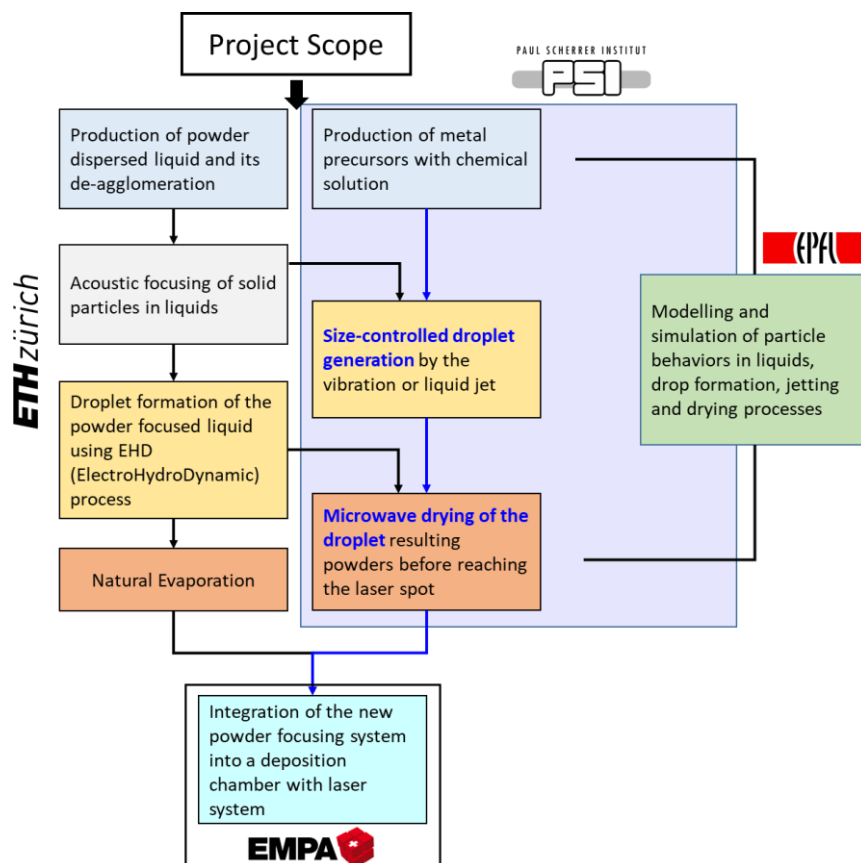


Fig. 1.5: Scope of research activities for "Powder Focusing".

1.3 Organization of the Thesis

A summary of each chapter of this thesis is given here, also providing an overview of the research flow.

Chapter 1. Introduces the background knowledge relevant to the AM technology and the purpose of the SFA-AM project, to which this work belongs. It focuses on areas requiring a new powder transport system to improve the resolution of the conventional metal AM process.

Chapter 2. Deals with the solution to accomplish the aforementioned goal. The fundamental concept that can produce and transport the powder based on microwave internal gelation, deriving from nuclear fuel production, is proposed and reviewed as an alternative. It also addresses candidate materials and synthesis processes and identifies feasibility for meeting project requirements. Lastly, an extraordinary regime composed of droplet generation and microwave drying is suggested as a final method to reach the objective.

Chapter 3. Describes the droplet generation using customized equipment with a permanent magnetic shaker. It analyses the resultant droplets in terms of size, gap distance, and linearity of their trajectories as the essential factors to guarantee the homogenous deposition of the AM technique. Some fluid-dynamic simulations based on the Navier-Stokes equation are carried out, not only to support the experimental result, but also to predict the break-up behavior of the droplet. The results can be used for the system setting.

Chapter 4. A newly developed coaxial microwave resonator is evaluated in terms of sensing performance. Firstly, the working principle that decides the resonance behavior is demonstrated by comparing to the conventional open-ended coaxial resonator. Furthermore, various water-ethanol mixtures with different concentrations are examined to extract the complex dielectric properties using different methodologies. Finally, to verify the microwave resonator's sensitivity, a tiny sample volume, being in the nano-liter range, is loaded through the micro-capillary into the module.

Chapter 5. This part is dedicated to microwave heating. A conventional cavity-type resonator and a modified coaxial resonator (Chapter 4) are experimentally tested in terms of heating. The aim is to achieve in-flight drying of dynamic droplets, which also corresponds to the final research goal. Additionally, statistical evaporation rates are demonstrated by droplet size measurements based on image processing.

Chapter 6. The heat and mass transfer-based verifications are adopted to demonstrate the initial temperature of the falling droplet in comparison with the data measured by a thermocouple. A numerical method is proposed to trace back the maximum temperature of the droplet that has just left the microwave resonator. This model includes a cooling effect until the water droplets reach the measuring device.

Chapter 7. All equipment being used for the thesis experiments is described including specifications. Moreover, some background information is given, in order to support the experimental work of this thesis.

Chapter 8. Finally, the conclusion and the meaningful outcome of the thesis are highlighted. In addition, some recommended continuation of the here treated research topic is presented.

Chapter 2 Preliminaries and Benchmark

In this chapter, the basic concept of microwave heating as the system's primary energy source is presented. Together with the droplet-based powder production and transport, this matched well the target of the en-framing project, where inflight drying of a droplet train is foreseen, in order to produce a highly focused powder stream for DED based additive manufacturing.

The chapter also states earlier work, which is useful to narrow down the relevant parameter windows for the concrete application. An important example for such a parameter is the frequency range.

In addition, a selection of materials, which are most appropriate for the targeted process, is given and justified. An important criterion here is the reaction mechanism, which would apply during the manufacturing process (potential gelation, drying process, entering the laser melt-pool, ...).

Finally, a new concept, that satisfies the entire project requirements, is proposed.

2.1 Overview of Microwave Heating

The project purpose is the development of a high resolution DED process, where the important aspect of providing a very narrow powder stream is researched here. Microscopic water droplets play therefore the role of keeping the powder concentrated in a stream. It follows a short description of how this is concretely implemented. Metallic powders (or metal powder precursors) are suspended in water. Droplets of this suspension are generated and directed towards the surface of the AM part under construction. The water droplets are evaporated during their flight. The dried metallic powder reaches the AM working surface ready for laser processing.

Microwave energy is selected as a heat source to provide a dried stream of powder to the processing surface, where the laser melting or sintering process is ongoing. In conventional heating methods, the heat can be transferred to the surface of materials by three types of mechanisms: conduction, convection, and radiation. The heating of the volume then occurs via thermal conduction, with the energy flowing from the surface to the center of the sample, until an equilibrium is reached. This process can be rather slow, leading to an initially pronounced temperature gradient. On the other hand, in microwave heating, microwave energy interacts with the dielectric materials by the electromagnetic field, usually because of the polarizability of the molecules. This means that the heating phenomenon arises from the inside of the sample entirely, with a dependency on the microwave penetration depth, which is mainly relevant for large samples (compared to wavelength); therefore, for rather small samples, microwave heating allows a uniform temperature distribution in the material compared to conventional heating that increases the surface temperature first. It can therefore be said, that microwaves provide volumetric heating. It also gives rise to rapid processing times directly causing time and energy savings. Hence, microwave heating is efficient for chemical synthesis, especially in nanoscale structures, to accelerate reaction speed with localized intensive heating. Furthermore, the resulting microstructure is very fine and homogeneous. It is, therefore, expected that the mechanical and chemical properties are more uniform and potentially better fulfill quality aspects. In addition, microwave processing also bears advantages for automated production systems, due to the instantaneous reaction time and also the capability to be combined with the conventional heating processes or by infrared laser, e.g., for compensation of surface cooling, in order to have most ideal processing conditions.

Nowadays, microwave technology is indispensable for the food industry. In addition, the utilization of microwave technology is extended more and more in the fields of materials and nuclear science, because of its applicability to a large variety of materials, such as metal, ceramic, wood, rubber, and chemical solutions. Especially, microwaves show various applications based on their wide frequency range and therefore also temperature control.

2.1.1 Energy Conversion

When microwaves encounter a load (contact with a media), three kinds of material interactions can be distinguished: transmission, reflection, and absorption, as shown in Fig. 2.1. Thus, there are different types and characteristics of heat generation. It can be, fast heating, heating after a particular time, or partial heating spots in electromagnetic field distribution based on anti-nodes. Moreover, there are cases where no heating is generated [31].

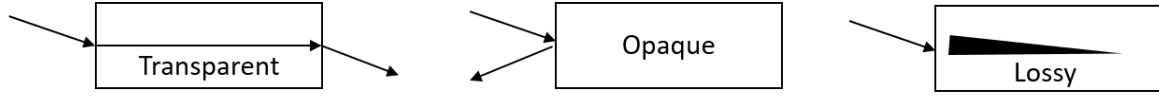


Fig. 2.1: Microwave interaction depending on the materials [31].

Microwave heating is an interaction between the targeted materials and electromagnetic field. The property of dielectric material can be characterized by (2-1):

$$\epsilon_{abs}(\omega) = \epsilon_0(\epsilon'(\omega) - j\epsilon''(\omega)), \quad (2-1)$$

where ϵ' is known as a dielectric constant representing the relative value of microwave energy density in the material. The ϵ'' accounts for the loss factor of each material corresponding to the internal energy loss, leading to the heating phenomenon. It means that highly lossy (large ϵ'') materials can absorb microwave energy well, converting it to heat energy. For typical dielectric heating, middle ranges of ϵ'' , ($10^{-2} < \epsilon'' < 3$), are suitable [31]. Through the complex form of ϵ , it is possible to anticipate the net absorption rate of the microwave energy in the materials.

There are multiple mechanisms for the energy conversion from microwave to heat, for example, dipole rotation, ionic conduction, stretching of molecules, and electronic and atomic displacement [31].

The details are handled in Chapter 4 for microwave sensing.

2.2 Microwave Internal Gelation Process

Internal gelation is one of the applications where microwaves can be utilized as an energy source to promote a temperature rise, which launches the chemical reaction leading to the gelation of a liquid phase. Alternatively, other heat sources can be used, with the disadvantage of potential contamination (e.g. silicon oil). The research of microwave triggered gelation has been carried out by many researchers regardless of their field, in particular, working in the nuclear field to implement an aqueous simplified production process, with less contamination risk, but also implying a new fuel concept called Sphere-PAC fuel, replacing the conventional pellet type for reactors using reprocessed fuel, especially SFRs [32–37].

The internal gelation method has encouraged the realization of sphere-pac fuel, as spheres of designed sizes are the direct product. Fig. 2.2 (a) shows the corresponding route, named the KEMA process. In brief, a feed solution as a result of mixing *HMTA*, urea, and nitrate solutions is prepared beforehand. In this stage, the experimenter should prevent premature gelation by keeping the solution at a low temperature of about 270 K. The mixture is then extracted from the droplet generator, where the droplet size is governed by variables such as the nozzle, flow rate, and generating frequency. The produced droplets fall into a silicon oil bath at about 373–379 K temperature to induce the gelation reaction, resulting in the particles.

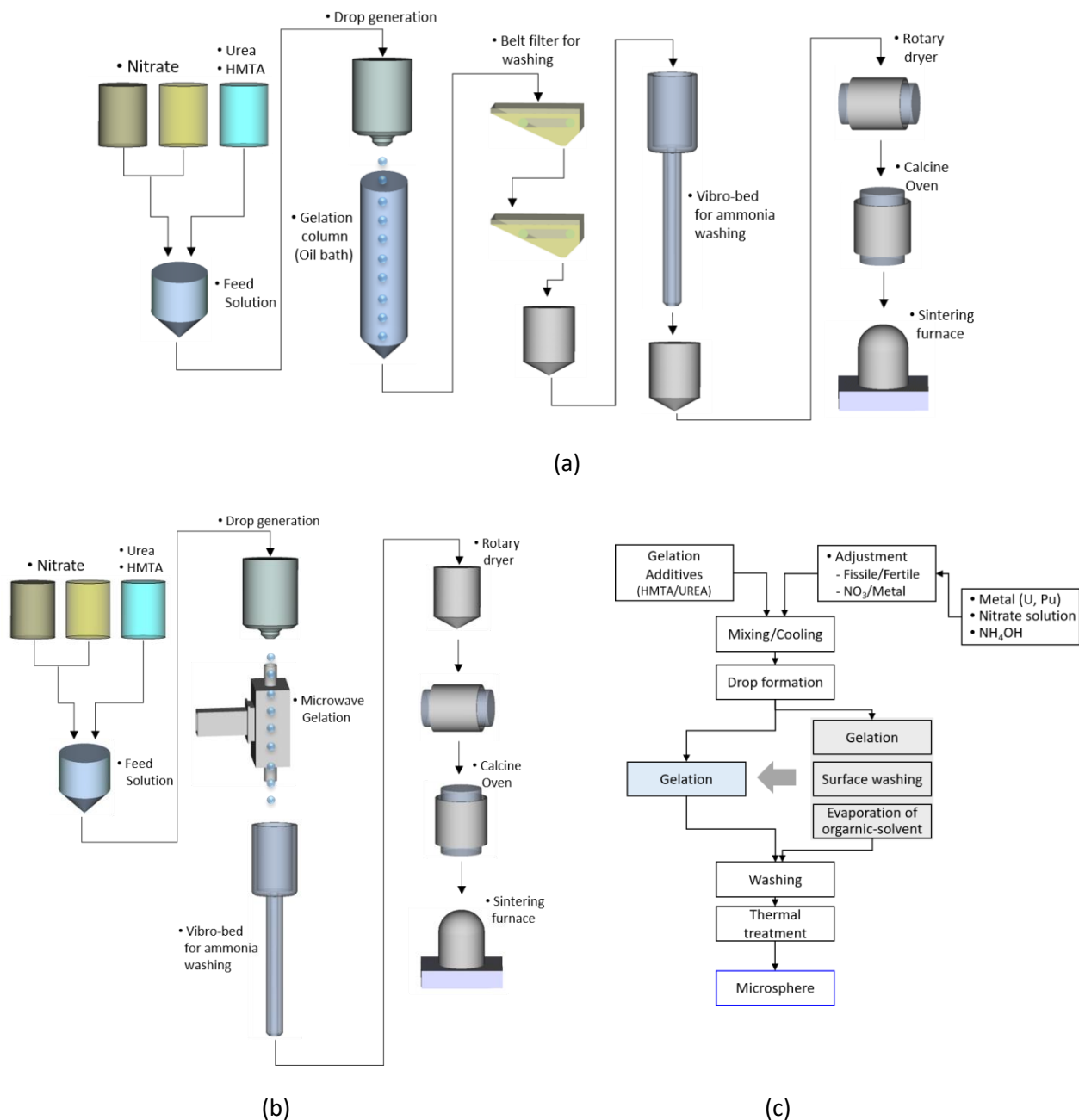


Fig. 2.2: Comparison of sphere-pac production processes: conventional method (a), microwave internal gelation [MIG] (b), and the procedure comparison (c) [34].

Subsequently, the particles pass a couple of belt filters for both, oil removal, as well as rinsing with organic solvents for washing. The sphere particles are lastly rewashed in ammonia solution to get rid of residual contamination that leads to undesirable chemical reactions. A final conventional sintering process follows to obtain the spheres in their final chemical and mechanically stable form, so that they can be introduced in the Sphere-pac.

In this process, it was first suggested to use microwave technology for drying (and calcination) of particles after the washing process as a batch-type process [32, 38]. Later, the continuous Microwave Internal Gelation [MIG] method, using a cavity resonator, was suggested by G. Ledergerber [33, 34]. In more detail, the droplets created from the droplet generator fall along the central axis of an X-band cavity (8.2 - 12.4 GHz), where several electric field nodes are present, inducing temperature rises and finally the gelation (Temperature

difference: $\approx 60 - 80$ K). For complete gelation, a power of 80 – 100 W was required. The comparison between MIG and the conventional method for gelation is described in Fig. 2.2 (b) by G. Ledergerber [33]. On the other hand, Yamagishi et al. conducted gelation experiments using 2.45 GHz and a power of 5 kW, to reach the same temperature shifts (80 K) as for the X-band operation at below 100 W [35–37]. Rosin et al. examined both experiments and conducted simulations using the software Quickwave-3D to research the efficiency of microwave range straightforwardly. They demonstrated that the efficiency at 12.4 GHz was two orders of magnitude higher than at 2.45 GHz to reach a temperature difference of 80 K for a droplet [39].

In other words, the latter study manifests that for the rapid heating of droplets the X-band frequency achieves significantly higher efficiencies, where the system components are also miniaturized compared to the S-band.

However, the requirements need to be clearly defined according to the planned usage, prior to the system configuration. The reason for that is the manifold parameters influencing the gelation or heating of droplets, for example, frequency, power, exposure time, properties of materials (thermal and dielectric), droplet size, cavity shape, E-field distribution, energy absorbance, and boundary conditions.

2.3 Candidate Materials

Fig. 1.2 (throughput vs. feature size) shows the performance of different AM processes, and especially that the liquid-based ones exhibit higher resolution although the productivity is rather low. The main reason is that these methods can offer feed materials in smaller sizes than commercially available powders.

Metal inks can be roughly categorized into two types such as suspension-based inks and precursor-based inks. The latter is known as Metal-Organic Decomposition ink (MOD-ink), consisting of a metal salt, amine/amino hydroxyl ligands, and other organic components that form the metal or oxidized metal by heat decomposition. The former stands for the dispersed fine-nano particles used for the ink-jet formulation. The ink is printed and then sintered using thermal processing. Suspension-based inks have some advantages compared to MOD inks in terms of loading amount and contact resistance between particles [40].

To obtain nanoparticles for suspension inks, both, high energy and long processing times, are needed. For example, a high-speed centrifuge and vacuum drying after a washing stage. Moreover, an amount of surfactant or additive is essential for the stabilization of the ink without aggregation, even though this can interfere with good metallic properties [41]. In addition, it is possible to clog the micro-nozzle in the droplet formation step due to potential unwanted agglomerations that can occur in the process.

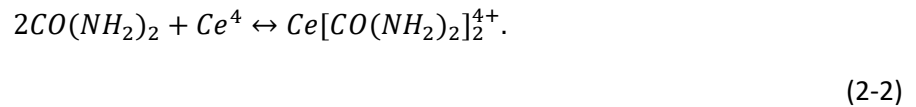
In contrast to suspension inks, MOD inks denote metal precursors dissolved in proper solvents or organic complexing agents that serve as solvents (water, formic acid, acetone, glyme, pyridine, xylene, amino hydroxyl compounds, etc.) [41]. There is no solid-state or any agglomeration caused in MOD inks. Here candidate procedures are introduced to obtain the gel or powder state that includes the metal ions, which is not only pure metal but can also be metal-oxide.

2.3.1 Material Reaction of the Internal Gelation

The “internal gelation”, which is one of the sol-gel chemical processes, can produce microspheres of hydrous metal oxides using *HMTA* (hexamethylenetetramine), Urea, and a metal nitrate solution [42]. This method was initially developed by M.E.A. Hermans and others at KEMA, Arnhem, the Netherlands. The process can be briefly explained as follows: the hydrolysis of hexamethylenetetramine [*HMTA*] $[(CH_2)_6N_4]$ in a uranyl nitrate solution releases the base NH_4OH , which results in rapid and uniform solidification of the solution drops into gel spheres [43–45]. It is called the ‘KEMA process,’ considered a standard process to produce UO_2 spheres as fuel particles for advanced concepts. This technology was emerging as state of the art in the 1970s because it would not only decrease the mechanical processing steps and difficulties connected to the pellet production but also be capable of remote operation. It only handles liquid-based materials or microspheres without dust. Therefore, connected with the right fuel concept, the gel-sphere preparation replaces the powder conversion [38]. An additional advantage of this method is that it can control the average size of spheres from 30 to 1500 μm [32, 38]. Hence, it can theoretically reach a packing ratio up to 90 % with the blending of ternary sphere sizes and more than 90% with vibration aid additionally. The packing ratio is almost the same as with pellets of 91 - 95 % [46–48].

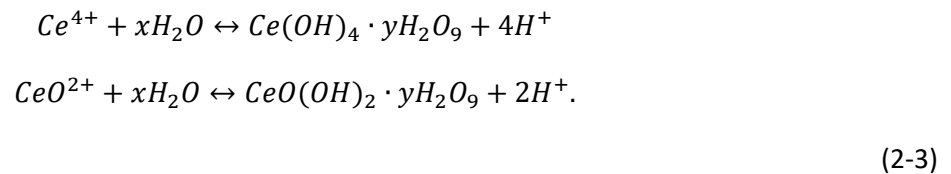
The essential chemical reactions of the internal gelation are described as [42, 49],

a) Complexation/Decomplexation



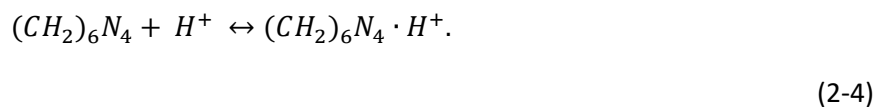
Urea plays a role as the complexing agent for the metal ion. It allows the solutions to be stable without unwanted reaction (precipitation) at low temperatures (e.g., 0 °C). The decomplexation occurs when the temperature is increased.

b) Hydrolysis



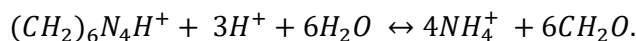
The decomplexation gives rise to the hydrolysis of the cerium.

c) *HMTA* protonation



It is a procedure to remove the H^+ from the solution. Therefore, *HMTA* decomposition does not take place even though the temperature reached 90 °C without the protonation of most of the *HMTA*.

d) HMTA decomposition



(2-5)

Protonated *HMTA* begins to decompose into ammonia molecules by removing three additional hydrogen ions. The resultants are formaldehyde and ammonium nitrate. The formaldehyde can react with the Urea to accelerate *HMTA/HNO₃* decomposition at a given temperature.

2.3.2 Material Reaction of the Thermal Decomposition

The final application of the SFA project is the 3D printing of a conductive material, a metal, with a very high-resolution. Unfortunately, most of the available conductive inks are based on noble metals like silver and gold regardless of their cost-competitiveness. Instead, beneficial for cost-effectiveness, copper is emerging which also has a substantially higher conductivity. However, to overcome the oxidation of copper, additional gas protection is needed for the fabrication process (e.g., for fabrication of electronic devices).

In this research, copper-formate ($Cu(HCOO)_2$) is considered as the candidate material. Numerous studies have been reported on the possibility of replacing noble conductive metals by using copper-formate in the electronic field. Because this material can not only be readily dissolved in water or other solutions, but it also decomposed by thermal energy, resulting in a pure metallic state of copper at around 200 °C. That is one of the methodologies to make a transmission line on an electric circuit board without damaging the substrate (e.g., the substrate being PI, PET, or PEN).

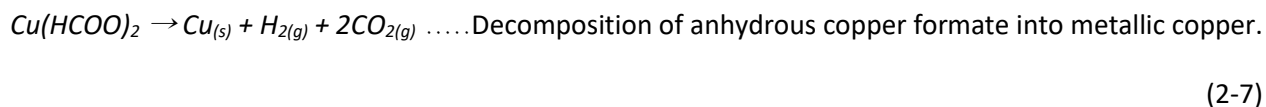
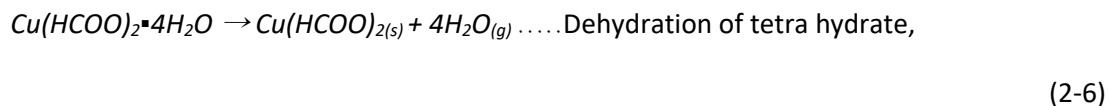
The by-products originating from thermal decomposition are not harmful to humans because they are composed of CO_2 , H_2 , and H_2O , except for the copper product. Water, as a solvent of copper-formate, is not evaporated faster than other organic solvents under ambient conditions, which means that the crystallization of copper is not occurring immediately. CO_2 and H_2 , by-products of copper-formate decomposition, may be operated as a shielding gas during the drying process, because of their chemical inertness.

To further optimize the conductivity, some researchers imposed a protecting layer on copper to prevent oxidation or used milled materials giving rise to a more dense structure. These techniques allow increasing the conductivity of a copper pattern more than 20 % of bulk metal. Besides, they also added an inert shielding gas in the sintering step to prevent oxidation [50–53].

The majority of the research about metal copper making from the copper-formate solution used typical screen-printing or spin coating before the sintering process. The coating layer that is not exposed to the interaction with the laser, is removed by a washing process [50, 52–54].

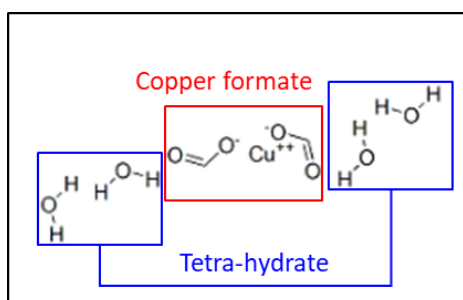
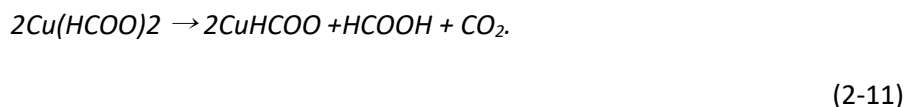
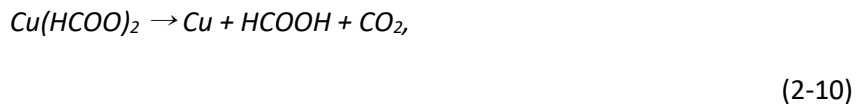
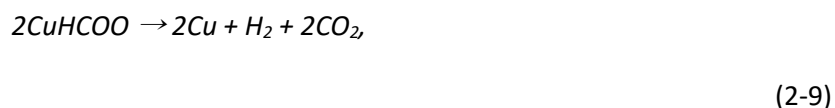
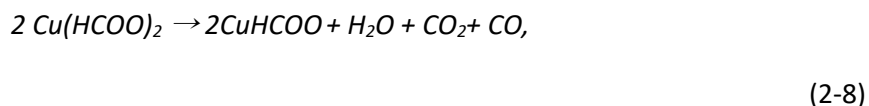
In this study, copper formate tetrahydrate ($Cu(HCOO)_2 \cdot 4H_2O$) was preliminarily tested as a candidate material because of its simple ligand complexity. The use of this material is covered in Chapter 5.

The general scheme of chemical decomposition is expressed as

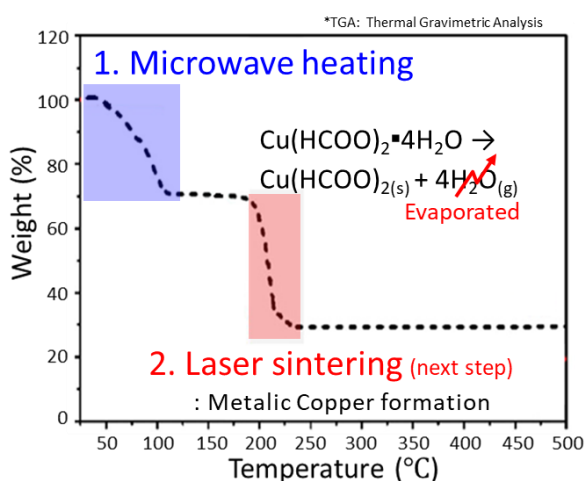


The first reaction (2-6) represents the first weight loss in Fig. 2.3 (b) that starts from near 50 °C and finishes at 114 °C because of dehydration of tetrahydrate. The reaction (2-7) corresponds to the second weight loss that starts around 188 °C and ends near 240 °C resulting in the decomposition of anhydrous copper(II) formate into metallic copper [55]. In the frame of this project, the microwave is in charge of the first reaction, and the green laser is responsible for the second reaction.

Another expression for the thermal reaction is also reported by Keller [56],



(a)



(b)

Fig. 2.3: The chemical structure (a) and TGA data (b) of the copper-formate tetrahydrate [55].

According to the information supported by a supplier, for copper-formate tetrahydrate, a maximum of 125 g can be dissolved in a water volume of 1 liter.

In the solution, the maximum mass of copper dissolved in one liter water is given by

$$Copper\ mass_{1l\ water} = \frac{Solubility_{cft} \cdot Purity_{cft} \cdot M_{Cu}}{M_{cft}}, \quad (2-12)$$

where subscript *Cft* and *Cu* indicate the copper formate tetra hydrate and copper.

The maximum size of copper powder after droplet generation and drying is given by

$$Diameter_{Cu} = \left(\frac{Volume_{Cu}}{Volume_{Cu} + Volume_{water}} \cdot Volume\ of\ droplet_{generator} \cdot \frac{3}{4\pi} \right)^{1/3}, \quad (2-13)$$

where M_{Cu} and M_{cft} are molecular weight of copper and copper formate tetrahydrate, respectively.

The size of the copper powder depends on the droplet generator and the nozzle size.

The advantage is that the process of the later elimination of the sacrificial layer is no longer required. Furthermore, a stepwise heating process composed of microwave drying and laser sintering can reduce the porosity of copper powder more than a laser process covering both drying and sintering simultaneously.

Moreover, water is efficient for microwave heating because of the high dielectric loss factor in the X-band range, as discussed before.

2.4 Concept for New 3D Printing

The idea to introduce a novel concept of additive manufacturing, based on the gelation process, formerly leading to the Sphere-PAC fuel concept, was registered as a patent by M.A Pouchon [57]. The sphere particle, as a result of the internal gelation method, motivates the possibility of producing a gel, whose dried phase can be used as powders for additive manufacturing, also the direct printing of the gel is considered. Moreover, this process is not limited to gelation reaction but can also extend to any metal precursor based on thermal decomposition. The powder for 3D printing should satisfy requirements such as size distribution, fluidity (sphericity), purity, oxidization, and absorbance of the energy. The properties described are highly relevant to the defect of structures fabricated by AM technology.

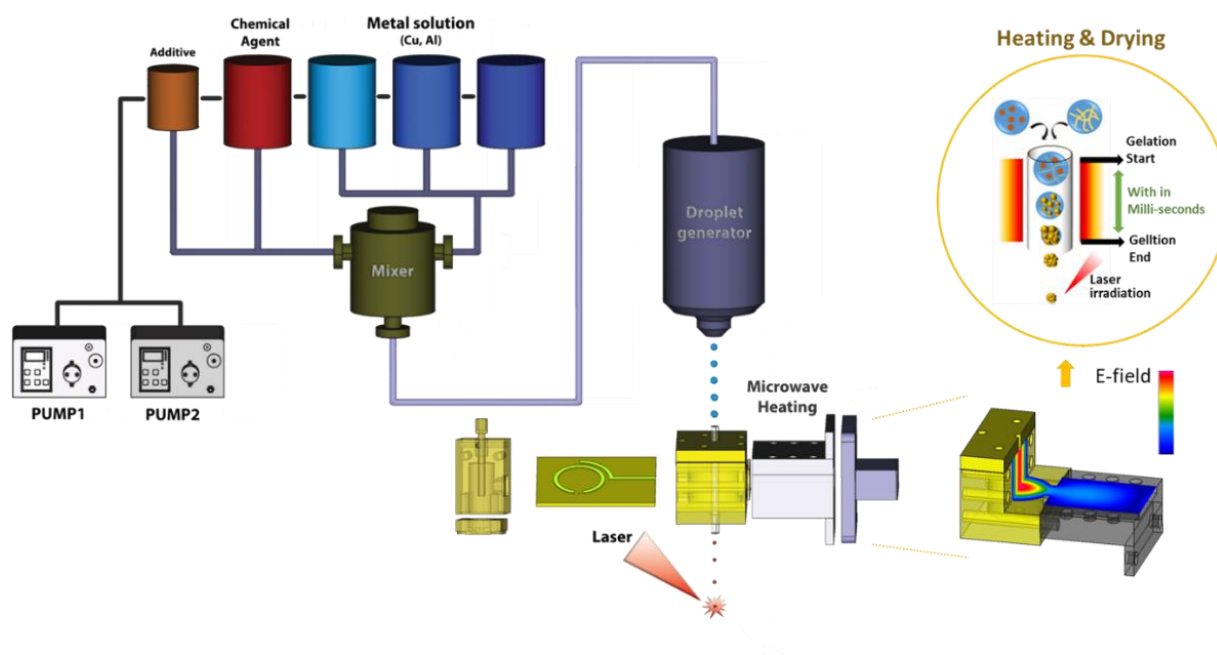


Fig. 2.4: Scheme for new 3D printing.

The microspheres produced from the sol-gel method can meet the requirement of 3D printing materials in many areas. The sphericity, the ratio of maximum diameter to minimum one, is about 1.1 in the case of a 500 μm ThO_2 (Thorium dioxide) sphere ball in diameter without density difference. The size distribution strongly depends on the droplet generation, and the result can be shown as the standard deviations of $< 1\%$ of the average diameter in the case of long-period operation of the droplet formation. In addition, the contents of oxide can be decided by environmental factors, which can be controlled during the process, for example, applying inert gas such as N_2 and Ar , in the stage of not only gelation but also the heat-treatment process. Of course, there is no way to achieve zero oxidation, but it can approach the lowest possible oxidation [45, 58, 59]. Typically, the uniformity of the sphere-pac concept in the nuclear field is more important than in the 3D printing field, because of fuel performance issues.

A modified concept for 3D printing is illustrated in Fig. 2.4. This process is almost identical to the MIG method. The apparent difference between them is the laser sintering process that will take place continuously after the MIG process to create the designed part.

The main objective of this project is the inflight drying process of droplets produced to be microscopic metal powder containers to improve the additive manufacturing resolution. Fig. 2.4 shows hereby the procedure. The research topics to accomplish this goal are roughly divided into the following two sections: droplet generation and microwave drying. Numerous research works have been carried out since Savart and Rayleigh to fully understand droplet behaviors. The details are handled in Chapter 3.

This project concentrates on the droplet generation with both, a small and uniform size of below 20 μm diameter, for the internal gelation or thermal decomposition, as well as a high throughput, unlike the drop-on-demand systems (e.g., for inkjet printing). Meanwhile, in terms of the microwave technique, most of the published studies using microwaves for a 3D printing process focus on the localized solidification during or after

the building process, which is fundamentally similar to the conventional ceramic sintering process [60, 61]. Nevertheless, in this project, a microwave resonator is used for the complete in-flight drying of the extracted droplets, which act as containers for the metal powder before laser irradiation as a manner to realize a highly focused ($< 20\text{ }\mu\text{m}$) powder feeding. There is only rare reference data for in-flight drying of droplets, especially in connection with making a powder stream for an AM process, except for the previous research from our lab [62–64]. This new approach will lead to a highly focused, precise, and convenient powder feeding technique, enabling high-resolution 3D printing. Various advantages are expected from the MIG system combined 3D-printing procedure as described hereafter. First, the user does not need to handle the hazardous powders in the preparation step. Second, it can be a fully automated system without user intervention, which potentially results in high and reproducible quality. The powder size can also be controlled in real-time, by adjustment of the droplet generator's parameters in the manufacturing process. The process is associated with the resolution improvement of the direct laser melting process. Moreover, the user does not need to care about nozzle clogging, as it is not a suspension with particles being contained. Lastly, it overcomes the cost burden of the powder, which is generally used for 3D printing, being expensive due to the yield rate of the gas atomization method.

The challenges to be addressed in order to attain the project goal remain at each step as follows:

1. Choice of appropriate material for the system.
2. Securing of uniform droplet generation (size, linearity, and gap distance between droplets).
3. Efficient microwave applicator with miniaturization to integrate with other systems.
(Co-plane, Co-planner, and Cavity resonator).
4. Optimization of laser sintering parameters with environmental circumstances.

The thesis encompasses the entire area except for topic 4, but mainly focuses on topics 2 and 3.

Chapter 3 Droplet Generation

This chapter introduces various methods to initiate droplet formation. Furthermore, the working principle of a customized droplet generator developed for the present project is explained with some emphasis on the break-up behavior.

The customized droplet generation system based on a permanent magnetic shaker was fabricated at PSI and studied to evaluate the parameter effects that mainly influence the droplet's characteristics, such as frequency and flow rate. The droplets obtained by the experiment are characterized with respect to their size distribution, gap distance, and distance from the average trajectory (i.e., Linearity), which strongly affect the uniformity of the AM deposition. In addition, numerical fluid dynamics simulations using the OpenFOAM open-source code are introduced to estimate and compare the droplet behavior. These computational studies also specifically help to identify the optimal conditions that can produce the smallest droplet size in the given experimental setup. Finally, the simulation results are compared with experimentally obtained data to determine the validity ranges of the droplet break-up principle. These simulation results offer the possibility of a new system construction that can generate defined droplets without repetitive experiments (e.g. piezo shaker).

3.1 Background

The liquid jet is typically defined as a stream of fluid ejected into the surrounding medium from a nozzle or orifice. A high fluid momentum compared to the environmental medium allows the flow to keep traveling a certain distance without dissipation.

The classical investigation of the liquid jet was performed by Savart in 1833, who proposed the two “Laws” of jet disintegration: (1) the length of the continuous jet stream is proportional to the jet velocity for a constant diameter, and (2) the stream length is proportional to its diameter for constant velocity [65]. It is the first quantitative analysis that figured out the relationship between the stream break-up (e.g., length of a continuous jet) and parameters such as jet diameter and velocity affected by the nozzle and the flow rate [66]. In 1873, Plateau carried out the experimental work based on Savart’s investigation and demonstrated that a continuous jet transforms into drops by decreasing the surface energy once the length of a jet cylinder exceeds a critical threshold. It was the basis for the widely known theory of jet stability [67].

In 1878, Lord Rayleigh extended the theory of instability from Plateau’s study for the liquid jet system in the way that a cylindrical fluid jet reduces its radius up to the break-up when the symmetrical disturbance wavelength in the axial direction is greater than the circumference of the cylinder jet. From the linearized analysis of the growth rate resulting from the infinitesimal disturbance, the break-up length is reasonably estimated considering the surface tension and inertia force. The liquid and surrounding medium properties should be taken into account additionally to represent the reality [68]. Weber conducted a further concrete analysis, which includes the effect of a viscous jet, considering its surface tension, and formulated this as a simplified form. He showed that the break-up of the viscous jet takes place slower than for an inviscid jet [69].

In addition to these significant studies conducted in the past, many other researchers demonstrated jet behavior theoretically and experimentally. The research history is concretely summarized in [66].

This topic is still in the spotlight because of the importance of jet stability and disintegration, and the understanding of these phenomena in numerous applications is driven by industrial needs. Dripping and atomization, for example, is a fundamental concept applied particularly for inkjet-based industries, including additive manufacturing.

3.1.1 Droplet Formation Mechanism

There are different mechanisms governed by parameter sets, which will define the type and reach of the initial liquid jet, and its breakup into droplets. Representative variables are nozzle size and velocity of the extruded liquid, gravity, surface tension, friction, and disturbance-related forces.

Fig. 3.1 represents the different mechanisms of droplet formation as a function of jet velocity into the quiescent air. These are classified as dripping, Rayleigh jet, first wind-induced break up, second wind-induced break up, and atomization, respectively.

The main criterion to distinguish all the mechanisms depend on the Weber number, We , which stands for the ratio of the inertia force against the surface tension force.

$$We_l = \frac{\rho_l \cdot v_l^2 \cdot d_l}{\sigma}, \quad We_g = \frac{\rho_g \cdot v_l^2 \cdot d_l}{\sigma}, \quad (3-1)$$

where ρ_l , v_l , d_l , and σ are the density, velocity, and diameter of the liquid jet and surface tension coefficient, respectively. When the velocity of the liquid jet is high enough (Mechanism III - V), the density of the gaseous medium, ρ_g , can replace the liquid property, ρ_l , to consider the density contribution of the surrounding gas, resulting in the change from We_l to We_g . Subscripts l and g indicate the liquid and gas status.

Mechanism I. The exit jet velocity is low; the single droplet forms on the nozzle and then is detached when the gravity force exceeds the inertial force governed by the surface tension.

Mechanism II. With increasing kinetic force, the droplet formation is not taking place directly on the nozzle due to the outflow velocity. The axis-symmetrical disturbance originating from the instability and surface tension can lead to a break-up of the droplet further down in the stream.

Mechanism III. Further increasing the outlet velocity over the Rayleigh regime results in a wavy appearance along an axis. The main driving force of the break-up arises from air friction. The break-up distance decreases in this mechanism.

Mechanism IV. The high friction force driven by the interaction between the velocity of the liquid jet and the quiescent air can burst the jet surface and split it into a tiny droplet. As a result, the flow is no more maintained in a laminar regime and changes to a turbulent flow resulting in a short break-up length.

Mechanism V. This is characterized by a very high velocity of the existing liquid. The atomization is generated after the nozzle instantaneously. The sizes of droplets are smaller than for other mechanisms but irregular.

Mechanism I and **Mechanism II** are both techniques mainly used to obtain size-controlled droplets, but **Mechanism II** is more suitable for mass production.

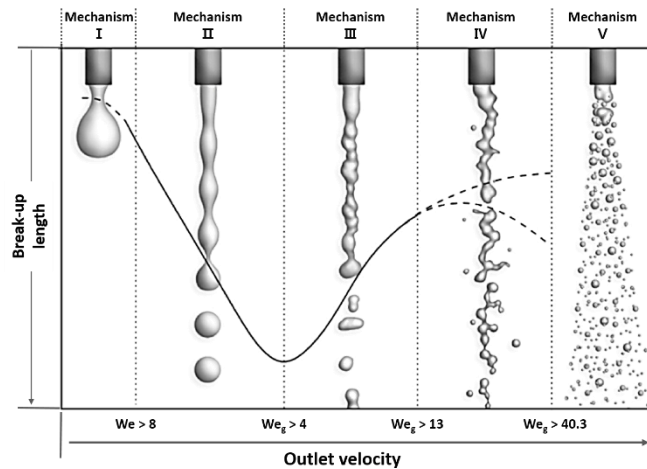


Fig. 3.1: The mechanisms of the droplet break-up in the quiescent air. Impact of outlet velocity on break-up length of injected liquid from a circular nozzle [70].

Other dimensionless numbers, such as Reynolds and Ohnesorge, are also critical factors that can influence the droplet formation setting of Newtonian fluids.

Reynold number, Re , and Ohnesorge number, Oh , dictate the ratio between the inertial force and the viscous force, as well as the interaction of the viscous force to the surface tension.

$$Re = \frac{\rho \cdot v \cdot d}{\mu}, \quad (3-2)$$

$$Oh = \frac{\sqrt{We}}{Re} = \frac{\mu}{\sqrt{\rho \sigma d}}, \quad (3-3)$$

where μ is the dynamic viscosity of the fluid.

Each of the explained droplet formation mechanisms is described in Fig. 3.2, established by Wolfgang von Ohnesorge in 1936.

In general, for inkjet printing, the number of Ohnesorge (Oh) to ensure a uniform jetting ranges approximately from 0.1 to 1.0.

Many satellite droplets accompany the primary drop at the low Oh values. In contrast, the high viscosity of the liquid induces abnormal liquid extraction, as the kinetic energy is insufficient to form the jet. Of course, the operating conditions and other experimental settings of droplet formation, including liquid properties, should be considered [71, 72].

The reference [73] summarizes well the details related to the droplet formation mechanism.

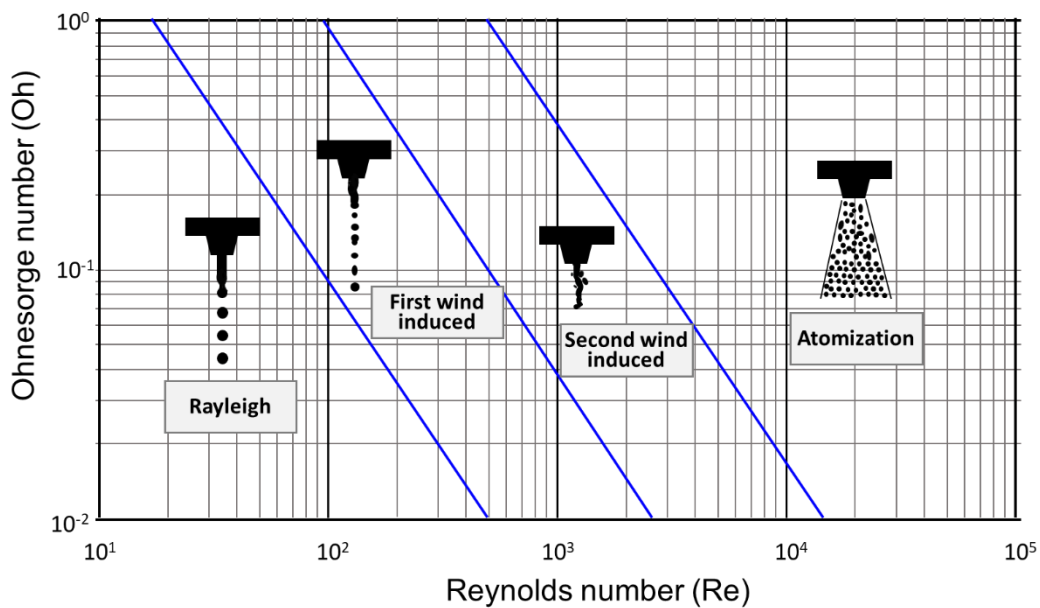


Fig. 3.2: The Ohnesorge diagram [74].

3.1.2 Droplet Generation Method

The inkjet industry's typical principles of forming droplets are divided into two ways. These are known as drop-on-demand (DOD) inkjet and continuous inkjet (CIJ), respectively, corresponding to the Dripping and Rayleigh ranges of the previous section. The DOD methodology is more appropriate to generate the individual drop at a precise position. A pressure force resulting from the piezoelectric transducer (mechanical actuation) or thin-film heater (bubble collapsing) promotes droplet formation and ejection.

However, due to the low productivity of the DOD methodology compared to the continuous process, this chapter is more dedicated to the continuous droplet formation. CIJ occasionally used to be evaluated as a wasteful process, since it could generate the droplet when no printing is required. Nonetheless, it is an appropriate approach to meet both the productivity and size-controlled droplet requirements, especially for direct energy deposition (DED) in additive manufacturing, where a laser and material are coaxially focused on a substrate to build a part. This high-throughput droplet generation is formed by the Rayleigh instability of the cylinder jet associated with capillary (surface tension) forces and inertia, inducing the uniformly-sized drop's break-up, with one drop produced per disturbance wavelength. Liquid jets can decompose into droplets at a certain distance from the nozzle due to the maximum growth rate of an axisymmetric disturbance [66]. Typical droplet formation techniques by different artificial disturbances are shown in Fig. 3.3 [73], and are listed below. Recently, this technology has been widely used in the medical field for powder manufacturing and microencapsulation.

1. Simple dripping:

This is the simplest way to create a droplet by the gravitational force of a liquid suspended in a nozzle. A common drawback is that there is no force to help break up the liquid, resulting in large droplet sizes.

2. Dripping supported by the concentric jet:

Concentric jets formulate shear forces in laminar jets. As a result of these perturbations, the liquid stream disintegrates into droplets. However, there is a limit to increase the flow rate and therefore the productivity.

3. Dripping supported by electrostatic forces:

Electrostatic forces are a common source of generating droplets in printing technology. An opposite charge is applied to the bath or other metal plate to create an electric field where the liquid jet passes. It is suitable for the laboratory scale or DOD application because of the flow rate restriction, which can give rise to the break-up similar to technology 2.

4. Dripping supported by the vibration force:

Size-controlled droplets can be easily obtained by vibrational techniques using piezoelectric materials, magnets, and other mechanical systems. The vibrating force can create a meniscus of the liquid attached to the nozzle and eject the droplet. Otherwise, it can perturb the laminar jet and accelerate instability, acting as a cause of droplet disintegration. The droplet size control is easily achieved by modulation of the oscillation frequency.

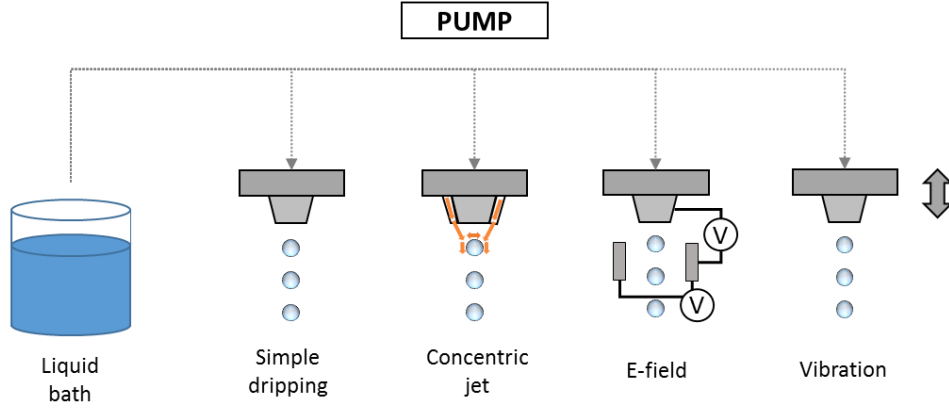


Fig. 3.3: Typical droplet generation methods [73].

In this study, a vibration technique is employed to split a laminar jet into uniform droplets with high throughput, and vibration-induced perturbations are responsible for breaking up the laminar jet.

3.1.3 Droplet Generation Mode

a. Natural Mode

In the absence of vibration, the size of a droplet is determined by the equilibrium between gravitational force and surface tension, which corresponds to the dripping mechanism.

$$d_{size} = \sqrt[3]{\frac{6 \cdot d_N \cdot \sigma}{g \cdot \rho}} \cdot K,$$

(3-4)

where d_{size} and d_N are the diameter of the droplet and the nozzle, σ , g , and ρ are the surface tension, acceleration of the gravity, and density of the dripping liquid. The K is a correction factor obtained by the experimental result for the approximation [75].

With increasing the flow rate of the liquid, Rayleigh's instability is working on the continuous stream. Consequently, the cylindrical jet is transformed into a droplet regime by the axial symmetric fluctuation of the laminar jet. However, it should satisfy the condition that the wavelength of the jet disturbance is longer than the circumference of the jet stream. Several mathematical formulas were proposed to predict the droplet size from the cylindrical jet under various conditions depending on the size of both the nozzle and jet, characteristics of fluids (e.g., viscosity), velocity, and other environmental aspects. For accurate estimation, adopting the calibration factor dependent on the variables described above is essential [76–79]. For instance, H.Teng suggested a methodology to estimate the droplet size in cylindrical jets, especially in low-velocity liquid jets, involving Newtonian/non-Newtonian with power-law fluids [76]. However, in principle, natural break-up by axial symmetrical vibration could not guarantee the outcome with perfectly controlled size. Since the disturbance is irregular, resulting in droplets of unequal size and shape [80].

b. Vibration Mode

The droplet formation induced by the vibrational force is more straightforward to understand the break-up phenomenon because it does not need to take additional complex factors into consideration. For example, in the Rayleigh mechanism, the vibration force plays a role in making the controlled disturbance on the laminar jet consecutively with a defined amplitude. This designed disturbance can accelerate the break-up of the droplet originating from the surface tension and ends up forming a drop with each vibration [80].

The droplet size is given by

$$d_{size} = \sqrt[3]{\frac{6 \cdot \varphi}{\pi \cdot f}} \quad (3-5)$$

The gap distance between the droplets is defined as

$$d_{gap} = \frac{\varphi}{A \cdot f} = \frac{4 \cdot \varphi}{\pi \cdot f \cdot d_N^2}, \quad (3-6)$$

where φ and f are the flow rate of the liquid and frequency of the vibration on the nozzle. Lord Rayleigh has demonstrated this relation by applying a sinusoidal vibration on the jet to obtain the size-controlled droplet reproducibly. According to (3-5), the droplet size depends on two main parameters: the applied frequency as well as the flow rate of the liquid. In addition, parameters such as nozzle size, liquid properties (e.g., rheology, surface tension, and others), and environmental conditions can also affect droplet formation. Finally, It is worth noting that a reproducible and regular break-up is obtained when the vibrational frequency is near the natural frequency of the jet itself [59]. A simple approach to approximate the natural frequency is expressed by the relationship between jet diameter (d) and velocity of the extruded liquid (v), as $v / 5d$ [81].

The high-throughput droplet generation, which is different from the natural mode governed by the equilibrium of strong cohesive force in molecules and the gravity forces, is an essential prerequisite for achieving the project goal. Therefore, water, which leads to rapid droplet disintegration due to high surface tension, is used as the medium for experimental validation.

3.2 Experimental set-up

A droplet generation system was fabricated at PSI to realize high-throughput droplet trains. It is principally composed of three parts: a power-amplifier, HPLC pump, and a permanent-magnet shaker, which are described below in Fig. 3.4. All detailed component specifications are dealt with in Chapter 7.

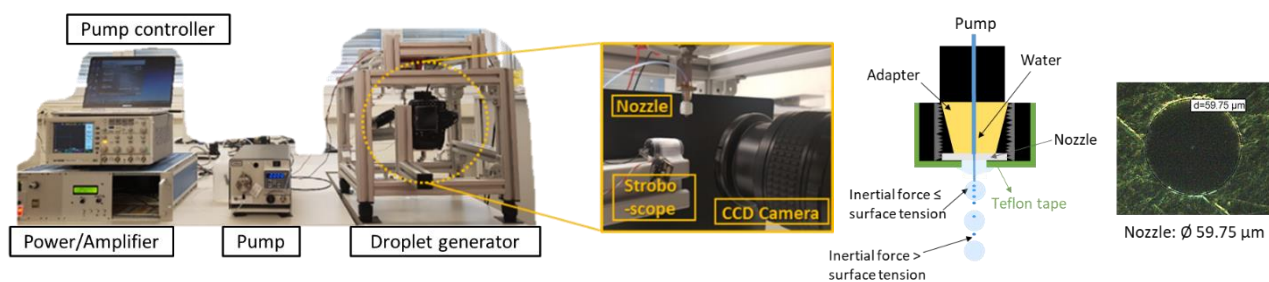


Fig. 3.4: Equipment for the droplet generator with a nozzle.

In this stage, these devices can produce various droplet sizes ($\varnothing 90 \sim 170 \mu\text{m}$) depending on the vibrations of the permanent-magnet shaker. The official oscillating frequency of the shaker by the supplier's recommendation is up to 13 kHz. However, it has been examined until 25 kHz to figure out the optimal working condition range. The generator's voltage can be increased up to 80 V; as a result, the shaker oscillates proportionally to the voltage applied with a certain amplitude. A nozzle for droplet formation is made out of a 100 μm thick stainless steel plate with a $\varnothing 60 \mu\text{m}$ hole machined by laser technology. The HPLC pump feeding the water from a container into the nozzle can control a flow rate from 0.001 up to 5 $\text{ml}\cdot\text{min}^{-1}$ with 0.2 % RSD. An in-line filter of 0.5 μm rating is included at the output port of the pump to prevent contamination. A CCD camera coupled with a high-speed flash can take an image of droplets during the operation of the shaker in real-time. To ensure more stable droplet formation, commercial PEEK tubes with diameters of 25 μm , 63.5 μm , and 100 μm (IDEX Health & Science Co.) are considered for use as nozzles for microwave sensing and heating in Chapter 5, Microwave Heating. An additional 1000 psi back pressure regulator was also installed to aid in pressure and flow rate stability. In conclusion, the $\varnothing 63.5 \mu\text{m}$ PEEK tube is eventually chosen in terms of droplet size, as the $\varnothing 25 \mu\text{m}$ tube cannot produce a spherical droplet shape with the current droplet generator settings. However, in this chapter, experiments were conducted using only the laser cutting nozzles due to the manufacturing precision.

3.3 Droplet Characterization

The droplets produced from the customized generator were investigated in terms of the size, gap distance, and linearity to obtain balanced feeding conditions of the material before entering the laser melt in the frame of the AM process, shown in Fig. 3.5. As an example, images of the droplet formation under the various frequencies with a 0.5 $\text{ml}\cdot\text{min}^{-1}$ flow rate are presented in Fig. 3.6. This is the minimum flow rate, where water droplets can be extracted from the nozzle of 60 μm \varnothing without sticking and forming a large drop. As a result, the droplets look quite uniform in the frequency range from 10 kHz (c) to 20 kHz (e). The post-processing of images was conducted based on a Mathematica® tool to quantify the uniformity (distance: 10 mm). Some hypotheses were assumed for image processing to define the interface between droplets and air, as explained below [82, 83]:

1. Light reflection is included in the droplet
2. The droplet has a circular shape
3. A compensation factor should be applied for the droplet size definition (inside the circle border)

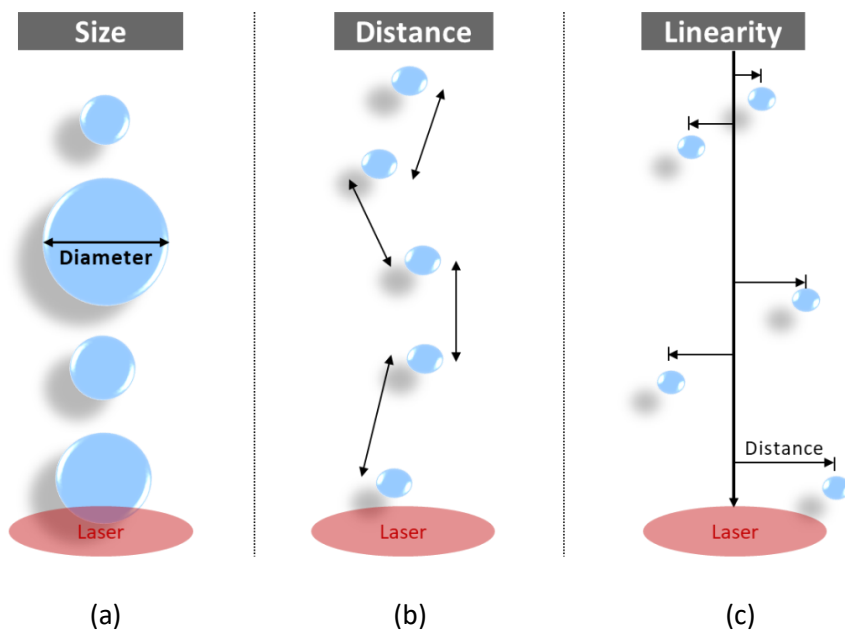


Fig. 3.5: Characterization factors of the droplet, size (a), gap distance (b) and linearity (c).

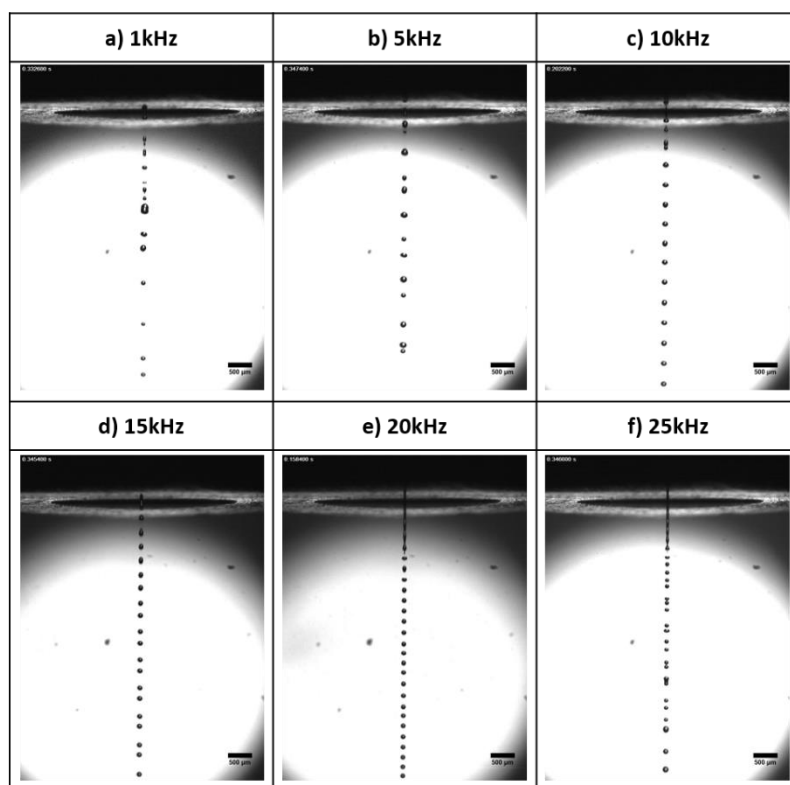


Fig. 3.6: Droplet formation images under various vibrational frequencies with $0.5 \text{ ml} \cdot \text{min}^{-1}$ flow rate.

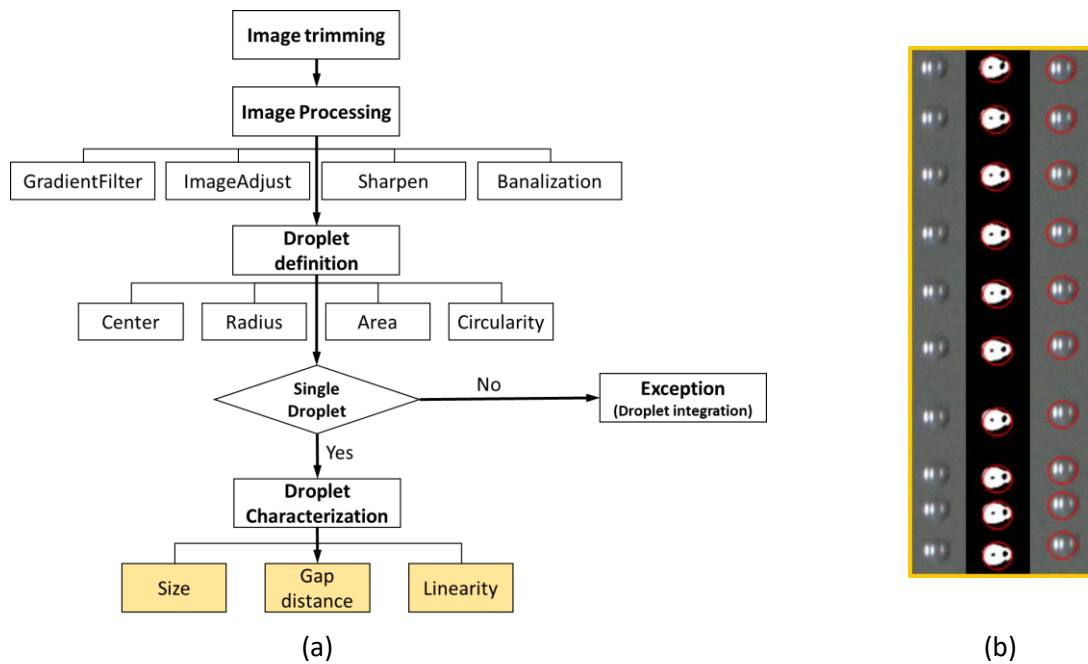


Fig. 3.7: The flow chart of the image procedure (a) and processed image (b) by Mathematica®.

Fig. 3.7 represents the flow chart for image processing using Mathematica® tools with an image example of how the droplet size is defined using before mentioned assumptions. The region of interest involved in the droplet trace is set up from a full-image size of (4912 x 7360 pixels) by trimming. An obvious droplet boundary can be extracted from a couple of image correction functions. The conducted image processing commands are described here,

1. Gradient filter:
Gives the magnitude of the gradient of $[data]$, computed using discrete derivatives of a Gaussian of sample radius $[r]$.
2. Image adjust:
Adjusts the levels in $[image]$, rescaling them to cover the range 0 to 1.
3. Sharpen:
Gives a sharpened version of $[image]$.
4. MorphologicalBinarize:
Creates a binary image from $[image]$ by replacing all values above the upper threshold $[t2]$ with 1, also including pixels with intensities above the lower threshold $[t1]$ that are connected to the foreground.

After the image modification, the droplet is defined in the shape of a circle and all hypotheses mentioned are applied. The droplet that could not satisfy the established condition in terms of its projected area and circularity, is regarded as an exception, because the droplet sometimes combines with the consecutive droplet leading to either an elongated or big droplet. The source of this can be the aerodynamic and experimental conditions, for example, the piston movement of the HPLC pump.

The droplet characterization is carried out with each single droplet addressing its size, gap distance, and linearity; all factors are essential for the uniform deposition of AM technology. All the error estimations are based on the uncertainty from the statistical evaluation, such as

$$u = \frac{s}{\sqrt{n}}, \quad (3-7)$$

where n is the number of droplets extracted from the image, and s is a standard deviation.

Fig. 3.8 shows the correlation between experimental and theoretical values under various frequency and flow rate conditions. Drag and gravity forces could be neglected because of the dominant driving force being attributed from the HPLC pump and mainly the short distance of analysis from the nozzle. At a frequency of 15 kHz with 0.4 ml·min⁻¹, the results show good linearity and are consistent with the theoretical calculations. When the flow rate is too low, the water passing through the 60 μm Ø hole in the stainless-steel membrane does not detach with the vibrational motion, but hangs on the nozzle wall without falling until a sum of both gravity and driving force of the water drop is bigger than surface tension. If the shaker's frequency is over a specific limit, the size of the droplet is increased again, and uniformity is degraded. The reason for these phenomena comes either from an insufficient displacement of the shaker for the break-up of the water stream or from an inhomogeneous water flow. One can refer to Fig. 3.8 to find the optimal droplet formation condition. A detailed study at fixed conditions, such as 15 kHz and a flow rate of 0.5 ml·min⁻¹, is necessary, as shown in Fig. 3.9 and Fig. 3.10. The reason for choosing these conditions lies in the regular extraction of the droplets and the consistency with theoretical calculation (3-5 and 3-6). In these results, we identify that the flow rate factor is more sensitive in droplet fabrication using the vibrational method. In other words, if the flow rate is properly defined considering the jet's natural frequency, the break-up occurs in every vibration cycle while satisfying the analytical calculation (3-5) introduced beforehand. A stable range of droplet formation is shown at a flow rate of 0.5 ml·min⁻¹ and a frequency from 15 to 20 kHz. The results of the generated droplet sizes at a frequency of 20 kHz are different in Fig. 3.8 and Fig. 3.9 due to extraction instabilities. This shows that unexpected results will occur if conditions such as frequency, flow rate, and their combination do not fulfill certain criteria.

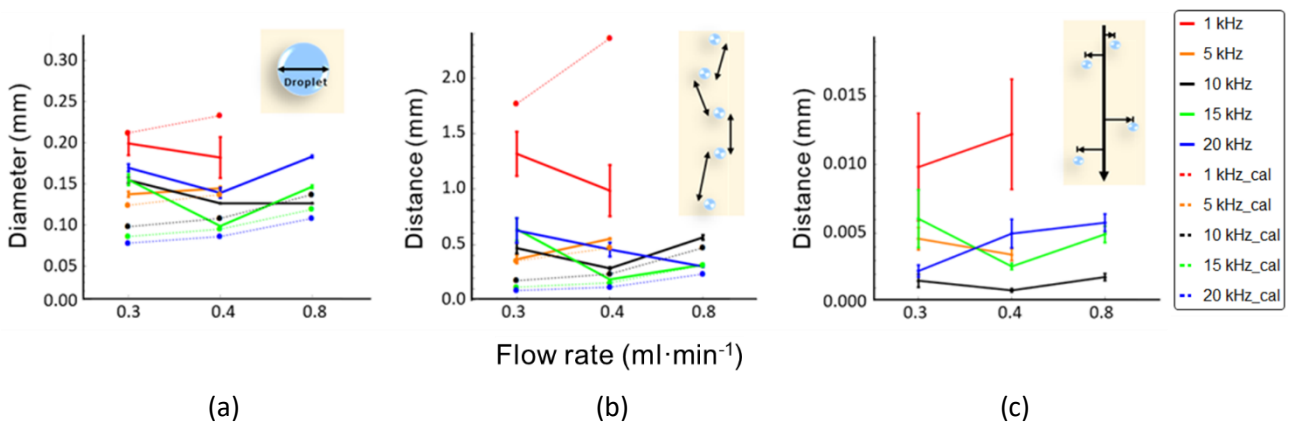


Fig. 3.8: Characterization of the droplet behavior under the various flow rates and vibrational frequencies by comparing with theoretical values in terms of size (a), gap distance (b), and linearity (c). Dotted lines are calculated, and solid lines are experimental values.

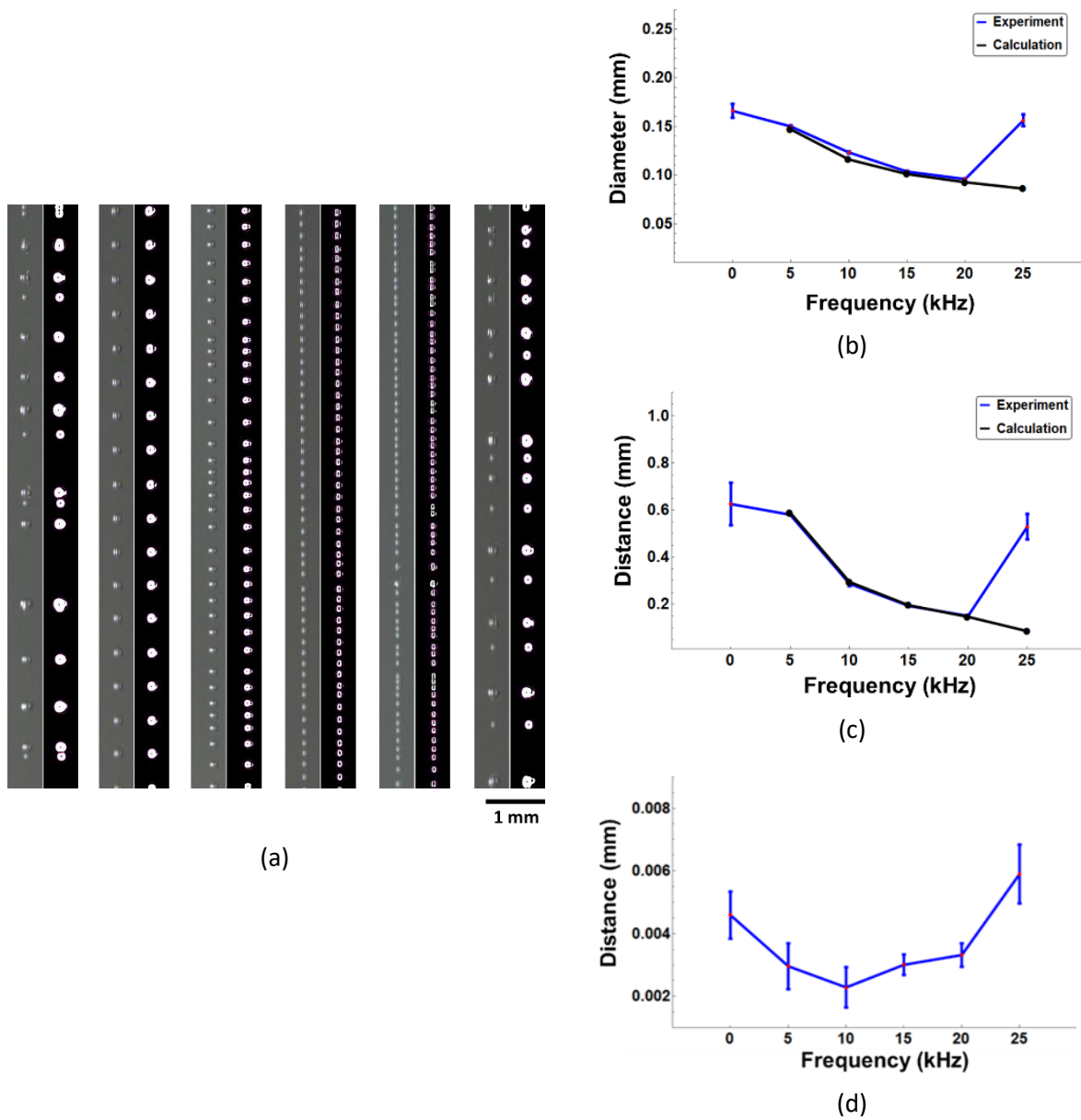


Fig. 3.9: Characterization of the droplet behavior under the fixed condition of $0.5 \text{ ml} \cdot \text{min}^{-1}$ flow rate: processed image (a), size (b), gap distance (c), and linearity (distance from the center line) (d) with various vibrational frequencies.

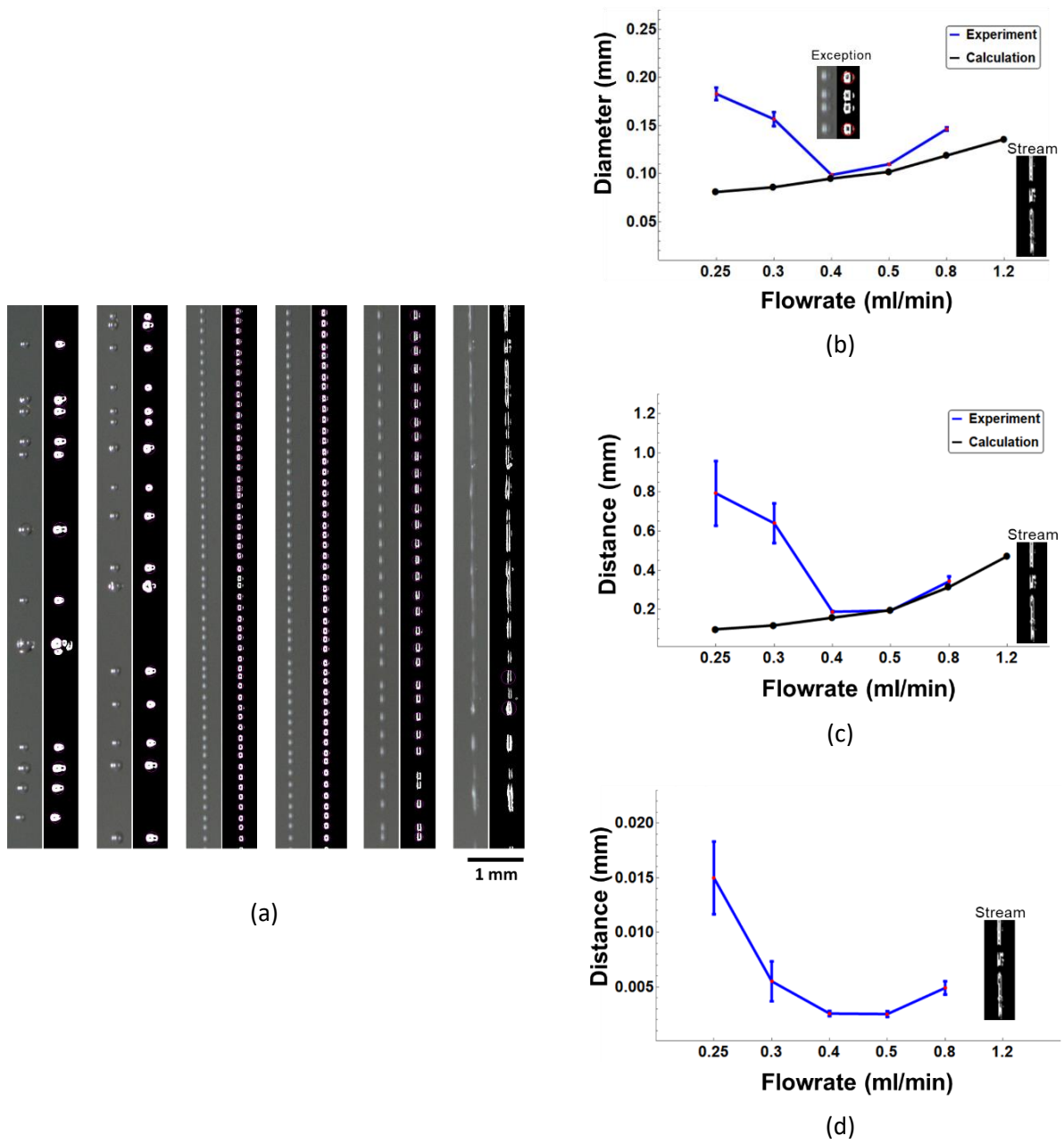


Fig. 3.10: Characterization of the droplet behavior under the fixed condition of 15 kHz vibrational frequency: processed image (a), size (b), gap distance (c), and linearity (distance from the center line) (d) with various flow rates.

3.4 Numerical Simulation for the Droplet Validation

To simulate the break-up phenomenon of water droplets under the various amplitudes of the shaker, which could not be controlled experimentally, the interDyMFoam solver in the OpenFoam software is imposed to reproduce an incompressible laminar flow (Reynolds number: 176.3) based on Navier Stoke's (NS) calculations. It represents a method to track an interface of two immiscible fluids for a volume of fluid (VOF) phase fraction using Finite-Volume-Method (FVM). OpenFOAM/ InterDyMFoam utilizes either a fixed Eulerian grid or a dynamic mesh technique based on an Arbitrary Lagrangian-Eulerian (ALE) description of the NS model. For an incompressible two-phase flow, the solver InterDyMFoam is favorable [84].

The designed channel length for the water passage was decided considering the hydrodynamic entry length, $L_{h,laminar}$, for a fully developed flow. In the case of a laminar flow, this length is given by [85]

$$L_{h,laminar} = 0.0575 R_e D, \quad (3-8)$$

where R_e is the Reynolds number and D is the diameter of the pipe. The used nozzle length for the simulation is 5,000 μm , almost eight times larger than the calculated value of 608 μm , which guarantees the flow characteristics no longer change with increased length along the cylindrical nozzle.

The details of the governing equation of the numerical methods can be found here,

1. The continuity equation

$$\nabla \cdot \vec{U} = 0. \quad (3-9)$$

2. The momentum equation

$$\frac{\partial \rho \vec{U}}{\partial t} + \nabla \cdot (\rho \vec{U} \vec{U}) = -\nabla p + \nabla \cdot \mu [\nabla \vec{U} + (\nabla \vec{U})^T] - g \cdot \vec{x} \nabla \rho + F_s + F_{ext}(z). \quad (3-10)$$

A time varying external momentum source is defined as a volumetric source as

$$F_{ext}(t) = \rho \cdot \alpha_{ad} = \rho \cdot \alpha_{max} \sin(2\pi ft), \quad (3-11)$$

α_{ad} dictates an additional acceleration expressed as a simple harmonic oscillation.

The details can be found in the previous study conducted by Shama [86].

3. The transport equation

$$\begin{aligned}
\frac{\partial \alpha}{\partial t} + \nabla \cdot (\vec{U} \alpha) &= 0, \\
\alpha &= 0 \text{ (air)}, \\
\alpha &= 1 \text{ (water)}, \\
0 < \alpha < 1 \text{ (interface)},
\end{aligned}
\tag{3-12}$$

where \vec{U} is the fluid velocity vector, p is the dynamic pressure, g is the acceleration of gravity, \vec{x} is the position vector of the control volume's center measured from the origin of the coordinates, ρ is the local density, and μ is the dynamic viscosity. Additionally, the term F_s comes from the contribution of the surface tension.

Estimating the fluid velocities and pressure is possible by implicitly solving (3-9) and (3-10), and the transport equation (3-12) is used to calculate the volume fraction function α and reconstruct the free surface after the fluid velocities are defined [87]. The volume fraction α is 0 when the discretized cell is filled with air, and α is 1 when the cell is entirely filled with water. Also, α varies between 0 and 1 when the water-air interface is located in the cell. The updated values of ρ and μ from the solver are determined with respect to the volume fraction function of the corresponding fluids (α), such as the liquid, gas, and interface regions.

The solver algorithm is called PIMPLE adopted for the coupling between the pressure and velocity field. It is a combination of the PISO (Pressure Implicit with Splitting of Operators) and the SIMPLE (Semi-Implicit Method for pressure-Linked Equations) algorithms, all of which are iterative solvers. Its main structure originated from the original PISO, but it can improve the stability by reducing the relaxation factor, and ensuring the convergence of all the equations at each time step. It will take longer, and therefore more outer correctors should be added (similar to steady-state, SIMPLE) [88, 89].

For a reasonable usage of computing resources, a 2D model was implemented. Moreover, the axisymmetric structure allows less time consumption for determining the parameter effect of interest.

The simulation has been carried out at conditions as shown in Table 3.1 with a mesh size of 3 μm , and results were interpreted based on the droplet size since the homogeneous diameter implied the uniform gap distance according to (3-5) and (3-6).

Fig. 3.11 and Table 3.2 indicate that the droplet break-up results under the different amplitudes with the condition of 0.5 $\text{ml}\cdot\text{min}^{-1}$ flow rate and 15 kHz frequency are found to be the optimal condition for droplet generator as demonstrated in the previous section, Chapter 3.3.

These results indicated that the amplitude of the new vibrator should be designed sufficiently large to guarantee the break-up of the droplets without the formation of irregular sizes of satellite drops. This is a reason why the new shaker consisting of a piezo-ceramic for the miniaturization should be made out of a stacked piezo-ceramic (typically > 8 μm displacement).

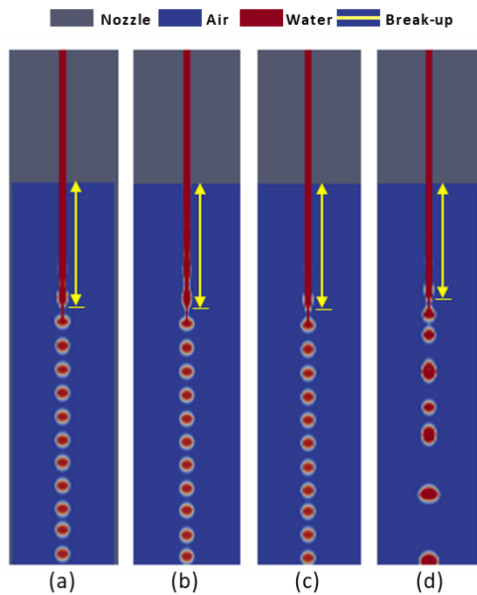


Fig. 3.11: Images of simulations at 4 ms under various vibrational amplitudes: 12 μm (a), 10 μm (b), 8 μm (c), and 6 μm (d) with 0.5 $\text{ml}\cdot\text{min}^{-1}$ flow rate / 15 kHz vibrational frequency.

Table 3.1: Simulation conditions for Fig. 3.11.

| Condition of simulation | |
|-------------------------|---|
| Surface Tension | 72 mN/m |
| Contact angle | 90° |
| Amplitude | a) 12 μm b) 10 μm c) 8 μm , d) 6 μm |
| Nozzle Diameter | 60 μm |
| Vibration | 15 kHz |
| Model | interDyMFoam + Dynamic motion |

Table 3.2: Simulation results under various amplitudes with 0.5 $\text{ml}\cdot\text{min}^{-1}$ flow rate / 15 kHz vibrational frequency.

| Case | Diameter | Uniformed droplet size | |
|----------------------|-------------------------|-----------------------------|-------------------|
| | | Break-up distance | Break-up Time |
| (a) 12 μm | 97 ~ 102 μm | \approx 984 μm | 670 μs |
| (b) 10 μm | 107 ~ 111 μm | \approx 990 μm | 670 μs |
| (c) 8 μm | 96 ~ 104 μm | \approx 990 μm | 680 μs |
| (d) 6 μm | 90 ~ 158 μm | \approx 924 μm | 670 μs |

Various conditions were examined by the variation of each variable based on the optimum conditions determined from the experimental results: the flow rate of 0.5 $\text{ml}\cdot\text{min}^{-1}$ and the frequency of 15 kHz. That is, the cases of various frequencies at a fixed flow rate of 0.5 $\text{ml}\cdot\text{min}^{-1}$ and several flow rates at a fixed frequency of 15 kHz were chosen for the comparison of numerical solutions and experimental results. The results are described in Fig. 3.12, Fig. 3.13, Table 3.3, and Table 3.4.

Let's assume that a jet diameter is simply identical to the nozzle diameter. The conditions of 15 kHz with the flow rate of 0.5 $\text{ml}\cdot\text{min}^{-1}$ is the lowest allowable flow rate, where droplets form, corresponding to the smallest possible droplet. This is in good agreement with the experimental result. It is also beneficial in terms of the break-up length that can minimize the space between the microwave applicator and droplet resonator. However, below a flow rate of 0.5 $\text{ml}\cdot\text{min}^{-1}$, the break-up formation at each vibration cannot be guaranteed. In other words, the vibration cannot separate the drops from the jet stream. This can be explained by the natural frequency to induce the droplet break-up being decreased compared to the optimal flow rate of 0.5 $\text{ml}\cdot\text{min}^{-1}$. In addition, the vibration wavelength is shorter than the circumference of the nozzle jet. As a result, the break-up condition is not satisfied according to the Rayleigh mechanism. A flow rate, faster than 0.5 $\text{ml}\cdot\text{min}^{-1}$ results in a larger droplet with the present set-up, therefore, it is not discussed in detail.

Fig. 3.14 and Fig. 3.15 summarize all results obtained from analytical calculations, experiments, and numerical analysis. Moreover, the most optimal condition is highlighted as the best fitting condition. With the fixed flow rate of 0.5 $\text{ml}\cdot\text{min}^{-1}$, the simulation result agrees with analytical estimation up to the frequency of 15 kHz since it is governed by the Rayleigh instability relevant to the relationship between a nozzle size and a liquid velocity. The natural frequency at which the perturbation cycle should be placed is about 9.8 kHz and can encompass frequencies from 5 kHz to 15 kHz for droplet formation.

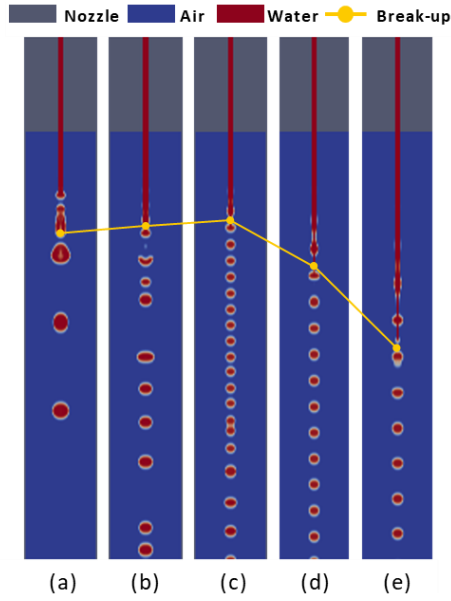


Fig. 3.12: Images of simulations at 4 ms under various flow rates: $0.3 \text{ ml} \cdot \text{min}^{-1}$ (a), $0.4 \text{ ml} \cdot \text{min}^{-1}$ (b), $0.5 \text{ ml} \cdot \text{min}^{-1}$ (c), $0.7 \text{ ml} \cdot \text{min}^{-1}$ (d), and $0.9 \text{ ml} \cdot \text{min}^{-1}$ (e) with a 15 kHz vibrational frequency.

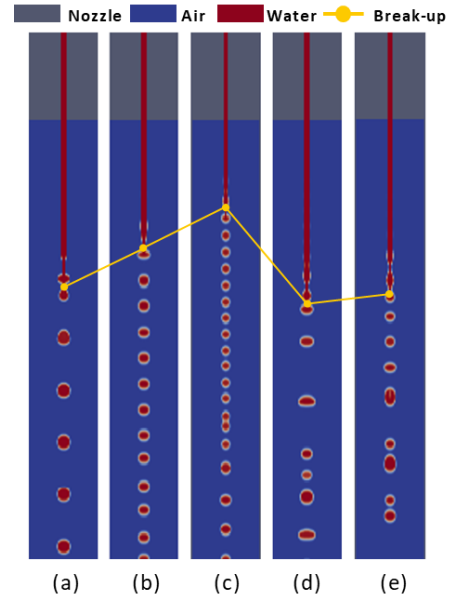


Fig. 3.13: Images of simulations at 4 ms under various vibrational frequencies: 5 kHz (a), 10 kHz (b), 15 kHz (c), 20 kHz (d), and 25 kHz (e) with a $0.5 \text{ ml} \cdot \text{min}^{-1}$ flow rate.

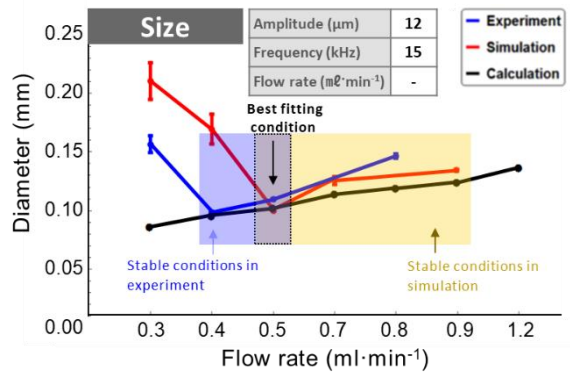


Fig. 3.14: Droplet size comparison under various flow rates with a 15 kHz vibrational frequency obtained from the experiment, simulation, and analytical calculation.

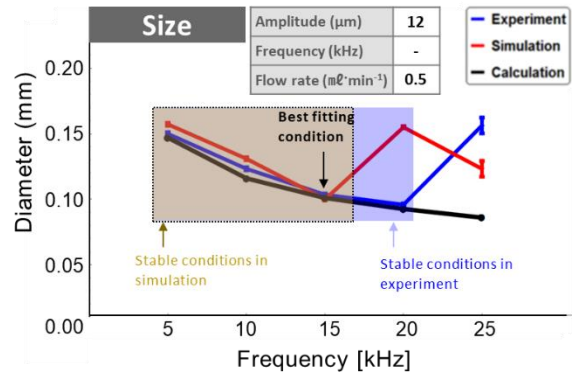


Fig. 3.15: Droplet size comparison under various vibrational frequencies with a $0.5 \text{ ml} \cdot \text{min}^{-1}$ flow rate obtained from the experiment, simulation, and analytical calculation.

Table 3.3: Simulation results under various flow rates with a 15 kHz vibrational frequency.

| Case | Diameter | Break-up distance | Break-up Time |
|--|--------------|-------------------|---------------|
| (a) $0.3 \text{ ml} \cdot \text{min}^{-1}$ | 167 ~ 233 μm | ≈ 778 μm | 1060 μs |
| (b) $0.4 \text{ ml} \cdot \text{min}^{-1}$ | 123 ~ 217 μm | ≈ 1116 μm | 1020 μs |
| (c) $0.5 \text{ ml} \cdot \text{min}^{-1}$ | 97 ~ 102 μm | ≈ 990 μm | 670 μs |
| (d) $0.7 \text{ ml} \cdot \text{min}^{-1}$ | 113 ~ 132 μm | ≈ 1616 μm | 530 μs |
| (e) $0.9 \text{ ml} \cdot \text{min}^{-1}$ | 133 ~ 138 μm | ≈ 2133 μm | 510 μs |

Table 3.4: Simulation results under various vibrational frequencies with a $0.5 \text{ ml} \cdot \text{min}^{-1}$ flow rate.

| Case | Diameter | Break-up distance | Break-up Time |
|------------|--------------|-------------------|---------------|
| (a) 5 kHz | 154 ~ 164 μm | ≈ 1750 μm | 740 μs |
| (b) 10 kHz | 121 ~ 134 μm | ≈ 1463 μm | 700 μs |
| (c) 15 kHz | 97 ~ 102 μm | ≈ 990 μm | 670 μs |
| (d) 20 kHz | 112 ~ 210 μm | ≈ 2052 μm | 1080 μs |
| (e) 25 kHz | 108 ~ 145 μm | ≈ 1947 μm | 1050 μs |

One difference between the numerical simulation and the experimental result is the droplet size at 20 kHz in frequency with a flow rate of 0.5 ml·min⁻¹. Uniform droplets are generated in the experiment, on the other hand, the numerically obtained finding cannot support this. That may result from experimental errors or coincidence effects. Consequently, the frequency of 15 kHz is determined as the best condition since that satisfies all analyses, such as analytical, experimental, and numerical methods.

A simple alternative for estimating the droplet formation criteria can be obtained from the equation (3-13):

$$f_{max} = \frac{v_{inlet}}{2 \pi r}, \quad (3-13)$$

where v_{inlet} , r , and f_{max} are velocity of a fluid, the radius of a nozzle, and the maximal frequency.

This well matched the simulation result to set the range of the vibration.

Chapter 4 Microwave Sensing

The object sensing or heating performance with microwaves is governed by the dielectric properties of the materials, as mentioned in Chapter 2, which relates to the energy coupling. This chapter focuses on the dielectric sensing using the microwave reflection technique that can be probed in parallel to microwave heating.

Sensing possibilities are explored in particular for water-based liquids that show high enough dielectric permittivity and high surface tension, and therefore are suitable candidates to be used for the suspension container of the 3D printing metal powder precursors.

This chapter introduces first the design of the miniature MW resonator. A solution is proposed taking into account 1) the ease of manufacture and 2) the sensing performance. The X-band resonator operates for samples in the nanoliter ranges. Various techniques are employed for the dielectric permittivity extraction based on experimental results and compared to find the most suitable approach in terms of precision and reliability. This is necessary as no conventional methods exist to achieve the sensing in this range except for the highly specialized metamaterial substrate resonator.

Secondly, an analytical sensing principle is derived to correlate the resonance behavior with the dielectric properties of the samples. In addition, a numerical simulation is employed to gain deeper insights into the sensing mechanism, particularly, the operating mode determination. Lastly, the miniature resonator is combined with the custom droplet generator described in Chapter 3 and preliminary measurements are performed. However, detailed validation remains out of the scope of the present work, and could be the topic of future investigations. For such extended work suggestions, see Chapter 8.2, Future work.

4.1 Background

Microwave sensors utilize an electromagnetic wave spectrum in the frequency range of 0.3 GHz to 300 GHz corresponding to the wavelength of 1 m to 1 mm. An electromagnetic field between transmitter and receiver is generated, resulting in an invisible volumetric space, in which objects can be detected. This space indicates the sensing region. The following expressions are commonly used depending on the operating frequency: Radar [Radio Detection And Ranging], RF [Radio Frequency], or Doppler sensor or motion sensor operated in the range defined above.

These sensors can be categorized into 2 classes: passive and active sensors. The former is a microwave instrument designed to observe and measure natural emissions or reflections produced from objects. The latter is a device that provides both the microwave source and the sensing device to evaluate the part of the signal emitted by the source and the part being reflected from the substance. Recently, microwave sensors are emerging prominently, since they can be miniaturized for integration with other fields, such as LOC (Lab On Chip) or microfluidics utilized in the chemical and medical area. Usually, they deal with extremely small amounts of fluids (10^{-9} to 10^{-18} l) [90]. The microwave technique can realize the function of non-destructive, non-contact, and instantaneous signal resolution related to sensitivity even though the object is exceedingly tiny [91].

4.1.1 Polarization Mechanism

The main principle of microwave sensing is based on material perturbation shown in Appendix 9.1. The existing electromagnetic field is affected once a dielectric material is introduced into the field area as the EM waves then penetrate the material. Then, the material can be polarized as shown in Fig. 4.1 [92].

The polarization relevant to the sensing and heating phenomenon comprises four mechanisms: ionic, dipolar, atomic, and electronic polarization. The main working principle of heating is governed by the operating frequency [93].

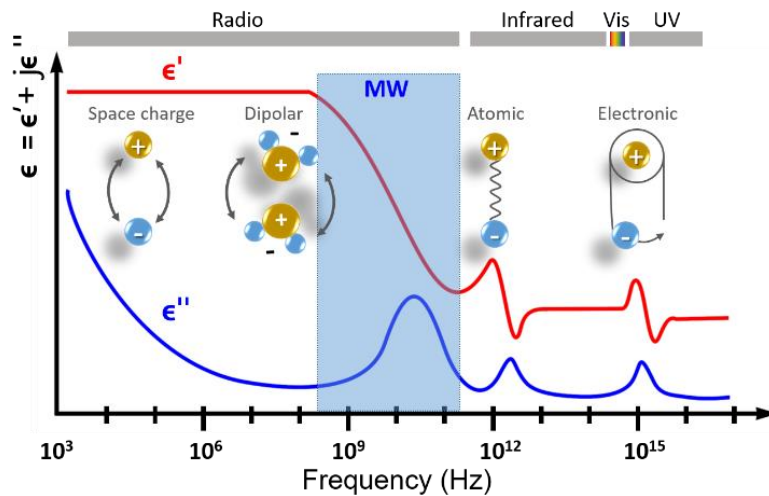


Fig. 4.1: Frequency response of dielectric mechanisms [92].

1. **The space-charge polarization** is formed in the interface due to the charge build-up between components in a heterogeneous system. This mechanism is dominant more at a relatively low frequency.
2. **Dipolar or molecular polarization** is attributable to a permanent dipole due to the asymmetric charge distribution, which tends to reorient under a changing external E-field. The friction involved in the redistribution process of molecular polarization causes dielectric losses and is converted into thermal energy. It is an essential mechanism in the microwave regime which arises due to the many aligned dipoles.
3. **Atomic polarization** arises due to the relative displacement of atomic nuclei because of the unequal charge distribution in molecule formation (e.g., stretch).
4. **Electronic polarization** results from the displacement of the electron around the nuclei. When the external field is excited, the movement of the charged particle in the dielectric gives rise to the induced dipole that can respond to the applied field. This occurs at very high frequencies because the ions are unable to follow the e-field sufficiently.

The net polarization (P_{net}) is determined by the sum of the total contributions described above:

$$P_{net} = P_{space-charge} + P_{dipolar\ or\ molecular} + P_{atomic} + P_{electronic}.$$

(4-1)

The dipolar or molecular polarization is the dominant mechanism in the microwave regime, especially for the heating application. In this range, the decrease in net polarization implies the reduction in the real permittivity, ϵ' , but the rise in the loss factor, ϵ'' . The energy delivered from the source is dissipated in the dielectric as thermal energy. The maximal energy absorption occurs when ϵ'' is near the peak position [93].

Fig. 4.2 shows the complex permittivity of both water and ethanol at different temperatures. This is the basis for sensing performance studies, as being described in this chapter. The values, such as the static permittivity, the high-frequency permittivity limit, and the relaxation frequency, as well as related equations for obtaining Fig. 4.2, are found in the references [94–96]. However, the reliability decreases once the frequency moves above 5 GHz since the ethanol characteristic is only measured up to this frequency, and values for higher frequencies are extrapolated. Onimisi et al. [97] used the same model based on 5 GHz parameters up to 10 GHz for ethanol.

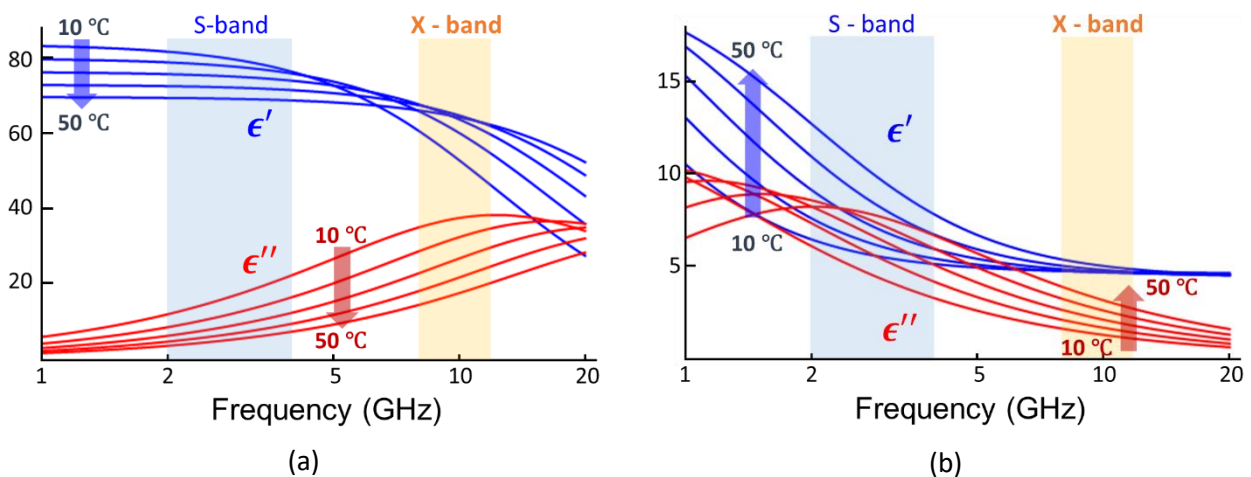


Fig. 4.2: Complex permittivity of water (a), and ethanol (b).

4.1.2 Complex Dielectric Constant

An applied rapidly oscillating E-field causes the polarization of the atoms or molecules in the dielectric material, because of the displacement of bound charged elements. It gives rise to the electric dipole moment, $\vec{\Delta p}$, in a certain volume of ΔV . The polarization density is defined as \vec{P} which plays a role in enhancing the total displacement flux, \vec{D} .

The dipole moment is defined by the bound charge q_i , and charge separation r_i , as shown in Fig. 4.3.

The sum of all the dipole moments in the dielectric is expressed using the average dipole moment \vec{m}_{el}

$$\vec{m}_{el} = \sum_{i=1}^N q_i r_i, \quad (4-2)$$

where q_i and r_i stand for the charges and the separation, respectively. N is the number of charges.

The polarization density \vec{P} of an infinitesimal volume in the dielectric volume, dV , with an infinitesimal dipole moment \vec{dp} is

$$\vec{P} = \frac{\vec{dp}}{dV} = \frac{d\vec{m}_{el}}{dV}. \quad (4-3)$$

Let's assume the ideal substance, which is homogeneous and isotropic. The polarization vector, \vec{P} , can be expressed as the integrations of each dipole moment distributed in the volume:

$$\vec{P} = N_D \vec{p} = N_D \vec{m}_{el}, \quad (4-4)$$

where N_D is dipole density per volume unit.

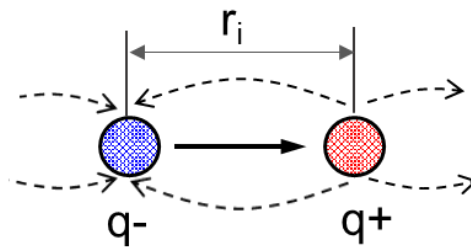


Fig. 4.3: Electric dipole moment [93].

The total charge or polarization of the system is given by the electric charge density vector \vec{D} , having the same definition as the total displacement flux, \vec{D} .

$$\vec{D} = \epsilon_0 \vec{E} + \vec{P}. \quad (4-5)$$

In the presence of a dielectric, the density vector reads as

$$\vec{D} = \epsilon_s \vec{E}, \quad (4-6)$$

ϵ_s is either the static dielectric constant or low limit permittivity relative to the vacuum permittivity

$$(\epsilon_0 = 8.854 \times 10^{-12} \text{ F} \cdot \text{m}^{-1}).$$

When the dielectric sample is immersed in the time-dependent electric field, then

$$\vec{E}(t) = E_0 \cos(\omega t), \quad (4-7)$$

where E_0 is the amplitude of the time-varying E-field so that it is independent of time, and $\omega/2\pi$ is the frequency in Hz. The displacement flux, \vec{D} , will be periodic with time; however, it will not necessarily be in phase with the electric field, \vec{E}

$$\vec{D}(t) = D_0 \cos(\omega t - \phi) = D_1 \cos(\omega t) + D_2 \sin(\omega t). \quad (4-8)$$

Through the use of trigonometry:

$$D_1 = D_0 \cos(\phi), D_2 = D_0 \sin(\phi), \quad (4-9)$$

with the relationship between D_0 and E_0 based on (4-6)

$$D_1 = \epsilon'(\omega)E_0, D_2 = \epsilon''(\omega)E_0. \quad (4-10)$$

Finally, the well-known complex form of permittivity is derived as

$$\epsilon^* = \epsilon'(\omega) - j\epsilon''(\omega). \quad (4-11)$$

The real part indicates the dielectric constant and the imaginary part is known as the loss factor.

It is possible to predict that ϵ'' stands for the energy loss in the dielectric due to the dipole phase shift ϕ . So, the loss tangent (ϵ'/ϵ'') can be zero when the frequency approaches zero since the $\epsilon'' \rightarrow 0$. It ends up being the static case identical to $\epsilon' \rightarrow \epsilon_s$ as no dielectric loss is occurring in the static field. This phase shift results from the polarization that cannot follow the rapidly oscillating field.

The imaginary part of permittivity encompasses the polarization as well as the conduction loss, defining the effective loss factor as

$$\epsilon''_{eff}(\omega) = \epsilon''_{space-charge} + \epsilon''_{dipolar\ or\ molecular} + \epsilon''_{atomic} + \epsilon''_{electronic} + \frac{\sigma}{\epsilon_0\omega}. \quad (4-12)$$

The last term of $\frac{\sigma}{\epsilon_0\omega}$ is the contribution due to the conductivity.

4.1.3 Representative Microwave Sensor

This section is dedicated specifically to the microwave applicator that can be used to determine the complex permittivity of liquids and their binary mixtures. The characteristics that this method can evaluate are generally limited to the complex permittivity (real and imaginary parts), and other material properties such as permeability and conductivity are excluded.

a) Open-ended coaxial sensor

Open-end coaxial resonators, consisting of a short and a shunt circuit at both sides, have been broadly used for dielectric property measurements in the microwave range over the last few decades, due to both, their simplicity and accuracy in wide frequency ranges. The fringing field in front of the open-end is perturbed when a sample of different complex permittivity is introduced within the field lines. From this influence, which results from changes in the measured reflection response, the complex permittivity can be extracted by comparing to calibration tests using standard materials (for example water).

A wave propagating from a feeding network is partially reflected at the discontinuity of the structure because of an impedance mismatch.

This method was investigated intensively by previous researchers on the basis of electromagnetic field analysis and coupling effects for sensing applications in industry [98–104]. The limitations of this exceptional method lie 1) in the quality of the close contact with the materials in all sensing areas without impurity and 2) in ensuring that the sample thickness is larger than the doubled penetration depth [105].

Nowadays, a modified coaxial resonator is researched for the versatile sensing of humidity and displacement in combination with a metal plate placed parallel to the open-end, in order to improve the electric field concentration [106, 107].

A commercial probe kit based on a traditional open-ended coaxial line [108] is available from Agilent inc. [85070E][109] in combination with a VNA. The capacitance termination is defined at an open-end, and it is separated in both factors, C_f and $C_0\epsilon$, by the capacitance model as shown in Fig. 4.4. The former is the fringing capacitance in the coax occurring through the dielectric, typically Teflon, with a characteristic impedance of 50 or 75 Ω . The latter represents the capacitance appearing at an open-end, affected by the test sample; in other words, C_0 refers to the capacitance when only air is present in the sensing area without a dielectric sample.

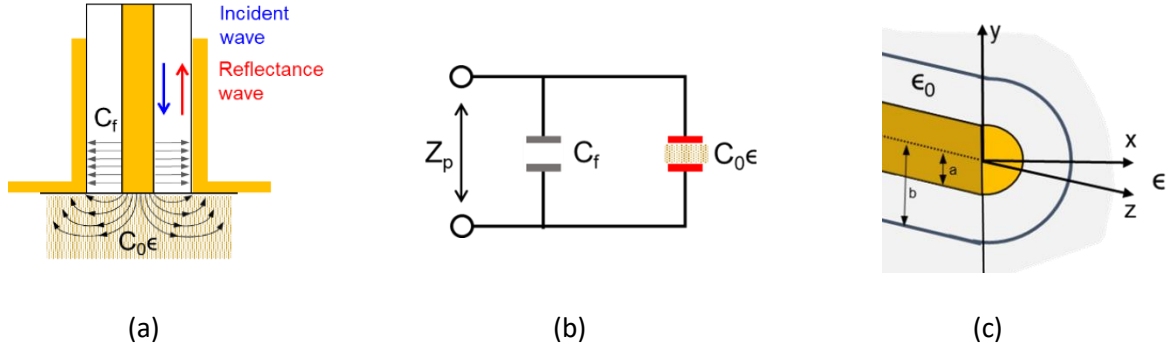


Fig. 4.4: The geometry of the open-ended coaxial probe with E-field distribution (a), the capacitance model of open-ended coax sensor (b), and the probe tip geometry (c), see also [110, 111].

The values of C_f and $C_0\epsilon$ are determined experimentally from the calibration process using a well known dielectric sample. These total capacitances are altered depending on the different complex permittivity of the test sample; in particular, it is affected by the sample's loss factor resulting in the change of the $C_0\epsilon$ capacitor. This equivalent model is valid at frequencies where the dimensions of the coaxial line are small compared to the wavelength, to prevent radiation loss. The sensor impedance Z_p is expressed based on [104, 110, 112],

$$Z_p = \frac{1}{j\omega(C_f + C_0\epsilon)}. \quad (4-13)$$

The VNA measures the reflection coefficient S_{11} corresponding to the ratio of the incident wave to the reflected wave at the input port:

$$S_{11} = |S_{11}|e^{j\varphi} = \frac{Z_p - Z_0}{Z_p + Z_0}, \quad (4-14)$$

where $|S_{11}|$ and φ are the modulus and phase of the complex reflection coefficient obtained from the VNA. Z_0 stands for the impedance of a coax cable located between the VNA and the sensor.

The complex permittivity can be obtained from the above formulas (4-13 and 4-14) as shown below, see [108, 112].

$$\epsilon' = \frac{-2|S_{11}|\sin\varphi}{\omega C_0 Z_0 (1 + 2|S_{11}|\cos\varphi + |S_{11}|^2)} - \frac{C_f}{C_0}, \quad (4-15)$$

$$\epsilon'' = \frac{1 - |S_{11}|^2}{\omega C_0 Z_0 (1 + 2|S_{11}|\cos\varphi + |S_{11}|^2)}. \quad (4-16)$$

The loss tangent is given by

$$\tan\delta = \frac{\epsilon''}{\epsilon'} = \frac{1 - |S_{11}|^2}{-2|S_{11}|\sin\phi}. \quad (4-17)$$

It can be concluded that the change of complex dielectric permittivity, located in front of the open circuit, influences the total capacitance involved in the impedance change. That is the main sensing principle to extract the dielectric permittivity of the sample.

For calibration, Agilent Technologies, Inc. recommends using air, shorting block, and distilled water at a positive temperature. Employing the Debye equation is a typical methodology to find the dielectric constant of liquids as a function of frequency.

$$\epsilon = \epsilon_{\infty} + \frac{\epsilon_s - \epsilon_{\infty}}{1 + j\omega\tau} + i \frac{\sigma}{\omega\epsilon_0}, \quad (4-18)$$

where ϵ_{∞} is the permittivity at the high-frequency limit, ϵ_s is the static frequency permittivity, and τ is the characteristic relaxation time of the medium. ϵ_{∞} and σ dictate the vacuum permittivity and ionic conductivity, respectively. At a high frequency, the conductivity contribution decreases, because the ions no longer follow the rapid oscillation of the stimulus. Detailed descriptions, including the measurement procedure, are available in [105, 113–115].

b) Metamaterial based sensors

Various types of planar sensors based on metamaterial have been emerging over the past decades, because of their compactness, resulting from the dimensions being smaller than the wavelength of incident electromagnetic (EM) waves [116]. An electromagnetic metamaterial is an artificial substance enabling changes in its permittivity or permeability continuously from positive to negative. It can amplify evanescent waves, providing both high-sensitivity and sub-wavelength resolution [117]. However, the used materials have unavoidable drawbacks associated with large absorption losses, making them unsuitable for heating applications. Therefore, this concept has rather been researched for different sensing purposes, such as displacement, rotation, and strain sensing [118–124]. One of the typical forms of the metamaterial-based sensor is named Split Ring Resonator (SRR), which has a pair of enclosed loops with splits in them at opposite ends on a dielectric substrate [125]. The concentric circle- or square-shaped loops are made of a highly conductive metal, for example, copper or gold-plated copper. The small gaps between the geometries give rise to the concentrated capacitance that changes its resonance frequency to a lower value.

To improve the sensing performance, this form is modified by changing or duplicating the array of metal parts on the dielectric, leading to designs such as CSRR (Complementary split-ring resonator), DSRR (Double Split Ring Resonator), and MSRR (Multi-split ring resonator)[126–128].

As described above, there is a significant capacitance effect at the gap. For the understanding of the sensing principle, an example that can extract the dielectric permittivity using a single SRR is introduced. The microwave is launched from an end of the microstrip and propagates in a quasi-TEM mode.

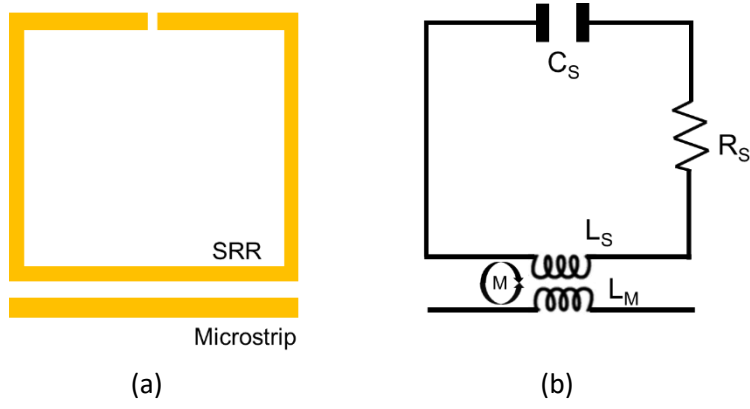


Fig. 4.5: Microstrip-coupled split ring resonator: diagram (a) and equivalent circuit (b) [129].

The inductance originating from the loop is expressed as L_S , and the gap capacitance is C_S . This SRR is converted as a form of a series RLC resonant circuit, as shown in Fig. 4.5.

The impedance of the circuit without considering the mutual inductance, M , is described as [129]

$$Z_S = R_S + j\omega L_S + \frac{1}{j\omega C_S}. \quad (4-19)$$

C_S is the capacitance near the gap between both conductors, where it is influenced by the introduced dielectric material,

$$C_S = C_0 + \epsilon_{sam} C_c, \quad (4-20)$$

where C_0 represents the entire capacitive effects of the dielectric substrate, channel walls, and surrounding space excluding the channel cavity. The term $\epsilon_{sam} C_c$ denotes the capacitive influence of the liquid sample loaded into the microfluidic channel. C_c is the capacitance when no sample is employed. ϵ_{sam} means the flowing liquid's properties consisting of the complex permittivity described as $\epsilon_{sam} = \epsilon'_{sam} - j\epsilon''_{sam}$.

The total resistance R_T and capacitance C_T are simplified as a function of complex permittivity

$$R_T = f_R(\epsilon'_{sam}, \epsilon''_{sam}), \quad C_T = f_C(\epsilon'_{sam}, \epsilon''_{sam}). \quad (4-21)$$

The resonance frequency is defined as

$$f_0 = \frac{1}{2\pi\sqrt{L_S(C_T)}}. \quad (4-22)$$

The quality factor of the resonator is given by

$$Q = \frac{1}{R_T} \sqrt{\frac{L_S}{C_T}}.$$

(4-23)

In short, it is clear that the SRR resonance and Q-factor are governed by the factors ϵ'_{sam} and ϵ''_{sam} . From this dependency between resonance behavior and complex permittivity, it's possible to approximate the dielectric properties of the sample. This method is excellent not only for sensing but also for miniaturization. However, this concept has an inevitable weakness in high power handling, e.g., heating applications, which stems from structural problems. Furthermore, the tunability and transmittable bandwidth are narrow, hence this option is not further considered in this study.

c) Cavity resonator

A cavity can be described as a transformation of a waveguide commonly used for high-power applications. The cavity resonator consists of closed metal walls, as short circuits, at both ends of the waveguide, to prevent the escape of electromagnetic radiation energy outside the system [130]. Therefore, energy is stored in the cavity and gradually dissipated as heat due to the resistance of inserted samples and the cavity wall. The electromagnetic field intensity inside the cavity is substantially high due to the superposition of both propagating and reflected waves, so it is called the resonant-cavity or the cavity resonator.

The cavity resonator is widely used for sensing and heating purpose by microwaves because it can be easily manufactured as a closed box that traps and amplifies the wave energy and is accompanied with a high quality factor indicating efficient sensing performance. Usually, the cavity resonator comes with a Q-factor number from 5000 to around 10000. This is a significantly higher Q-value compared to the one of microwave resonators for gas or liquid flow sensing, which is usually less than 1000. Several studies that used the microwave cavity for sensing applications are described in [131–134].

Detailed information about the Q-factor is elaborated in Appendix 9.2.

Typical cavity types are shown in Fig. 4.6. The cylindrical cavity is a commonly used applicator for heating liquid samples and is covered in detail in Chapter 5.3, Microwave Cavity.

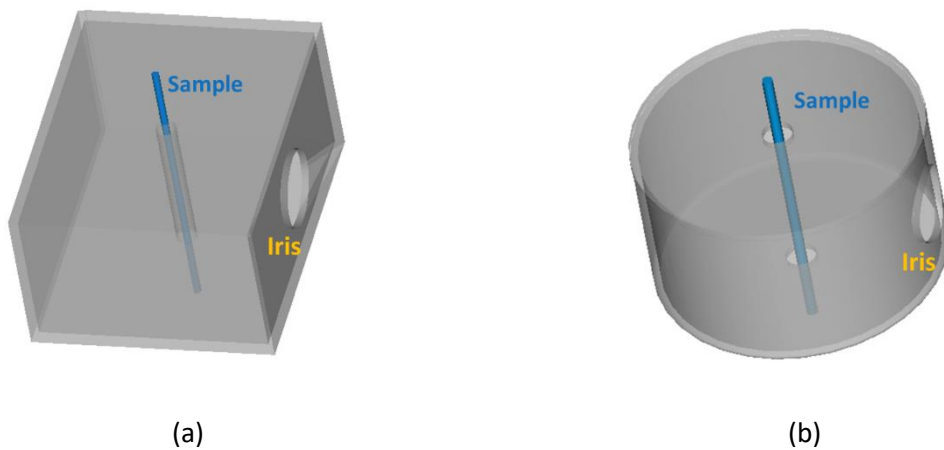


Fig. 4.6: Typical resonant cavities with inserted samples: rectangular cavity (a) and cylindrical cavity (b).

The perturbation theory is useful for understanding the change in properties when a material is placed in the electric field of a cavity, based on the complex resonance frequency shift. It is naturally affected by the position, shape, concentration, and size of the introduced material, in addition to the operation mode of the electromagnetic field in the cavity. The change of the complex angular resonance frequency can be described as [131, 135–138]

$$\frac{\omega_2 - \omega_1}{\omega_2} = \frac{\int_{V_c} [(\mu_2 - \mu_1) H_1 \cdot H_2 - (\epsilon_2 - \epsilon_1) E_1 \cdot E_2] dV}{\int_{V_c} (\epsilon_1 E_1 \cdot E_2 - \mu_1 H_1 \cdot H_2) dV}, \quad (4-24)$$

where ω_1 and ω_2 are the complex angular resonant frequencies before and after the perturbation caused by the sample insertion. $\epsilon_1, \epsilon_2, \mu_1$, and μ_2 are the complex permittivity of air and the sample as well as the complex permeability of air and the sample. E_1, E_2, H_1 , and H_2 are the electric and magnetic fields of the cavity. Subscripts 1 and 2 indicate the state before and after samples are inserted. V_c is the total cavity volume.

This theory has adopted several hypotheses where the following assumptions must be made:

1. A sample is homogenous and small enough compared to the cavity volume.
2. The loss due to the cavity wall is the same regardless of the sample's existence.
3. Only the region where the sample is placed is perturbed in terms of the electromagnetic field. The behavior of the electromagnetic field outside the sample is always the same regardless of the dielectric material (no degenerated modes).
4. The quality factor is measured at the same condition, not only concerning the frequency but also the coupling.
5. The small dielectric is placed in the region of the high-intensity electric field where the magnetic field is negligible.

These assumptions lead to (4.25)

$$\frac{\omega_2 - \omega_1}{\omega_2} = - \left(\frac{\epsilon_r - 1}{2} \right) \frac{\int_{V_s} (E_1 \cdot E_2) dV}{2 \int_{V_c} |E_1|^2 dV}. \quad (4-25)$$

V_s and ϵ_r represent the volume and relative complex permittivity of the sample, respectively.

The complex angular resonant frequency can be expressed with respect to the real part of the resonance frequency and the quality factor

$$\omega = \omega_r + j\omega_i = \omega_r \left(1 + j \frac{1}{2Q} \right), \quad (\omega_r = 2\pi f, Q = \frac{\omega_r}{2\omega_i}). \quad (4-26)$$

With the assumption that $\omega_{r1} = \omega_{r2}$ and $\omega_i \ll \omega_r$ applied

$$\frac{\omega_2 - \omega_1}{\omega_2} \approx \frac{f_2 - f_1}{f_2} + j \left(\frac{1}{2Q_2} - \frac{1}{2Q_1} \right), \quad (4-27)$$

$$\frac{f_2 - f_1}{f_2} + j \left(\frac{1}{2Q_2} - \frac{1}{2Q_1} \right) = - \left(\frac{\epsilon_r - 1}{2} \right) \frac{\int_{V_s} (E_1 \cdot E_2) dV}{\int_{V_c} |E_1|^2 dV}. \quad (4-28)$$

The (4-28) is simplified becoming (4-29) and (4-30) using the coefficient A

$$2 \left(\frac{f_1 - f_2}{f_2} \right) = A (\epsilon'_r - 1), \quad (4-29)$$

$$\frac{1}{Q_2} - \frac{1}{Q_1} = A \epsilon''_r, \quad (4-30)$$

$$A = \frac{\int_{V_s} (E_1 \cdot E_2) dV}{\int_{V_c} |E_1|^2 dV}. \quad (4-31)$$

The parameter A is assumed to be a constant related to the entire system without the sample. The formulas (4-29) and (4-30) mean that the perturbation theory can realize the permittivity extraction of the sample from the measurable values of f and Q . Usually, the A value is obtained from the standard sample, and its permittivity is already known through the calibration procedure.

The detailed basis of the cavity perturbation principle can be found in Appendix 9.1.

4.2 TEM (Transverse Electro-Magnetic) Mode Resonator for Sensing

This chapter introduces a self-developed, miniaturized microwave sensing device operating in a TEM mode. It is designed based on a standard coaxial line with a simple modification and evaluated in terms of its sensing performance in nano-liter volumes using water-based solutions.

This chapter covers from the sensing principle with a numerical calculation to the experimental validation using different binary mixtures of water and ethanol with varying concentrations. In particular, not only the sensing of a fully media-filled volume, like the region of the open-end coax being entirely filled with gas or a liquid, is elaborated, but also the sensing formalism for a partially filled space is given, based on the capacitance at the open-end coax. The benefits of such resonator's design are cost-effectiveness and a simple fabrication route, which can also be implemented for miniaturized sizes.

4.2.1 Design of a Microwave Resonator with the Experimental Equipment

The typical coaxial line-based microwave resonator can have both impedances: either 50 or 75 Ω .

These can be fixed by the size ratio of the inner and outer conductors. The 50 Ω impedance is general because it is already optimized not only for the power handling but also for low losses. However, it is still a good idea to use a 75 Ω -based structure due to a minimal insertion loss for the case, where detecting the unloaded Q-factor associated with the sensing performance is more relevant.

Here, theoretical sensing mechanisms for the custom resonator are investigated, and the 75 Ω -applicator is intensively validated based on experimental results. In X-band, the imaginary part of the dielectric permittivity, relevant for the Q-factor, is of major interest for industrial applications, especially for water-based materials.

A modified coaxial resonator working in the X-band range has been designed and fabricated in PSI based on simulation results by CST Microwave Studio. Fig. 4.7 shows the proposed resonator with the cutting plane used for simulation. The integral dimensions of the coaxial resonator are described in Table 4.1

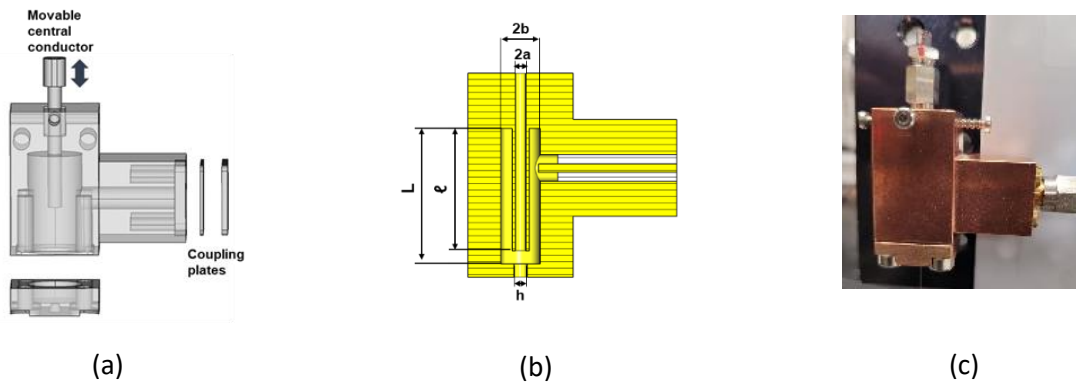


Fig. 4.7: Coaxial microwave resonator: drawing (a), simulation model (b), and photograph (c).

Table 4.1: Geometrical parameter of the coaxial microwave resonator.

| Radius of inner conductor (a) | Radius of outer wall (b) | Length of inner conductor (ℓ) | Length of outer wall (L) | Hole (h) |
|-------------------------------|--------------------------|--------------------------------------|--------------------------|----------|
| 1.3 mm | 4.6 mm | 15.6 ~ 19.6 mm | 20.6 mm | 2 mm |

The knob placed on top of the device can tune the wave-trapping distance by a central conductor movement affecting the resonance frequency. The effective movable distance of the central conductor is flexible within a 4 mm range, and the 1 mm gap between the central conductor and the outer wall prevents a short circuit. The screws near the knob on the wall are utilized not only for the fixation of the movable conductor but also for fine-tuning the coupling under the DUT (Device under Test) environment. For the excitation of the resonator, a commercial coaxial probe, 23_SMA-50-0-3/111_NE (HUBER+SUHNER), was introduced with plates of various thicknesses (0.5 t, 1 t, and 2 t). It influences the electromagnetic coupling by adjusting the distance between the central conductor and the electric probe of the SMA. The central conductor consists of a hollow rod and a fixation adapter, allowing the sample to be positioned at the same location through the borosilicate capillary. The capillaries used for this experiment were 100 μm and 200 μm in outer diameter with a wall thickness of 10 μm . These corresponded to the sample volumes of 5 nl and 25 nl considering the focused gap capacitance distance and the purchased capillaries from Hilgenberg inc. Therefore, they are generally used for X-ray analysis since the dimension reliability is considerably uniform. Moreover, all measurements were performed with a Vector Network Analyzer (Agilent 8720D). This resonator enables flexibility regarding the working frequency and the sample volume exposed in the electromagnetic field. However, in this study, the smallest loading volume, meaning the closest gap capacitance, is examined to determine the maximum sensitivity of the resonator.

4.2.2 Theoretical Background of New Microwave Resonator for Sensing

The design of the coaxial cavity shown in Fig. 4.7 aims to operate at TEM mode in the X-band range ($\frac{3}{4}\lambda$). The concept of this resonator is similar to a conventional open-ended quarter-wave resonator modeled by shorting the one end between the central conductor and the wall structure in a typical coaxial line but without the dielectric material (e.g., PTFE). The electric field created at the open capacitance is the main sensing source of a conventional open-end dielectric measurement method. Electrically, this capacitance plays a role in extending the resonator's length, changing its intrinsic resonant properties. Hence, both, the physical and electrical length control are fundamental criteria to characterize the coaxial-resonant system. The resonator proposed in this study has the flexibility to control the electrical distance by modulating not only the physical length of the resonating area but also the confined capacitance intensity generated at the open end due to the laminated metal wall over the opening.

For the interpretation of the resonance frequency relevant to the sensitivity of this system, two methods are suggested based on the quarter wavelength approximation coming from the acoustic field (4-32) and the phase-matching method (4-33), see also [106, 139].

$$f_r = \frac{c(2m+1)}{4\ell\sqrt{\epsilon_r}} \quad (m = 0, 1, 2, 3 \dots), \quad (4-32)$$

$$f_r = \frac{c(2m\pi + \varphi_1 + \varphi_2)}{4\pi\ell\sqrt{\epsilon_r}} \quad (m = 0, 1, 2, 3), \quad (4-33)$$

where c , ϵ_r , and ℓ denote the speed of light, the relative permittivity of a medium (e.g., air), and the length of an inner conductor. φ_1 is the reflection phase shift of π attributed to the short circuit on the near end of the electrical probe, and φ_2 is the gap capacitance induced phase shift, expressed by

$$\varphi_2 = 2 \tan^{-1} \frac{Z_0}{X_c}, \quad (4-34)$$

$$X_c = -\frac{1}{\omega C_{gap}}, \quad (4-35)$$

where X_c , ω , C_{gap} , and Z_0 are the susceptance, angular resonance frequency, capacitance at the open-end gap, and characteristic impedance, respectively [140].

As described above, the capacitance present in an open circuit is responsible for determining the resonant behavior in the phase matching method. In short, (4-32) only accounts for the resonance frequency governed by the length of the central conductor. On the other hand, (4-33) additionally considers the interaction of the capacitance in the gap driven by the central conductor. In [102, 141], the static capacitance of the fringing field over the aperture is well described for the TEM excitation.

$$C_{gap} = C_1 + C_2, \quad (4-36)$$

$$C_1 = \frac{\epsilon_1}{[\ln(\frac{b}{a})]^2} \int_a^b \int_a^b \int_0^\pi \frac{\cos(\theta) dr_1 dr_2 d\theta}{\sqrt{r_1^2 + r_2^2 - 2r_1 r_2 \cos(\theta)}}, \quad (4-37)$$

$$C_2 = \frac{4\epsilon_1}{[\ln(\frac{b}{a})]^2} \sum_{n=1}^{\infty} \left(\frac{1 - \epsilon_{12}}{1 + \epsilon_{12}} \right)^2 \int_a^b \int_a^b \int_0^\pi \frac{\cos(\theta) dr_1 dr_2 d\theta}{\sqrt{r_1^2 + r_2^2 + 4n^2 d^2 - 2r_1 r_2 \cos(\theta)}}. \quad (4-38)$$

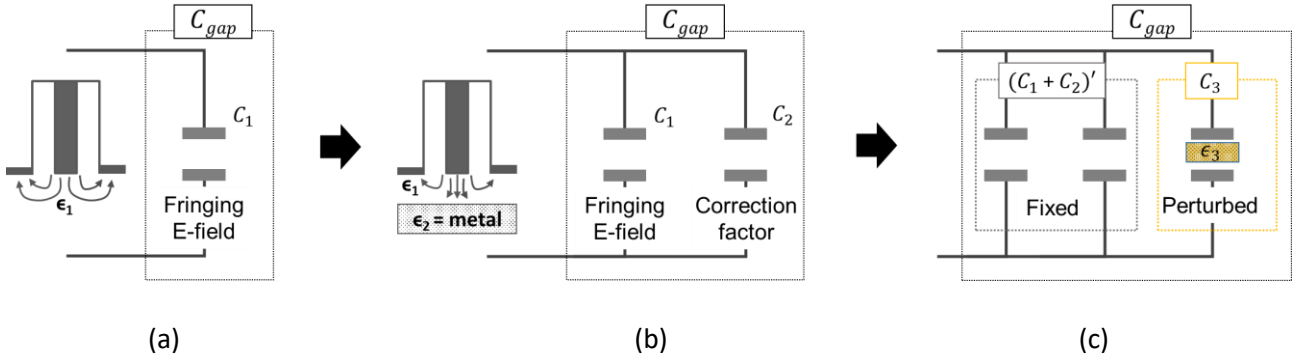


Fig. 4.8: Open-ended coaxial resonator and capacitance (a), with metal wall (b), plus material samples (c).

C_1 , the first term of C_{gap} in (4-36), represents the capacitance of a conventional open-ended coaxial sensor with an infinite dielectric material thickness located below the sensing region, corresponding to Fig. 4.8 (a). On the other hand, the second term, C_2 , implies the correction factor to reflect a finite thickness of the dielectric material because of the introduced medium (e.g metal) layer below it, as shown in Fig. 4.8 (b). The $\epsilon_1, \epsilon_{12}, a, b$ and d stand for the dielectric permittivity of the first material, the ratio of the dielectric properties between the first medium, ϵ_1 , and the back layer, ϵ_2 , (e.g., ϵ_1/ϵ_2), radii of the inner and outer conductors, and the opened gap distance in the axial direction. r_1, r_2 , and θ represent the radial and the azimuthal components, respectively.

In this research, the metal wall is regarded as a second layer, so the ratio of the dielectric properties (ϵ_{12}) will be zero. Thus (4-36) is simplified as a function of the gap distance with the constants k_1 and k_2 determined by the resonator dimensions:

$$C_{gap} = C_1 + C_2 = \epsilon_1 (k_1 + k_2 f(d)). \quad (4-39)$$

In short, the proposed resonator's capacitance is linearly proportional to the permittivity of the first medium. k_1 is obtained by numerically solving the triple integral of C_1 , and C_2 is variable according to the gap distance, which is the result of controlling the inner conductor's displacement. If the system is used for a sensing application with a fixed gap distance, the capacitance of the system (C_{gap}) at the open-end is only dominated by the dielectric permittivity of the first medium (ϵ_1) as a variable

$$C_{gap} = \epsilon_1 k, \quad (4-40)$$

$$\epsilon_1 = \epsilon_1' - j\epsilon_1''. \quad (4-41)$$

The permittivity is expressed as a complex form (4-41), and k is a constant obtained from (4-37) and (4-38). The dielectric loss of ϵ'' is ignored once the loss tangent is lower than the value of 1/10, so the relative permittivity (ϵ_1') replaces a complex number of ϵ_1 . Many types of gaseous states fall into this category. Hence, (4-40) means that the capacitance is a linear function of the relative permittivity, ϵ_1' , and is appropriate for gas or humidity sensing.

The case described above is only valid once the sample is brimmed uniformly in all areas where the electric field occurs. For the representation of a partial material filling inside the E-field of this applicator, the perturbation theory is adopted, as shown in Fig. 4.8 (c). (Example: a sample with permittivity ϵ_3 partially interferes with the focused E-field of the resonator)

According to the perturbation theory, (4-36) is transformed into

$$C_{gap} = (C_1 + C_2)' + C_3, \quad (4-42)$$

C_3 in (4-42) denotes the perturbed capacitance when a dielectric material is inserted into the gap of the resonator. The capacitance outside of sample $(C_1 + C_2)'$ is presumed as a fixed capacitance not affected by the changed condition.

Assuming that the electric field under the central conductor, especially where the sample interacts, shows a uniform distribution in a microscopic volume, the perturbing capacitance ΔC_3 becomes equivalent to the case of a parallel metal plate with a correction factor k_3 . Of course, the sample must be homogeneous and much smaller than the inner conductor for using the perturbation theory.

$$\Delta C_3 = k_3(\epsilon_3 - \epsilon_{air}) \frac{A_s}{d}, \quad (4-43)$$

A_s and ϵ_3 indicate the cross-section and complex permittivity of the introduced material, respectively.

A total capacitance considering the sample loading, C'_{gap} , is manifested as

$$C'_{gap} = (C_1 + C_2)' + C_3 + \Delta C_3 = C_1 + C_2 + \Delta C_3. \quad (4-44)$$

And the generalized form of (4-44), with a fixed gap distance, is simply expressed by

$$C'_{gap} = \epsilon_1 k + [\epsilon_3] k'_3 \quad ([\epsilon_3] = \epsilon_3 - \epsilon_{air}), \quad (4-45)$$

k'_3 denotes the modified correction factor with all the constants in (4-43), such as A_s and d being included.

Air is substituted for ϵ_1 to validate the sensing performance in the nanoliters range with a fixed gap

$$C'_{gap} = k + k'_3 f(\epsilon'_3 - 1, \epsilon''_3). \quad (4-46)$$

In short, the capacitance of the gap is variable depending on the function of the sample's complex permittivity, ϵ_3 , and consequently influences the resonance behavior shown in (4-33). It is the basic principle of the developed sensing device. However, an analytical Q-factor estimation is complicated, since the amplitude of the reflection coefficient is changeable depending on various factors, such as sample size, resonator's structure, operating frequency, and the coupling effect between the electrical probe and resonator for the one port system. It is therefore evaluated by experiments [142].

To avoid an excitation mode distortion of the coaxial resonator (e.g., TE or TM), the cutoff frequency of the next higher mode TE₁₁ (approximately, $\frac{c}{\pi(\frac{a+b}{2})\sqrt{\epsilon_r}} = 16.17$ GHz) is considered as an upper boundary for designing the resonator. This threshold is obtained based on the ratio of radii (a) and (b) [130].

$$f_{max} = \frac{c k_c}{2\pi\sqrt{\epsilon_{air}}} \dots \dots \dots \left(k_c = \frac{2}{(a+b)}\right), \quad (4-47)$$

k_c is the cutoff wavenumber, and ϵ_{air} indicates the dielectric constant of air. Therefore, a TEM mode is guaranteed up to 15.36 GHz with a 5 % safety margin.

The detection mechanism for the small quantity of liquid is consequently defined by (4-33), including the concept of (4-46). The real part of the sample's permittivity changes the resonance frequency, and the imaginary part is more relevant to the Q-factor.

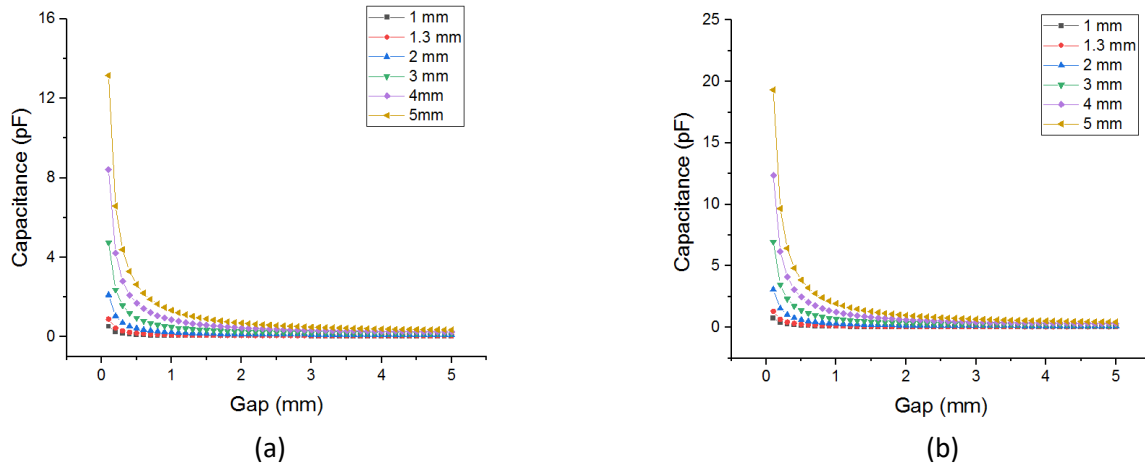


Fig. 4.9: Gap capacitance at the open-end of 50 Ω (a), and 75 Ω (b).

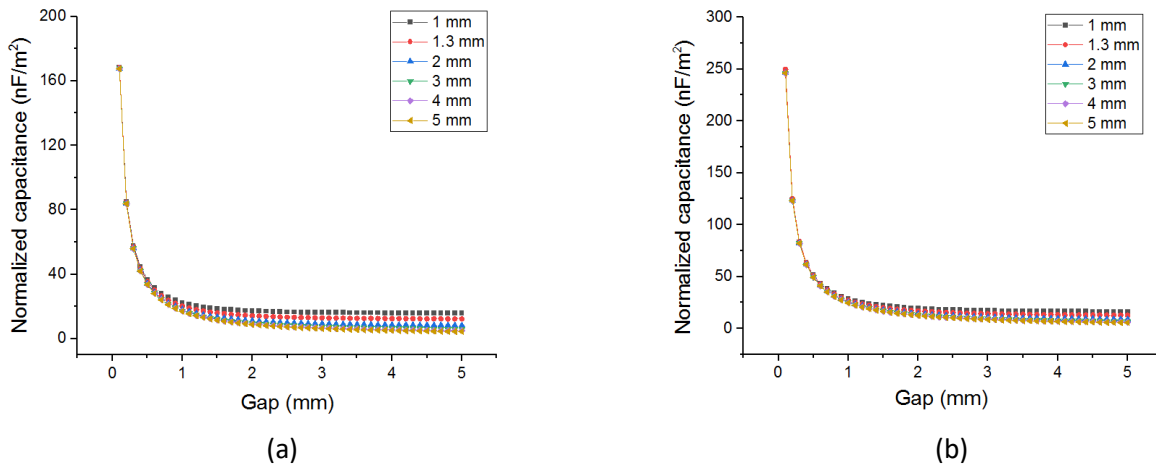


Fig. 4.10: Normalized gap capacitance at the open-end by the cross sectional area of 50 Ω (a) and 75 Ω (b).

As described beforehand, the gap capacitance is an essential factor in evaluating the sensing performance, and the strength of an electric field that increases in proportion to the capacitance also affects the sensing resolution. However, the analytical solution of the triple integral formula is not practical, so the Mathematica® software is employed for the numerical calculations (convergence) of the gap capacitance, C_{gap} .

Fig. 4.9 shows the total gap capacitance at the open end of the resonator with a varying size of the central conductor, and the outer wall dimension is changed to maintain a fixed characteristic impedance based on the lossless case of the coaxial line (4-48) [130]

$$Z_0 = \sqrt{\frac{L}{C}} = \frac{\ln\left(\frac{a}{b}\right)}{2\pi} \sqrt{\frac{\epsilon_0}{\mu_0}}, \quad (4-48)$$

where L, C, a, b, ϵ_0 and μ_0 are inductance, capacitance, the diameter of inner and outer conductor wall diameter, vacuum permittivity, and vacuum permeability.

Moreover, Fig. 4.10 is the normalized capacitance with respect to the area of the center conductor with a characteristic impedance of 50 Ω and 75 Ω .

It is natural that capacitance increases as the gap decreases. However, according to Fig. 4.9 and Fig. 4.10, it can be seen that the total quantitative capacitance rises as the area of the central conductor broadens. However, there is no significant difference in the capacitance normalized to the central conductor's dimension. Rather, it exhibits higher capacitance depending on the gap size in a small area. The reason for normalizing by the central conductor's cross-section is that most of the capacitance exists between the central conductor and the outer wall. In addition, a relatively small plate is relevant in determining the gap capacitance for parallel metal plates.

4.2.3 Validation of the MW Resonator (Experiment and numerical simulation)

Eigenmode and time-domain solver based on the FIT (Finite Integration Technique) simulations have been carried out using the CST Studio Suite®2021 software to verify the operation mode and the resonance frequency of the microwave system. Fig. 4.11 (a) shows the resonance frequency of the proposed $\frac{3}{4}$ wavelength resonator obtained by (4-32) and (4-33), CST eigenmode solver, time-domain solver, and the experimental results. The field distribution can be found in Fig. 4.13 (a) on page 60. It indicates that the phase matching method (4-33) is appropriate for predicting the resonant frequency, particularly for the sensing zone of interest. (4-33) and simulation results show more differences when the spacing is less than 1 mm, which is equivalent to the length of the center conductor > 19.6 mm. This is due to the hole-influence on both the wall and the inner conductor leading to capacitance losses at the center of the resonator through which the sample penetrates, as shown in Fig. 4.13 (b) on page 60. However, it is inevitable for the sample introduction, and the electric field is still concentrated where sample detection is required.

The results demonstrate that the role of the capacitance at the opening is more dominant in determining the resonance frequency. Specifically, infinite capacitance is achieved once the gap approaches zero, as shown in Fig. 4.11 (b). However, it should be borne in mind that the losses of the electric field resulting from the

holes in the conductors are interconnected when the gap between the conductors approaches zero, and there is no longer a concentrated electric field in the middle of the resonator. Therefore, the experimental validation should be carried out in order to determine the gap's range of the central conductor, as shown in Fig. 4.14 on page 61. That will be dealt with again later.

The resonator properties of interest focus on the smallest detectable volume with reasonable accuracy. Fig. 4.11 (c) and (d) show the reflection response expressed by the Smith-chart and S_{11} spectra according to gap changes. Technically, a gap of 1.10 mm is the minimum dimension equal to the smallest loading volume considering manufacturing tolerances (Designed gap: 1 mm). However, due to the assembly tolerance, the resonator cannot satisfy this gap without pushing the continuous force to the central conductor.

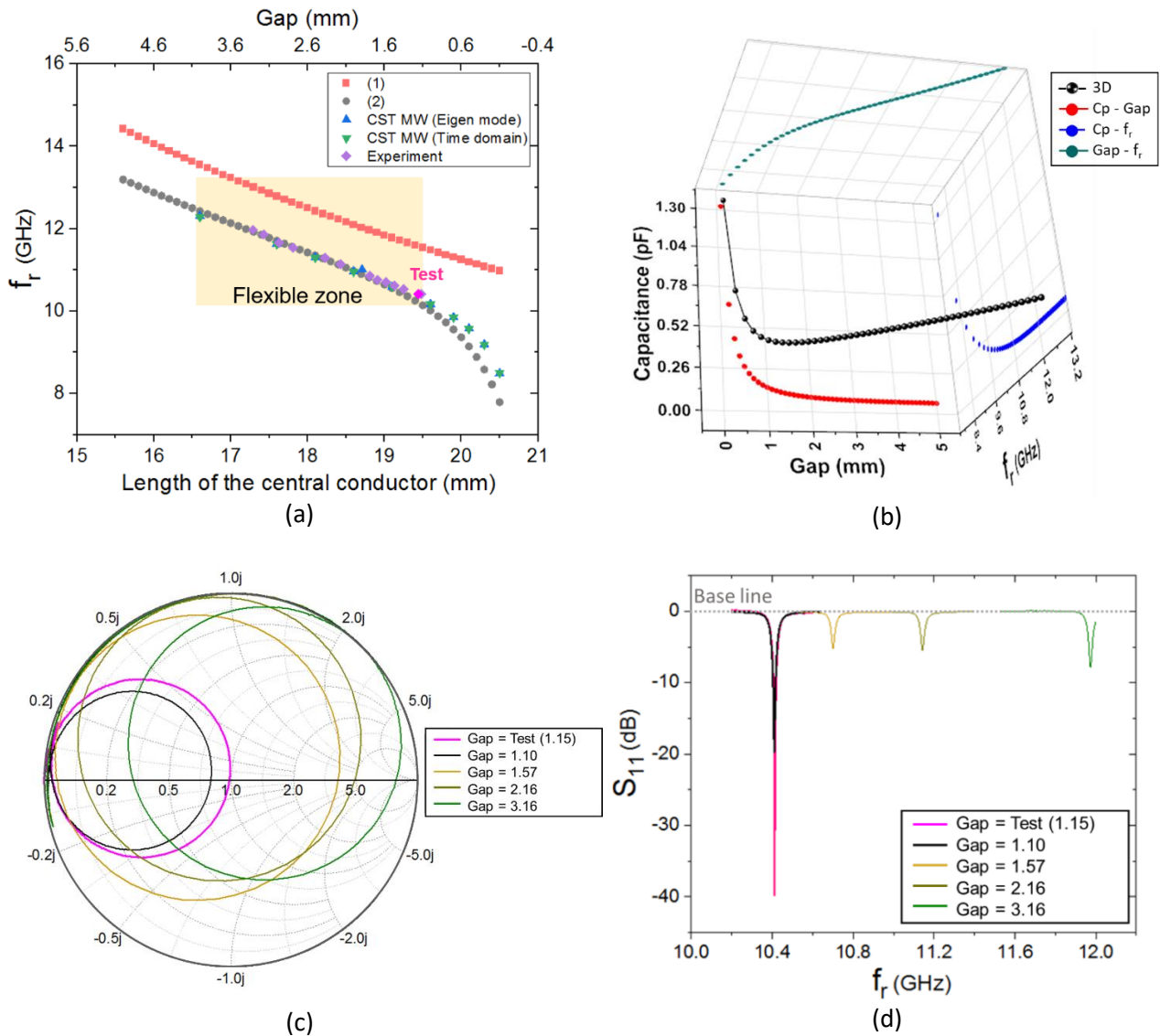


Fig. 4.11: Resonance frequency as a function of the central conductor's length (a), the 3D relationship among the capacitance - C_p , resonance frequency - f_r , and gap distance (b), the Smith-chart (c) and S_{11} (d) as a function of gap distance.

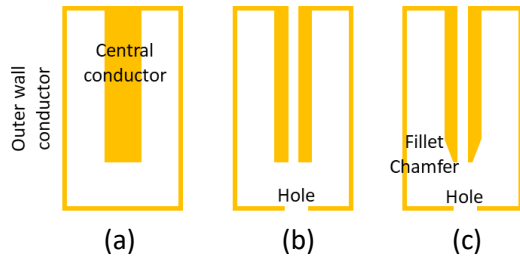
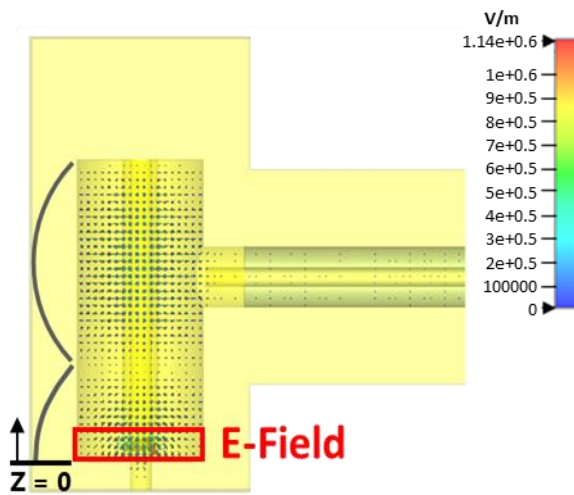


Fig. 4.12: Schematics for the analytical method (a), simulation (b), and experiment (c).

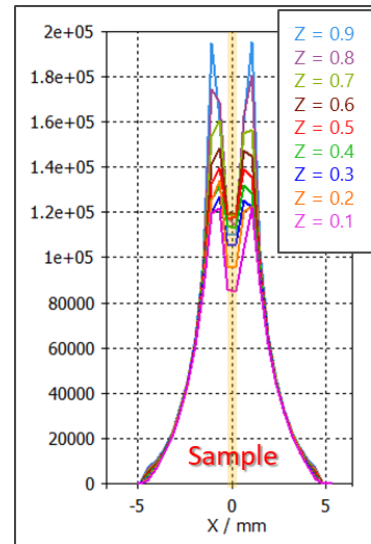
Hence, sensing experiments are performed at a 1.15 mm gap as the closest distance. The central conductor can approach the wall up to 1.15 mm without an additional effort, and the corresponded resonance frequency slightly changes from 10.410 GHz to 10.413 GHz. Fig. 4.11 (c) and (d) show that the gap of 1.15 mm adopting a 0.5 t coupling plate reaches an almost critically matched condition under the DUT (Device Under Test) environment, indicating that the test conditions are reasonably determined.

The resonant frequencies obtained from the analytical method (4-33), simulations (e.g., eigenmode and time domain), and experiments were 10.013 GHz, 10.168 GHz, 10.166 GHz at 1 mm gap, and 10.410 GHz at 1.10 mm gap, respectively. The deviation is expected because the simulation model contains a hole effect for the material loading. Besides, the central conductor utilized in the experiment enhanced the electric field intensity in the limited sensing zone by using a round fillet and a chamfer on its edge. However, it does not imply an increase in the overall capacitance. Fig. 4.12 shows the schematic for each case. These factors contribute to an increase in the resonance frequency by reducing the total capacitance of the gap. Therefore, the discrepancy between the simulation and the experiment is under 2.5 %. This is acceptable, given all manufacturing tolerances and energy dissipation in the material.

As already mentioned, Fig. 4.13 shows the electric field distribution inside this resonator. The electric field is not maximal at the center of the resonator but substantially uniform along the z-axis, except for the vicinity of the inner conductor that generates an edge-effect. In addition, the electric field is still concentrated in the gap utilized for sensing. The mode of this resonator corresponds to TEM and works as a $\frac{3}{4}$ wavelength resonator, which is the initial design objective.



(a)



(b)

Fig. 4.13: Electric field distribution (a) and intensity as a function of z-axis position (b) by CST.

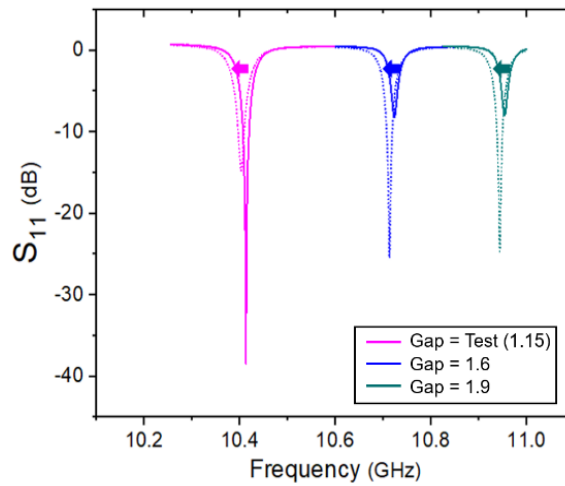


Fig. 4.14: Resonance frequency changes when the water-filled \varnothing 100 μ m capillary is loaded into the resonator with the various gap distances: \bullet lines - without water & \bullet dotted line - with water.

Table 4.2: Resonance frequency corresponding to Fig. 4.14.

| Gap (mm) | 1.15 (test) | | 1.6 | | 1.9 | |
|--------------------|-------------|----------------------------|--------|----------------------------|--------|----------------------------|
| | Empty | Water \varnothing 100 | Empty | Water \varnothing 100 | Empty | Water \varnothing 100 |
| f_r (GHz) | 10.413 | 10.403 | 10.723 | 10.713 | 10.954 | 10.944 |
| Δf_r (GHz) | 0.01 | | 0.01 | | 0.01 | |

Fig. 4.14 and Table 4.2 show the resonant frequency change when a \varnothing 100 μ m capillary filled with water is inserted into the microwave resonator. The designed device has a complementary concept because the interaction volume is proportional to the gap distance, but the electric field strength is inversely proportional to this gap dimension. As shown in Fig. 4.14, there is no difference in the resonant frequency position according to the gap distance modulation. It indicates that the smallest gap corresponding to the minimum loading volume is consistent with the maximum sensitivity, based on the ratio of the sample volume to the resonance change.

All solvers and an excitation port used for the validation of this microwave resonator by the software CST Microwave Studio are covered in Appendix 9.4.3

4.3 Dielectric Property Sensing with TEM (Transverse Electro-Magnetic) Mode Resonator

4.3.1 Experimental Measurement

Binary ethanol-water (Milli-Q) mixtures with various concentrations are tested through microcapillary tubes of both $\varnothing 100 \mu\text{m}$ and $\varnothing 200 \mu\text{m}$ to demonstrate the customized resonator in terms of sensing ability. In particular, attention is paid to the complex permittivity ($\epsilon = \epsilon' - j\epsilon''$) that affects the resonant frequency and the behavior of the Q-factor. The reason, two mediums are selected is to examine the resonator in a broad range of complex permittivity by different mixing ratios (See, Fig. 4.2).

The volume fraction of these mixtures is controlled from 0 to 100 % with a maximum step size of 10 %.

Fig. 4.15 (a) and (b) show the measurement results of the reflection response (S_{11}), which is the ratio of the reflection to the drive signal at the same terminal, recorded by the Vector Network Analyzer for both capillaries, $\varnothing 100 \mu\text{m}$ and $\varnothing 200 \mu\text{m}$. The displacement of the resonance characteristic is proportional to the sample volume, as expected. The resonance frequency is extracted from the peak position of the reflected spectra, and the Q-factor is calculated by the reflection-type method since this resonator has only one port [143, 144]. The error bar is obtained from the combined standard uncertainty [145].

The resonance frequency acts on an inverse relation with the volume fraction of water (100 μm capillary: 10.410 GHz \rightarrow 10.402 GHz, 200 μm capillary: 10.404 GHz \rightarrow 10.352 GHz), and the lowest Q-factor exists at around 10 % volume fractions of ethanol, as shown in Fig. 4.15 (c). A non-linear curve-fitting model is proposed to characterize the resonator. The values gained by this method enable, through the LSM (Least Square Model) method, determining the simplified linear equation, which represents the system configuration. The reference of [114] demonstrates the nonlinearity of the complex permittivity with respect to the fractional volume ratio of the water-ethanol mixture in the microwave regime. In addition, real and imaginary parts of the complex permittivity show similar trends to the inversed behavior of the resonance frequency and Q-factor attained from the fabricated resonator.

To minimize errors in the mixing step, all concentrations of the binary mixtures were tested at least three times with a commercially available open coaxial dielectric probe kit (HP 85070B) and to acquire a reliable complex permittivity. The average values were chosen as standard data to characterize the device.

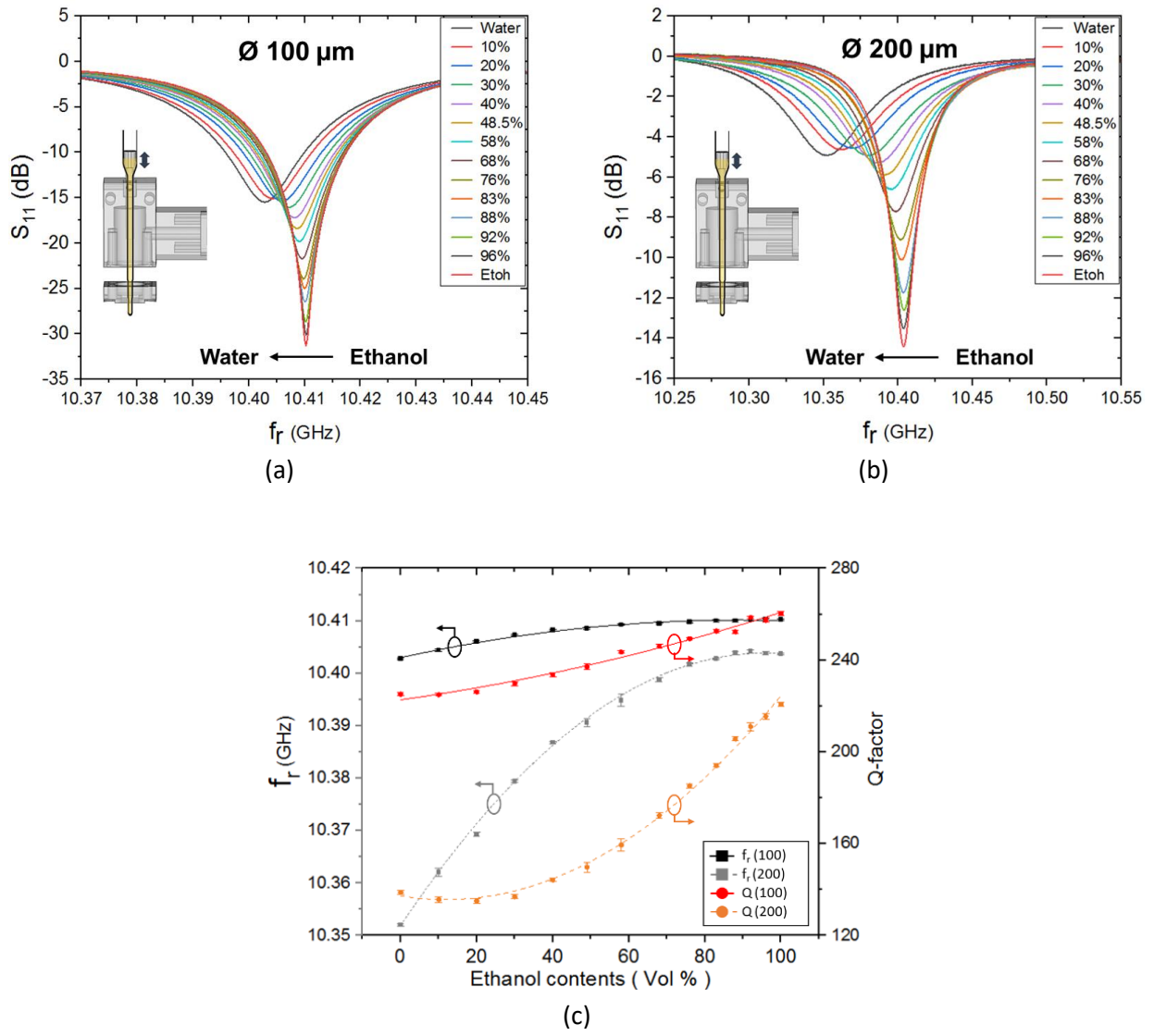


Fig. 4.15: S_{11} spectra for inserted capillaries of $\varnothing 100 \mu\text{m}$ (a), $\varnothing 200 \mu\text{m}$ (b), and resonance frequency & Q-factor (c). All as a function of ethanol contents in various water-ethanol mixtures.

4.3.2 Device Characterization

This section is dedicated to a novel resonator validation as a sensing device, especially for estimating the complex permittivity of an unknown sample. The property is extracted based on the change of the resonance frequency and Q-factor with various analytical methods. Lastly, the processed complex permittivities for this resonator are compared with the reference data to determine the most suitable method for this resonator (methods describe hereafter in a) to d)).

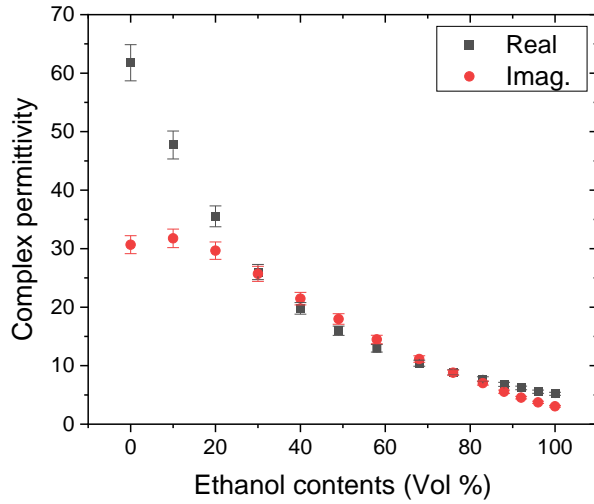


Fig. 4.16: The mixture's complex permittivity with an estimated error at 10.413 GHz (f_r of the empty cavity) obtained from the open-ended coaxial dielectric probe kit (HP 85070B).

Table 4.3: Complex permittivity corresponding to Fig. 4.16.

| EtOH (Vol %) | ϵ' (Real) | ϵ'' (Imag.) |
|-----------------|--------------------|----------------------|
| 0 % (Water) | 61.7747 | 30.6728 |
| 10 % | 47.7219 | 31.7554 |
| 20 % | 35.5263 | 29.6555 |
| 30 % | 26.0047 | 25.6950 |
| 40 % | 19.7852 | 21.4559 |
| 49 % | 15.9727 | 17.9753 |
| 58 % | 12.9713 | 14.4740 |
| 68 % | 10.4213 | 11.1392 |
| 76 % | 8.8603 | 8.7914 |
| 82 % | 7.7182 | 7.0208 |
| 88 % | 6.8034 | 5.5533 |
| 92 % | 6.1936 | 4.5379 |
| 96 % | 5.5477 | 3.7310 |
| 100 % (Ethanol) | 5.1960 | 3.0581 |

a) Open-Ended Coaxial Method (Standard)

A commercial open-ended coaxial probe kit (HP 85070B, Accuracy: $\pm 5\%$) based on the reflection measurement has been utilized for attaining reliable permittivity data of the samples at 10.413 GHz (resonance frequency of the empty cavity).

Table 4.3 and Fig. 4.16 show the measurement results. This instrument was calibrated before the data acquisition using air, a short circuit, and 25 °C Milli-Q (MQ) water.

The main algorithm of this system to obtain the permittivity of the various samples with varying ethanol concentrations is the Debye model:

$$\epsilon = \epsilon_{\infty} + \frac{\epsilon_s - \epsilon_{\infty}}{1 + j\omega\tau}, \quad (4-49)$$

where ϵ_{∞} is the permittivity at the high-frequency limit, ϵ_s is the static frequency permittivity, and τ is the characteristic relaxation time of the medium [105, 114, 115].

b) Perturbation Method (PM)

The perturbation method (PM) can be applied if the electromagnetic field of the system is assumed constant regardless of the sample introduction. Furthermore, this sample volume should be small enough compared to the entire EM field affected zone. In other words, the electromagnetic field is perturbed only in the sample area without changing the total stored energy in the cavity. The typical perturbation method can be described as (4-50), and the variations of both the resonance frequency and Q-factor are expressed as a function of the complex permittivity when the sample is located in the maximal electric field like (4-51) and (4-52) [130, 136].

$$\frac{\omega_2 - \omega_1}{\omega_2} = \frac{(\mu_2 - \mu_1) \iiint_{V_s} H_1 \cdot H_2 dV - (\epsilon_2 - \epsilon_1) \iiint_{V_s} E_1 \cdot E_2 dV}{2 \iiint_{V_c} \epsilon_1 |E_1|^2 dV}, \quad (4-50)$$

$$\frac{f_1 - f_2}{f_2} = A (\epsilon'_{sam} - \epsilon'_e) \frac{V_{sam}}{V_c}, \quad (4-51)$$

$$\frac{1}{Q_2} - \frac{1}{Q_1} = B (\epsilon''_{sam} - \epsilon''_e) \frac{V_{sam}}{V_c}, \quad (4-52)$$

where $\omega, \mu, \epsilon, H, E$, and V represent the complex angular frequency, magnetic permeability, dielectric permittivity, magnetic field and electric field in the cavity, and the volume.

The subscript 1 and 2 designate the state before and after electromagnetic field perturbation attributable to the sample's introduction in the resonator. In addition, c and sam represent the cavity and the sample, respectively.

f, Q, ϵ' , and ϵ'' indicate the real part of the resonant frequency, quality factor, and decomposed complex permittivity. Here, ethanol is used as an initial medium (not air) to judge the variation of the resonance properties resulting from the water concentrations. Therefore, ϵ'_e and ϵ''_e stand for the complex permittivity of ethanol. The unloaded Q-factor is adopted for PM, as shown in Fig. 4.17. It can exclude the excitation effect while taking into account coupling [143, 144].

Coefficients A and B are affected by the cavity configurations, including the operation mode. They are obtained in a calibration step using a reference material whose permittivity has already been investigated (e.g., water).

This method does not consider the interrelationship of $\epsilon' \leftrightarrow Q$ and $\epsilon'' \leftrightarrow f_r$, meaning that each variable only influences matching factors, such as $\epsilon' \leftrightarrow f_r$, or $\epsilon'' \leftrightarrow Q$.

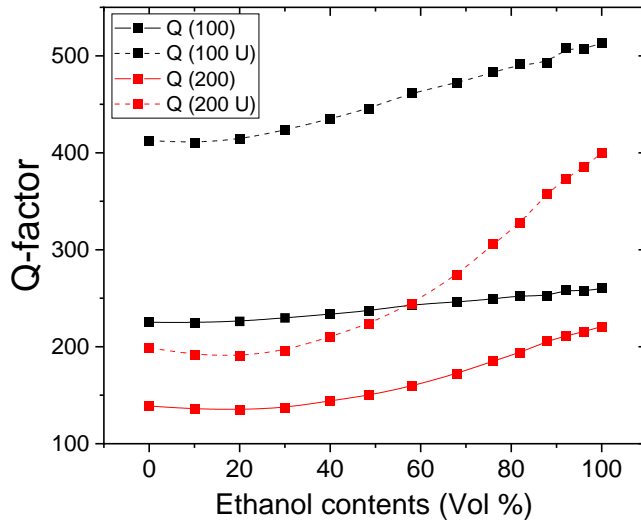


Fig. 4.17: The loaded Q-factor and un-loaded Q-factor with different size of the capillary (Number: capillary size, and U: un-loaded).

c) Least-Square Model (LSM)

The least-squares model is a readily used methodology for the characterization of split-ring resonators using TEM mode excitation. The main principle is capacitance-based sensing around the gap.

The model is formulated from the set of measurement results with respect to the frequency shift and the Q-factor changes to correlate with the dielectric property. Consequently, a simple mathematical model is derived as a function of the complex permittivity that considers the uncertainty of the measurement. The detailed derivation is elaborated in [146, 147].

$$\begin{bmatrix} m_{11} & m_{12} \\ m_{21} & m_{22} \end{bmatrix} \begin{bmatrix} \Delta \epsilon' \\ \Delta \epsilon'' \end{bmatrix} = \begin{bmatrix} \Delta f_r \\ \Delta Q_r \end{bmatrix}, \quad (4-53)$$

where $\Delta \epsilon' = \epsilon'_{sam} - \epsilon'_{49\%}$, $\Delta \epsilon'' = \epsilon''_{sam} - \epsilon''_{49\%}$, $\Delta f_r = f_{r,sam} - f_{49\%}$ and $\Delta Q_r = Q_{r,sam} - Q_{49\%}$ of the material under test. The subscripts 49 % and *sam* indicate 49 % ethanol volume fraction mixture and various samples, respectively.

The dielectric permittivity of these mixtures, ϵ'_{sam} and ϵ''_{sam} , are acquired from a standard open-ended coaxial dielectric probe kit (HP 85070B), and a 49 % volume fraction mixture is employed as a reference value. The (4-54) and (4-55) denote the characterized matrix for a \varnothing 100 μ m capillary and a \varnothing 200 μ m capillary, respectively.

$$\begin{bmatrix} \epsilon'_{sam} \\ \epsilon''_{sam} \end{bmatrix} = \begin{bmatrix} -0.115 & -0.036 \\ 0.273 & -1.638 \end{bmatrix} \begin{bmatrix} \Delta f_r \\ \Delta Q_r \end{bmatrix} + \begin{bmatrix} \epsilon'_{49\%} \\ \epsilon''_{49\%} \end{bmatrix}, \quad (4-54)$$

$$\begin{bmatrix} \epsilon'_{sam} \\ \epsilon''_{sam} \end{bmatrix} = \begin{bmatrix} -0.730 & -0.457 \\ 1.779 & -5.698 \end{bmatrix} \begin{bmatrix} \Delta f_r \\ \Delta Q_r \end{bmatrix} + \begin{bmatrix} \epsilon'_{49\%} \\ \epsilon''_{49\%} \end{bmatrix}. \quad (4-55)$$

This method reflects the interdependencies between factors approximated in the form of linear equations.

d) Log-Linear Model (LLM)

This method is called an algebraic or log-linear mixing model (LLM) that is usually adopted for estimating the liquid mixture's physicochemical properties by the simplified mixing rule [148].

$$\ln X_m = f_w \ln X_w + f_e \ln X_e, \quad (4-56)$$

where X is the dielectric property of the mixture, and f denotes the fractional factor. The subscripts w , e , and m stand for water, ethanol, and water-ethanol mixture, respectively.

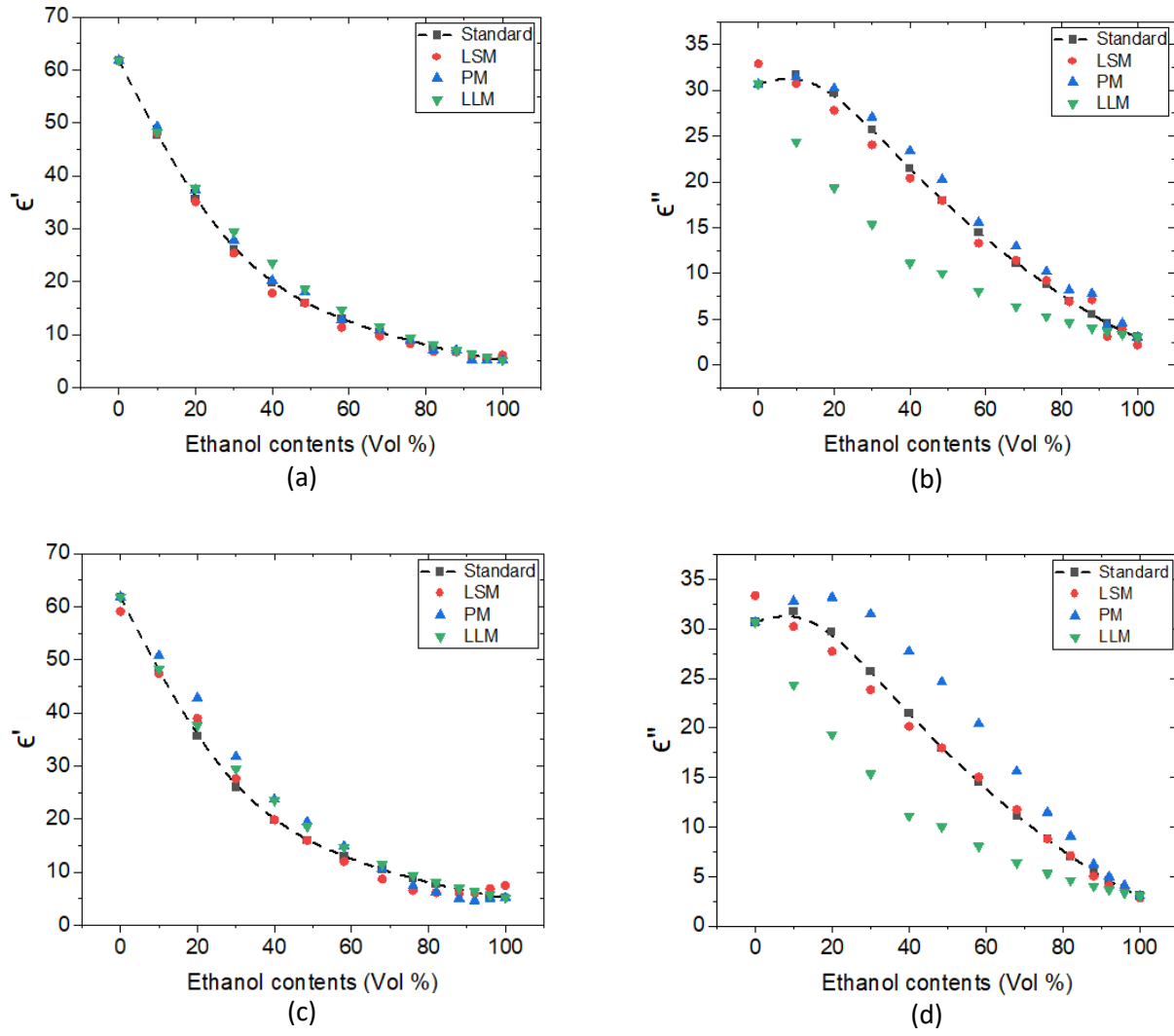


Fig. 4.18: The complex permittivity comparison obtained by Standard, PM, LSM, and LLM methods. ϵ' for 100 μm capillary (a), ϵ'' for 100 μm capillary (b), ϵ' for 200 μm capillary (c), and ϵ'' for 200 μm capillary (d).

Fig. 4.18 shows the obtained complex permittivity by all schemes elaborated above (methods a-d). All manners of the real-permittivity estimation follow the reference's trend, but the imaginary permittivity may have discrepancies because the Q-factor does not come from the direct measurement. Therefore, the process which estimates the Q-factor might introduce errors, affecting the ϵ'' values [143].

Specifically, the LSM method is the most appropriate tool to predict the dielectric permittivity regardless of the capillary size. In the range below 58 vol. % ethanol, the maximum deviation is only 12.5 % in all cases. In particular, if it is limited only to the case of \varnothing 100 μm , the same maximum deviation is maintained up to 82 % of the ethanol volume mixing ratio. The main reason is that the characteristic matrix representing the resonator is obtained by non-linear curve fitting based on standard data in all fractional volume ranges. It already includes manufacturing tolerances. In addition, this method deals with the reciprocal interaction of the complex permittivity that can simultaneously influence the change of the resonance frequency and the Q-factor. A disadvantage of this method is that it is unable to reflect correction factors on data that deviate from the overall fitted curve defined by the matrix form.

Another alternative is the perturbation method. In particular, the case of using a \varnothing 100 μm capillary is more consistent with the reference data than the case of a \varnothing 200 μm one. It is worth noting that \varnothing 100 μm capillary PM results not only follow standard data within a 12.7 % tolerance within 58 % ethanol volume but also reflect the behavior of ϵ'' where the inflection point appears around 10 vol. % ethanol of the binary mixture. This error is valid up to 88 vol. % ethanol in terms of the dielectric constant, and increases up to 16 % within 82 % ethanol volume for the imaginary permittivity. A notable feature of the PM methodology is that it does not take into account the complex interdependencies between permittivity and resonant properties. In other words, ϵ' affects only the resonant frequency and ϵ'' changes the Q-factor, respectively. This scheme is superior for extracting complex permittivity close to the standard value for nanoliter liquid volumes (e.g. 5 nL).

The complex permittivity trend of a \varnothing 200 μm capillary case obtained by the PM matches the standard data. However, values seem to be overestimated as the electric field is inhomogeneous in the radial direction resulting in stronger perturbation as shown in Fig. 4.13. It represents the maximum electric field present around the central conductor due to the edge effect. Moreover, the magnitude of the S_{11} variation related to the Q-factor is weaker than for the \varnothing 100 μm case, reflecting the sensitivity generated by the coupling effect with the samples. Another predictable cause is attributable to the calibration process conducted using only pure water and then applied to all the samples. The deviation could be reduced by adopting the calibrated water's permittivity with non-linear curve fitting.

The log-linear model considerably approximates the real permittivity. However, it is not suitable for anticipating the imaginary permittivity of the sample since the tendency of ϵ'' is not correlated to the fractional volumes of the specimens. The log-linear model contains the maximum error at 40 % water content.

The sensing capability based on the microwave resonator works better once the water content is high, and the error tends to increase when the value of the complex permittivity is small. This result is consistent with the reference that the small coaxial resonator is suitable for high water content, but in contrast, the larger coaxial size provides better accuracy for low moisture content [112].

Chapter 5 Microwave Heating

The basics of microwave physics have already been covered at the beginning of this thesis and in Chapter 4. Therefore, this chapter focuses more on the microwave heating subject to meet the research goal: drying in-flight droplets. The study is based both, on theoretical and experimental work. Both cavity and coaxial resonators, fabricated at PSI, have been tested with micro water droplets for their heating performance evaluation. The designs of the implemented microwave resonators are unique; for instance, they included movable or changeable structures that can cover the impedance mismatch between the excitation and the resonator.

The heating efficiency characterization is challenging because the droplet velocity is not only fast ($> 3 \text{ m} \cdot \text{s}^{-1}$) but the droplets are also tiny ($\leq 100 \text{ }\mu\text{m}$ in diameter), making accurate temperature measurement impossible. Moreover, installing the measurement device inside the concentrated electric field is arduous, since the resonator is a closed structure to prevent any field leakage except for the small hole where the droplet passes through. Furthermore, any further opening for observation could also influence the field distribution leading to changes in the resonance behavior. Hence, the temperature changes of droplets after passing through the developed resonator and the resulting evaporation rate are experimentally verified in this chapter.

Fundamental heat and mass transfer principles of the falling droplet that can estimate not only the initial temperature but also microwave heating efficiency are covered in the next chapter based on the measurement method presented here.

5.1 Background

Microwave application plays an important role in drying and heating processes in many fields, which can be research or industry related, such as food and material processing, because it can achieve a rapid energy transfer with improved efficiency and it can also be selective compared to any other type of conventional heating. The main reason is that the volumetric energy absorption results in multiple (dispersive) heat generations over the entire volume [93, 149].

Usage of microwave energy for heating emerged in 1937 by Kassner [150, 151]. He elaborated on the internal energy change due to the dipolar substance yet without attaining a heating effect. In 1940, the commercial use of dielectric heating by microwaves began at a company in Richmond, Virginia, for the rapid hardening of bonding cement for plywood [152]. In addition, references from the late 1940s [150] and [154] already demonstrated the engineering design principles of radiofrequency heating and the benefits for food processing. Raytheon unveiled the first microwave oven operating at 2.45 GHz in 1947, and General Electric's oven product working at 915 MHz was launched during the same year [31]. The related microwave study had been concretely investigated by Von-Hippel in the early-1950s for the organic and inorganic material characterization in the frequency ranges from 100 Hz to 10 GHz [155]. Eventually, W.B. Westphal and various researchers demonstrated manifold microwave applications, from food to oil-shale heating [156].

Nowadays, microwave heating is more widely utilized not only for scientific work but also for industrial applications, such as drying organic materials [157, 158], ceramic sintering [159–161], polymer processing [162, 163], chemical synthesis of nanomaterials [164, 165], melting & joining [166, 167], and 3D Printing [61].

Many references focused on the typically used frequency 2.45 GHz and 915 MHz, but this thesis addresses the X band operation, especially between 10 and 11 GHz.

5.1.1 Microwave Penetration Depth

As mentioned before, the most outstanding characteristic of microwave heating is that the microwave penetrates into the material. The heat generating locations are therefore within the material volume, and for relatively small dimensions, the heat transfer takes place from inside to outside of the sample. The penetration depth of microwaves (D_p) is defined as the distance at which the initial power dissipated up to e^{-1} times equal to, 36.8 %, which means that 62.8 % of the power intensity at the entrance remains in the material.

Microwave energy is reduced and partially converted to thermal energy by the interaction with a dielectric load placed in its propagation path. The dissipated power depends on the interacted distance through this relationship

$$P_z = P_0 e^{-2\alpha z},$$

(5-1)

where α , P_z , and P_0 are attenuation constant, microwave power propagating along the z-axis, and the initial power value at the entrance without attenuation.

In conventional furnaces, heat transfer is based on thermal electromagnetic radiation. However, the penetration depth corresponding to infrared radiations (0.3 - 400 THz) is very small for most materials, typically $Dp \ll 10^{-4}$ m. Thus, it is only possible to deliver heat within a thin outer layer, the rest is governed by the heat transfer properties of the material, especially heat conduction, resulting in the temperature gradient along the central axis.

In contrast to infrared heating, the microwave penetration depth lies between millimeters and meters, depending on the frequency, temperature, and physicochemical properties. This difference in penetration is evident, since the working frequencies of microwaves, ranging from 0.3 to 300 GHz, are much lower than the infrared working frequency [168]. This property enables uniform heating across the material for a limited size, allowing rapid heating and homogeneous properties of the outcome. It means that an adequate determination of operating frequency, being inversely proportional to the penetration depth, is critical to accomplish the targeted outcome by microwave heating, depending on the size and properties of the loaded sample. In practice, the penetration depth is affected by both electrical and magnetic properties. However, in the framework of this thesis, only microwave heating of dielectric materials, such as water, has been conducted. The magnetic effect, due to permeability in free space, is negligible, ($\mu'_r = 1$, and $\mu''_r = 0$), [93].

The attenuation constant, α , is simplified as

$$\alpha = \frac{2\pi}{\lambda_0} \left(\frac{1}{2} \epsilon' (\sqrt{1 + \tan^2 \theta})^{\frac{1}{2}} - 1 \right)^{\frac{1}{2}}. \quad (5-2)$$

Moreover, the penetration power is defined by the 36.8 % of the original power

$$P_{Dp} = P_0 e^{-1}. \quad (5-3)$$

The penetration depth is possible to be expressed as

$$Dp = \frac{1}{2\alpha} = \frac{\lambda_0}{2\pi \sqrt{2\epsilon'(\sqrt{1 + \tan^2 \theta} - 1)}}, \quad \tan \theta = \frac{\epsilon''}{\epsilon'}, \quad (5-4)$$

where P_{Dp} , Dp , and λ_0 are penetration power, depth, and wavelength in free space, respectively [93, 169]. This penetration depth is a crucial factor that decides the microwave heating performance.

The loss tangent, $\tan \theta$, refers to the phasor in the complex plane, corresponding to the electrical energy dissipation from an electromagnetic field within a material.

5.1.2 Microwave Power Absorption

Molecular depolarization has been explained as the main working principle for the interaction between a material and microwaves in Chapter 4. For the non-magnetic case, the dielectric property, especially the loss factor (ϵ''), determines the power attenuation as an electromagnetic field penetrates a material. The dipole lag occurs from the inertial and frictional losses during the movement of the dipoles, driven by the alteration of the external electric field, and finally creating volumetric heating.

The absorbed power into the dielectric object is expressed as

$$P_d = 2\pi f \epsilon_0 \epsilon''_{eff} |E_{rms}|^2 V. \quad (5-5)$$

The power absorption depends on the sample volume, V , the imaginary part of permittivity, ϵ''_{eff} , which can be expressed as a function of the loss factor, and the averaged electric field, E_{rms} . In other words, the power absorption rate strongly depends on the resonator's ability and the material. If the material accompanies a magnetic loss, the terms resulting from the permeability should be plus, and the complete form is expressed by adding the imaginary part of permeability, μ''_{eff} , and the averaged magnetic field, H_{rms} ,

$$P_d = 2\pi f \epsilon_0 \epsilon''_{eff} |E_{rms}|^2 V + 2\pi f \mu_0 \mu''_{eff} |H_{rms}|^2 V. \quad (5-6)$$

This includes the magnetic wall domain and electron spin loss [93].

5.2 Microwave Feasibility Test

Fig. 5.1 summarizes all microwave resonators examined for their heating capability with the verified droplet generation system covered in Chapter 3. Various resonator types, for example, coplanar (R1, R2), coaxial (R3, R6, R7), and cavity-shapes (R5, R7), have been considered for the preliminary heating test.

The designed operating frequency ranges are the S-band and X-band typically used for appliance and telecommunication. The temperature measurements are performed by an infrared camera (Telops - M3k) or a K-type thermocouple. As expected from Chapter 2, the S-band frequency is not enough for drying a dynamic droplet that has a high-speed ($\approx 3 \text{ m} \cdot \text{s}^{-1}$). As a result, just the resonator heats up. However, there is no noticeable difference in terms of the temperature of the water droplet.

Unlike for sensing applications, sufficient input power should be ensured for heating experiments. Hence, closed structures are preferred. The resonators, such as coplanar (R1, R2), loop-gap (R4), and a couple of open-coaxial geometries (R3, R7) were tested with an additional perforated metal barrier to protect the possible microwave leak out of the device. Finally, a cavity-type and a closed coaxial resonator that exhibits potential for heating are selected and dealt with in this chapter.


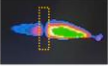

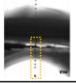

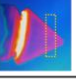
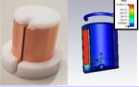

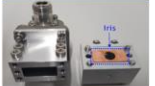
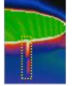



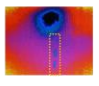
| Droplets | | | | | | |
|----------|--|---|---------------------------|-----------------|-------------|---|
| | Type | Image | Resonance Frequency (GHz) | Loaded Q-factor | Heating | Experiment |
| R1 | Split ring (Hole: $\varnothing 1$) |  | 2.460 | 39.7 | X |  |
| R2 | Split ring (Hole: $\varnothing 3$) |  | 2.468 | 17.2 | X |  |
| R3 | Coaxial |  | 2.451 | 47.6 | X |  |
| R4 | Loop gap resonator |  | 2.384 | - | X |  |
| R5 | Cavity |  | 11.275~ 11.394 | 500 ~ 2500 | \triangle |  |
| R6 | Coaxial |  | 10.413 | 263.1 | O |  |
| R7 | Etc. |  | 2.464 | 35.7 | X |  |

Fig. 5.1: All resonators examined for their heating performance (O: Heating, \triangle : Partial heating, and X: No heating).

5.3 Microwave Cavity

This chapter describes the microwave cavity as one of the potential final tools to achieve the thesis objective and introduces the cavity heating mechanism. In particular, it is verified in terms of design, coupling, and heating efficiency based on the operating principle of conventional cavity resonators such as rectangular and cylindrical resonators. The basic information about the cavity resonator concept is covered in Section 4.1.3.

Fig. 5.2 shows typical cavity types. Cylindrical cavities are commonly used applicators for heating liquid samples because of the appearance of a centrally focused electric field along the z-axis resulting in sufficient interaction distance ($d < 2.1 \times a$, in Fig. 5.2 (b)). Here, the content focuses on the resonant behavior, the coupling and design of the cavity, and the experimental results. At the same time, the propagation modes and derivations for field distributions are dealt with in Appendix 9.3.

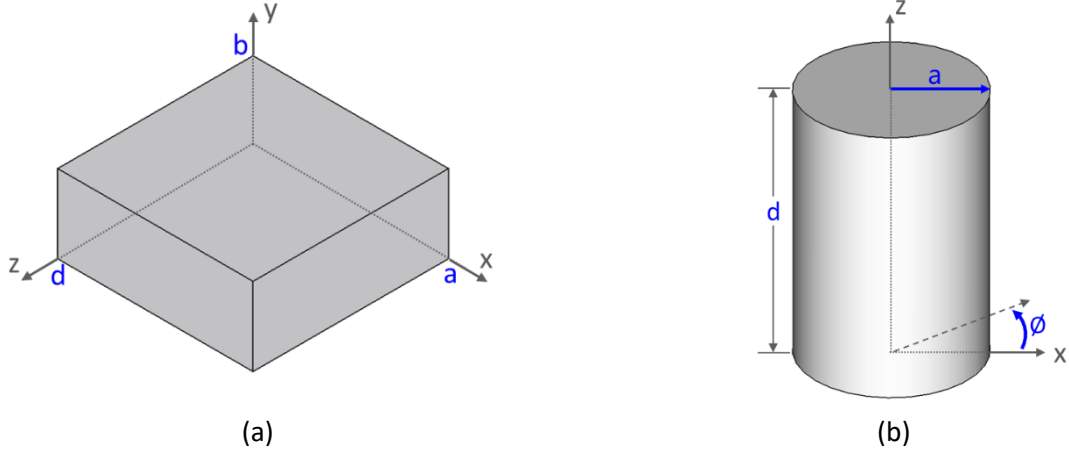


Fig. 5.2: Typical resonant cavity: rectangular cavity (a), and cylindrical cavity (b).

5.3.1 Resonance Frequency

a. Rectangular cavity

In Cartesian coordinates, the transverse electric (TE) field mode of a rectangular waveguide is given by

$$\bar{E}_t(x, y, z) = \bar{e}(x, y)[A^+ e^{-j\beta_{mn}z} + A^- e^{j\beta_{mn}z}], \quad (5-7)$$

where $\bar{e}(x, y)$ is a transverse electric field component at this mode, and (A^+, A^-) represent the amplitudes of the forward and backward wave, respectively.

The m, n -th TE or TM mode's propagation constant, β_{mn} , is written as

$$\beta_{mn} = \sqrt{k^2 - \left(\frac{m\pi}{a}\right)^2 - \left(\frac{n\pi}{b}\right)^2}, \quad (k = \omega\sqrt{\mu\epsilon}). \quad (5-8)$$

The term k is a wavenumber indicating the spatial frequency of a wave expressed in radians per unit distance.

The boundary condition of $[\bar{E}_t = 0 \text{ at } z = 0, d]$ is applied to the equation (5-7) due to the closed end

$$\begin{aligned} A^+ &= -A^-, \\ \bar{E}_t(x, y, d) &= -\bar{e}(x, y)[A^+ 2j \sin\beta_{mn}d] = 0, \\ \beta_{mn}d &= l\pi, \quad l = 1, 2, 3, \dots \end{aligned} \quad (5-9)$$

The wave number of a rectangular cavity is notated by

$$k_{mnl} = \sqrt{\left(\frac{m\pi}{a}\right)^2 + \left(\frac{n\pi}{b}\right)^2 + \left(\frac{l\pi}{d}\right)^2}. \quad (5-10)$$

The resonance frequency of a rectangular cavity can be expressed as

$$f_{mnl} = \frac{c}{2\pi\sqrt{\epsilon_r\mu_r}} \sqrt{\left(\frac{m\pi}{a}\right)^2 + \left(\frac{n\pi}{b}\right)^2 + \left(\frac{l\pi}{d}\right)^2}. \quad (5-11)$$

The meaning of m , n , and l corresponds to the number of antinodes in the standing wave pattern present inside the rectangular cavity along the x , y , and z directions, respectively.

b. Circular cavity

The transverse electric field of a circular waveguide is given by

$$\bar{E}_t(\rho, \phi, z) = \bar{e}(\rho, \phi) [A^+ e^{-j\beta_{mn}z} + A^- e^{j\beta_{mn}z}], \quad (5-12)$$

where $\bar{e}(\rho, \phi)$ is the transverse variation at the corresponding mode, and (A^+, A^-) represent arbitrary amplitudes of the forward and backward wave, respectively.

The propagation constants of both the TE_{mn} and TM_{mn} modes are described as

$$\begin{aligned} \beta_{mn} &= \sqrt{k^2 - \frac{P'_{mn}}{a}} \text{ for TE mode,} \\ \beta_{mn} &= \sqrt{k^2 - \frac{P_{mn}}{a}} \text{ for TM mode, } (k = \omega\sqrt{\mu\epsilon}), \end{aligned} \quad (5-13)$$

where P'_{mn} , P_{mn} , and a dictate the n -th zero of the derivative ($J'_m(x)$) of the Bessel function of the first kind $J_m(x)$, n -th zero of the Bessel function of the first kind ($J_m(x)$), and radius of the cavity.

The boundary condition of $[\bar{E}_t = 0 \text{ at } z = 0, d]$ is applied to the equation (5-12) due to the closed end

$$\begin{aligned} A^+ &= -A^-, \\ A^+ \sin\beta_{mn}d &= 0, \\ \beta_{mn}d &= l\pi, \quad l = 0, 1, 2, 3, \dots \end{aligned} \quad (5-14)$$

The resonance frequency of a circular waveguide can be expressed as

$$\begin{aligned} f_{mnl} &= \frac{c}{2\pi\sqrt{\epsilon_r\mu_r}} \sqrt{\left(\frac{P'_{mn}}{a}\right)^2 + \left(\frac{l\pi}{d}\right)^2} \text{ for TE}_{mnl}, \\ f_{mnl} &= \frac{c}{2\pi\sqrt{\epsilon_r\mu_r}} \sqrt{\left(\frac{P_{mn}}{a}\right)^2 + \left(\frac{l\pi}{d}\right)^2} \text{ for TM}_{mnl}, \end{aligned} \quad (5-15)$$

The indices m , n , and l refer to the number of full-period variations of the field along the circumferential direction, half-period variations of the field in the radial direction, and half-period variations in the z -direction, respectively. The d represents the height of the cavity.

Detailed derivations and the Bessel function relevant to the cavity resonator are described in Appendix 9.3.

5.3.2 Cavity Coupling

In general, the resonator's impedance is not the same as the impedance of the excitation device, so it is necessary to incorporate a matching network, for example, between the cavity and the waveguide.

Not only for microwave heating but also for all the RF transmission circuits, the most important procedure for commissioning is the coupling between the external source through a feeding device (e.g., coaxial cable or waveguide) and the operating cavity. The reason for this is the strong coupling effect on the power propagation efficiency. For example, in case of a coupling mismatch, a strong reflection occurs, and the energy cannot be delivered adequately into the cavity resonator from the feeding line. As a result, the system is not excited, and most of the input power is dissipated without heating. The coupling mechanism is determined by the dipole moment or magnetic flux generated in the electromagnetic field of the coupling device, which corresponds to the operation mode of the cavity. Therefore, it is also named by two terms, electric or magnetic coupling. Typically utilized coupling structures are antenna, loop, and waveguide with iris (e.g., aperture) couplers, as shown in Fig. 5.3.

Loop coupling is conjugated for magnetic coupling. A magnetic field generated around a loop, made out of the dismantled centroid conductor of a coaxial cable, can induce a magnetic dipole flux into the cavity. The coupling loop must be located in the maximum magnetic field, and the direction of the magnetic dipoles created by the loop should follow the magnetic field of the cavity mode the user plans to excite. The strength of the coupling is associated with the loop area and input power, i.e., the inductivity of the loop.

The antenna coupling (or probe coupling) utilizes the electric field combination between the coaxial probe and the cavity. The electric dipole related to the electric current on its surface leads to excitation of the structure once the orientation of electric dipole flux is matched to the electric field of the cavity resonant mode. The antenna is therefore placed in the maximum electric field to enhance the coupling intensity. As a result, the coupling efficiency is proportional to the current density of the antenna created in a tangential direction.

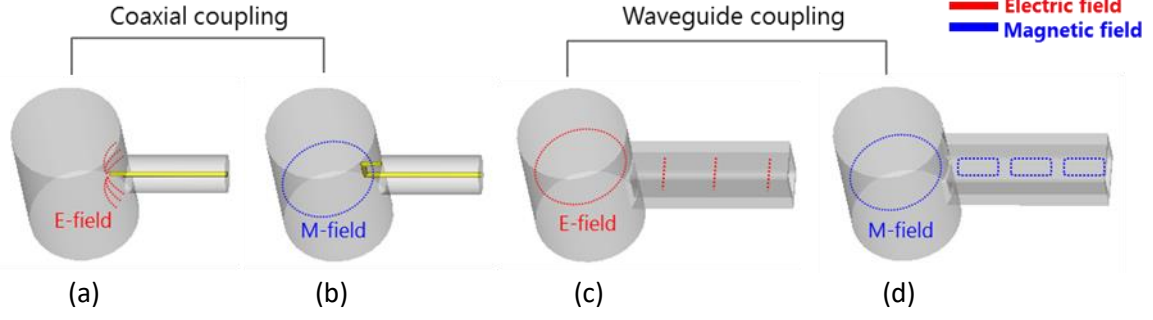


Fig. 5.3: Coaxial coupling using electric field (a), magnetic field (b), waveguide coupling using electric field (c), and magnetic field (d).

The waveguide coupling through the iris also follows the previous principle. The electromagnetic dipole flux induced on the iris between the waveguide and the cavity is the principal source of the power coupling. Thus, the propagation behavior of the waveguide should be considered carefully to excite the proper mode a user has purposed.

The cases, that cannot efficiently convey power, mainly result from the iris mismatching. Accordingly, the cavity used in this research is designed with an adaptable iris size to achieve the best condition for power coupling. The selection of a coupling method for the cavity depends on the planned power handling capacity. For high-power transmission like for heating purposes, typically, the waveguide is preferred over coaxial coupling.

a. Coupling coefficient

The coupling network acts as a transformer to be in agreement with the characteristic impedance of the excitation and the microwave resonator, resulting in the energy loss minimization in the transition area.

The reflection coefficient is directly linked to the coupling quality, e.g., a small reflection represents a well-matched coupling in terms of the mutual impedance.

A new coupling parameter, β' , is introduced to evaluate the coupling effect, called the effective coupling factor relevant for the resistance loss of the cavity and characteristic impedance of the waveguide [93].

$$\Gamma = \frac{1 - (\frac{1}{\beta'})}{1 + (\frac{1}{\beta'})} \quad (5-16)$$

1. $\beta' \ll 1$, the resonator is under-coupled to the feed line which represents a reflection coefficient close to -1
2. $\beta' \gg 1$, the resonator is over-coupled to the feed line which shows a reflection coefficient close to +1
3. $\beta' = 1$, the resonator is critically (perfectly) coupled to the feed line which dictates a reflection coefficient of 0

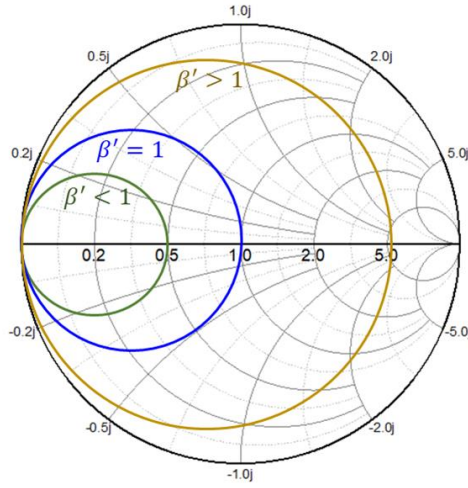


Fig. 5.4: Smith-chart expressing the reflection coefficient as a function of the coupling coefficient, β' , in the case of a parallel RLC circuit. For example, under coupling ($\beta' < 1$), over coupling ($\beta' > 1$), and critical coupling ($\beta' = 1$).

The reflection spectra with modulations of the coupling coefficient are illustrated in the Smith-chart as shown in Fig. 5.4. It helps to figure out the status of the coupling more straightforwardly.

The resonator's resistance is equal to the characteristic impedance of the connected device when the circumference crosses the center of the Smith-chart ($\beta' = 1$). The transmission line between the resonant circuit and the measuring device allows the circle to rotate around the origin of the Smith-chart [170].

Critical coupling is the best condition, not only for sensing but also for heating, because it provides energy transfer with minimal losses, including the sample influence, from the power generator to the microwave device.

If we expand the concept of the coupling parameter, which encompasses the aspect of the external circuit corresponding to the power source influence, it can be described as [171]

$$\beta' = \frac{P_{ex}}{P_0} = \frac{Q_0}{Q_{ex}}, \quad (5-17)$$

where P_{ex} , P_0 , Q_{ex} , and Q_0 dictate the dissipated powers and quality factors of the external circuit and unloaded resonator. It accounts for the coupling coefficient as a ratio of the power dissipated in the external circuit to the power loss in the unloaded resonator.

The detailed impedance matching by VNA (Vector Network Analyzer) is covered in Chapter 7.2.

5.3.3 Design of the Microwave Cavity

For drying of the liquid droplet produced from the droplet generator, a cylindrical cavity resonator was developed as a heating applicator in the X-band range (8 ~ 12 GHz), as shown in Fig. 5.5. Then, it was tested and evaluated with distilled water to validate the heating efficiency.

The design of the cylindrical cavity shown in Fig. 5.5 aims at TM₀₁₀ mode operation. The main reason why that mode is broadly used for heating applicators is not only for the simple design but also its electric field characteristics. The E-field is forming in the center of this cavity and is distributed uniformly along the z-direction. Therefore, the heating of the dielectric sample is taking place in the entire region of the cavity height when the sample's trajectory is not getting out of the central axis. The resonance frequency of the designed cylindrical cavity locates around 11.4 GHz based on the formula (5-18),

$$f_{(mnl)} = \frac{c}{2\pi\sqrt{\mu_r\epsilon_r}} \sqrt{\left(\frac{P_{mn}}{a}\right)^2 + \left(\frac{l\pi}{d}\right)^2}, \quad (5-18)$$

which is mainly driven by the height and radius of the cavity. The parameters, c , μ_r , ϵ_r , P_{mn} , a , and d are the speed of light, the media permeability and permittivity of vacuum, the n -th zero of the m -th Bessel function, and both radius plus height of the cavity, respectively. In order to reduce negative influences, such as energy degradation or an unexpected mode change, the cavity was modeled for operation in the single TM₀₁₀ mode, being dominant based on formula (5-19) and as shown in Fig. 5.6.

$$h < 2.1 a.$$

(5-19)

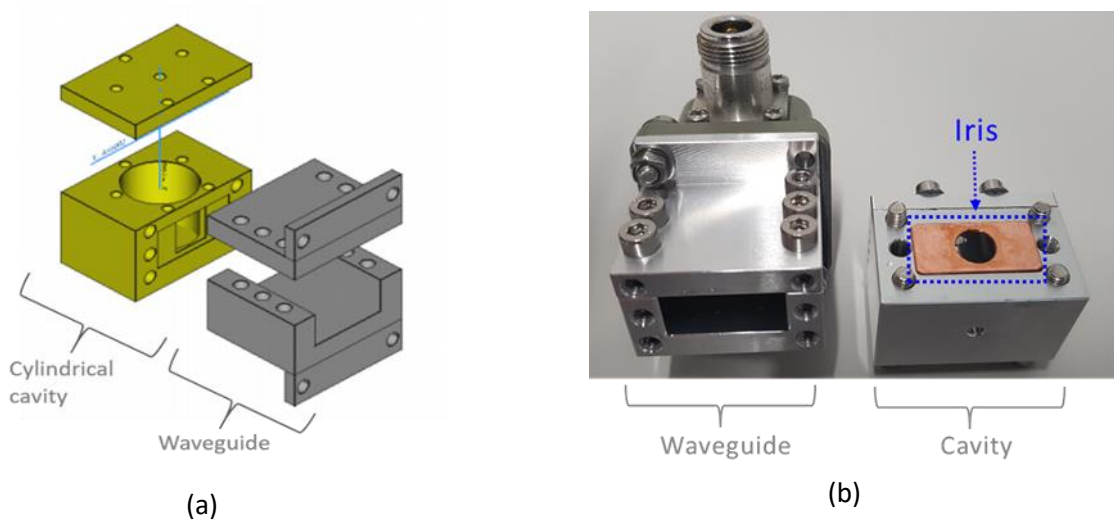


Fig. 5.5: Cylindrical microwave cavity: model (a) and real part (b).

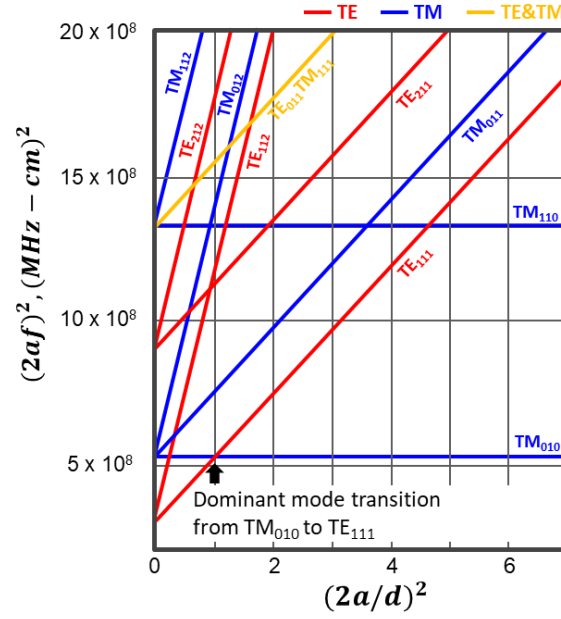


Fig. 5.6: Resonant mode chart for a cylindrical cavity [172].

The rectangular waveguide, propagating the microwave signal from the wave generator to the cavity, is designed for the TE_{101} mode, its dimensions are in accordance with the standard WR 90 waveguide (22.86×10.16), which is suitable for the X-band working range. The total length is decided based on the guide wavelength (λ_{guide}), at the resonance frequency (f_r)

$$\lambda_{guide} = \frac{c}{f_r} \times \frac{1}{\sqrt{1 - \frac{c^2}{2a^2 \cdot f_r^2}}}.$$

(5-20)

The waveguide and cavity are made of aluminum, which has advantages in terms of low absorptivity of microwaves, ease of machining, heat-, and corrosion-resistance.

5.3.4 Numerical Simulation

FDTD (Finite Difference Time Domain) simulations have been carried out using the QWED 6.5V software to verify the electromagnetic mode of the microwave cavity before manufacturing. FDTD is a method based on the leapfrog regime described in Chapter 4, and more detailed information can be found in Appendix 9.4, including the EM field modeling rules.

The model mesh size is 0.2 mm, which is about 1/131 of the excitation wavelength. This way the rule that the size variation with the neighboring mesh is within a factor of five is kept, as the water loading is $\varnothing 100 \mu\text{m}$, and the mesh size assigned for the water is 0.05 mm, corresponding to 2 cells in the radial direction.

All dimensions for the cavity design are described in Fig. 5.7 and Table 5.1, and the resonant frequency is placed at 11.34 GHz using an iris hole size of 8 mm. The hole size has been experimentally determined as close as possible to the critical coupling and is explained in detail in Section 5.3.5, Impedance matching.

Fig. 5.8 demonstrates that the maximum E-field is distributed uniformly along the z-axis, which coincides with the path of passing liquid droplets. It confirms that the operation mode of this cavity corresponds to TM_{010} , which is the initial design objective.

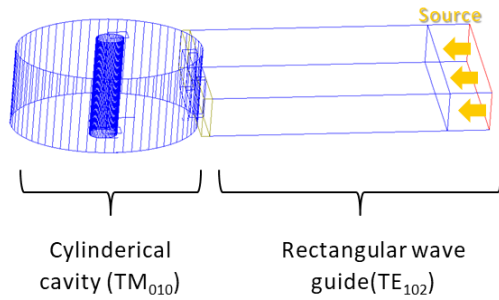


Fig. 5.7: Simulation model for the software QWED.

Table 5.1: Cavity dimensions and the operation mode.

| | | |
|-----------------------------|--------------------------------|-----------------|
| Dimension of waveguide (mm) | 20.86 (W) x 10.16 (H) x 30 (L) | |
| Dimension of cavity (mm) | Radius | 10 |
| | Height | 20 |
| | Hole dia. | \varnothing 3 |
| Iris size (mm) | \varnothing 8 | |
| Resonance Frequency (GHz) | 11.34 | |
| Excitation mode | TE | |
| Resonance mode | TM_{010} | |

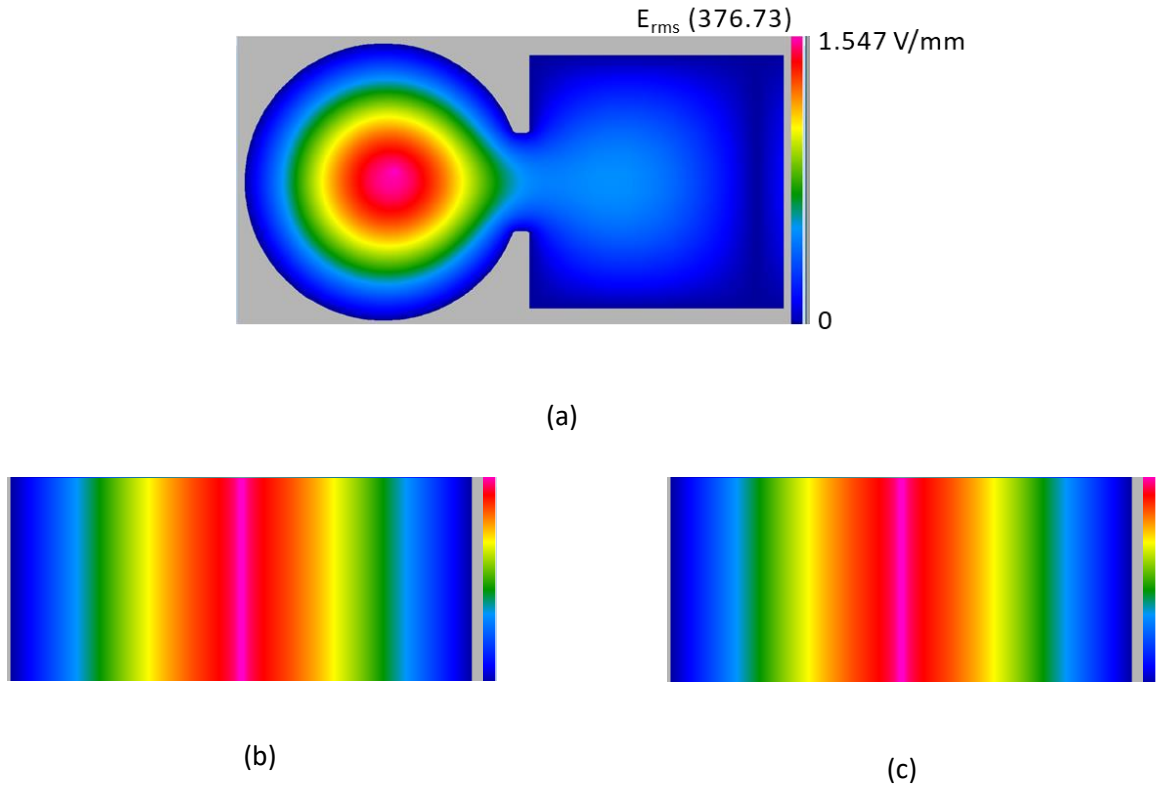


Fig. 5.8: E-field distributions of the cylindrical cavity: x-y plane (a), y-z plane (b), and x-z plane (C).

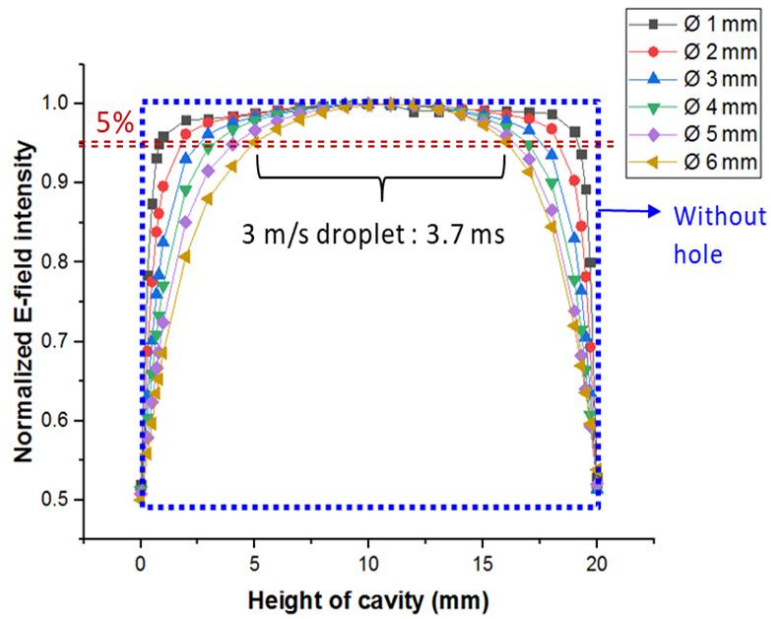


Fig. 5.9: Normalized E-field distribution as a function of hole-sizes of the cavity without water.

To allow the passage of droplets, the cavity is equipped with holes along the trajectory, on the upper and lower ends. Due to these openings of the cavity, the E-field intensity is diminished near the cavity extremities. Using the Quickwave software, FDTD simulations as a function of various hole sizes were implemented to determine the portion of the z-axis along which the E-field concentration value exceeds 95 %. Fig. 5.9 shows the normalized E-field intensity as a function of different z-axis positions, where 0 mm is at the top and 20 mm is at the bottom of the cavity, which at the same time represents its full length. The smallest hole size of $\varnothing 1$ mm approaches the uniformly distributed E-field without losses along the z-axis. However, only half of the cavity height has a sufficient E-field intensity with over 95 % of the normalized E-field value, in the case of $\varnothing 6$ mm holes.

A hole size of $\varnothing 3$ mm is finally selected, considering the electric field intensity at each cavity position and the fluid flow that should not touch the resonator.

5.3.5 Impedance Matching and Experimental Details

Prior to the heating experiment, a coupling evaluation of the entire system is performed to guarantee an efficient energy transfer. For the impedance matching between the water loaded cavity and the waveguide, circular irises with different hole sizes ($\varnothing 2, 4, 6, 8, 10$ mm) are employed in the interface between the cavity and the waveguide. The hole size is changeable depending on the dielectric properties of the loaded material in the cavity to accomplish “the critical coupling” and minimize the power reflection. Therefore, a unique construction is applied for this microwave cavity resonator to be able to replace the iris according to the loaded material.

A thin quartz capillary is used for liquid sample loading into the cavity, and it is made by applying a manual pulling force, after softening by a plasma torch. The quartz capillary used for this experiment has an inner

diameter of $115\text{ }\mu\text{m}$ and an outer diameter of $185\text{ }\mu\text{m}$ with a tolerance of $\pm 3\%$, as shown in Fig. 5.10 (a) to approximate the $\varnothing 100\text{ }\mu\text{m}$ droplet in diameter. In this experiment, the effect of the quartz capillary is negligible since both the size and the dielectric properties are relatively small. Furthermore, the surface tension and adhesion between water and the quartz tube allow water to stay in the capillary, accompanying ease of experiment. Fig. 5.10 (b) and (c) show the S_{11} parameter representing the reflection coefficient at the input port. This represents the coupling state between the waveguide and the cavity depending on both iris sizes and water loading.

Finally, an iris with a $\varnothing 8\text{ mm}$ hole is chosen to achieve critical coupling between the cavity and the waveguide. This allows the unloaded system to display over-coupling. Nonetheless, it changes to the lowest possible reflected power, i.e., close to critical coupling, once the water is loaded through a microcapillary. The cavity with a $\varnothing 8\text{ mm}$ iris shows, as a result, a resonance frequency of 11.3219 GHz without water and 11.3106 GHz with $0.21\text{ }\mu\text{L}$ water through the $\varnothing 115\text{ }\mu\text{m}$ quartz capillary in inner diameter. Accordingly, the magnitude of the S_{11} parameters, corresponding to both resonant frequencies before and after water loading, are -2.7230 dB and -43.2167 dB , respectively. This can be explained by over-coupling designed on purpose considering the loading factor, as described above.

Two schemes are examined with this cavity condition: 1) static scheme, and 2) dynamic scheme. The former stands for a water-filled capillary located inside the cavity. On the other hand, the latter indicates the regime working alongside the droplet generation. The volume of water interacting with the microwave can be determined by the capillary size, cavity height, and the spacing between consecutive droplets. The details are discussed together with the experimental results in the next session.

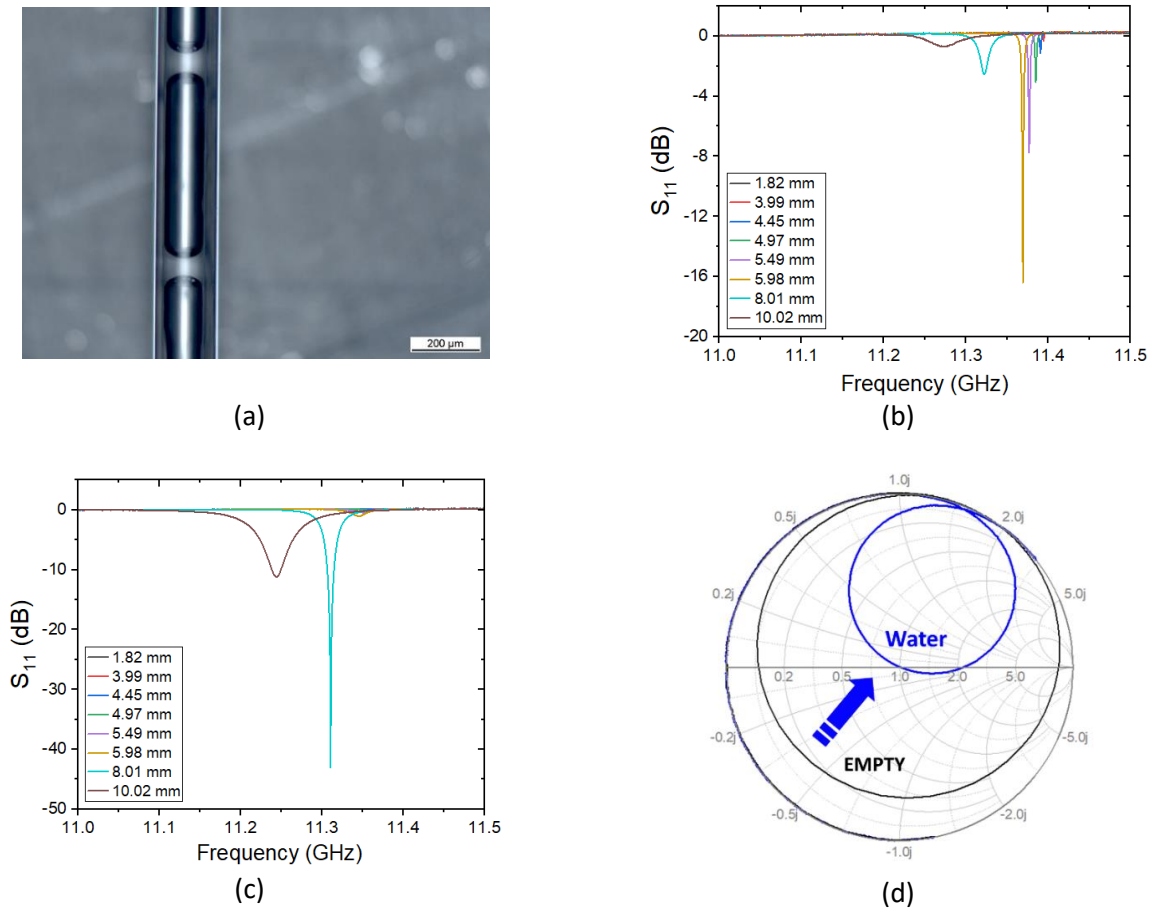


Fig. 5.10: A quartz capillary used for the impedance matching (a), S_{11} parameters as a function of various iris hole sizes without water b), with water (c), and Smith-chart representations with an $\varnothing 8\text{ mm}$ iris (d).

5.3.6 Experimental result

a. Static scheme

The custom-made microwave cavity has been investigated with water in terms of heating efficiency for the static scheme, as shown in Fig. 5.11. The loaded material is continuously flowing in the cavity through a connected PEEK tube of $\varnothing 254 \mu\text{m}$ inner diameter. This method is similar to the one used in chemical synthesis, but being adopted for the here used microwave arrangement. The desired temperature is readily achieved since the residence time of the sample under the focused electric field can be controlled by the sample's flow rate. Fig. 5.11 (c) shows that the maximal difference in temperature is 39.4°C with a microwave power of 5 W , a flow rate of $0.2 \text{ ml} \cdot \text{min}^{-1}$, and measured by a thermocouple placed 1 cm below the cavity. The apparent rapid drop in temperature during the experiment is an artifact due to a water droplet, which did not detach from the nozzle due to surface tension. This experiment demonstrates that water is heated inside the cavity by microwave, not due to the direct interaction of a thermocouple with a potentially leaking microwave field.

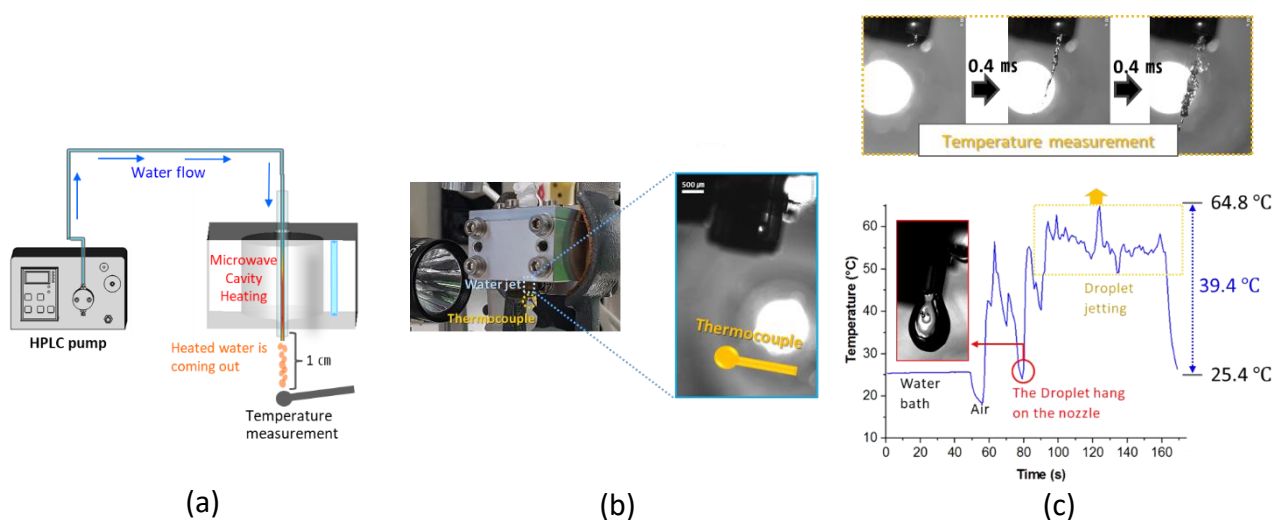


Fig. 5.11: Microwave heating test for the static scheme (a), experimental setup (b), and temperature log (c).



Fig. 5.12: Sample preparation of Copperformate tetrahydrate.

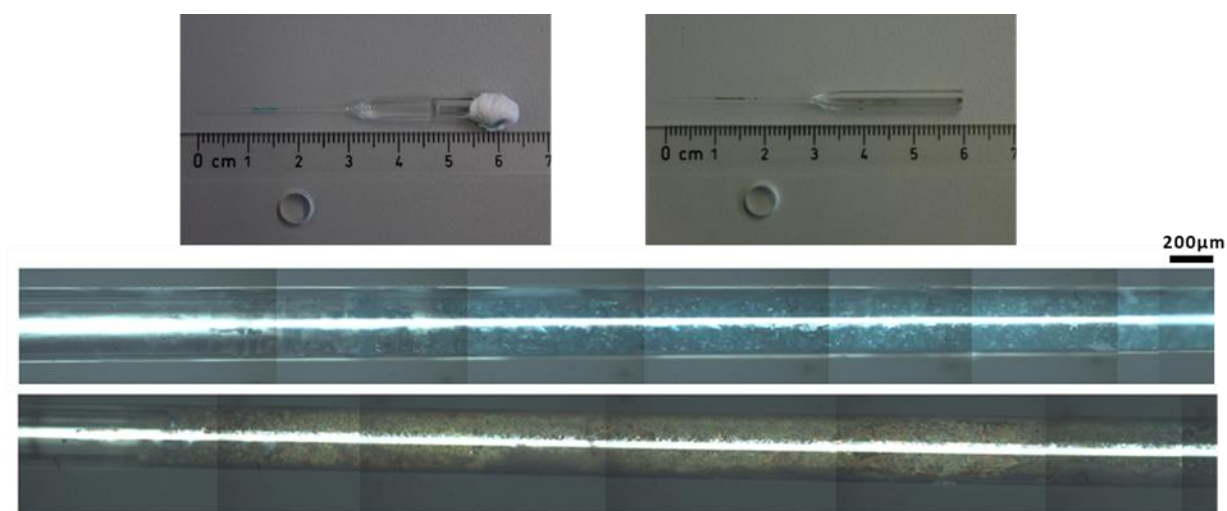


Fig. 5.13: The deposited copper formate on the glass capillaries with microwave power values of 10 W (blue) and 40 W (brown).

The candidate material, copper formate-tetrahydrate, has been examined in a static manner to prevent material contamination in the cavity. This material was expected to produce metallic copper by thermal decomposition, as already covered in Section 2.3.2, and to show the feasibility of the microwave as a heat source instead of using a conventional furnace.

The liquid feeding line was changed from a PEEK tube to a glass capillary with an inner diameter of 200 - 250 μm to be as close as possible to the diameter of the PEEK tube. The solution used in this experiment was prepared in three steps shown in Fig. 5.12: dissolving in water (concentration 7 %, 0.3 M), stirring at 50 $^{\circ}\text{C}$ for 15 hours, and filtration (4-7 μm porous Papier filter membrane).

At a heating power of 10 W, the liquid began solidifying on the inner wall of the glass capillary, and the deposited color inside the quartz wall changed from blue to brown as a result of sequentially increasing the power to 40 W, as shown in Fig. 5.13.

The Bragg–Brentano X-ray diffraction method with coupled two theta/theta scans was performed to verify the phases of the resulting deposited powder. The used instrument was a BRUKER Discovery D8 diffractometer (Bruker Corporation, USA) with Cu K α radiation ($\lambda = 1.5148 \text{ \AA}$) at 40 kV and 40 mA.

Fig. 5.14 shows the phase results obtained by the X-ray diffraction. It seems that pure copper metal is dominant in the product, and some copper oxide might originate from air exposure in the cooling process as well as the preparation step for the XRD analysis. This result implies the possibility of metal powder production from copper formate using microwaves, which is the subject of the SFA project.

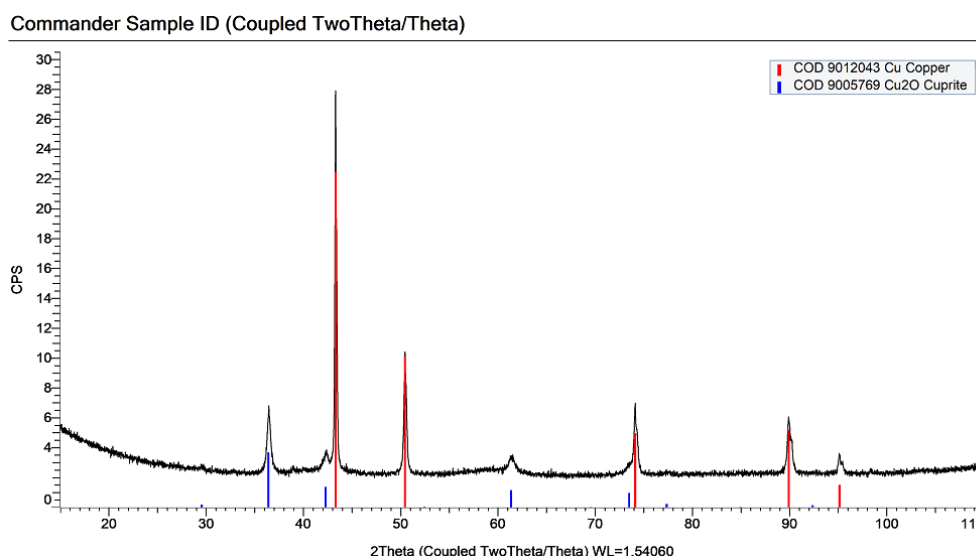


Fig. 5.14: XRD pattern of the copper formate tetrahydrate deposited on the glass capillary.

b. Dynamic scheme

For the dynamic regime shown in Fig. 5.15 (a), a Kapton film produced from Dupont or a quartz tube (Robson scientific) is set up inside the cavity to avoid its contaminations by the sample. The used Kapton (Dupont 536-3968) is a 0.075 mm thick polyimide series with a mechanical and chemical stability up to 400 °C.

The two protector materials, quartz and Kapton, have similarities in that the dielectric constant is uniform and the loss tangent is low (< 0.002). Temperature measurements are performed by a thermocouple and infrared camera, as shown in Fig. 5.15 (b).

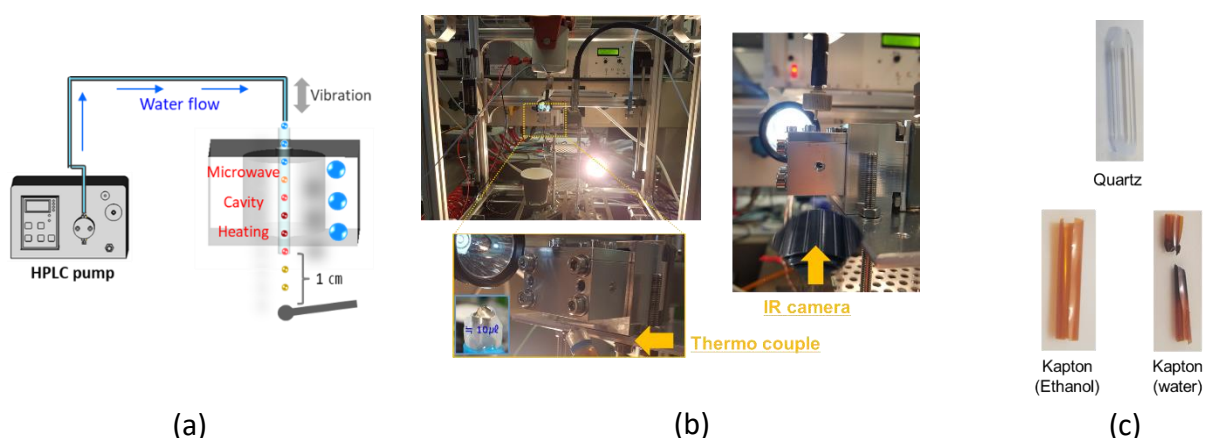


Fig. 5.15: Microwave heating test for the static scheme (a), experimental set up (b) and the introduced materials for preventing contamination during microwave test with a power of 20 W (c).

A K-type thermocouple is positioned 10 mm below the cavity to measure the temperature, and a high-speed infrared camera (Telops-M3k) allows for capturing the real-time temperature of the droplet train. The utilized tube, which acts as a nozzle here, has a diameter of $\varnothing 63.5 \mu\text{m}$ (IDEX Health & Science Co.) similar to the stainless nozzle ($\varnothing 59.8 \mu\text{m}$) in Chapter 3, allowing the use of previously determined optimal conditions.

Fig. 5.15 (c) shows a fractured Kapton tube, which occurred due to burning. It is assumed that the microwave interaction between overlapping Kapton inserted into the cavity and condensed or atomized residual water led to overheating, despite the high heat resistance of the Kapton. This hypothesis is confirmed through experiments where no appreciable damage arises once ethanol is used instead of water with the same input power of 20 W.

The optimal condition determined in Chapter 3, a flow rate of $0.5 \text{ ml}\cdot\text{min}^{-1}$ and vibration of 15 kHz, is tested with 20 W microwave power in the experimental configuration shown in Fig. 5.16 (a). The medium is still water, but the protector is replaced by a quartz tube due to its excellent heat resistance. Fig. 5.16 (b) and (c) represent the temperature rises obtained by a thermocouple and an infrared camera, indicating 3.4°C and even less than 2°C , respectively. The latter value is acquired with repeated power cycling (on/off) within 3 seconds, which means an instantaneous temperature change excluding effects of the heat exchange with the hot cavity. This temperature variance is reliable compared to the thermocouple-based measurement, since the cavity reached more than 30°C in temperature during the test. It means that the remaining temperature increase might come from the cavity being hotter than the initial state.

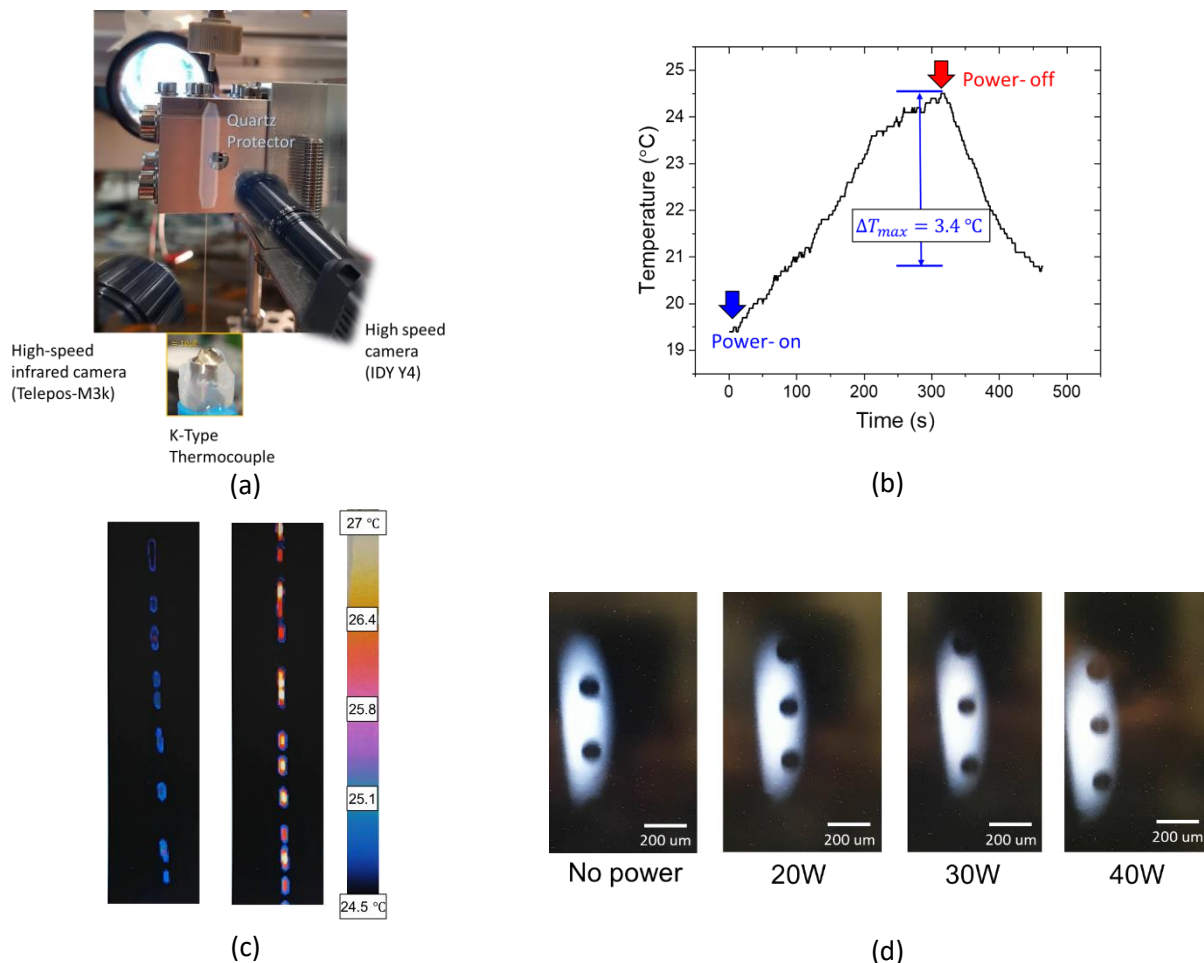


Fig. 5.16: Experimental setup (a), temperature logs obtained from a thermocouple (b) and IR camera (c), and images taken by the high-speed camera (IDY Y4) inside the cavity (d).

Additional experiments are implemented to observe the changes in the droplet's behavior while applying the microwave power via a high-speed camera (IDY Y4). The frame rate of 5 kHz with 1 μ s exposure time is chosen to take a distinct droplet picture inside the cavity. Images collected under these conditions are shown in Fig. 5.16 (d). There is a slight shrinkage in droplet size with applied microwave power compared to an absent microwave field. Nevertheless, no significant correlation is found in terms of size and gap of droplets while increasing the input power. There are lots of predictable causes, for example, a filling factor of dielectric in the cavity, route inconsistency between the droplet's trajectory and concentrated E-field. The permittivity differences of materials such as air, quartz, and water according to the wave propagating direction (air-quartz-air-water) can be another reason hampering the energy coupling.

Hence, the microwave resonator developed in Chapter 4 is examined to validate the heating effectiveness, because the cavity-based structure is insufficient for drying the droplets, which is an initial research goal. In addition, this resonator has the potential to overcome the aforementioned problems by regulating the concentrated E-field region.

5.4 Modified Coaxial Resonator

A heating experiment with the newly developed microwave resonator, covered in Chapter 4, was performed in a dynamic scheme, with falling, vibration generated droplets, consistent with the final research goal. The dimensions of the MW resonator were adjusted to have the same characteristic impedance of 50 Ω as the rest of the equipment, such as microwave amplifier, generator, and all cables, to minimize the reflected power. In addition, the gap distance between the central conductor and the outer wall was changed from 1 mm to 0.5 mm. As a consequence, the microwave interaction time is reduced on one hand, but on the other hand, the electric field is more focused. For the working principle and overall mechanism of the device, please refer to Chapter 4.

5.4.1 Experimental Procedure

A vector network analyzer (HP 8720D) has been utilized for the reflection coefficient measurement (S_{11}) to define an appropriate nozzle position that does not affect the electromagnetic field. The procedure is as follows:

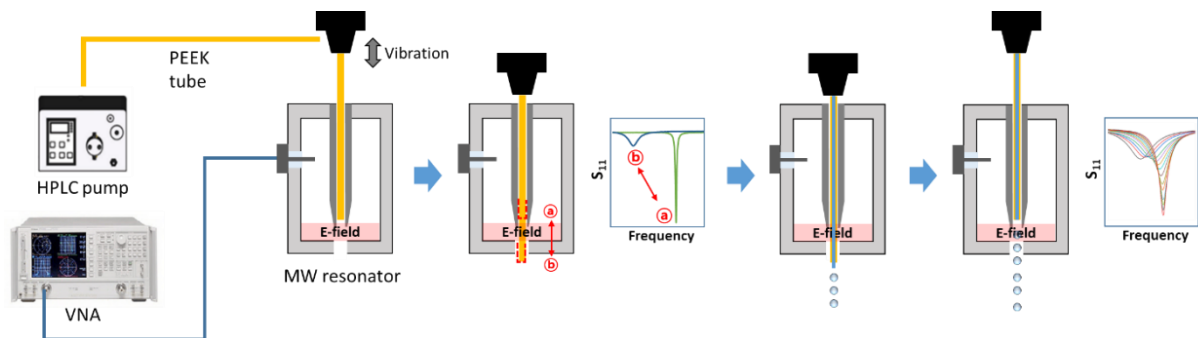


Fig. 5.17: Experimental procedure for the dynamic droplet heating.

Adjust the initial coupling as near as possible to critical coupling under the test.

1. The nozzle should completely penetrate the cavity because the initial droplet or liquid flow could block the hole of the resonator resulting in an experimental failure.
2. Define the location where the nozzle does not influence the electric field in the resonator by moving it stepwise by 0.1 mm using a motorized XYZ stage. The initial position at which the droplet generation starts is determined after measuring the resonant frequency at least five times in a non-liquid flowing state. The total travel distance of the nozzle is 6 mm from the position defined in step 1.
3. The HPLC pump is switched on to generate the liquid flow when the nozzle completely penetrates the resonator, and then the nozzle relocates back to the defined place in step 2 where the electric field is not disturbed. The regime of a continuous jet stream or a droplet train can be determined by adjusting the vibrator.
4. The MW amplifier is powered on, and after the experiment powered off again.
5. The resonator moves down again to prevent contamination in the heating area once the experiment is finished without switching off the HPLC pump.

Fig. 5.17 schematically illustrates the process described above, and Fig. 5.18 shows the used experimental setup.

The K-type thermocouple was placed a certain distance below the MW resonator while enlarging the applied power from the amplifier gradually to evaluate the heating performance. Preliminary experiments were conducted only with the running microwave system, but without droplets, to confirm the absence of thermocouple heating due to microwave leakage. Liquid flow is activated when no temperature change is observed depending on the input power.

All pictures representing the droplet behavior as a function of the input power were obtained from a CCD camera (Nikon D800) and demonstrated the evaporation of the sample (here, water) by calculating the droplet volumes in the defined area. The image processing for the droplet characterization is similar to the procedure introduced in Chapter 3, droplet generation, but the sphere model could not be applied for the droplet capturing. This is because the droplets had irregular shapes due to the insufficient time to form the spherical droplet. In other words, the stand-off distance is deficient not only for the disintegration of the stream but also for the recombination of the satellite droplets generated from the nozzle. Moreover, microwave heating further weakens the surface tension of the water droplets, hindering sphere shape formation. The first step of the image process, for acquiring the droplet volume, is to make the images more evident by increasing contrast before binarization, and then a closing function helps to fill the inside of the droplet. Otherwise, porous droplets might be obtained due to the different reflected light intensity, giving rise to an error in the volume estimation. The Mathematica® tools could calibrate the image to arrange the droplet train straight from the first and final droplet's centroid and extract the pixel-based contour of each droplet that shows the clear droplet boundary after image processing. The range analyzed is about 4.5 mm after the bottom of the coaxial MW resonator.

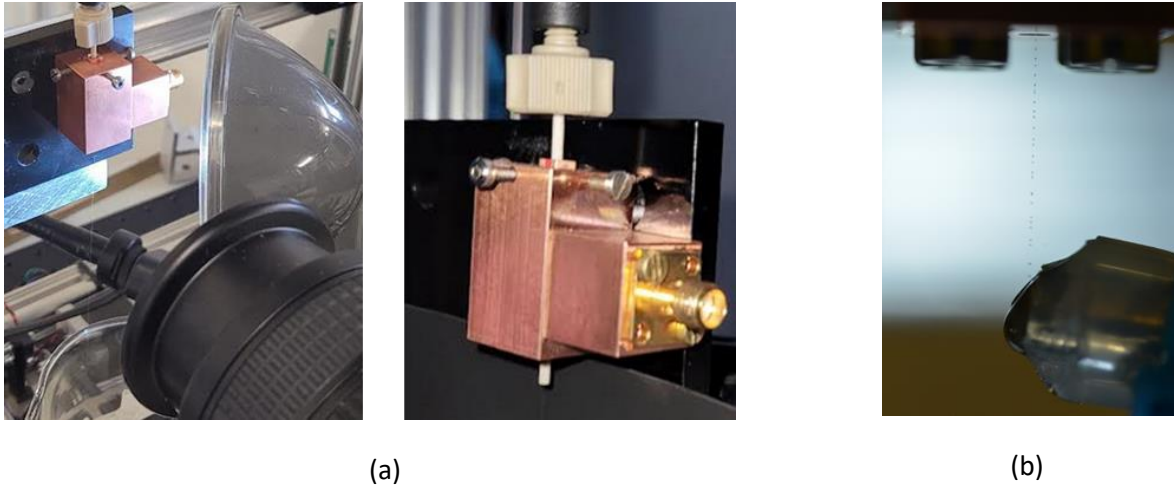


Fig. 5.18: Experimental set up (a) and the temperature measurement (b).

The integral calculus of the droplet's contour split by the centroid allows the prediction of the droplet volume. Finally, both sides of the contours are rotated based on each droplet's centerline, and the average value is chosen as a final droplet volume to avoid over or underestimation depending on the shape.

Fig. 5.19 shows the image processing steps to approximate the final volume of the droplet and the executed functions.

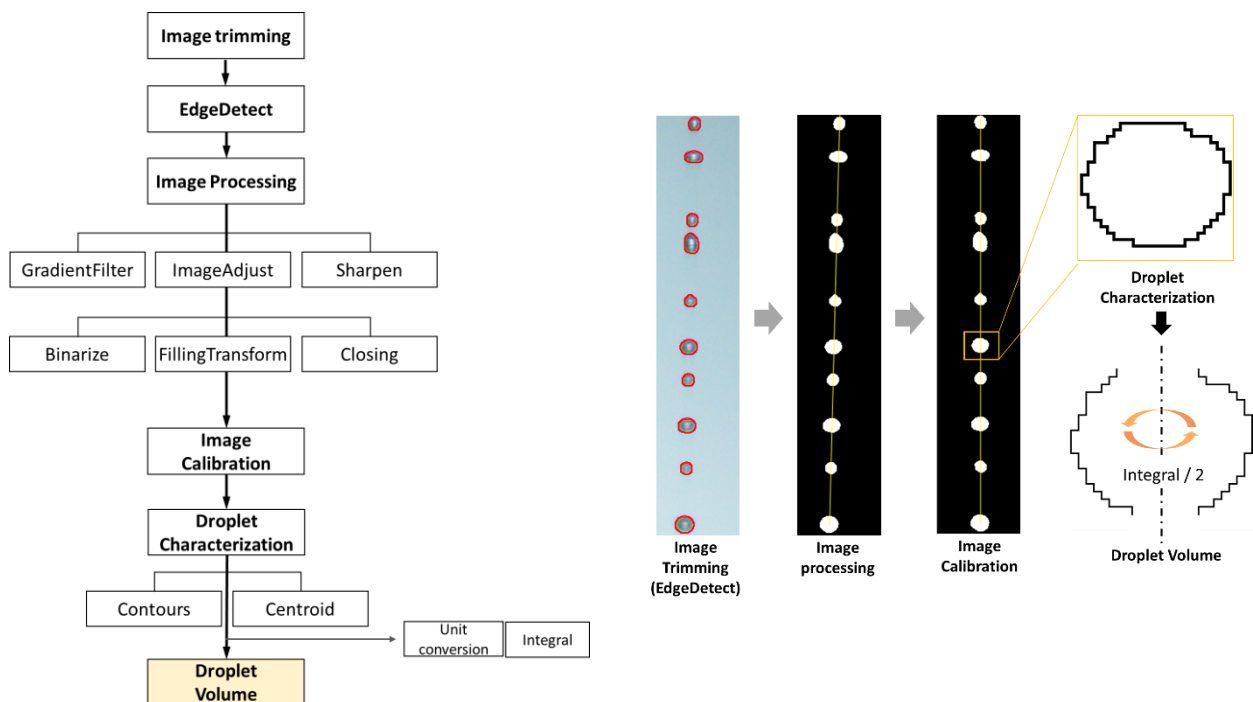


Fig. 5.19: Image processing procedure for the droplet volume characterization.

5.4.2 Experimental Result

For the test conditions, a flow rate of $0.5 \text{ ml} \cdot \text{min}^{-1}$ and a vibration of 15 kHz was selected based on the results of Chapter 3 using a PEEK nozzle.

The shape and material of the nozzle are different from the previous stainless steel plate type nozzle, so calibration is required. The utilized nozzle size is $63.5 \mu\text{m}$ in diameter according to the manufacturer's specifications. However, the actual size must be measured to cover all errors that occur in the cutting process for fitting the nozzle length to the resonator. The actual nozzle size is determined in the pictures from the extracted laminar flow's thickness just below the nozzle, prior to disturbance initiation. The measured diameter ranges from 45 to $59 \mu\text{m}$, and an average value of $54 \mu\text{m}$ is determined.

A nozzle length of 5 cm not only assures a sufficiently developed laminar flow but is well guided by the central conductor, preventing multi-mode vibration. The resonant frequency was sequentially changed from 10.491 GHz to 10.485 GHz with operating time, and the temperature was measured using a thermocouple installed 14.8 mm below. This measurement cannot represent the instantaneous temperature change of the droplet with increasing power because of the accumulated droplet volume hanging on the thermocouple, resulting in a relatively large heat capacity. However, it is possible to estimate the average temperature of the droplet train when there is no further temperature change, and losses can be neglected. The power was modulated when the recorded temperature stabilized after reaching its highest peak.

Fig. 5.20 (a) shows the raw data measured from the K-type thermocouple. The ambient temperature is about 19.8°C , and the temperature tends to decrease down to 17°C with water flow. However, the recording temperature rises to 19.1°C again with all equipment operation. e.g., amplifier and stroboscope. This temperature is set as the initial temperature. Fig. 5.20 (b) summarizes the temperature and evaporation results obtained in the experiment. The temperature of water rises more as the power increases, resulting in more evaporation. For instance, the volume reduction is 16.1 % within a total distance of 4.2 mm. Furthermore, microwave interaction time relies on the fluid speed determined by the pump flow rate and the gap distance where the E-field is present. The affected E-field region is identified in step (2) of the measurement procedure in Fig. 5.17 on page 88. For example, the reflection spectrum (S_{11}) shows the alternation while the nozzle's location moves in the microwave interaction zone with 0.1 mm steps along the z-axis. The influenced area by the microwave is approximately 1.7 mm, more than three times the gap distance (0.5 mm) since a fringing field appears inside the hole of both conductors, particularly on the bottom hole. The droplet's velocity adopted for calculating the microwave interaction time is $3.6 \text{ m} \cdot \text{s}^{-1}$ derived from the nozzle size and flow rate.

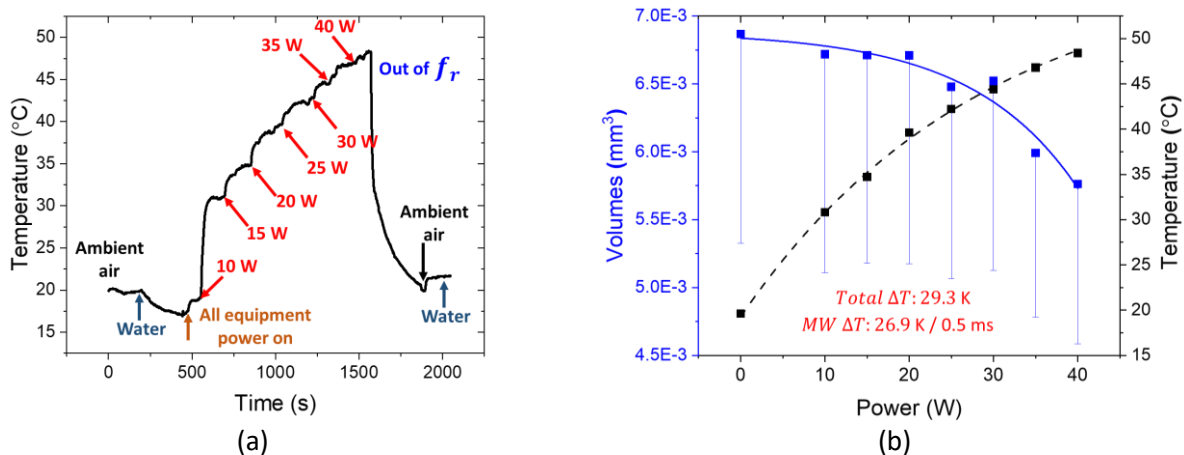


Fig. 5.20: Heating performance as a function of the input power: temperature log (a), and overall result (b).

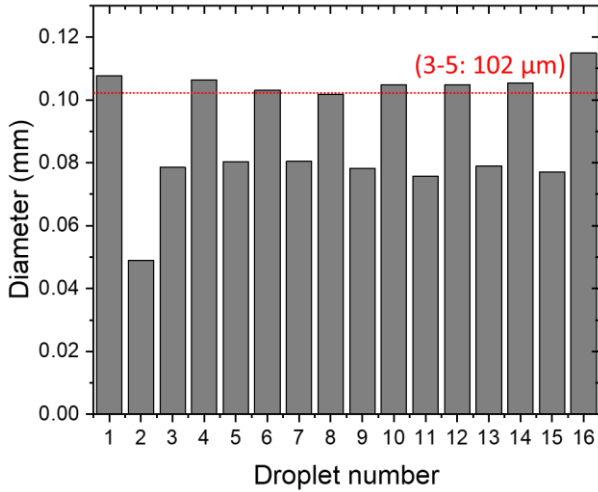


Fig. 5.21: A spherical droplet diameter corresponding to the irregular volume of droplets (no power).

Consequently, the achieved maximum temperature difference is 29.3 K in 0.5 ms with a power of 40 W, which shows an improved heating performance compared to the previous research using the rectangular cavity. Especially, the developed resonator is smaller than a quarter of the one in reference [173].












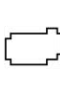


































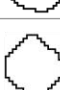











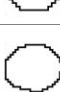







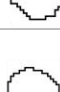
However, Fig. 5.20 (a) indicates that the measured water temperature passing through the resonator is 21.5 °C without microwave heating or any other power supply, after the experiment was terminated. It can be explained by the thermal inertia and conduction effect of the heated nozzle and the resonator. Hence, the temperature increment of water attributable to the microwave contribution is about 26.9 K, as shown in Fig. 5.20 (b). An image processing can overestimate the volume of the droplet due to

the blurring at the boundary. The error bar indicates the minimum volume based on a one-pixel deviation in the radial direction. Enlarging the input power gives rise to water evaporation and heating of the resonator, resulting in a resonance frequency change. Therefore, such an increase does not show the instantaneous temperature change anymore, requiring a frequency adjustment. The sudden drop in temperature is caused by a forced resonant frequency mismatch (out of f_r in graph), not because of the input power termination. It demonstrates that the medium is being heated by the resonance of electromagnetic waves, not by electrical breakdown.

The temperature change of the water bath is negligible since the location is approximately 1 m apart from the main setup. The obtained temperature deviation cannot accurately represent the effect resulting from microwave heating since it includes not only the liquid volumes accumulated on the thermocouple but also the cooling effect already progressed before the measurement. Predicting the initial temperature of the droplet that has just escaped from the electric field is covered in Chapter 6 with numerical methods.

Fig. 5.21 is the calculated diameter of the droplet with the assumption that the droplet is spherical when no power is applied. A red dotted line based on the equation (3-5) on page 28, indicates the analytical diameter (102 μm), and half of the created water droplets satisfy this value within a 6 % deviation. However, most of the remaining water droplets are 23 % smaller than (3-5) in diameter. It is complex to deduce the exact causes since numerous factors should be considered, such as the unexpected multi-vibration originating from the extended nozzle, the non-uniform nozzle cross-section, and the mechanical friction and aerodynamics due to the resonator geometry. Moreover, the distance for recombination and droplet break-up is not guaranteed, as described earlier. Therefore, the statistical analysis of droplets generated without vibration is performed in the next section to find the evaporation amount at a constant flow rate.

Unfortunately, the power handling capacity is limited due to the coaxial-based experimental configuration. All droplet trains to evaluate the evaporation rate in Fig. 5.20 (b) and the droplet size in Fig. 5.21 are illustrated in Fig. 5.22. These were obtained by following the image process described in Fig. 5.19 on page 90.

| No | Power | | | | | | | | | | | |
|----|--|---|----------------------------|--|---|---|--|---|---|--|---|----------------------------|
| | 0 W | | | 10 W | | | 15 W | | | 20 W | | |
| | Original Image | Image Process | Volume (mm ⁻³) | Original Image | Image Process | Volume (mm ⁻³) | Original Image | Image Process | Volume (mm ⁻³) | Original Image | Image Process | Volume (mm ⁻³) |
| 1 |  |  | 0.000655 |  |  | 0.000259 |  |  | 0.000245 |  |  | 0.000555 |
| 2 | |  | | | 0.00049 |  | | 7.74E-05 |  | | 0.00024 | |
| 3 | |  | 6.12E-05 | |  | 0.000237 | |  | 0.000509 | |  | 0.000589 |
| 4 | |  | 0.000255 | |  | 0.000156 | |  | 0.000367 | |  | 0.000241 |
| 5 | |  | 0.00063 | |  | 0.000578 | |  | 0.000621 | |  | 0.000778 |
| 6 | |  | 0.000272 | |  | 0.000258 | |  | 0.000235 | |  | 0.000218 |
| 7 | |  | 0.000575 | |  | 0.000553 | |  | 0.000522 | |  | 0.000931 |
| 8 | |  | 0.000273 | |  | 0.000227 | |  | 0.000354 | | | |
| 9 | |  | 0.000552 | |  | 0.000167 | |  | 0.000499 | |  | 0.000516 |
| 10 | |  | 0.000251 | |  | 0.000528 | |  | 0.000238 | |  | 2.65E-05 |
| 11 | |  | 0.000604 | |  | 2.83E-05 | |  | 0.000481 | |  | 0.00038 |
| 12 | |  | 0.000228 | |  | 0.000749 | |  | 0.000365 | |  | 0.000493 |
| 13 | |  | 0.000603 | |  | 0.000243 | |  | 0.000589 | |  | 0.000305 |
| 14 | |  | 0.000259 | |  | 0.000594 | |  | 0.000243 | |  | 0.000677 |
| 15 | |  | 0.000614 | |  | 0.000297 | |  | 0.000795 | |  | 0.00076 |
| 16 | |  | 0.00024 | |  | 0.000509 | |  | 0.000571 | | | |
| 17 | |  | 0.000795 | |  | 0.000844 | | | | | | |
| 18 | | | | | | | | | | | | |


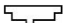








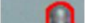

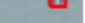



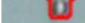

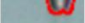










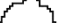


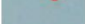
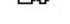
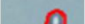








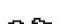




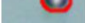





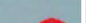


























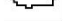














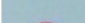



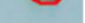






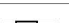

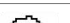






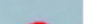





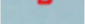





| No | Power | | | | | | | | | | | |
|----|---|---|----------------------------|---|---|----------------------------|---|---|----------------------------|---|---|----------------------------|
| | 25 W | | | 30 W | | | 35 W | | | 40 W | | |
| | Original Image | Image Process | Volume (mm ⁻³) | Original Image | Image Process | Volume (mm ⁻³) | Original Image | Image Process | Volume (mm ⁻³) | Original Image | Image Process | Volume (mm ⁻³) |
| 1 |  |  | 1.01E-05 |  |  | 0.000842 |  |  | 0.000676 |  |  | 0.00097 |
| 2 |  |  | 0.000866 |  |  | 0.000221 |  |  | 0.000759 |  |  | 0.00066 |
| 3 |  |  | 1.72E-05 |  |  | 0.000564 |  |  | 0.000807 |  |  | 0.000235 |
| 4 |  |  | 0.000879 |  |  | 0.000217 |  |  | 0.000677 |  |  | 0.000887 |
| 5 |  |  | 0.000759 |  |  | 0.000759 |  |  | 0.000215 |  |  | 0.000774 |
| 6 |  |  | 0.000866 |  |  | 0.000759 |  |  | 0.000647 |  |  | 0.000754 |
| 7 |  |  | 0.000614 |  |  | 3.2E-05 |  |  | 0.000672 |  |  | 0.000746 |
| 8 |  |  | 0.000754 |  |  | 0.000738 |  |  | 0.000747 |  |  | 0.000702 |
| 9 |  |  | 0.000728 |  |  | 0.00081 |  |  | 2.75E-05 |  |  | 3.21E-05 |
| 10 |  |  | 0.000317 |  |  | 0.000762 |  |  | |  |  | |
| 11 |  |  | 0.00061 |  |  | 0.000818 |  |  | |  |  | |
| 12 |  |  | 0.000816 |  |  | |  |  | |  |  | |
| 13 |  |  | |  |  | |  |  | |  |  | |
| 14 |  |  | |  |  | |  |  | |  |  | |
| 15 |  |  | |  |  | |  |  | |  |  | |
| 16 |  |  | |  |  | |  |  | |  |  | |

Fig. 5.22: Image processing of the droplet trains as a function of input power.

5.4.3 Statistical Analysis

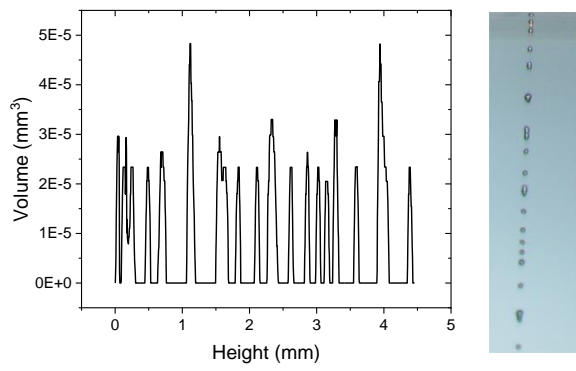
For a reliable determination of the droplet evaporation, a statistical analysis has been carried out with a maximum microwave power of 45 W. However, for the droplet generation, no vibration was applied because of the lack of uniform droplet formation time and the generation of unequal-sized droplets.

8-images were taken under the same condition and utilized for the evaporated volume estimation analyzing each pixel row as a function of height. The motivation is to derive the evaporation rate and ultimately to estimate the temperature decrease from the evaporated water volumes. A simple approach is that all evaporation contributes to the droplet's temperature loss.

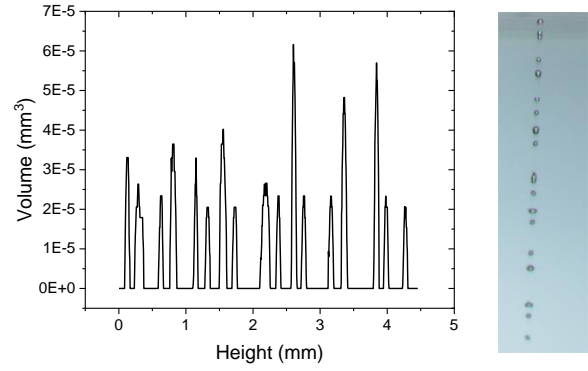
Fig. 5.23 shows all the images used for the statistic analysis, where 0 on the x-axis stands for the location directly below the resonator. The entire distance adopted is 4.458 mm from the microwave device's bottom. No distinct trend is observed. Nevertheless, there were only individual droplets below the resonator and no remaining jet stream. In addition, a gap broadening between the peaks demonstrates that satellite droplets or irregularly connected droplets participate in forming larger droplets. So it seems that the amount of water observed inflates as the distance from the nozzle is increasing. Accordingly, the gap of the droplet train is elongated, as shown in Fig. 5.23 (f) and (h). Droplet formation is also affected by the pump. For example, a consecutive smaller droplet is formed during a forward piston motion that pushes the medium. However, the instantaneous pressure drop due to the piston's returning motion results in a larger droplet with sufficient spacing between the droplets like Fig. 5.23 (d). Hence, the statistical analysis is adopted to reflect all these influences.

The average water volume of Fig. 5.23 is presented in Fig. 5.24. The regression line directly illustrates the volume reduction of the droplet train as a function of the height. Statistical analysis can exclude a single dominant value in samples and shows a tendency of decreasing volume as flight duration increases.

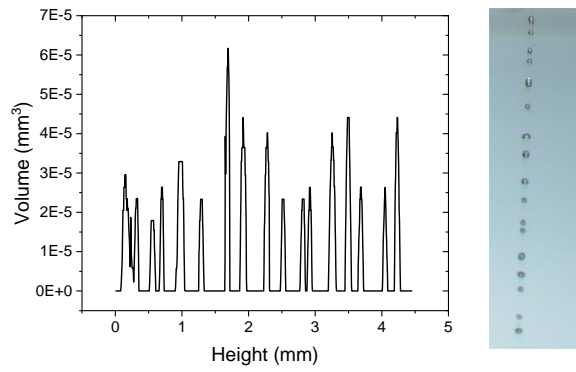
Fig. 5.24 allows a direct estimation for the evaporative amount of water droplets. An exponential curve fitting is performed to anticipate the evaporative trend since the evaporation rate is proportional to the medium's temperature. Furthermore, the cooling rate of an object is relative to the temperature difference between the body and the surrounding condition, according to Newton's law. It backs up the validity of using exponential fitting. Furthermore, the red line indicates a simple linear regression to compare the exponential fitting. Both curves are almost identical, meaning no significant change in water volume after passing through the resonator. There are two predictable assumptions. First, a saturation status has almost been reached within the resonator. This phenomenon can be explained by the dynamic equilibrium between the rates of evaporation and condensation. However, the measured droplet's temperature and humidity are definitely higher than the environmental condition, representing the vapor film generated around the droplet train that hampers the evaporation and cooling of the medium. Second, the section where rapid evaporation occurs is not revealed due to statistical errors or a shortage of the analysed distance. According to the extracted equations based on the fitted curves in Fig. 5.24, volume reductions corresponding to a flight distance of 4.458 mm from the resonator are approximately 8.23 % and 8.25 % for exponential and linear fittings, respectively. If all the heat energy of vaporization comes from the inside of the remaining water volume, the temperature change of this remaining droplet is in the range of 48 to 52 °C. However, the measured temperature at 14.3 mm below the resonator is over 52 °C, meaning that the attainable maximum temperature by microwave heating is higher than the boiling point of water. Even considering the high surface tension of microdroplets, this is not realistic. Therefore, numerical models that can approximate the temperature profile of the falling droplet are introduced in Chapter 6 based on the heat and mass transfer model.



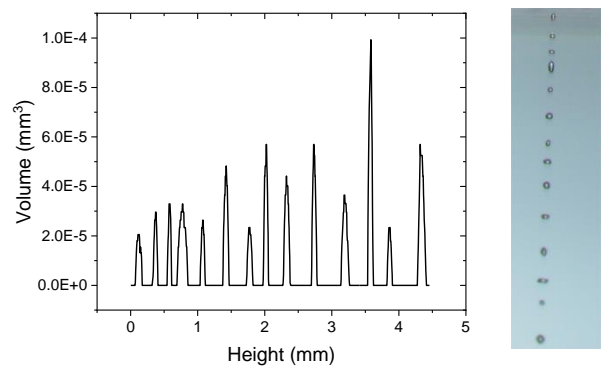
(a)



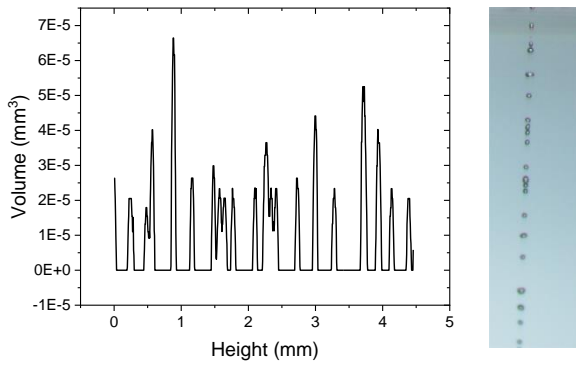
(b)



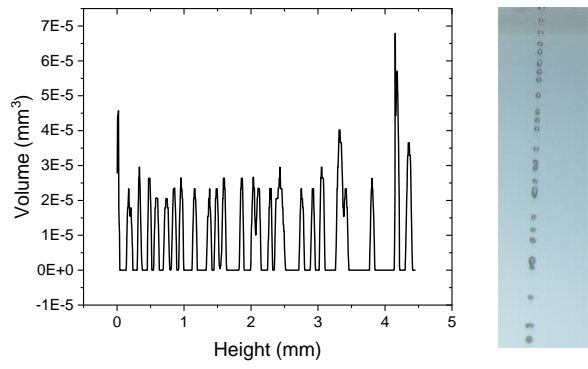
(c)



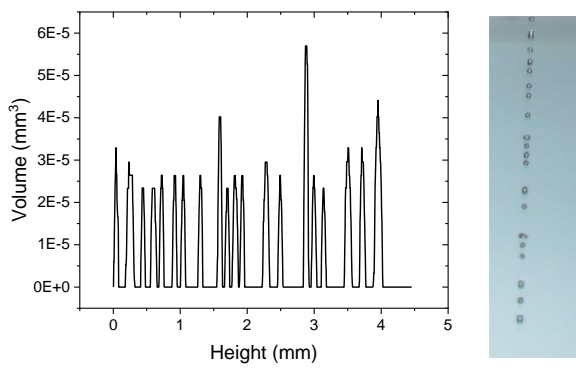
(d)



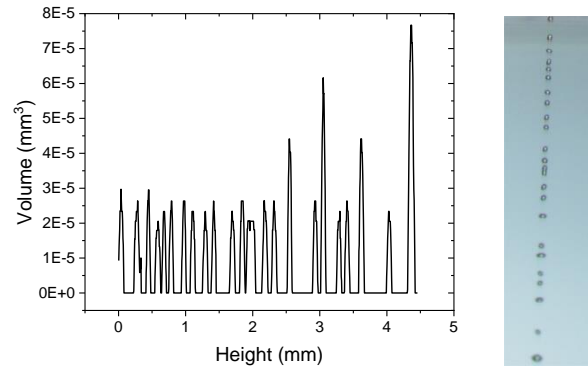
(e)



(f)



(g)



(h)

Fig. 5.23: Images for the statistical analysis.

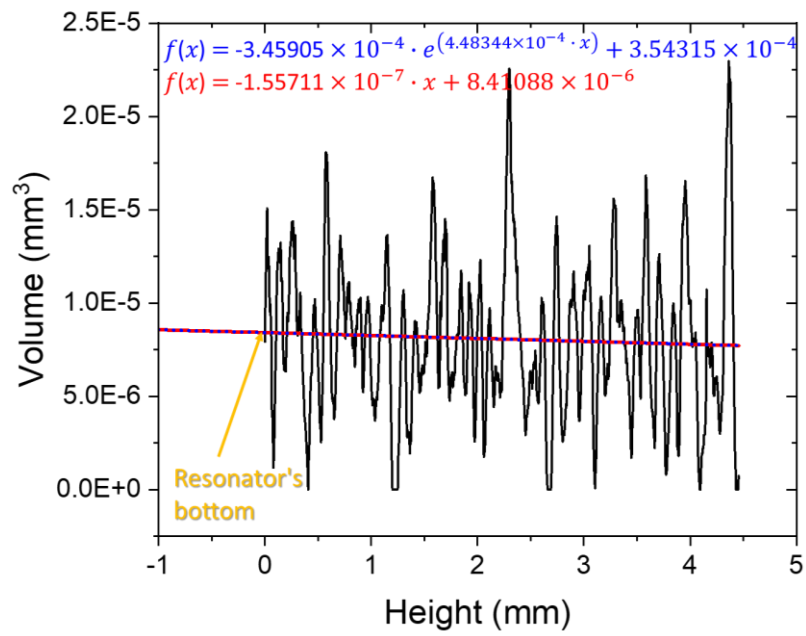


Fig. 5.24: Averaged volume of Fig. 5.23 as a function of height.

Chapter 6 Heat and Mass Transfer Model

This chapter deals with droplet evaporation and the associated temperature drop based on heat and mass transfer. In particular, it introduces a simple derivation of the droplet evaporation rate in quiescent air and convective air, the latter corresponding to droplets falling with a specific velocity consistent with the research objective. In addition, fundamental heat transfer and mass transfer-related parameters applicable to the previously performed experimental work in the thesis are described with justified assumptions. Doing so makes it possible to trace back the maximum temperature of a droplet when it just left the focused electric field before cooling. Furthermore, it allows anticipating the microwave power absorption for water droplets with the field strength of the microwave device.

6.1 Heat Transfer

According to the second law of thermodynamics, contacting bodies or fluids with different temperatures undergo an energy exchange until thermal equilibrium is reached. This is a basic definition well known as heat transfer. This chapter introduces governing heat transfer mechanisms, heat equations derivated from the energy balance, and the typical boundary conditions for numerical calculations. The heat transfer is regarded as the main factor in inversely tracking the maximum temperature of the water before initiation of the droplet's cooling.

6.1.1 Mechanism

a. Convection

Convection is the internal energy transfer flowing into or out of an object by the dynamic motion of the surrounding fluid. It is, therefore, a common phenomenon whenever the substance is hotter or colder than the surrounding fluid, including air. This convective heat transfer is not simple to analyze, since it depends on the fluid motion, which enhances the heat exchange rate depending on its intensity. The convective heat transfer is expressed as Newton's law of cooling

$$Q_c = A h_c (T_s - T_\infty), \quad (6-1)$$

where h_c is the convective heat transfer coefficient in units of (W/m²·K), A is the surface area of an object exposed in the fluid, T_s is the surface temperature and T_∞ is the environmental fluid temperature. The convective heat transfer coefficient depends on several factors such as the shape of the surface, fluid motion, velocity, viscosity, and other properties, which can change as a function of temperature. The convective heat transfer coefficient h_c is usually positive and experimentally determined.

Table 6.1 shows typical convective heat transfer coefficient for some common cases.

Table 6.1: Typical convective heat transfer coefficient.

| Medium | Type | Convective heat transfer coefficient (W/m ² ·K) |
|--------|-------------------|--|
| Water | Free Convection | 20 -100 |
| | Forced Convection | 50 -10,000 |
| | Boiling | 3,000 – 100,000 |
| | Condensing | 5,000 – 100,000 |
| Air | Free Convection | 5 - 25 |
| | Forced Convection | 10 - 200 |

A direct approach for expressing the droplet's convective coefficient, derived from experimental data, was established by Ranz and Marshall (1952) using the dimensionless number of Nusselt [174]:

$$Nu = \frac{h_c d}{k} = 2 + 0.6 Pr^{1/3} Re^{1/2} \quad (6-2)$$

Nusselt number is given as the ratio of convective to conductive heat transfer at the fluid boundary equivalent to the temperature gradient at the surface. d and k are the fluid's characteristic length and thermal conductivity, respectively. Pr is the Prandtl number defined as the diffusivity ratio attributable to the momentum and thermal characteristics

$$Pr = \frac{\gamma}{\alpha} = \frac{\mu/\rho}{k/c_p\rho} = \frac{\mu c_p}{k}. \quad (6-3)$$

The variables α , γ , μ , c_p , and ρ , are the thermal diffusivity, kinematic viscosity implying the momentum diffusivity, dynamic viscosity, specific heat, and density of the fluid. Re is the Reynold number in which the droplet diameter replaces the characteristic length, see Chapter 3.1.1 "Droplet Formation Mechanism".

In general, there are two types of convection: natural convection and forced convection. The natural convection results from the density difference induced by the temperature difference, for example, the buoyancy effect.

On the other hand, the accelerated fluid motion by external sources, e.g., pumps, fans, and others, is attributed to the forced convection regime. This concept is an efficient way to transport large amounts of thermal energy, especially suitable for the field of electronics, air-conditioning, heat exchangers, and other applications.

b. Radiation

Thermal radiation is a type of internal energy transfer by electromagnetic waves. The main characteristic different from other kinds of heat transfer, such as conduction and convection, is the needlessness of mediums. Because of the missing absorption and scattering, vacuum is the most efficient condition for radiative energy transfer.

The radiated power from a body follows the Stefan-Boltzmann law that demonstrates the total radiation energy per unit surface of the blackbody across all wavelengths per unit time, expressed as

$$j^* = \sigma T^4, \quad (6-4)$$

where j^* , σ , and T are radiant emittance of the blackbody, Stefan-Boltzmann constant ($5.67 \times 10^{-8} \text{ W} \cdot \text{m}^{-2} \cdot \text{K}^{-4}$), and thermodynamic temperature.

Nevertheless, most substances cannot accomplish a perfect exchange efficiency, meaning that the incident radiation cannot be entirely absorbed and emitted like a blackbody. So, (6-4) turns into (6-5) considering the relative emissivity (ε) of the object

$$j = \varepsilon \sigma T^4. \quad (6-5)$$

Emissivity stands for the matter's intrinsic efficiency in terms of emitting radiation through the surface, and the water shows an emissivity of about 0.95. The unit of the radiant emittance j is the same as the energy flux taking into account both time and area.

In the case where two bodies interact by the thermal radiation transfer, the net radiative heat exchange rate from body 1 to body 2 is given by

$$Q_{r\ 1 \rightarrow 2} = j_1 A_1 - j_2 A_2 = \varepsilon \sigma A (T_1^4 - T_2^4), \quad (6-6)$$

where A represents the surface of the interacted bodies, and $A_1 = A_2$ when the A_1 is surrounded by A_2 . However, this effect is negligible owing to both the large density and small mean beam length of the liquid media compared to convective and conductive heat transfer. Therefore, the mean beam length is used to evaluate the radiative heat transfer between an isothermal gas volume and its boundary, as defined by Hottel [175].

c. Conduction

Conduction is the energy transfer within a body or between bodies that stands for the energy heading towards a low internal energy from an energetically higher potential by colliding or displacing the particles at the molecular level. The majority of heat conduction takes place because of the temperature difference in all phases, without bulk motion. The energy exchanges until the objects are in thermal equilibrium. Typical heat transfer occurs in physically contacted solids that have a temperature gap. The mobile electrons also play a crucial role in heat transfer. Therefore, metallic bodies possess a superior conductive heat transfer capability than dielectric materials, where conduction functions by the lattice waves. On the other hand, the liquid and gas phases have larger intermolecular gaps with a random movement of the molecules. Hence energy transfer is less efficient than in a solid phase. The diffusion at an atomistic or molecular level is the principal contributor to heat conduction for both gas and liquid phases.

Thermal conduction is stated as Fourier's law that the heat flux, q_{flux} , is proportional to the negative temperature gradient, ∇T , and the thermal conductivity k

$$q_{flux} = -k \nabla T, \quad (6-7)$$

where ∇ is the 3D Nabla mathematical operator.

Considering a homogeneous material of 1D geometry between both points that have constant temperatures, the heat flow rate per unit area normal to the heat flow direction is expressed as

$$\dot{Q} = \frac{kA}{\Delta x} (T_2 - T_1),$$

(6-8)

where \dot{Q} , A , k , T_1 , T_2 , and Δx are the heat flow rate in the unit time interval, cross-sectional surface, temperatures of the two points, and path length where the heat is flowing.

The thermal diffusivity, α , expressed as the ratio of the thermal conductivity, k , and the volumetric heat capacity of the medium, ρc_p , is the foremost variable that determines the heat transfer velocity for all the phases.

$$\alpha = \frac{k}{\rho c_p}$$

(6-9)

It is the basis of the heat equation to quantify the heat diffusion through a given region, described as the partial differential equation

$$\frac{\partial u}{\partial t} = \alpha \nabla^2 u,$$

(6-10)

$\frac{\partial u}{\partial t}$ is the rate of change in temperature at a point over time, and u dictates the temperature as a function of space and time.

6.1.2 Heat Equation

The heat equation is a way to determine the heat distribution over time, considering all the heat transfer schemes explained above. It is an energy exchange that occurs in more than two objects (e.g., fluids) derived from the law of conservation of energy. This equation accounts for the balance between the heat production rate and the heat loss rate in the interacting bodies.

According to thermodynamics, the absorbed or released total energy, resulting from the temperature difference ($T_i \rightarrow T_f$) in the object, is obtained from

$$H = \int_{T_i}^{T_f} \rho c_p dT.$$

(6-11)

The heat change rate is simply notated as

$$\dot{H} = \frac{\partial H}{\partial t} = \rho c_p \frac{\partial T}{\partial t},$$

(6-12)

where the enthalpy H implies the total energy change per unit volume, and both the initial and final temperature are given as T_i and T_f . The specific heat capacity, c_p , specifies the amount of heat energy needed to raise the temperature of the material in unit mass by one-degree kelvin.

The energy conservation allows to assume the temperature diffusion inside of an isotropic material:

$$\rho c_p \frac{\partial T}{\partial t} + \rho c_p V \cdot \nabla T + \nabla \cdot (-k \nabla T) = Q. \quad (6-13)$$

The first term on the left-hand stands for the stored heat energy. The diffusive term $\nabla \cdot (-k \nabla T)$ attributable to the thermal conduction results in a non-linear heat equation because of the temperature-dependent thermal conductivity, k .

The expression $\rho c_p V \cdot \nabla T$ stands for the convective term related to a flow velocity V to determine the internal heat convection. It is sometimes neglected once solids or internal flow does not play a significant role in heat transfer. The term Q denotes the heat source where the heat generation ($Q > 0$) or absorption ($Q < 0$) takes place within the domain. The volumetric heat energy originating from the microwave corresponds to Q .

Typical forms of heat equations are shown below without considering the internal flow.

Cartesian coordinate (x, y, z):

$$\rho c_p \left(\frac{\partial T}{\partial t} + u \frac{\partial T}{\partial x} + v \frac{\partial T}{\partial y} + w \frac{\partial T}{\partial z} \right) = k \left(\frac{\partial^2 T}{\partial x^2} + \frac{\partial^2 T}{\partial y^2} + \frac{\partial^2 T}{\partial z^2} \right). \quad (6-14)$$

Cylindrical coordinate (r, Θ , z):

$$\rho c_p \left(\frac{\partial T}{\partial t} + v_r \frac{\partial T}{\partial r} + \frac{v_\theta}{r} \frac{\partial T}{\partial \theta} + v_z \frac{\partial T}{\partial z} \right) = k \left(\frac{1}{r} \frac{\partial}{\partial r} \left(r \frac{\partial T}{\partial r} \right) + \frac{1}{r^2} \frac{\partial^2 T}{\partial \theta^2} + \frac{\partial^2 T}{\partial z^2} \right). \quad (6-15)$$

Spherical coordinate (r, Θ , \emptyset):

$$\rho c_p \left(\frac{\partial T}{\partial t} + v_r \frac{\partial T}{\partial r} + \frac{v_\theta}{r} \frac{\partial T}{\partial \theta} + \frac{v_\emptyset}{r \sin \theta} \frac{\partial T}{\partial \emptyset} \right) = k \left(\frac{1}{r^2} \frac{\partial}{\partial r} \left(r^2 \frac{\partial T}{\partial r} \right) + \frac{1}{r^2 \sin \theta} \frac{\partial}{\partial \theta} \left(\sin \theta \frac{\partial T}{\partial \theta} \right) + \frac{1}{r^2 \sin^2 \theta} \frac{\partial^2 T}{\partial \emptyset^2} \right). \quad (6-16)$$

These simplified heat energy forms are suitable when the conditions described below are satisfied,

1. Constant fluid conductivity
2. Zero internal heat generation
3. Negligible viscous dissipation and compressibility effect

Most heat transfer occurs at the surface, and boundary conditions are needed to impose the overall heat transfer mechanisms to the thermal equation. This topic is elaborated in the next session.

6.1.3 Boundary Conditions

Boundary conditions are essential to simulate the phenomenon as close as possible to reality by solving a system of equations, not only for heat transfer but also for mass and pressure transfer. For the case of the falling droplet, which is a major aspect of this research, most of the energy transport is taking place at the surface, so the choice of the proper external boundary condition determines the reproduction of the cooling effect of the microwave-heated water droplet.

The common boundary conditions used for the heat and mass transfer modeling are the Dirichlet boundary condition, Neumann boundary condition, and Periodic boundary condition.

a. Dirichlet boundary condition

The Dirichlet condition assigns a specific temperature or concentration to the border or surface of the part for both heat and mass transfer application. It can be called an isothermal or fixed boundary condition applied in heat transfer problems, since it gives a constant value on the boundary. This is different from the Neuman boundary condition, dealing with a temperature gradient.

b. Neuman boundary condition

This type of boundary condition defines the heat or mass flux, \hat{q} , on the border or surface of the object where the energy transfer happens. The utmost purpose of this condition is to quantify the energy flow that appears at the interacting element boundary, for example, a liquid droplet surrounded by air. This boundary condition is used for the representation of the convection and the radiation mechanism, expressed as

$$k \left[\frac{\partial T}{\partial n} \right]_s = h_c(T_s - T_\infty) + \varepsilon \sigma A(T_s^4 - T_\infty^4),$$

(6-17)

where \vec{n} is the normal vector, perpendicular to the boundary, $k, h_c, \varepsilon, \sigma, A, T_s, T_\infty$ are the conductivity, convection heat transfer coefficient, emissivity, Stephan-Boltzmann constant, the area as a surface boundary,

temperature of a surface, and an environmental condition (e.g., Air). The heat transfer phenomenon occurring on the surface of a falling droplet must satisfy (6-17).

The following equation (6-18) is employed when two objects are in contact with each other, so that conductive heat transfer acts as the primary energy exchange mechanism

$$-k_1 \left[\frac{\partial T_1}{\partial n} \right] = -k_2 \left[\frac{\partial T_2}{\partial n} \right]. \quad (6-18)$$

The subscript 1 and 2 denote two different layers of substances in which heat transfer occurs. T_1 and T_2 are the surface temperatures at each layer. This boundary condition is applied to compute a numerical model that traces back the initial temperature of the falling droplet.

c. Periodic boundary condition

This boundary condition stipulates variables, such as the temperature and the concentration, at a fraction of the boundary, to be the same at another location. It is mainly used for the modeling of the domain's periodicity. For example, an object passes through a certain cell's entrance plane, and then it turns up again on another side with the same plane properties as previously. This condition is suitable to approximate a large system composed of an infinite number of unit cells, commonly called mesh in a computer simulation.

6.2 Droplet Evaporation

6.2.1 Droplet evaporation in the quiescent air

A simple approach to the natural evaporation process of atomized droplets, without additional input energy, is described based on empirical calculations. This case does not need to consider the velocity of the droplet, since it can be assumed that the environmental condition is stationary without flow, and the droplet is levitated without momentum. Therefore, this approach is valid for approximating the lifetime of a droplet and helps to understand how the droplet diffuses into the surrounding. The calculation is performed without numerical iteration, resulting in minor errors arising from non-updated variables. It involves not only the cooling object but also the environmental conditions corresponding to the thin interlayer between the droplet and the surrounding air. The saturation vapor pressure of the water droplet, P_s , is empirically determined by the equation (6-19)[176]

$$P_s = \exp \left(16.7 - \frac{4060}{T_d - 37} \right). \quad (6-19)$$

For droplets larger than 0.1 μm , the partial vapor pressure at the droplet surface, P_d , is identical to the P_s at the given droplet surface temperature, T_d , without the Kelvin evaluation.

The steady-state temperature elevation between the surface of the droplet and the ambient air ($T_d - T_\infty$), being at the equilibrium state in the energy exchange, is independent of the droplet size. This difference is given as an empirical formula, since an explicit solution is impossible due to the dependency of the partial vapor pressure (p_d) on the temperature of the droplet surface (T_d), as seen in [176]

$$T_d - T_\infty = \frac{(6.65 + 0.345 T_\infty + 0.0031 T_\infty^2)(S_R - 1)}{1 + (0.082 + 0.0782 T_\infty) S_R}, \quad (6-20)$$

S_R is the ratio of the partial vapor pressure in air to the saturation vapor pressure at the given system temperature.

The temperature-dependent air-water diffusion coefficient, D_w , can be estimated by using the regression curve fitting based on Bolz and Tuve (1976) [177, 178]

$$D_w = -2.775 \times 10^{-6} \left[\frac{m^2}{s} \right] + 4.479 \times 10^{-8} \left[\frac{m^2}{s \cdot K} \right] T + 1.656 \times 10^{-10} \left[\frac{m^2}{s \cdot K^2} \right] T^2. \quad (6-21)$$

The extinction rate of the droplet by the evaporation is eventually obtained from

$$\frac{d(d_w)}{dt} = \frac{4 D_w M}{R \rho_w d_w} \left(\frac{p_\infty}{T_\infty} - \frac{p_d}{T_d} \right), \quad (6-22)$$

where M , R , ρ_w , and d_w are the molecular weight, gas constant, density, and diameter of the water droplet. The subscript d , and ∞ mean the surface of the droplet and the ambient condition.

By integrating equation (6-22), the droplet's lifetime can be expressed as

$$t = \frac{R \rho_w d_w^2}{8 D_w M \left(\frac{P_d}{T_d} - \frac{P_\infty}{T_\infty} \right)}. \quad (6-23)$$

The equation (6-23) is applicable for droplets larger than 1.0 μm . Otherwise, a correction factor, called the Fuchs factor, should be applied for calibration. This comes from the kinetic processes associated with the mean free path being the decisive mechanism for mass transport in this case, compared to molecular diffusion at the droplet surface.

The calculated lifetimes of water droplets, exposed to given conditions, are shown in Fig. 6.1, the values are derived by solving (6-23). This shows the proportional relationship to the square of the initial droplet size as expected from the d^2 -law and (6-23).

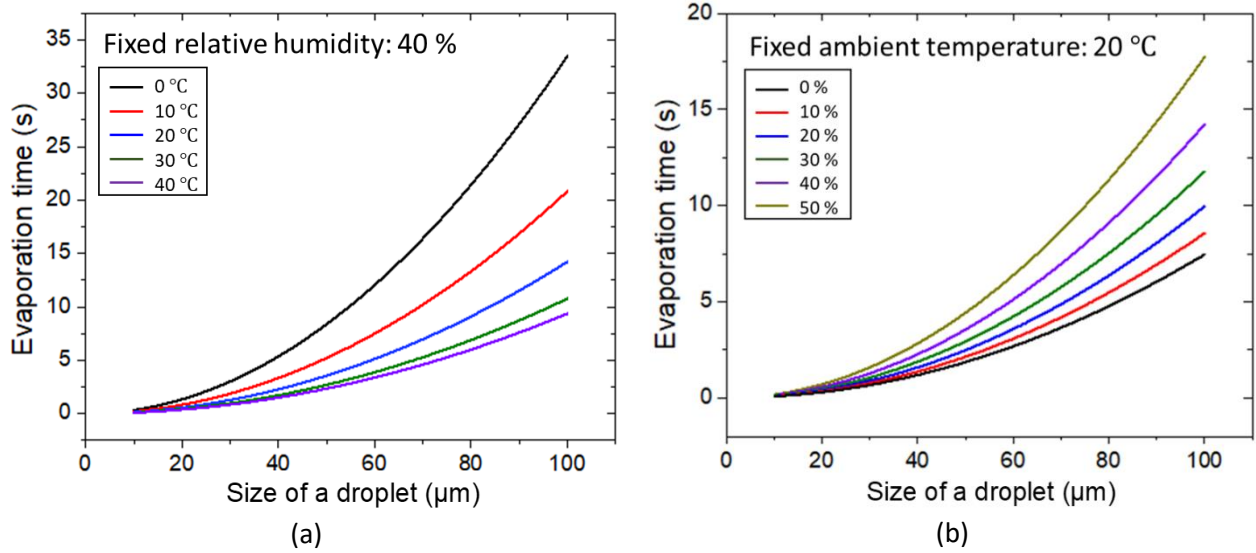


Fig. 6.1: Lifetime of the water droplets under different surrounding conditions: fixed relative humidity (40 %) with various temperatures (a) & fixed ambient temperature (20 °C) with various relative humidities (b) in the quiescent air.

Another obvious phenomenon is also observed, that higher ambient temperatures and lower humidities promote the evaporation rate. However, this model did not recognize a wind factor affecting mass diffusion and heat transfer at the material surface. This factor works for relatively large droplets, typically larger than 50 μm. For example, the evaporation rate is 31 % higher than the value predicted in (6-23) in the case of a 100 μm droplet [176].

6.2.2 Droplet evaporation in the convective air

The convective air implies an interchangeable relative velocity between the object and the surrounding area. In the here relevant case, the relative speed between the quiescent air and a falling droplet, driven by initial exit speed from the nozzle and the gravitational force, is such a convective situation. Also, devices that use atomization or droplet generation, such as combustors and inkjets, eject droplets at a speed relative to the air. This relative speed enhances the occurring heat and mass transfer, increasing both cooling and evaporation. This can be explained by the droplet's movement, replacing the surrounding saturated air with dry air, resulting in continuous evaporation.

Williamson and Threadgill proposed a method that could estimate the evaporation of a spherical drop in the air, taking into account its relative velocity, in 1974 [179]. The size reduction rate of the droplet is similar to the one form (6-23), but additional variables, the Re and Sc numbers, are employed as shown in (6-24)

$$\frac{d(d_w)}{dt} = \frac{4 D_w M}{R \rho_w d_w T_s} (p_s - p_\infty) \left(1 + 0.276 R_e^{\frac{1}{2}} S_c^{\frac{1}{3}} \right), \quad (6-24)$$

where T_s and p_s represent the temperature and pressure near the droplet. Other parameters are the same as those used in 6.2.1. The temperature and pressure near a droplet are replaced by conditions at the droplet's surface, enabling the use of (6-19) and (6-20).

The Schmidt number represents the ratio of momentum diffusivity to mass diffusivity and is used for the fluid flow characterization related to the simultaneous momentum and mass diffusion convection (e.g., mass transfer boundary layer)

$$Sc = \frac{\gamma_a}{D_w} = \frac{\mu_a}{\rho_a D_w}. \quad (6-25)$$

By integrating (6-24), the droplet's lifetime is described as (6-26)

$$t = \frac{R \rho_w d_w^2 T_s}{8 D_w M (p_s - p_\infty) (1 + 0.276 R_e^{1/2} + S_c^{1/3})}. \quad (6-26)$$

The droplet velocity is assumed to be constant at $3.6 \text{ m} \cdot \text{s}^{-1}$ as determined in Chapter 5, and the effect of the surrounding environment on the droplet's lifetime as a function of size is shown in Fig. 6.2.

The evaporation tendency according to the ambient conditions is similar in both cases: the quiescent and convective air. However, the difference in droplet lifetime in these two cases varies from less than 0.5 % to more than 54 %. The larger the size and the lower the temperature and humidity, the greater the variance in terms of the extinction time ratio.

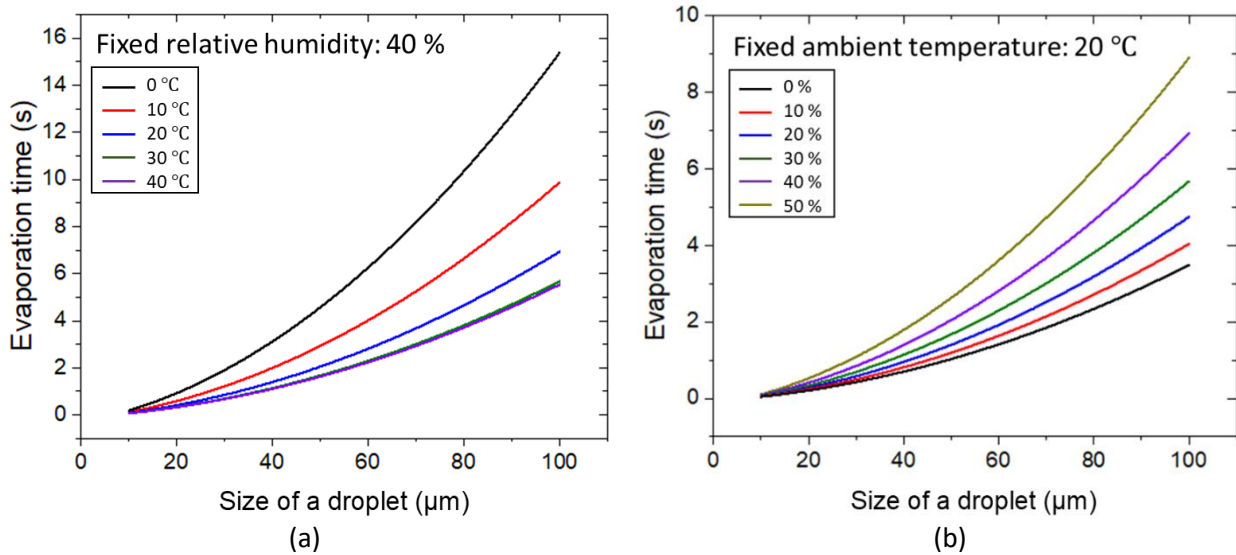


Fig. 6.2: Lifetime of the water droplets under different surrounding conditions: fixed relative humidity (40 %) with various temperatures (a) & fixed ambient temperature (20 °C) with various relative humidities (b) in the convective air.

6.3 Heat and Mass transfer-based Numerical models of the Falling droplet

This section focuses on the energy transfer of falling droplets consistent with the proposed research scheme. Heat and mass transfer of free-falling droplets have been well elaborated based on an analytical engineering design in reference [180]. However, in the frame of the present research work, the direct temperature measurement of the falling droplet during the microwave interaction is impossible. It is therefore estimated from the temperature acquired from a thermocouple located a few tens of millimeters below the microwave device after the droplet passed through the resonator.

It is necessary to determine the falling speed to evaluate the temperature change of a droplet governed by heat and mass transfer. The jet splits into individual droplets by cause of a combination of inertia, aerodynamics, and surface tension, and this break-up is promoted by vibrational forces. The droplet velocity gradually decreases due to the drag force and then converges to the terminal velocity. Several cases of terminal velocity of falling droplets are detailed in the reference literature [180, 181].

The basic mathematical form that does not take into account any influences except gravity and drag is expressed from the net force

$$U_t = \sqrt{\frac{2mg}{\rho_a A C_D}}. \quad (6-27)$$

With super slow motion of the fluid flow, once the advective inertial forces are relatively small compared to the viscous force, the terminal velocity of a spherical object is given by Stokes' law, considering the fluid viscosity in which the droplet falls,

$$U_t = \frac{g(\rho_w - \rho_a)d^2}{18\mu}. \quad (6-28)$$

The formula considering buoyancy that acts opposite to the gravitation force, similar to the drag force, is

$$U_t = \sqrt{\frac{4dg(\rho_w - \rho_a)}{3\rho_a C_D}}, \quad (6-29)$$

where d , g , C_D , ρ_w , and ρ_a are the droplet diameter, gravitational acceleration, drag coefficient, and density of water and air, respectively.

Chen et al. [182] proposed a formula for determining the drag coefficient for a liquid droplet:

$$C_D = \frac{24}{Re} + \frac{6}{1 + \sqrt{Re}} + 0.27, \quad 1 < Re < 1000. \quad (6-30)$$

According to the formulas (6-27), (6-28), (6-29), and (6-30), the terminal velocity of a $\varnothing 100 \mu\text{m}$ water droplet converges below $0.3 \text{ m}\cdot\text{s}^{-1}$ with a drag coefficient of 17.5. However, the temperature measurement location is near the microwave resonator (within 23 mm), so it can be assumed that the initial velocity of the jet is maintained without a significant speed decrease until the droplet is in contact with the thermocouple.

In order to analyze the cooling rate of the falling droplet, both, internal mixing and non-mixing model are proposed based on the Biot number, a simple index defined by the relationship between the heat conduction in the droplet and the heat convection at the surface, as expressed in

$$Bi = h_c \frac{d}{k_w}, \quad (6-31)$$

where d and k_w are the characteristic diameter and thermal conductivity of the falling droplet, respectively. And h_c indicates the convective heat transfer coefficient. In general, the temperature profile is assumed to be uniform throughout the substance's volume at low Biot number conditions (typically, $Bi < 1$), especially when the droplet's Biot number is less than 0.1 [183]. The value of 0.1 states a body as "thermally thin", meaning that in this case the internal heat conduction is much faster than the heat convection working at the surface of the body.

The optimized droplet size of $100 \mu\text{m}$ in Chapter 3, generated by a stainless steel nozzle, corresponds to a Biot number of 0.18. This value increases with the usage of a PEEK nozzle, due to the velocity rise (smaller diameter). However, it is debatable which model these droplets belong to, so all models are contemplated.

As mentioned earlier, for the former approach ($Bi < 0.1$), a vigorous temperature exchange within the droplet is assumed, resulting in a uniform heat distribution without a temperature gradient. Energy transfer only occurs at the droplet boundary, and the surface temperature represents the overall temperature. This concept is defined as a mixing model in this thesis. The governing equation for this energy transfer is also based on the energy conservation, consisting of three kinds of heat fluxes, corresponding to the convection term, Q_c , evaporation term, Q_e , and radiation terms, Q_r .

$$\rho_w c_p V \frac{dT_w}{dt} = -A[Q_c + Q_e + Q_r] = -A[h_c (T_w - T_\infty) + h_d \rho_a h_{fg} (W_s - W_\infty) + \sigma \varepsilon (T_w^4 - T_\infty^4)]. \quad (6-32)$$

Table 6.2: Variables for (6-32).

| | | | | | |
|-----------|------------------------|------------|--------------------------------------|---------------|---------------------------|
| ρ_w | Water density | T_w | Droplet temperature | W_s | Saturation humidity ratio |
| ρ_a | Air density | T_∞ | Air temperature | W_∞ | Ambient humidity ratio |
| $c_{p,w}$ | Specific heat of water | h_c | Convective heat transfer coefficient | σ | Stefan-Boltzmann constant |
| V | Droplet volume | h_d | Convective mass transfer coefficient | ε | Emissivity |
| A | Droplet surface | h_{fg} | Enthalpy of vaporization of water | $c_{p,a}$ | Specific heat of air |

Table. 6.2 stands for the variables used in (6-32).

The left-hand side of the equation (6-32) stands for the rate of energy variation in the falling droplet. The right-hand side implies the energy transfer because of convection, evaporation, and radiation on the droplet surface. In addition, this differential equation includes the evaporative cooling coming from the mass transfer. The variables, h_c and h_d , are time dependent. However, these changes are neglected since the temperature measurement location by a thermocouple is very close to the microwave resonator, and the flight time of the droplet is maximal 10 ms.

In contrast, the alternative model ($Bi > 0.1$) does not consider an internal mixing flow, turning into the conventional transient heat conduction equation with the evaporative cooling effect added heat transfer boundary conditions. This approach is named a non-mixing model in this thesis.

A 1D spherical coordinate is chosen to simulate the droplet temperature profile, because of the domain simplicity, as expressed in (6-33)

$$\rho_w c_p \frac{\partial T_w}{\partial t} = k_w \frac{1}{r^2} \frac{\partial}{\partial r} \left(r^2 \frac{\partial T_w}{\partial r} \right), \quad 0 < r \leq R, \quad (6-33)$$

where r and R indicate the radial component and radius of the droplet.

The initial condition is given as (6-34)

$$T_{t=0, r < R} = T_0. \quad (6-34)$$

Also, the boundary condition at the middle of the droplet is written as (6-35)

$$\left. \frac{\partial T_r}{\partial r} \right|_{r \rightarrow 0} = 0. \quad (6-35)$$

An additional boundary condition to define the outer surface, where both mass and heat transfer are mostly acting on, is ($r = R$)

$$-k_w \left. \frac{\partial T_w}{\partial r} \right|_R = h_c (T_w - T_\infty) + h_d \rho_a h_{fg} (W_s - W_\infty) + \sigma \varepsilon (T_w^4 - T_\infty^4). \quad (6-36)$$

The convective heat transfer coefficient can be obtained from the Nusselt number described in (6-2).

In addition, the convective mass transfer coefficient, h_d , is introduced from the relation among the droplet's Sherwood number, Schmidt number, and Reynold number,

$$Sh = \frac{h_d d}{D_w} = 2 + 0.6 Sc^{1/3} Re^{1/2}. \quad (6-37)$$

The Sherwood number is a typically used parameter for the mass transfer expressed by the ratio of convective to the rate of diffusive mass transport. Another approach to estimating the convective mass transfer coefficient is by using the Lewis number, defined as the interaction between thermal diffusivity and mass diffusivity. This number is employed for the fluid characterization when mass and heat transfer take place at the same time, and is given by

$$Le^{2/3} = \frac{h_c}{\rho_a c_{p,a} h_d} \cong \left(\frac{\alpha}{D_w} \right)^{2/3}. \quad (6-38)$$

The Lewis number is a constant value for water vapor in air at room temperature, and is approximately 0.85.

The humidity ratio (x , kg_{water}/kg_{dry-air}) is derived from the relationship between the actual water vapor mass (m_w) in moist air and dry air mass (m_a), usually expressed as

$$x = \frac{m_w}{m_a}. \quad (6-39)$$

It can also be manifested in terms of vapor partial pressure by the ideal gas law

$$x = 0.62198 \frac{p_w}{(p_a - p_w)}. \quad (6-40)$$

The constant 0.62198 is from the ratio between the molar mass of water (18.015 g/mol) and the dry air (28.965 g/mol). p_w and p_a are partial pressures of water vapor in moist air (Pa) and an atmospheric pressure of moist air (Pa). The saturated pressure of water vapor (p_{ws}) is replaced instead of the p_w for the case of the maximum water vapor in air, $p_{ws} = p_w$.

The specific humidity ratio of a vapor mixture (Ambient humidity) is acquired by adding the relative humidity factor (ϕ) as

$$x = 0.62198 \phi \frac{p_w}{(p_a - p_w)}. \quad (6-41)$$

Fig. 6.3 and Table 6.3 show the saturation humidity ratio, W_s , with the polynomial curve fitting obtained using (6-40). This curve is utilized for each iteration of (6-32) and (6-33).

Fig. 6.4 represents the temperature change of a 100 μ m diameter falling water droplet as a function of time calculated by the mixing and non-mixing models. The initial temperatures of the droplets are 70 °C and 50 °C, establishing a uniform temperature profile inside the droplet due to volumetric heating.

Determining the temperature and relative humidity of the surrounding air near the droplet is complex, since consecutively followed droplets evaporated and condensed simultaneously. Therefore, the cases of surrounding temperatures at 20 °C and 40 °C with 40 % and 80 % relative humidities were chosen as representative examples to understand the influence of environmental conditions on the droplet's cooling.

The adopted parameters for both models are described in Table 6.4. Tools of the software system Mathematica® enables numerical calculations for the heat and mass transfer of the falling droplets. In the case of the non-mixing model, the average temperature compensated for the difference between the inside and the outside of the droplet is substituted. Numerical integration helps to gain the mean temperature value over the radial direction of the droplet.

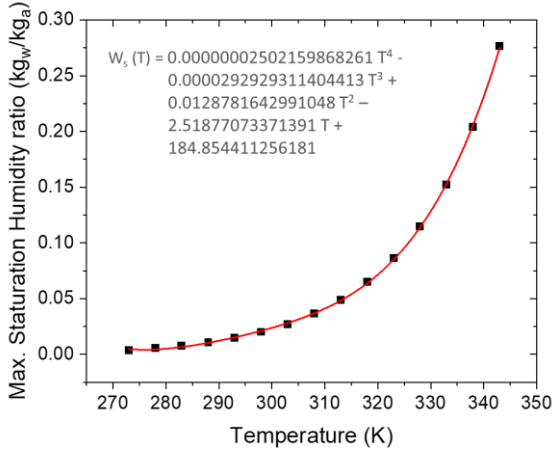


Fig. 6.3: Saturation humidity ratio with a polynomial curve fitting.

Table 6.3: Saturation humidity ratio (kg_w/kg_a) [184].

| Temperature (K) | Vapour pressure of water (Pa) | Saturation Humidity Ratio of Air (kg _w /kg _a) |
|-----------------|-------------------------------|--|
| 273 | 611.3 | 0.003775220 |
| 278 | 872.6 | 0.005402955 |
| 283 | 1228.1 | 0.007631142 |
| 288 | 1705.6 | 0.010649021 |
| 293 | 2338.8 | 0.014695855 |
| 298 | 3169 | 0.020080837 |
| 303 | 4245.5 | 0.027200553 |
| 308 | 5626.7 | 0.036570084 |
| 313 | 7381.4 | 0.048870633 |
| 318 | 9589.8 | 0.065020448 |
| 323 | 12344 | 0.086284950 |
| 328 | 15752 | 0.114492059 |
| 333 | 19932 | 0.152314147 |
| 338 | 25022 | 0.203965553 |
| 343 | 31176 | 0.276423733 |

Table 6.4: Values used for the calculation for (6-32) and (6-33).

| | | | | | | | |
|----------------------------------|------------------------|--|-----------------------|----------------------------------|--|---------------------------------|-------|
| $c_{p,w}$ (J/kg · K) | 4190 | $c_{p,a}$ (J/kg · K) | 1006 | ρ_a (kg/m ³) | 1.204 | h_c (W/m ² · K) | (6-2) |
| ρ_w (kg/m ³) | 998 | h_d (m/s) | (6-38) | h_{fg} (J/kg) | $-1.2684442066 T^2 - 1617.1375351228 T + 3036524.9863468000$ | T_{ex} (K) | 293 |
| ε | 0.95 | σ (W/m ² · K ⁴) | 5.67×10^{-8} | ν_a (m ² /s) | 1.516×10^{-5} | α | Air |
| μ_a (kg/m · s) | 1.825×10^{-5} | k_w (W/m · K) | 0.598 | k_a (W/m · K) | 0.02514 | w | Water |

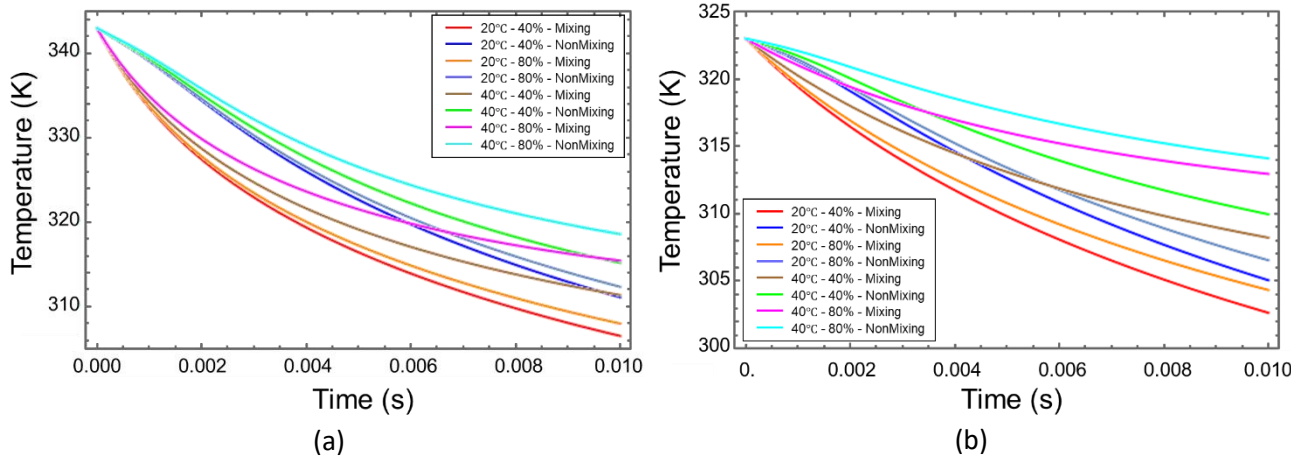


Fig. 6.4: Temperature profiles of a \varnothing 100 μm falling water droplet with respect to different conditions: ambient temperature ($^{\circ}\text{C}$) - Humidity (%) - Model (Mixing / NonMixing), with the initial temperatures of 343 K - 70 $^{\circ}\text{C}$ (a) and 323 K - 40 $^{\circ}\text{C}$ (b).

Naturally, the cooling rate of the mixing model is faster than the non-mixing model, since the overall temperature is governed by the boundary temperature only, with the interior's temperature being equal. On the other hand, cooling in the non-mixing model first starts at the droplet boundary and is transferred to the center by a diffusion mechanism, resulting in a temperature gradient in the radial direction of the droplet.

A rise in the evaporation rate of the falling water droplets corresponds to a proportionally improved cooling rate, which operates more vigorously at lower ambient humidity. In addition, a larger temperature difference between the ambient temperature and the droplet gives rise to a higher cooling rate attributable to a more pronounced heat exchange. Moreover, this cooling gradient becomes steeper once the initial temperature increases. The flight distance, corresponding to 0.01 seconds flight time in Fig. 6.4, is about 36 mm considering the initial speed, and the maximum cooling leads to a more than 30 K lower value compared to the initial temperature. This means that the cooling rate of hot falling water droplets is extremely fast.

Experimental validation of the temperature drop of falling droplets is covered in the next session including the results of numerical models.

6.4 Microwave validation

6.4.1 Numerical temperature estimation by the droplet cooling

Environmental conditions around the droplet path of both models, the mixing and the non-mixing one, are adjusted in a way that the temperature variations as a function of the flight distance approach the experimental findings. This way the temperature obtained in the experiment, and the above numerical model, can be correlated. It is intuitively obvious that the humidity and temperature around the droplet flow are higher than in the distant surroundings, as the heated droplet train flows and evaporates continuously.

Thermocouples were installed at different heights to calculate the cooling rate of the droplet according to the flight time reversely and to track the initial maximum temperature of the droplets. The experimental configuration and the measured results are shown in Fig. 6.5.

The stream is ejected from the nozzle and remained up to an E-field gap. It is then transformed into water droplets inside the resonator's outer wall and begins cooling. Hence, only the droplet shape is visible below the resonator. However, the breakup location is not absolutely consistent, resulting in the probability of errors (e.g., Fig. 6.5 shows the breakup distance of 2.7 mm from the nozzle). Here, the temperature of interest is the one before cooling starts, as it represents the temperature rise by microwave heating. Therefore, the flight distance of the droplet is set to the measured length in Fig. 6.5 and increased by 1 mm, which is half of the resonator wall thickness. In other words, the space between the bottom of the resonator and the thermocouple plus 1 mm is assumed to be the affected path by cooling.

Measurements started after warming up the system for at least 10 minutes with an applied power of 45 W, to assume a steady state of ambient conditions and flow. Moreover, the average value of the recorded temperature for a minute was used.

The cooling speed is assumed to be slower than the one of an isolated droplet introduced in Chapter 6.2, due to the growing vapour film around the droplet train that plays a role in hindering further cooling and evaporation. This film's condition is assumed to be constant after warming up, replacing the ambient state infinitely distant from the system configuration. The primary idea in this chapter is to adjust these layer parameters containing vaporized water, in order to match the numerical and experimental findings, and to be able to track the initial temperature. Changing the experimental conditions each time is complex, but numerical models allow adjustments effortlessly.

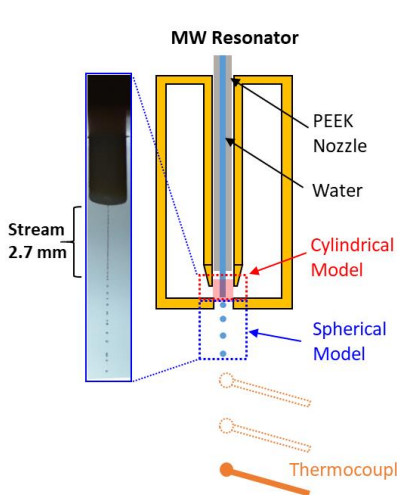
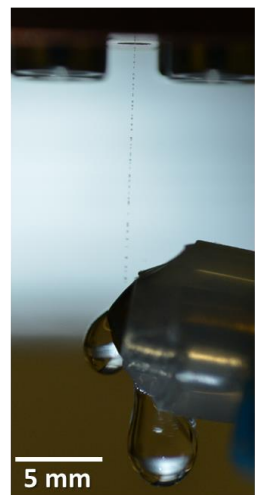


| Scheme | Point 1 | Point 2 | Point3 |
|---|---|--|---|
|  |  |  |  |
| Flight Distance(mm) | 14.255 + 1 | 18.003 + 1 | 22.451 +1 |
| Flight time (ms) | 4.238 | 5.279 | 6.514 |
| Temperature (°C) | 52.04 | 49.75 | 48.05 |

Fig. 6.5: Experimental configuration with the measured results.

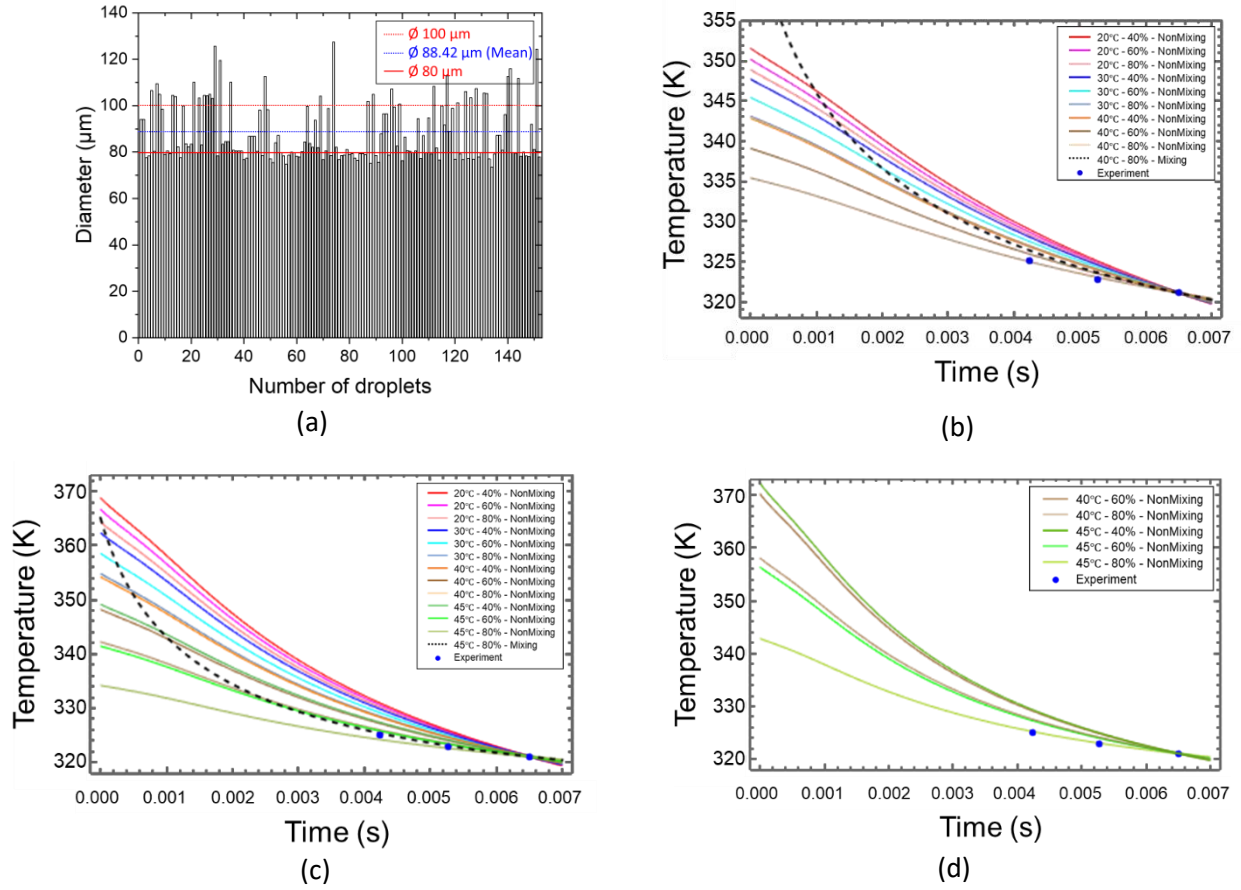


Fig. 6.6: Size distribution (a) and temperature profiles of the droplets based on numerical models: \varnothing 100 μm (b), \varnothing 90 μm (c), and \varnothing 80 μm (d) in diameter.

152 droplets, generated without applying vibration to the nozzle, were analyzed to determine the effective diameter for the numerical method. The average diameter shows 88.4 μm once the droplets are assumed to be perfectly spherical, as shown in Fig. 6.6 (a).

Therefore, droplets of \varnothing 100 μm , \varnothing 90 μm , and \varnothing 80 μm are selected as the final sample sizes for numerical models, and their temperature profiles as a function of the time are illustrated in Fig. 6.6 (b), (c), and (d). The zero on the x-axis denotes the initial temperature when cooling begins. Detailed values are given in Tables 6.5, 6.6, and 6.7.

The experimentally obtained temperature is less sensitive than the numerically calculated one of a single droplet, due to the accumulated droplet volume hanging on the thermocouple. This relatively large heat capacity cannot allow tracking the instantaneous temperature change of the droplet, but it helps to represent the average temperature of the droplet train. However, an inherent temperature measurement delay occurs with some amount of cooling.

Therefore, the first step for the temperature prediction is to designate the lowest height (distance: 23.451 mm) among the three temperature measurement positions as the reference value, since the measured value cannot be higher than the genuine droplet's temperature. Then, numerical results are approximated to this value by changing the environmental conditions. Eventually, any points of interest, including the initial temperature, can be extracted using two models already fitted from the reference value.

As described above, the cooling rate is much faster in the non-mixing model, so the calculated initial temperature is even higher than the boiling point of water in most cases. Therefore, any case in which the initial temperature exceeded 100 °C is excluded in Fig. 6.6.

The environmental temperature is adjusted from 20 °C to 40 °C in 10 °C increments, and 40 %, 60 %, and 80 % of ambient humidity are selected as representative examples. The cooling proceeds faster in the case of droplet diameters of \varnothing 90 μ m and \varnothing 80 μ m than \varnothing 100 μ m, so the surrounding temperature of 45 °C is supplemented to derive results close to experimental data. The boundary condition is such that the surrounding status should be lower than the measured temperature of droplets and 100 % relative humidity, even though vapor film has been formulated around the droplet's trajectory. Finally, conditions of the numerical model that exist within a temperature error range of 5 %, based on the measured values, are selected, as shown in the blue square in Tables 6.5, 6.6, and 6.7. The initial temperatures of selected conditions are to be compared with the water temperature immediately after heating by microwave.

Table 6.5: All temperature data in Celsius (°C) for Fig. 6.6 (b).

| | | Experiment | | | | | | | | | | Samples | |
|---|--|---|--------------|--------------|--------------|--------------|--------------|--------------|--------------|--------------|--------------|--------------|--------------|
| Surrounded Condition Flight Time (s) | | Non-Mixing | | | | | | | | | | Mixing | |
| | | Experiment | 20 °C - 40 % | 20 °C - 60 % | 20 °C - 80 % | 30 °C - 40 % | 30 °C - 60 % | 30 °C - 80 % | 40 °C - 40 % | 40 °C - 60 % | 40 °C - 80 % | 40 °C - 80 % | 40 °C - 80 % |
| | | Calculated temperature for \varnothing 100 droplet (°C) | | | | | | | | | | | |
| 0 | | - | 78.586 | 77.223 | 75.926 | 74.743 | 72.451 | 70.115 | 69.866 | 66.097 | 62.399 | 95.862 | |
| 4.2375 | | 52.04 | 55.9626 | 55.6252 | 55.3191 | 55.0382 | 54.492 | 53.9117 | 53.8515 | 52.9057 | 51.9581 | 53.3679 | |
| 5.278611 | | 49.75 | 52.0078 | 51.8221 | 51.6647 | 51.5248 | 51.2541 | 50.966 | 50.9364 | 50.4697 | 49.9954 | 50.5735 | |
| 6.514167 | | 48.05 | 48.086 | 48.0502 | 48.0502 | 48.05 | 48.0502 | 48.05 | 48.0503 | 48.0502 | 48.05 | 48.05 | |

Table 6.6: All temperature data in Celsius (°C) for Fig. 6.6 (c).

| | | Experiment | | | | | | | | | | | | | Samples | |
|---|--|--|--------------|--------------|--------------|--------------|--------------|--------------|--------------|--------------|--------------|--------------|--------------|--------------|--------------|--------------|
| Surrounded Condition Flight Time (s) | | Non-Mixing | | | | | | | | | | | | | Mixing | |
| | | Experiment | 20 °C - 40 % | 20 °C - 60 % | 20 °C - 80 % | 30 °C - 40 % | 30 °C - 60 % | 30 °C - 80 % | 40 °C - 40 % | 40 °C - 60 % | 40 °C - 80 % | 45 °C - 40 % | 45 °C - 60 % | 45 °C - 80 % | 45 °C - 80 % | 45 °C - 80 % |
| | | Calculated temperature for \varnothing 90 droplet (°C) | | | | | | | | | | | | | | |
| 0 | | - | 95.848 | 93.709 | 91.383 | 89.364 | 85.591 | 81.847 | 81.249 | 75.198 | 69.229 | 76.143 | 68.437 | 61.172 | 92.076 | |
| 4.2375 | | 52.04 | 57.9388 | 57.5932 | 57.1737 | 56.8218 | 56.1468 | 55.4528 | 55.3423 | 54.1884 | 52.9578 | 54.3613 | 52.7945 | 51.1995 | 52.3618 | |
| 5.278611 | | 49.75 | 52.8544 | 52.6905 | 52.4833 | 52.311 | 51.9756 | 51.6365 | 51.5988 | 51.0308 | 50.4375 | 51.1211 | 50.3511 | 49.5819 | 50.0487 | |
| 6.514167 | | 48.05 | 48.0501 | 48.0501 | 48.0501 | 48.05 | 48.0501 | 48.05 | 48.05 | 48.05 | 48.0502 | 48.05 | 48.05 | 48.0502 | 48.05 | |

Table 6.7: All temperature data in Celsius (°C) for Fig. 6.6 (d).

| | | Experiment | | | | | | Samples | |
|---|--|--|--------------|--------------|--------------|--------------|--------------|---------|--|
| Surrounded Condition Flight Time (s) | | Non-Mixing | | | | | | | |
| | | Experiment | 40 °C - 60 % | 40 °C - 80 % | 45 °C - 40 % | 45 °C - 60 % | 45 °C - 80 % | | |
| | | Calculated temperature for \varnothing 80 droplet (°C) | | | | | | | |
| 0 | | - | 97.273 | 85.121 | 99.316 | 83.391 | 69.833 | | |
| 4.2375 | | 52.04 | 56.1247 | 54.5306 | 56.3503 | 54.2843 | 52.216 | | |
| 5.278611 | | 49.75 | 51.8444 | 51.1027 | 51.9501 | 50.9812 | 50.0162 | | |
| 6.514167 | | 48.05 | 48.05 | 48.05 | 48.05 | 48.05 | 48.05 | | |

6.4.2 Numerical temperature estimation by the droplet heating

The droplet temperature is highest just after being heated by the microwave interaction and before evaporation and cooling begin. Of course, the water temperature rises by thermal conduction when it moves through the nozzle, as the central conductor of the resonator gets hot, but this is a minor contribution compared to the one from the microwaves.

Equation (5-5), representing the amount of microwave power absorption by a dielectric, is utilized to demonstrate water droplet heating in the heat equation (6-13), resulting in (6-42)

$$\rho c_p \frac{\partial T}{\partial t} + \nabla \cdot (-k \nabla T) = 2\pi f \epsilon_0 \epsilon''_{eff} |E_{rms}|^2 V. \quad (6-42)$$

The temperature rise, while the water droplet passes through the concentrated electric field, can be calculated using the initial temperature derived from the numerical model. In addition, the absorbed power, according to the temperature deviation, can also be traced back from the thermal equation. Here, the time adopted for the power calculation comes from the interaction distance between the microwave and the falling droplet, obtained in the experiment. Furthermore, this power value should be consistent with the power absorption, acquired from the strength of the electric field inside the dielectric, being derived by CST Microwave Studio software simulations.

A frequency domain solver is employed for the electric field and power absorption analysis. The applied adaptive mesh refinement and the S_{11} parameter are shown in Fig. 6.7. The resonance frequencies by simulation and measurement are 10.46 GHz and 10.49125 GHz, respectively. A deviation of 0.3 % may come from material properties adopted in the simulation or from tolerances in manufacturing.

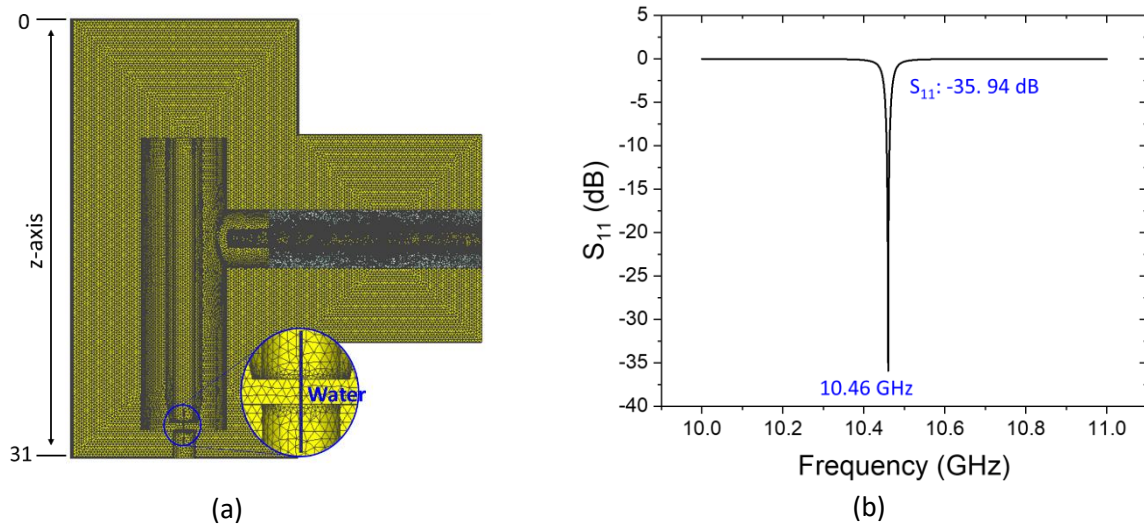


Fig. 6.7: Adaptive mesh refinement and S_{11} result of the model.

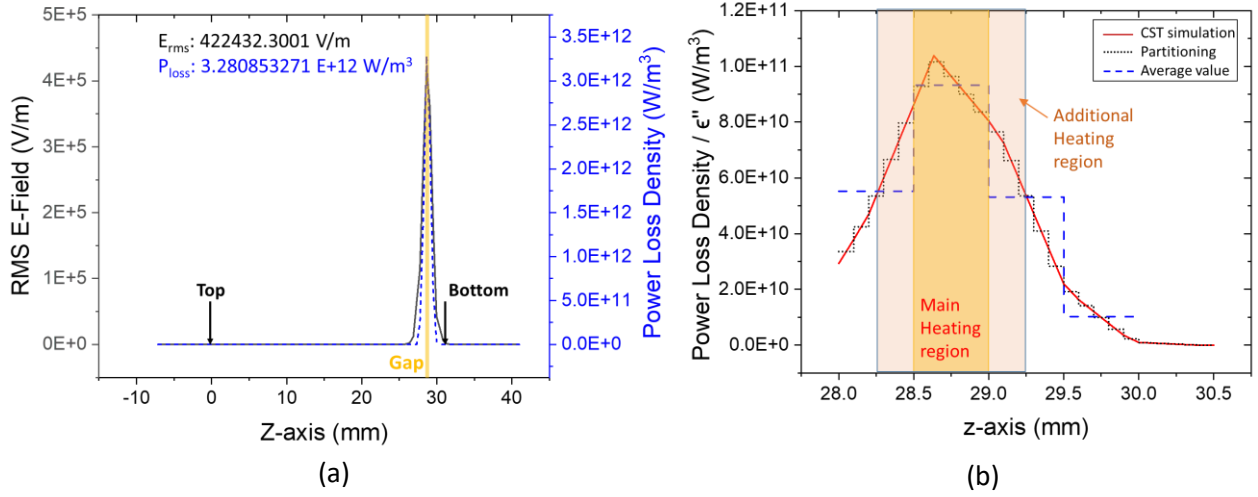


Fig. 6.8: Simulation results of E-field intensity (RMS), power loss density (a), and average power loss density normalized by the temperature-dependent ϵ'' (b) along the z-axis.

Fig. 6.8 (a) describes the root mean square E-field strength and power loss density along the z-axis corresponding to the center of the droplet's trajectory once 45 W power is applied. Power absorption depends on the E-field strength according to (5-5), but the simulation does not consider the change in the medium's temperature dependant permittivity. Adopting a fixed loss factor overestimates the electric field, resulting in a higher water temperature rise than the actual one.

In fact, the complex permittivity, ϵ' and ϵ'' , simultaneously affects the strength of the electric field strength. Nonetheless, for convenience of calculation, it is assumed that the dielectric constant more decisively influences the electric field strength, while the imaginary permittivity plays a dominant role in the microwave absorption into the medium, respectively.

Fig. 6.9 shows the complex permittivity of water as a function of temperature in the range of 20 °C to 90 °C [94]. Accordingly, this temperature-dependent complex permittivity can be expressed in a mathematical form using polynomial curve fitting as in (6-43) and (6-44). Established dielectric constant and loss factor in the simulation are 61.22 and 31.59 at 10.46 GHz based on the Debye model. The average dielectric constant is 61.56 in this range, similar to the simulation. On the other hand, the dielectric loss shows a huge discrepancy within the specified temperature range. Hence, the curve fitting shown in Fig. 6.9 (b) substitutes the fixed ϵ'' value, using (6-44).

$$\epsilon'(T) = -0.0000008895 T^4 + 0.0012461354 T^3 - 0.6555286630 T^2 + 153.2545999749 T - 13'357.6842090105, \quad (6-43)$$

$$\epsilon''(T) = 0.0035526042 T^2 - 2.6795210134 T + 513.5393326824. \quad (6-44)$$

Fig. 6.8 (b) shows the normalized power density by ϵ'' based on a 0.1 mm wide rectangle partitioning.

The average value of Fig. 6.8 (b) multiplying (6-44) represents the modified power absorption and is used for the numerical calculation of (6-42).

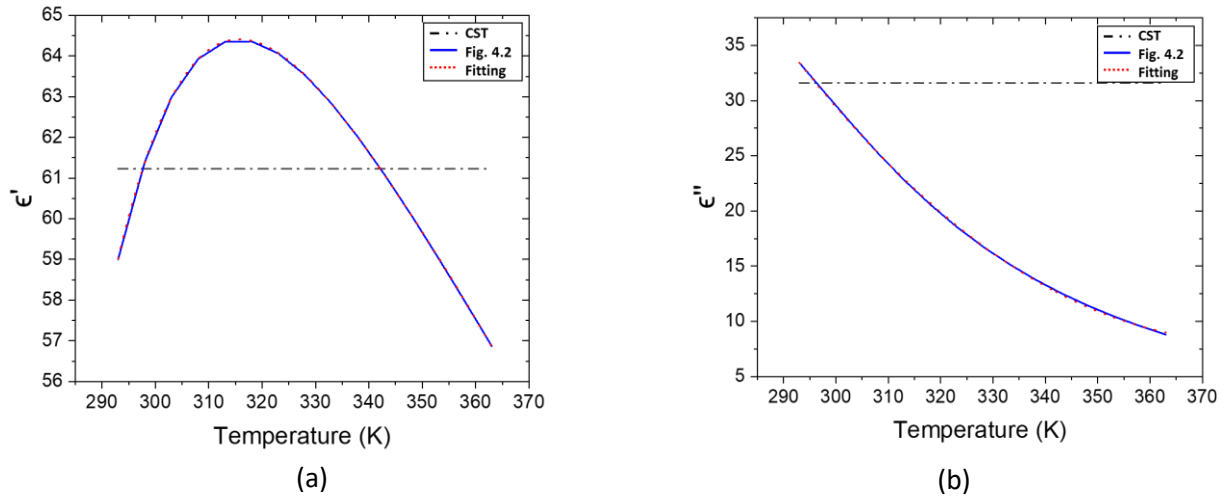


Fig. 6.9: Complex dielectric permittivity ϵ' (a) and ϵ'' (b): ■ black dash dot - CST simulation, ■ blue line - Fig. 4.2 (Debye model), and ■ red dot - polynomial curve fitting.

Two different coordinates are used to simulate the heating and cooling of water using a 1D numerical model, as shown in Fig. 6.5. A 2D model with Dirichlet condition cooling is performed to represent continuous flow at the top boundary, but there is no apparent difference ($< 0.2\%$) between the 1D and the 2D model within a given short time. Therefore, this is not further elaborated here.

1) Cylindrical coordinate (MW Heating + Cooling): a jet stream starts at the nozzle and remains up to the outer wall. Therefore, this jet passes through the concentrated electric field. This model takes into account the entire volume heating of the stream by microwaves and simultaneous cooling at the surface. The mixing model cannot present the energy absorption inside the medium, since it only works at the boundary. Thus, only non-mixing models are performed to extract the temperature rise.

2) Spherical coordinate (Cooling): there is no more stream after the bottom of the resonator, which means only droplets are left. This model corresponds to the numerical droplet cooling methods in Chapter 6.3.

The initial temperature of the introduced water is $19.2\text{ }^{\circ}\text{C}$, but the average temperature after an hour of testing is $24.35\text{ }^{\circ}\text{C}$ without input power. This phenomenon can be understood as a heat transfer effect from other components, attributable to the temperature rise of both, the resonator and the stroboscope. Boundary conditions are the same as the numerical model introduced in Chapter 6.3.

According to the CST simulation, the electric field strength, spreading into the conductor's interior, is substantially high leakage into opening. Considering the extension of the electric field, twice the gap distance is set as an additional heating zone for the numerical model. However, it is assumed that heating mainly occurs in the gap between the conductors, as shown in Fig. 6.8 (b). A finer mesh generation may reduce the range and strength of the electric field appearing inside the conductor, obtaining a more accurate result. In addition, the stream-to-droplet transition attenuates the microwave power absorption immediately, due to the depolarization factor (Sphere: $1/3$) and the discontinuity of water.

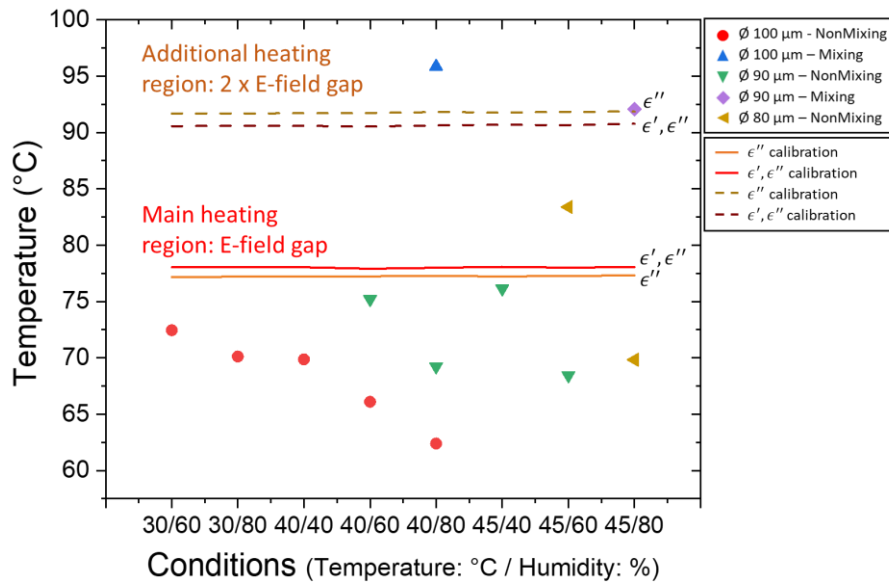


Fig. 6.10: Maximum temperature comparison by different numerical methods: ■ lines - only considering the main heating region, and ■ dashed lines - additionally considering the extended heating region. Both are calculated by the cylindrical coordinate model taking into account MW heating with cooling. ■ symbols - calculated by the spherical coordinate model considering only cooling.

Fig. 6.10 shows the maximum temperature of water derived from different approaches. The line and dashed line indicate the temperature by microwave heating, including surface cooling, and the symbols are the results tracked by converting the cooling effect from the selected conditions in Tables 6.5, 6.6, and 6.7. In other words, lines represent the attainable maximum temperature as the final temperature of the water stream after microwave interaction finishes, and symbols dictate the initial temperature of the droplet before cooling starts. Ideally, both temperatures should be the same.

The calibrated lines using both ϵ' and ϵ'' are also provided, based on the inverse relationship between the electric field and dielectric constant. The procedure utilized polynomial curve fitting in the same way aforementioned for ϵ'' but using (6-43) for ϵ' .

It can be seen that the microwave heating effect is not significantly affected by the surrounding environment, within a given short time. This is due to the numerical model that confines the microwave absorption only to the medium. Practically, it is sensitive to environmental conditions, e.g., humidity.

Considering only the main heating area, the initial temperature of the $\varnothing 90 \mu\text{m}$ droplet under the environmental conditions of $40^\circ\text{C} / 60\%$ and $45^\circ\text{C} / 40\%$ (temperature/humidity) with the non-mixing model approaches the stream temperature obtained by microwave heating with up to 98.5 % accuracy. The $\varnothing 90 \mu\text{m}$ is approximately identical to the average size obtained in Fig. 6.6 (a), $88.42 \mu\text{m}$. In addition, only $80 \mu\text{m}$ droplets in the environmental conditions of $45^\circ\text{C} / 60\%$ fall within the effective range ($< 10\%$, based on microwave heating, dashed line in Fig. 6.10), unless the mixing model is employed once the extended heating zone is applied. The reason for this is the mixing model, and that small droplets have a fast cooling rate resulting in an increase of the initial, back calculated, temperature.

The average temperature discrepancies by the microwave heating model using ϵ' and ϵ'' simultaneously and using only ϵ'' in the calibration step are 0.79°C and 1.13°C , considering the main heating area and the additional heating zone, respectively. It does not show a large difference, as expected.

In conclusion, the selected conditions to track the initial droplet temperature, do not perfectly reflect the actual status around the droplet train. However, all errors in the experimental process are included, showing reasonable results. Therefore, all temperature values are positioned within the same order of magnitude, demonstrating the validity of this numerical approach.

Chapter 7 Experimental equipment

This chapter describes the experimental setup with the composition that allows the microwave sensing and heating tests conducted in this thesis. Then, the detailed specification of the individual parts follows.

In addition, the measurement techniques, that included the calibration method, are also presented.

7.1 Equipments

The experimental configuration is shown in Fig. 7.1.

The VNA can be utilized as a power source instead of a signal generator and shows the real-time variations in resonant frequency since the attenuated reflection signal is delivered to the VNA through the directional coupler. Descriptions of some significant equipment are presented with detailed specifications.

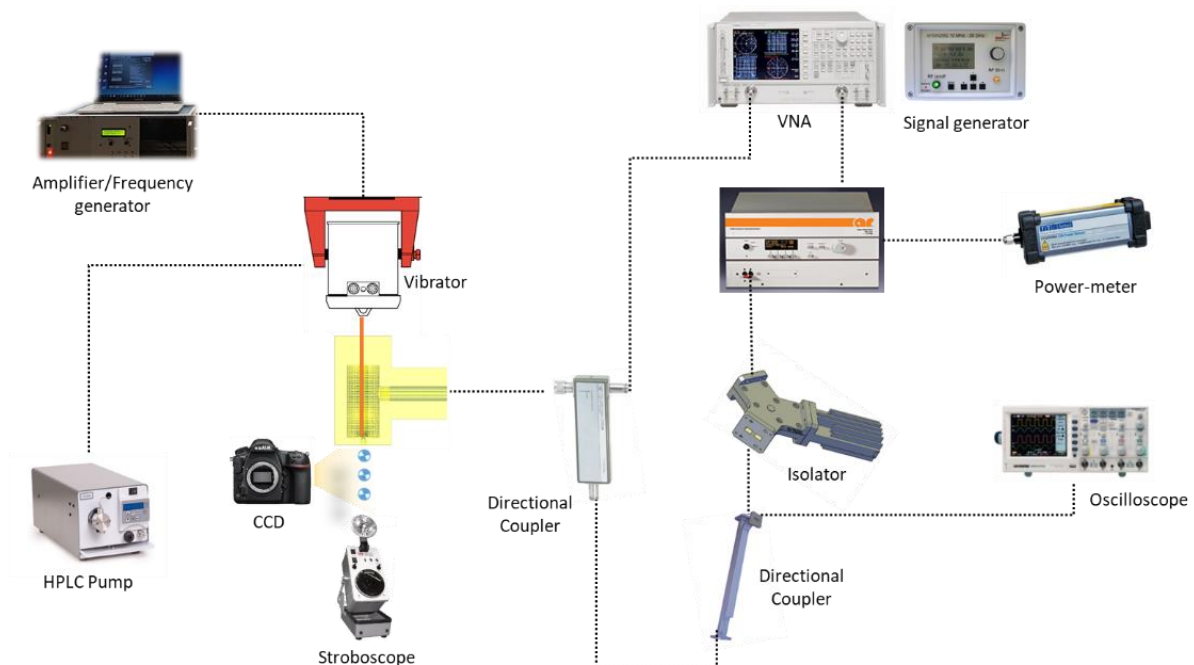


Fig. 7.1: Experimental configuration.

1. Motorized XYZ stage.

The XYZ stage was exploited and revised from the FDM/FFF (Fused Deposition Modeling / Fused Filament Fabrication) based 3D printing machine of K8200 manufactured by Velleman inc.

- Movement: NEMA 17 stepper motor
- X / Y movement: 0.1 mm with $120 \text{ mm} \cdot \text{s}^{-1}$
- Z movement: 0.1 mm , $2.5 \text{ mm} \cdot \text{s}^{-1}$
- Dimensions of the movement area: $20 \times 20 \times 20 \text{ cm}$
- Power supply: $12 \text{ V} / 3 \text{ A max.}$
- Communication: FTDI USB 2.0 to Serial

2. Droplet generator (Permanent Magnetic shaker)

The permanent magnetic shaker model LSD v201 (Fig. 7.2) manufactured by the company Brüel & Kjær was utilized for the droplet formation. This shaker is cost-effective, reliable, and easy to control. In addition, no need to adopt the cooling system with a field power supply because the source of this shaker is a permanent magnet.

Technical specifications of this shaker are,

- Frequency range: up to 13 kHz
- Shaker velocity sine peak: $1.83 \text{ m} \cdot \text{s}^{-1}$
- Shaker displacement: 5 mm
- Max acceleration sine peak: 136 g
- Effective mass of moving element: 200 g
- System velocity sine peak: $1.49 \text{ m} \cdot \text{s}^{-1}$

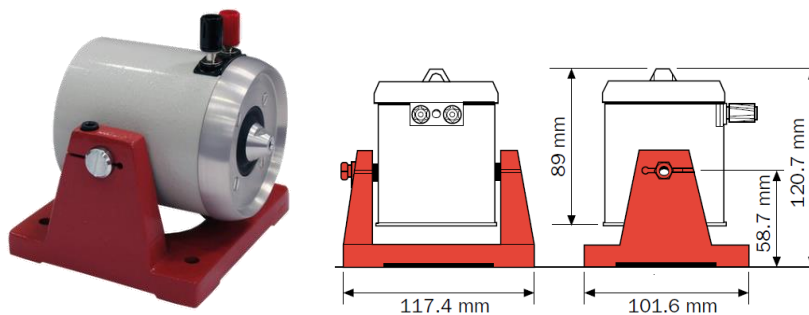


Fig. 7.2: LSD v201 with dimensions - Brüel & Kjær.

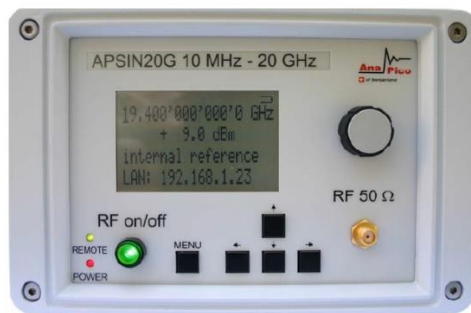
3. Microwave system

- Signal generator

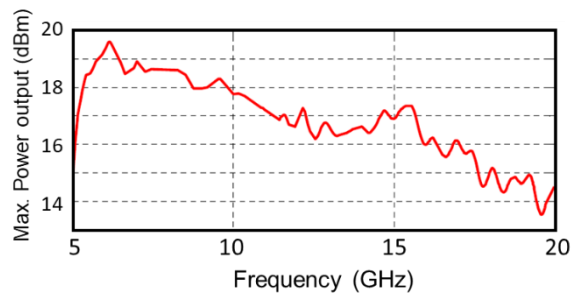
The model APSIN20G (Fig. 7.3) made by the Anapico AG has been selected as a signal generator for the microwave drying experiment enabling the frequency generation range of 10 MHz to 20 GHz. Moreover, it supports many advantages, not only being a signal generator or modulator with high accuracy but also general conveniences such as remote controllability for automation, portability, and so on.

The technical features are summarized here,

- Frequency response: 10 MHz to 20 GHz
- Frequency resolution: 0.001 Hz
- Power level: -90 to +13 dBm
- Power resolution: 0.05 dB
- Power accuracy: ± 1.3 dB
- Harmonics: < -30 dBc
- Switching speed: $< 200 \mu\text{s}$
- Modulation: AM, DC/AC, FM, PM, Pulse, Freq-Chirp



(a)



(b)

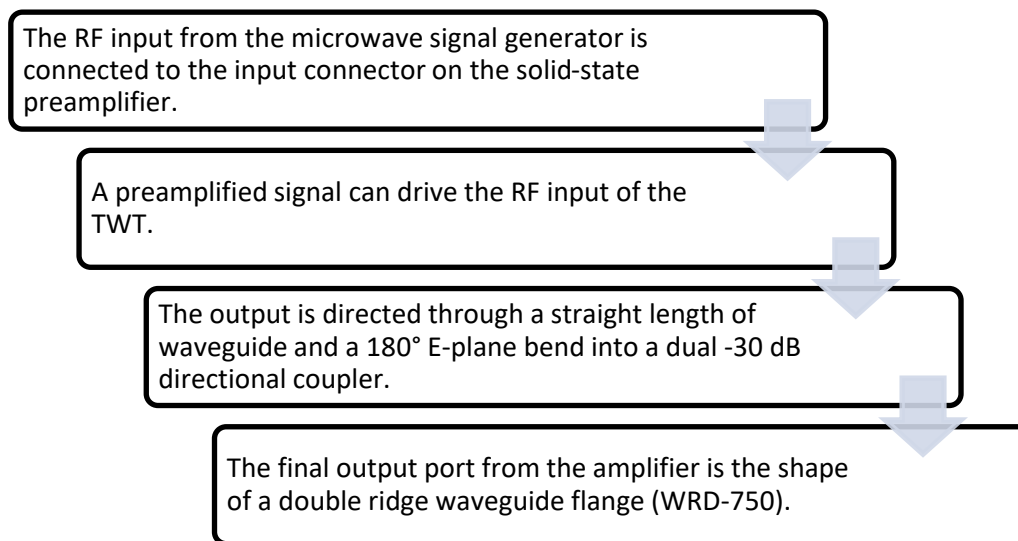
Fig. 7.3: APSIN20G signal generator - Anapico AG (a) with maximal output power in frequency ranges (b).

- Amplifier

The model of 250TR7z5g18 amplifier (Fig. 7.4) manufactured by AR has been chosen to apply proper power to the resonator for the microwave heating experiment. This amplifier uses a 300 W traveling wave tube (TWT) to provide a maximum of at least 250 W output over the entire bandwidth. The instrument consists of two principal sub-systems: a power assembly and a TWT power supply.

- Power assembly

The TWTA (Traveling Wave Tube Amplifier) is composed of the main two-stage of amplification: a solid-state preamp assembly with adjustable gain (E01175-000) and a traveling wave tube amplifier (E08114-000). The signal propagation procedure through the amplifier is explained here,

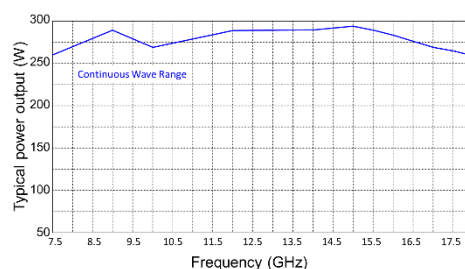


In addition to the amplification, there are some other features noteworthy.

The reverse port on the directional coupler is connected to a detector diode for measuring the VSWR (Voltage Standing Wave Ratio). The data obtained from this coupler is directly conjugated for the reflected power evaluation related to the amplifier protection from excessive power reflection. The coupled port of the -10 dB coupler is attached to the power sample port on the rear panel resulting in -40 dB attenuation.



(a)



(b)

Fig. 7.4: 250TR7z5g18 microwave amplifier - AR (a) with typical output power in frequency ranges (b).

- TWT Power supply

The TWT power supply is of modular construction.

1. Low voltage power supply module
 - 1.1 Low voltage power supply module (A23687-001):
low voltage power supply assembly, preamplifier, and HPA interface
 - 1.2 Control assembly with HPA logic (A16485-000): control logic and TWT protection
 - 1.3 Modulator Assembly: bias and pulse top voltage for the TWT grid
2. High voltage power supply
 - 2.1 Power factor correction module (A23683-230): conversion of the line voltage to DC
 - 2.2 Pulse width modulation board (A10017-500): control for the high voltage switching supply.
 - 2.3 High voltage Diode/cap Assembly (A22818-002): the high voltage transformer and rectifiers.
 - 2.4 HV filter Assembly (A212461-000): high voltage DC filtering
3. Heater power supply module(A10010-000): drives the TWT DC heater

The remarkable specifications of the amplifier are,

- Power: nominal 280 watts, Minimum 250 watts
- Flatness: ± 12 dB maximum
- Frequency response: 7.5 - 18 GHz instantaneously
- Input for rated output: 1.0 mW maximum
- Gain (at maximum setting): 54 dB minimum
- Gain adjustment (continuous range): 35 dB minimum
- Input impedance: 50 Ω , VSWR - 2.0:1 maximum
- Output impedance: 50 Ω , VSWR - 2.5:1 typical
- Mismatch tolerance: 50 W
- Harmonic distortion:
 - Below 10 GHz, -5 dBc maximum, -7 dBc typical;
 - 10-12 GHz, -8 dBc maximum, -12 dBc typical;
 - Above 12 GHz, -20 dBc maximum, -30 dBc typical
- Cooling: forced air (self-contained fans), air entry, and exit in the rear.

- Isolator

The Model WRD750D24 isolator (Fig. 7.5) consists of two-part, a circulator and a matched termination. The circulator is a three-port ferromagnetic device to control the microwave propagation to a designed direction within a circuit.

For example, a signal entering port 1 can transmit to port 2. Similarly, the incident signal at port 2 can be delivered to port 3. However, the wave that arrives at port 3 is directly dissipated since the termination device exists at the end of port 3. It prevents the excessive redirected signal that may induce amplifier damage.

In short, the purpose of this combined device is not only to manage the directivity of the incident flow but also to guarantee amplifier safety under the endurance limit.

- Frequency response: 8-18 GHz
- Isolation: 15 dB
- Insertion loss: Max. 0.5 dB
- VSWR: 1.40 : 1
- Maximum average power: 250 W
- Maximum peak power: 2 kW

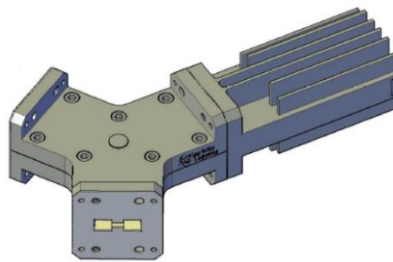


Fig. 7.5: WRD750D24 isolator: termination combined circulator.

- Waveguide Directional coupler

The WR90 directional coupler (Fig. 7.6) has been imposed for microwave experiments to analyze the forward or backward power from the cavity. It can decrease the power delivered at the rate of the coupling indicated on the specification to measure by the instrument without damage.

- Frequency response: 8.2-12.4 GHz
- Directivity: Min. 35 dB
- Coupling: 20 ± 0.5 dB



Fig. 7.6: WR90 waveguide directional coupler.

- Coaxial Directional coupler

The 779D directional coupler (Fig. 7.7) produced by Agilent Technologies was used for the microwave experiment to figure out the forward or backward power from the microwave resonator. It can decrease the power delivered at a coupling ratio, indicated in the specification, to prevent the instrument's damage.

- Frequency range: 1.7 to 12.4 GHz
- Nominal coupling: $20 \text{ dB} \pm 0.75 \text{ dB}$
- Directivity: $> 30 \text{ dB}$ for 1.7 to 4 GHz, $> 26 \text{ dB}$ for 4 to 12.4 GHz
- Maximum SWR: 1.2
- Insertion loss: $< 0.60 \text{ dB}$
- Power rating average, Peak: 50 W, 250 W
- Connectors: primary line 1-N(m), 1-N(f); auxiliary arm N(f)
- Weight: 2 lb; Size: 114.3 mm (4.5 in) H x 25.4 mm (1.0 in) W x 196.9 mm (7.75 in) L

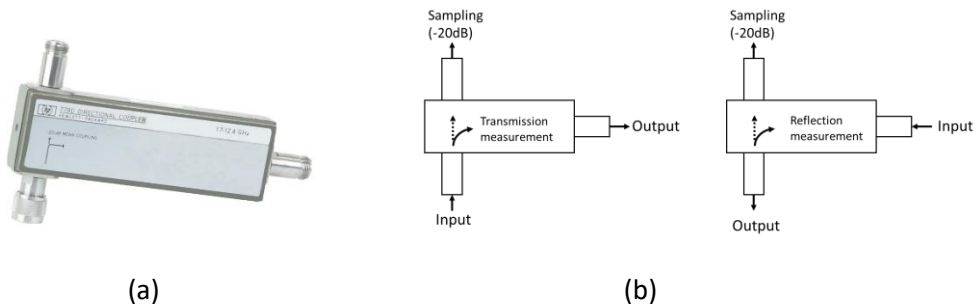


Fig. 7.7: 779D coaxial directional coupler - HP (a) with the connected direction (Forward & Reverse) (b).

- Adaptor

A quarter wavelength adaptor (Fig. 7.8) is applied to the system to convert the waveguide to coax. A remarkable specification of the part used for the experiment is described below.

- Size: WR-90
- Coax connector impedance: 50 Ω
- Coax connector: N type, Female
- Frequency range: 8.2~12.4 GHz
- Max. VSWR: 1.20 : 1
- Max. power capacity: 50W

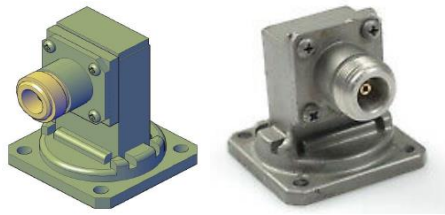


Fig. 7.8: WR 90 waveguide to coax adapter.

- Vector Network Analyzer

The vector network analyzer is an essential instrument to measure the S-parameter relating to the reflection and transmission of the electrical network. The Agilent 8720D VNA (Fig. 7.9) manufactured by HP works in the range of frequencies from 50 MHz to 20 GHz with a resolution of 100 kHz. This analyzer has been used to evaluate the customized microwave resonator in terms of the coupling, Q-factor, and even the signal generator source. It can not only extract the amplitude and the phase data every time by change of the impedance difference resulting from the loaded materials but also cover the frequency range from 50 MHz up to 20 GHz. With this analyzer, it is possible to control the signal entering the cavity by a Lab-view program via the GPIB interface while monitoring is running. Moreover, it facilitates tracking the resonance frequency down automatically in real-time.



Fig. 7.9: Agilent 8720D Vector network analyzer.

- Attenuator

Measurement instruments such as oscilloscopes and VNA are required to evaluate the reflection or transmission signal. Both measurement systems have a maximal voltage capacity, which results in a power limitation, to avoid damage. For example, the crystal detector that rectifies the alternating current signal is very vulnerable to power capacity. Therefore, an attenuator has been placed before the receive port of the measurement instrument to protect against a system's breakdown. For safety reasons, a general rule of thumb is to match the sum of the entire attenuations to the maximal amplification generated from the amplifier.

4. HPLC Pump

The LS class HPCL pump (Fig. 7.10) consisted of single-headed positive displacement piston pumps incorporating advanced cam designs. The micro-stepping motor was used for the droplet generation to secure exceptionally low pulsation. It can control the liquid feeding rate from a container into the nozzle with 0.2% RSD in full ranges of enabling flow rate. An in-line filter of 0.5 μm rating is included at the output port of the pump for dispensing liquid in general laboratory use.

A detailed specification follows below,

- Flow rate: 0.001 ~ 5.000 ml·min⁻¹
- Pressure accuracy: ± 2 % of full scale pressure
- Pressure zero offset: ± 2 psi
- Flow accuracy: within 2 % of set flow rate
- Pulsation: ≤ 2 % @ 1 ml·min⁻¹ and 1000 psi
- Operation environment: ambient temperature of 10 to 30 °C
relative humidity of 20 to 90 %



Fig. 7.10: LS class HPCL pump - Teledyne SSI.

5. Stroboscope

An electronic stroboscope 1538-A (Fig. 7.11) supplied by the General Radio Company was used for capturing the dynamic micro droplet moving at a speed of $3 \text{ m} \cdot \text{s}^{-1}$.

This equipment is optimized not only for measuring the fast-moving device but also for observing stopping or slowing high-speed motion by the optical effect using the very short flash duration compared to the conventional stroboscope. The conditions that typically took a picture were flash duration of $0.8 \mu\text{s}$, the energy of 0.014 Ws^{-1} , and the beam intensity of 10^6 cd .

- Flash rates: 110 to 150,000 fpm with $\pm 1.0 \%$ accuracy
- Flash duration: 0.5 to $3.0 \mu\text{s}$
- Light output : beam width 10° at $\frac{1}{2}$ intensity points



(a)



(b)

Fig. 7.11: Stroboscope 1531-A (a) and an extension lamp - IET Labs (b).

Table 7.1: Specification of the stroboscope 1531-A.

| Flash / minute | Duration (us) | Energy (Ws^{-1}) | Beam intensity (cd) |
|----------------|---------------|-----------------------------|---------------------|
| At 690 | 3 | 0.5 | 15×10^6 |
| At 4170 | 1.2 | 0.09 | 5×10^6 |
| At 25,000 | 0.8 | 0.014 | 10^6 |
| At 150,000 | 0.5 | 0.0023 | 0.16×10^6 |

7.2 Impedance matching by Vector Network Analyzer

In this study, Agilent8720D (HP) is used to measure the S_{11} parameter representing the reflection coefficient at an input port, to determine the coupling status of the waveguide to the cavity. This instrument is capable of covering all X-band ranges (8 ~ 12 GHz) and is conjugated for acquiring both magnitude and phase data coming back from the system. The maximum designation numbers representing the highest resolution are up to 1601 points with 800 μ m sweep time. It can also be utilized as a microwave signal generator with a power of up to 21 dBm. Before the operation of VNA, this machine should be calibrated each time in the range the user wants to test for characterization. The calibration kit working in the range from 0 to 18 GHz can calibrate the VNA with charges supplied from the kit (short, open, load). The Smith-chart is adequately used to certify the calibration quality of VNA in impedance mode. For an open circuit, the voltage generated from VNA is reflected with the same phase of an incident wave so that the open circuit is placed on the right side of the Smith-chart (reflection coefficient, $\Gamma = +1$, and normalized impedance, $z = \infty$). The short circuit appears at the far left of the Smith-chart's circle because the reflected voltage should cancel the incident voltage (180 °); for this reason, only the zero potential has remained (reflection coefficient, $\Gamma = -1$, and normalized impedance, $z = 0$). Lastly, the load is settled in the middle of the Smith-chart circle (reflection coefficient, $\Gamma = 0$, and normalized impedance, $z = 1$). It implies that the critical coupling is successfully taking place between the loaded kit (in this case, 50 Ω) and VNA. In other words, there is no reflection from the load.

The reflection coefficient is expressed as

$$\Gamma = \frac{V^-}{V^+} = \frac{R_L - Z_c}{R_L + Z_c}, \quad (7-1)$$

where R_L is resistive load and Z_c is the characteristic impedance of transmission line connected with VNA, respectively. Moreover, V^+ and V^- state the amplitudes of the forward and reflected waves.

Short-Circuit : $R_L = 0$

$$\Gamma = \frac{R_L - Z_c}{R_L + Z_c} = \frac{0 - Z_c}{0 + Z_c} = -1. \quad (7-2)$$

Open-Circuit : $R_L = \infty$

$$\Gamma = \frac{R_L - Z_c}{R_L + Z_c} = \frac{1 - \frac{Z_c}{R_L}}{1 + \frac{Z_c}{R_L}} = 1. \quad (7-3)$$

Matched-Circuit : $R_L = Z_c$

$$\Gamma = \frac{R_L - Z_c}{R_L + Z_c} = \frac{Z_c - Z_c}{Z_c + Z_c} = 0. \quad (7-4)$$

Chapter 8 Conclusion and Outlook

A new feeding system for additive manufacturing has been explored, it is based on the generation of droplets containing particle suspensions and drying of these. Such systems should eventually improve the resolution of conventional direct energy deposition (DED) below 20 microns by developing a new powder production and transport system before the laser sintering process. Specifically, to increase the precision of the AM process, PSI suggested the liquid droplet-based powder production concept consisting of droplet generation and microwave drying. The fundamental idea is derived from the internal gelation technique using X-band microwaves developed to produce the Sphere-Pac fuel in the nuclear industry. In that process, the flying distance of the drops across the resonator is over 100 mm and the drop size ranges from 0.2 to 2 mm. Shortening the distance while simultaneously reducing the drop's diameter below 0.2mm with keeping the heating efficiency at the same time is the main challenge of miniaturization of such an applicator being designed for an additive manufacturing process. The here presented work is therefore regarded as the most challenging venture among all SFA-AM projects.

This chapter consists of two sections, 1) a summary of findings based on the meaningful results, and 2) recommended research topics not covered in this thesis.

8.1 Conclusion

In the present work, a comprehensive collection of mechanisms toward high-resolution 3D printing is investigated, in particular, a technique based on focused powder transportation.

A liquid-based raw material (precursor dissolved solution) as a material container is proposed to increase the metal 3D printing precision instead of the conventional powder-based approach, owing to the advantage of ejected material size controllability without clogging the nozzle. The whole thesis consists of two parts:

1. development of a device allowing the generation of a stable and reproducible train of monodisperse droplets and
2. development of a miniaturized microwave resonator for the heating/drying of in-flight droplets.

Droplet generation :

The first part of this thesis is devoted to evaluating a customized, vibrating droplet generator based on a permanent-magnetic shaker. The system allows the setting and control of different droplet sizes depending on parameters, such as the frequency, flow rate, and nozzle size. With the final setup, a size-controlled droplet of about 100 μm could be obtained, the main factor to guarantee the process reliability for precise, high resolution additive manufacturing. Furthermore, an analytical principle to formulate the droplets has been proven by experimental results in terms of size, speed and gap distance. In addition, Navier-Stoke's based hydrodynamic simulations were performed using OpenFoam. These supported the findings, identified in the experimental data. As a final result the optimal conditions, for generating the smallest reliable droplets, have been identified at a flow rate of $0.5 \text{ ml}\cdot\text{min}^{-1}$ and a frequency of 15 kHz.

Microwave device:

The second part focuses on the development of a miniaturized microwave resonator that demonstrates a strong coupling between the sample and electromagnetic energy. Generally, the need for miniaturization of such devices has emerged from the technological progress, with very specialized and space limited applications. In particular, this technology is employed by microfluidics or lab-on-chip-based industry in the chemical and biological fields (i.e., ten to hundreds of micrometers).

New coaxial resonator:

Design: a new coaxial resonator, operating in the X-band, has been designed and investigated to achieve the project requirements in terms of sensing and heating applications. The main differences from a traditional open coaxial probe are as follows:

- Firstly an extended metal wall structure is introduced, covering the sensing area, to confine the electric field to a capacitive gap.
- Secondly a movable central conductor enables the controllability of both, the resonance frequency and the E-field concentration at the sample location.

The working mechanism is the electric field perturbation, where a dielectric introduced in the gap will change both, the resonance frequency and the Q-factor. This coaxial resonator is designed to operate as a $\frac{3}{4}$ wavelength resonator with TEM (Transverse Electro-Magnetic) mode, and the phase-matching method is utilized as a sensing principle. Furthermore, a full-wave electromagnetic simulation confirms the working principle, based on the finite integration time domain solver with the eigenmode solver using the software CST microwave studio.

Testing: the dielectric properties of various water-ethanol mixtures in the volume range of nanoliters, loaded through a microcapillary, were investigated.

These sample-dependent variations are analyzed to estimate the complex permittivity by various methods, such as perturbation (PM), least-squares model (LSM), and log-linear model (LLM). All processed permittivities are compared with reference data obtained from a commercially available open coaxial probe (HP 85070B) to select an appropriate method representing the sensing performance. The results acquired from both PM and LSM with a 100 μm capillary show a well corresponding trend to the reference data with a tolerance of 12.7% compared to the conventional mixing rule. It means that a small volume of sample can be detected by this resonator even if it only affects a part of the sensing area (in this research $< 0.15\%$).

Microwave heating:

A modified conventional cylindrical cavity and the newly developed coaxial resonator were configured and examined to understand their heating efficiency. However, the cylindrical cavity could not make the high-speed ($\approx 3\text{ m}\cdot\text{s}^{-1}$) droplets attain a sufficiently high temperature during the short E-field exposure time (time for passing through $\approx 6.7\text{ ms}$). Therefore, the latter is more concretely studied.

In the case of the coaxial resonator, after a certain distance, the water droplets showed a volume decrease, which was proportional to the applied microwave power. A temperature difference of 30 K was achieved when setting the power to 45 W, and for a microwave exposure time of 0.5 ms. In addition, the evaporation rate was quantified by Mathematica[®] image processing with the basic theory of evaporation focusing on heat and mass transfer. It is possible to further improve the increase in temperature, by changing the microwave resonator design to a waveguide-based structure, and therefore extend the power capacity. Another alternative would be the increase in interaction time. The temperature increase could be cross-checked from the cooling and heating side.

Achievement of the project goal:

The SFA project research goal is the clarification of potential for a modified metal AM technology into widespread industrial applications. The improvement of the modification lies in satisfying both, high productivity and resolution, by having an aqueous material feed.

The research of the present thesis is concerned with the important step of transforming the aqueous stream into a powder for the laser processing, using microwave heating. Water is the most challenging medium, as other precursors potentially absorb more energy and are easier to be evaporated. Therefore the water based feed is studied here as the most conservative case. As partial drying could be achieved, this work represents a good basis for the project goal.

8.2 Future work

Several directions of research, related to the microwave technology for efficiently heating up microscopic droplets, remain open. Some interesting topics are suggested below.

1. One of the recommendations relevant to this thesis is to demonstrate the real-time evaporation rate of the inflight droplet that could not be fully covered. With decreasing size, evaporative cooling is an increasingly dominant factor, and importantly influences the droplet size as well as the temperature distribution compared to the other heat transfer. How the primarily volumetric heating of microwaves affects the droplet evaporation with the key factors like the surface tension and the evaporative cooling effect at high-speed, is an attractive topic. The energy interaction between the dynamic droplets within its train is an important subject worthy to be explored, as it also influences the chemical reaction, for example, gelation.
2. The second topic is the real-time sensing and monitoring for the dynamic sample characterization. If the coupling between the sample and microwave resonator is strong enough, the sample's dielectric characteristics can affect the electromagnetic field, resulting in the reflected signal alteration. For example, the specified range of the condition for the homogeneous droplet generation can be established by microwave sensing based on the size and the gap distance. Even if the exact value can not be extracted directly, It would be beneficial if the quality management of the droplet production is possible without the visualization of each sequence. To validate the feasibility of this approach, preliminary tests were performed. The MW resonator was investigated with water at various flow rates in terms of real-time monitoring ability.

Fig. 8.1 shows both, the resonant frequency and magnitude of the reflection coefficients, obtained from a vector network analyzer following the procedure described in Fig. 5.17 on page 88.

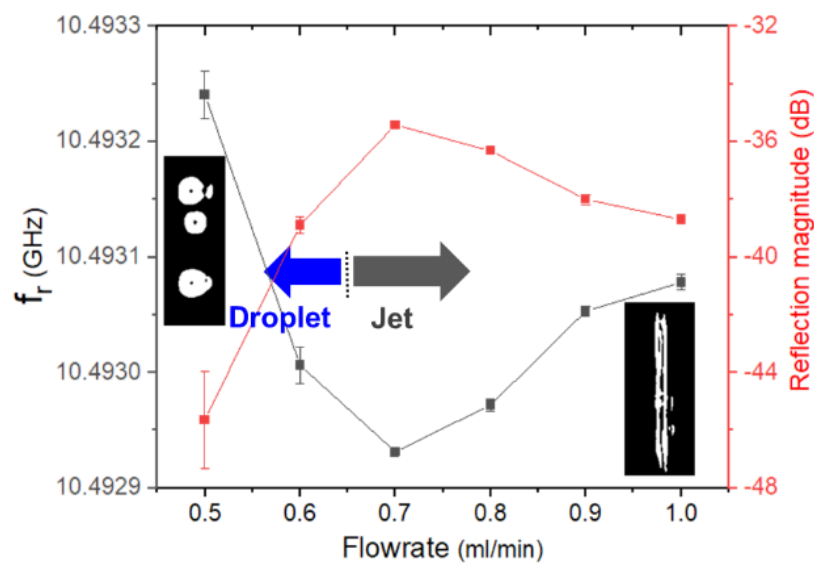


Fig. 8.1: Reflected signal changes as a function of various water flow rates.

Measurements in all cases were repeated ten times for reliability. The research idea is motivated by the concept that a microwave resonator can statistically distinguish a droplet flow that contains sufficient air gaps between the droplets from a continuous flow, using the reflected microwave signal. A flow consisting of water droplets and air gives rise to an alteration of the resonance frequency since the volume interfered with the electric field is changed in the time sequence; on the other hand, the continuous flow does not induce a comparable variation. Jet transitions can be expected to occur between flow rates of $0.6 \text{ ml}\cdot\text{min}^{-1}$ and $0.7 \text{ ml}\cdot\text{min}^{-1}$. Coupling can be also evaluated in the S_{11} magnitude. For example, a flow rate of $0.5 \text{ ml}\cdot\text{s}^{-1}$ touches the critical coupling and switches to under-coupling as the flow rate increases. The resonant frequency rising again at flow rates above $0.7 \text{ ml}\cdot\text{min}^{-1}$ may be attributable to the higher flow speed, producing the non-uniform jet in the axial direction, and also resulting in a thinner flow at the initial point. In addition, a hydrophobic nozzle could contribute to a slim jet formation with a high exit velocity.

3. Another recommendation is using a water-based jet in medical industry (e.g. needle-free injection). Technological advancements in this field look promising nowadays, even more so during the COVID-19 pandemic, which also call for further optimization. For the high-speed injection, a piezo-, mechanical vibrator-, and laser-based power source can be used to inject the medication, resulting in needle-less dermal penetration. The microwave has many advantages that meet this application's requirement since the X-band wave is efficient for water based medium in power absorption that can transform microwave energy into heat. In addition, by controlling the frequency, the injection volume relevant to the driving force is changed, and it is also possible to realize the repetitive jet, by fulfilling the resonance at certain filling factors. Fig. 8.2 shows an example tested in the condition of $0.4 \text{ ml}\cdot\text{min}^{-1}$ with 11 W power with a $250 \text{ }\mu\text{m}$ tube in diameter.

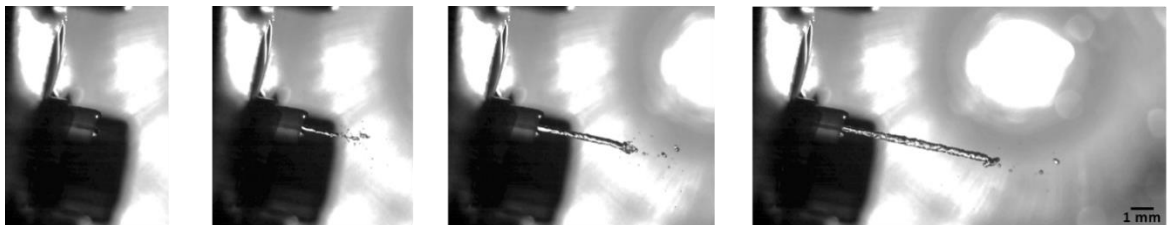


Fig. 8.2: Possibility for the needle-free injection ($\Delta t = 0.4 \text{ ms}$, total $t = 1.2 \text{ ms}$).

Chapter 9 Appendix

9.1 Cavity Perturbation

The cavity perturbation theory is used for several purposes, for example, the heating cavity whose volume can be modified. In detail, either the movable wall or screws inserted can change the internal volume of the microwave cavity and result in the alteration of the resonance frequency depending on the experimental condition. Another application is typically applied to find out the dielectric properties of tiny materials loaded in the cavity by measuring the resonance behavior variations. Nevertheless, in most cases, the loaded material should be relatively small. For example, in the case of a cylindrical cavity with the same shape as loading materials, the radius of loaded materials should be smaller than 1/10 of the cavity radius because the perturbation method is designed based on the electromagnetic-field approximation. It assumes that the actual strength of the electromagnetic field does not change much once the introduced sample size is relatively small compared to the cavity's internal volume [93].

9.1.1 Material Perturbation

Material perturbation is caused by changes in permittivity or permeability due to the filling material in the cavity.

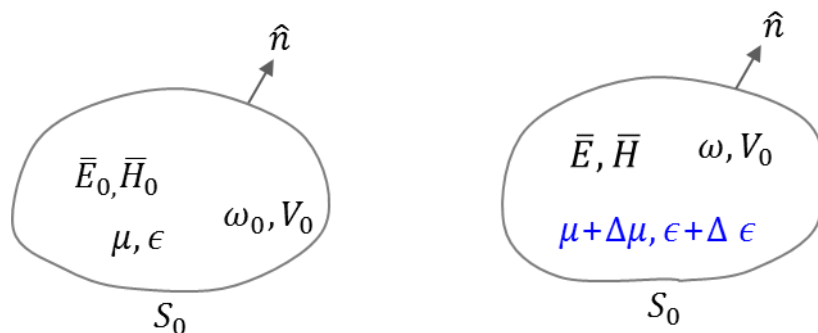


Fig. 9.1: Material perturbation.

Specifically, Faraday's law and Maxwell-Ampere's law in the overall Maxwell's equations can be expressed as follows for both empty and material-loaded cavities:

$$\begin{aligned}
\nabla \times \bar{E}_0 &= -j\omega_0\mu\bar{H}_0, \\
\nabla \times \bar{H}_0 &= j\omega_0\epsilon\bar{E}_0, \\
\nabla \times \bar{E} &= -j\omega(\mu + \Delta\mu)\bar{H}, \\
\nabla \times \bar{H} &= j\omega(\epsilon + \Delta\epsilon)\bar{E},
\end{aligned} \tag{9-1}$$

where $\Delta\epsilon$ and $\Delta\mu$ represent the change of both permittivity and permeability due to the introduced samples resulting in cavity perturbation. And \bar{E}_0 , \bar{H}_0 , \bar{E} , and \bar{H} are the electromagnetic field of the original cavity and the perturbed cavity, respectively. ω_0 and ω stand for the resonant frequency before and after the perturbation.

By multiplying \bar{H} , \bar{E} , \bar{H}_0^* , \bar{E}_0^* on conjugates (*) of (9-1), it can be rewritten as

$$\begin{aligned}
\bar{H} \cdot \nabla \times \bar{E}_0^* &= j\omega_0\mu\bar{H}_0^* \cdot \bar{H}, \\
\bar{E} \cdot \nabla \times \bar{H}_0^* &= -j\omega_0\epsilon\bar{E}_0^* \cdot \bar{E}, \\
\bar{H}_0^* \cdot \nabla \times \bar{E} &= -j\omega(\mu + \Delta\mu)\bar{H}_0^* \cdot \bar{H}, \\
\bar{E}_0^* \cdot \nabla \times \bar{H} &= j\omega(\epsilon + \Delta\epsilon)\bar{E}_0^* \cdot \bar{E}.
\end{aligned} \tag{9-2}$$

After subtraction of obtained equations, a couple of equations are derived based on vector identity

$$\begin{aligned}
\nabla \cdot (\bar{E}_0^* \times \bar{H}) &= j\omega_0\mu\bar{H}_0^* \cdot \bar{H} - j\omega(\epsilon + \Delta\epsilon)\bar{E}_0^* \cdot \bar{E}, \\
\nabla \cdot (\bar{E} \times \bar{H}_0^*) &= j\omega_0\epsilon\bar{E}_0^* \cdot \bar{E} - j\omega(\mu + \Delta\mu)\bar{H}_0^* \cdot \bar{H}.
\end{aligned} \tag{9-3}$$

These equations are added to each other and then integrated over the volume of V_0 .

According to the divergence theorem

$$\begin{aligned}
\int_{V_0} \nabla \cdot (\bar{E}_0^* \times \bar{H} + \bar{E} \times \bar{H}_0^*) dv &= \oint_{S_0} (\bar{E}_0^* \times \bar{H} + \bar{E} \times \bar{H}_0^*) \cdot d\bar{s} \\
&= j \int_{V_0} (\omega_0\mu\bar{H}_0^* \cdot \bar{H} - \omega(\mu + \Delta\mu)\bar{H}_0^* \cdot \bar{H} + \omega_0\epsilon\bar{E}_0^* \cdot \bar{E} - \omega(\epsilon + \Delta\epsilon)\bar{E}_0^* \cdot \bar{E}) dv = 0.
\end{aligned} \tag{9-4}$$

By the relation of normal vector $\hat{n} \times \bar{E} = 0$ on the closed surface S_0 , this surface integral should be zero.

As a result, it can be represented in the form of an equation

$$\frac{\omega - \omega_0}{\omega} = \frac{-\int_{V_0} (\Delta\epsilon \bar{E}_0^* \cdot \bar{E} + \Delta\mu \bar{H}_0^* \cdot \bar{H}) dv}{\int_{V_0} (\epsilon \bar{E}_0^* \cdot \bar{E} + \mu \bar{H}_0^* \cdot \bar{H}) dv}. \quad (9-5)$$

However, it is not possible to accurately determine the actual electromagnetic field, \bar{E} , and \bar{H} . It is thus approximated as an unperturbed electric and magnetic field as well as resonance frequency by substituting \bar{E}_0 , \bar{H}_0 , and ω_0 .

Consequently, the equation well known for the perturbation method is obtained as

$$\frac{\omega - \omega_0}{\omega_0} \approx \frac{-\int_{V_0} (\Delta\epsilon |\bar{E}_0|^2 + \Delta\mu |\bar{H}_0|^2) dv}{\int_{V_0} (\epsilon |\bar{E}_0|^2 + \mu |\bar{H}_0|^2) dv}. \quad (9-6)$$

The equation (9-6) means that any increase of ϵ or μ results in a decrease in the cavity resonance frequency.

9.1.2 Shape Perturbation

The shape perturbation is usually utilized for understanding their relevance to the cavity volume modulation by introducing screws or movable-wall. It is also derived from Maxwell's curl equations:

$$\begin{aligned} \nabla \times \bar{E}_0 &= -j\omega_0\mu\bar{H}_0, \\ \nabla \times \bar{H}_0 &= j\omega_0\epsilon\bar{E}_0, \\ \nabla \times \bar{E} &= -j\omega\mu\bar{H}, \\ \nabla \times \bar{H} &= j\omega\epsilon\bar{E}, \end{aligned} \quad (9-7)$$

where $\bar{E}_0, \bar{H}_0, \omega_0, \bar{E}, \bar{H}$, and ω represent the electromagnetic field and resonance frequency of the original cavity, as well as the electromagnetic field and resonance frequency of the perturbed cavity, respectively.

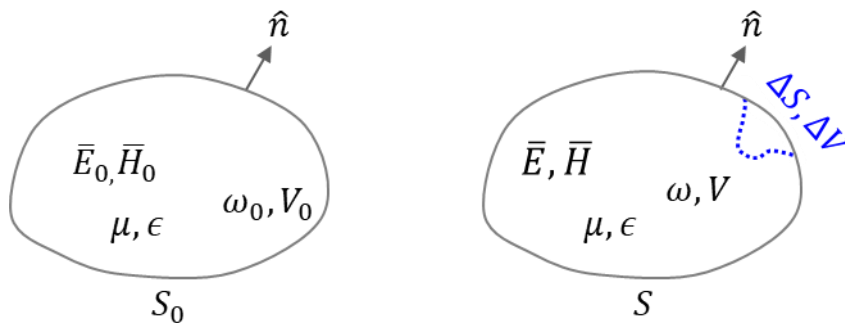


Fig. 9.2: Shape perturbation.

Identical to the stated procedure in materials perturbation, it can be reformulated by multiplying \bar{H} , \bar{E} , \bar{H}_0^* , and \bar{E}_0^* on conjugates (*) of (9-7)

$$\bar{H} \cdot \nabla \times \bar{E}_0^* = j\omega_0 \mu \bar{H}_0^* \cdot \bar{H},$$

$$\bar{E} \cdot \nabla \times \bar{H}_0^* = -j\omega_0 \epsilon \bar{E}_0^* \cdot \bar{E},$$

$$\bar{H}_0^* \cdot \nabla \times \bar{E} = -j\omega \mu \bar{H}_0^* \cdot \bar{H},$$

$$\bar{E}_0^* \cdot \nabla \times \bar{H} = j\omega \epsilon \bar{E}_0^* \cdot \bar{E}.$$

(9-8)

After subtraction of obtained equations above, two formulas are derived using vector identity

$$\nabla \cdot (\bar{E}_0^* \times \bar{H}) = j\omega_0 \mu \bar{H}_0^* \cdot \bar{H} - j\omega \epsilon \bar{E}_0^* \cdot \bar{E},$$

$$\nabla \cdot (\bar{E} \times \bar{H}_0^*) = -j\omega \mu \bar{H}_0^* \cdot \bar{H} + j\omega_0 \epsilon \bar{E}_0^* \cdot \bar{E}.$$

(9-9)

Combine both equations and then integrate them over the volume of V .

According to the divergence theorem

$$\begin{aligned} \int_V \nabla \cdot (\bar{E} \times \bar{H}_0^* + \bar{E}_0^* \times \bar{H}) dv &= \oint_S (\bar{E} \times \bar{H}_0^* + \bar{E}_0^* \times \bar{H}) \cdot d\bar{s} = \oint_S \bar{E}_0^* \times \bar{H} \cdot d\bar{s} \\ &= -j(\omega - \omega_0) \int_V (\epsilon \bar{E}_0^* \cdot \bar{E} + \mu \bar{H}_0^* \cdot \bar{H}) dv. \end{aligned}$$

(9-10)

By the relation of $\hat{n} \times \bar{E} = 0$ on the perturbed surface S ,

$$S = S_0 - \Delta S,$$

$$\oint_S \bar{E}_0^* \times \bar{H} \cdot d\bar{s} = \oint_{S_0} \bar{E}_0^* \times \bar{H} \cdot d\bar{s} - \oint_{\Delta S} \bar{E}_0^* \times \bar{H} \cdot d\bar{s} = - \oint_{\Delta S} \bar{E}_0^* \times \bar{H} \cdot d\bar{s}.$$

(9-11)

By the relation of $\hat{n} \times \bar{E}_0 = 0$ on S_0

$$(\omega - \omega_0) = \frac{-j \oint_{\Delta S} \bar{E}_0^* \times \bar{H} \cdot d\bar{s}}{\int_V (\epsilon \bar{E}_0^* \cdot \bar{E} + \mu \bar{H}_0^* \cdot \bar{H}) dv}.$$

(9-12)

However, the electric field \bar{E} , magnetic field \bar{H} , and resonance frequency ω , are still unknown once the cavity is perturbed, hence both \bar{E} and \bar{H} are approximated as \bar{E}_0 and \bar{H}_0 , respectively in the case of the very small ΔS

$$\oint_{\Delta S} \bar{E}_0^* \times \bar{H} \cdot d\bar{s} \approx \oint_{\Delta S} \bar{E}_0^* \times \bar{H}_0 \cdot d\bar{s} = \int_{\Delta V} (j\omega_0 \mu |\bar{H}_0|^2 - j\omega_0 \epsilon |\bar{E}_0|^2) dv. \quad (9-13)$$

The perturbation method is derived as

$$\frac{\omega - \omega_0}{\omega_0} \approx \frac{\int_{\Delta V} (\mu |\bar{H}_0|^2 - \epsilon |\bar{E}_0|^2) dv}{\int_{V_0} (\mu |\bar{H}_0|^2 + \epsilon |\bar{E}_0|^2) dv} = \frac{\Delta W_m - \Delta W_e}{W_m + W_e}. \quad (9-14)$$

The derived final equation form states that the total energy of the perturbed cavity is regarded as the stored energy in the unperturbed one.

In (9-14), W_m and W_e indicate magnetic and electric energy stored in the cavity. Moreover, ΔW_m , and ΔW_e stand for the changes in the stored magnetic and electric energy due to the perturbation. The resonant frequency can move with volume change according to (9-14).

9.2 Quality Factor

The resonance appears when the stored average magnetic energy (W_m) in the inductor L is the same as the stored average electric energy (W_e) in the capacitor C ,

The angular resonance frequency is defined as

$$\omega_0 = \frac{1}{\sqrt{LC}}. \quad (9-15)$$

Another meaningful parameter for the resonance circuit is Q , called the Quality factor, expressed as

$$Q = 2\pi \frac{\text{Total stored energy}}{\text{Dissipated energy/Cycle}} = \omega \frac{W_m + W_e}{P_l}, \quad (9-16)$$

where P_l indicates the total dissipated energy in the resonator.

A measurement of the response sharpness of a resonator to external excitation is the quality factor representing the loss of a resonant circuit [93]. The lower loss implies a higher Q-factor, and higher losses degrade the Q-factor [130].

If the energy dissipates because of the wall and a dielectric located in the cavity, the unloaded Q-factor, Q_0 , is introduced. It is worth noting that this factor is an intrinsic value without considering the external power source and is given by

$$Q_0 = 2\pi \frac{\text{Total stored energy}}{\text{Dissipated energy in the wall and dielectric/Cycle}} = \omega \frac{W_m + W_e}{P_s + P_w}, \quad (9-17)$$

P_s , and P_w are the powers that dissipated because of the wall and dielectric in the cavity, respectively.

For the empty cavity without any dielectric, the factor of P_w is neglected.

The characteristics of the cavity should take into account the influence of the external circuit expressed as

$$Q_{ex} = 2\pi \frac{\text{Total stored energy}}{\text{Dissipated energy in the external circuit/Cycle}} = \omega \frac{W_m + W_e}{P_{ex}}, \quad (9-18)$$

P_{ex} is the energy dissipation in the external circuit. The loaded Q-factor is consequently defined as

$$Q_L = \omega \frac{W_m + W_e}{P_s + P_w + P_{ex}}. \quad (9-19)$$

The relationship between the loaded Q-factor and unloaded Q-factor is summarized as

$$\frac{1}{Q_L} = \frac{1}{Q_0} + \frac{1}{Q_{ex}}. \quad (9-20)$$

The Q-factor is alternatively determined as the ratio of a resonator's center frequency of f_r or ω_r to its half-power bandwidth Δf or $\Delta\omega$ using the general expression as

$$Q = \frac{f_r}{\Delta f} = \frac{\omega_r}{\Delta\omega}. \quad (9-21)$$

9.3 EM-Field Distribution of Microwave Cavity

9.3.1 Rectangular cavity [130]

a. TE Mode

The abbreviation of the TE mode means the transversal electric mode to the wave propagation direction, e.g., z-axis in Fig. 5.2 (a), so that the electric field in the z-axis is zero, $E_z = 0$.

The general solution for the longitudinal magnetic field component $h_z(x, y)$ in two dimensions is

$$h_z(x, y) = (A \cos k_x x + B \sin k_x x)(C \cos k_y y + D \sin k_y y). \quad (9-22)$$

Applying boundary conditions of the electric field component on the rectangular plate's side wall in the direction of both the x-and y-axis, the tangential component on the waveguide wall will be zero

$$\begin{aligned} e_x(x, y) &= 0, \text{ at } y = 0, b, \\ e_y(x, y) &= 0, \text{ at } x = 0, a. \end{aligned} \quad (9-23)$$

From Maxwell's curl equations,

$$\begin{aligned} e_x &= \frac{-j\omega\mu k_y}{k_c^2} (A \cos k_x x + B \sin k_x x)(-C \sin k_y y + D \cos k_y y), \\ e_y &= \frac{-j\omega\mu k_x}{k_c^2} (-A \sin k_x x + B \cos k_x x)(C \cos k_y y + D \sin k_y y). \end{aligned} \quad (9-24)$$

The final solution H_z is obtained by employing the above boundary conditions (9-23) to (9-24)

$$H_z(x, y, z) = A_{mn} \cos \frac{m\pi x}{a} \cos \frac{n\pi y}{b} e^{-j\beta z}. \quad (9-25)$$

The meaning of m and n corresponds to the number of antinodes in the standing wave pattern present inside the rectangular cavity along the x and y directions, respectively.

The transverse and longitudinal field of TE mode can be summarized as

$$\begin{aligned} E_x &= \frac{j\omega\mu n\pi}{k_c^2 b} A_{mn} \cos \frac{m\pi x}{a} \sin \frac{n\pi y}{b} e^{-j\beta z}, \\ E_y &= -\frac{j\omega\mu m\pi}{k_c^2 a} A_{mn} \sin \frac{m\pi x}{a} \cos \frac{n\pi y}{b} e^{-j\beta z}, \\ E_z &= 0, \\ H_x &= \frac{j\beta m\pi}{k_c^2 a} A_{mn} \sin \frac{m\pi x}{a} \cos \frac{n\pi y}{b} e^{-j\beta z}, \\ H_y &= \frac{j\beta n\pi}{k_c^2 b} A_{mn} \cos \frac{m\pi x}{a} \sin \frac{n\pi y}{b} e^{-j\beta z}, \\ H_z &= A_{mn} \cos \frac{m\pi x}{a} \cos \frac{n\pi y}{b} e^{-j\beta z}, \\ m &= 0, 1, 2, \dots / n = 0, 1, 2, \dots, \end{aligned} \quad (9-26)$$

where A_{mn} is an arbitrary amplitude constant dominated by the magnitude of incident power and wave-number in the x- and y-axis directions, respectively. a and b indicate the width and height of the waveguide. The propagation constant β_z in the z-direction and cutoff wavenumber k_c are dealt with later.

The expression above is for the waveguide mode that both ends are opened-structure for the traveling wave. In order to realize the cavity mode, in which both ends are closed, the additional boundary condition relevant to the z-direction should be taken into consideration as $E_x = E_y = 0$, at $z = 0, d$.

The parameter d dictates the length of the cavity along the z-axis.

The electromagnetic fields inside the cavity are expressed as

$$\begin{aligned}
 E_x &= \frac{\omega \mu n \pi}{k_c^2 b} A_{mn} \cos \frac{m \pi x}{a} \sin \frac{n \pi y}{b} \sin \frac{l \pi z}{d}, \\
 E_y &= -\frac{\omega \mu m \pi}{k_c^2 a} A_{mn} \sin \frac{m \pi x}{a} \cos \frac{n \pi y}{b} e^{-j \beta z} \sin \frac{l \pi z}{d}, \\
 E_z &= 0, \\
 H_x &= \frac{j m l \pi^2}{k_c^2 a d} A_{mn} \sin \frac{m \pi x}{a} \cos \frac{n \pi y}{b} \cos \frac{l \pi z}{d}, \\
 H_y &= \frac{j n l \pi^2}{k_c^2 b d} A_{mn} \cos \frac{m \pi x}{a} \sin \frac{n \pi y}{b} \cos \frac{l \pi z}{d}, \\
 H_z &= -j A_{mn} \cos \frac{m \pi x}{a} \cos \frac{n \pi y}{b} \sin \frac{l \pi z}{d}, \\
 m &= 0, 1, 2, \dots // n = 0, 1, 2, \dots // l = 1, 2, 3, \dots
 \end{aligned}
 \tag{9-27}$$

b. TM mode

The abbreviation of the TM mode means the transversal magnetic mode based upon the wave propagation direction, e.g., z-axis in Fig. 5.2 (a), so that the magnetic field in the direction of the z-axis is zero, $H_z = 0$.

The general solution for the longitudinal electric field component $e_z(x, y)$ in two dimensions is

$$e_z(x, y) = (A \cos k_x x + B \sin k_x x)(C \cos k_y y + D \sin k_y y).
 \tag{9-28}$$

The electric field component, $e_z(x, y)$, will be zero at the rectangular plate's side wall in both the x- and y-axis direction

$$e_z(x, y) = 0, \text{ at } x = 0, a,$$

$$e_z(x, y) = 0, \text{ at } y = 0, b.$$

$$\tag{9-29}$$

The transverse and longitudinal field of TM mode can be summarized as

$$\begin{aligned}
E_x &= -\frac{j\beta m\pi}{k_c^2 a} B_{mn} \cos \frac{m\pi x}{a} \sin \frac{n\pi y}{b} e^{-j\beta z}, \\
E_y &= -\frac{j\beta n\pi}{k_c^2 b} B_{mn} \sin \frac{m\pi x}{a} \cos \frac{n\pi y}{b} e^{-j\beta z}, \\
E_z &= B_{mn} \sin \frac{m\pi x}{a} \sin \frac{n\pi y}{b} e^{-j\beta z}, \\
H_x &= \frac{j\omega\epsilon n\pi}{k_c^2 b} B_{mn} \sin \frac{m\pi x}{a} \cos \frac{n\pi y}{b} e^{-j\beta z}, \\
H_y &= -\frac{j\omega\epsilon m\pi}{k_c^2 a} B_{mn} \cos \frac{m\pi x}{a} \sin \frac{n\pi y}{b} e^{-j\beta z}, \\
H_z &= 0, \\
m &= 1, 2, 3, \dots // n = 1, 2, 3, \dots,
\end{aligned}
\tag{9-30}$$

where B_{mn} is an incident power related constant. The parameters, a , b , and d indicate the width, height, and length of the cavity or the waveguide.

The additional boundary condition, $E_x = E_y = 0$, at $z = 0, d$, represents the perfectly conducting end-plates in the z -direction.

$$\begin{aligned}
E_x &= -\frac{lm\pi^2}{k_c^2 ad} B_{mn} \cos \frac{m\pi x}{a} \sin \frac{n\pi y}{b} \sin \frac{l\pi z}{d}, \\
E_y &= -\frac{ln\pi^2}{k_c^2 bd} B_{mn} \sin \frac{m\pi x}{a} \cos \frac{n\pi y}{b} \sin \frac{l\pi z}{d}, \\
E_z &= B_{mn} \sin \frac{m\pi x}{a} \sin \frac{n\pi y}{b} \cos \frac{l\pi z}{d}, \\
H_x &= \frac{j\omega\epsilon n\pi}{k_c^2 b} B_{mn} \sin \frac{m\pi x}{a} \cos \frac{n\pi y}{b} \cos \frac{l\pi z}{d}, \\
H_y &= -\frac{j\omega\epsilon m\pi}{k_c^2 a} B_{mn} \cos \frac{m\pi x}{a} \sin \frac{n\pi y}{b} \cos \frac{l\pi z}{d}, \\
H_z &= 0, \\
m &= 1, 2, 3, \dots // n = 1, 2, 3, \dots // l = 0, 1, 2, \dots
\end{aligned}
\tag{9-31}$$

For understanding both TE and TM mode expressions, several equations are given as described below. The cutoff wavenumber is expressed as

$$k_c = \sqrt{(m\pi/a)^2 + (n\pi/b)^2}.$$

(9-32)

The propagation constant β is

$$\beta = \sqrt{k^2 - k_c^2} = \sqrt{\omega^2 \epsilon \mu - \left(\left(\frac{m\pi}{a}\right)^2 + \left(\frac{n\pi}{b}\right)^2\right)}. \quad (9-33)$$

Therefore, the cut-off frequency f_c is derived as follows

$$f_c = \frac{c}{2\pi\sqrt{\epsilon\mu}} \sqrt{\left(\frac{m\pi}{a}\right)^2 + \left(\frac{n\pi}{b}\right)^2}. \quad (9-34)$$

The dominant mode as the lowest cut-off frequency of TE mode is TE₁₀ and the cut-off frequency is given by

$$f_{c\text{TE}10} = \frac{c}{2a\sqrt{\epsilon\mu}}. \quad (9-35)$$

The dominant mode of TM mode is TM₁₁ and the cutoff frequency applicable is

$$f_{c\text{TM}11} = \frac{c}{2\pi\sqrt{\epsilon\mu}} \sqrt{\left(\frac{\pi}{a}\right)^2 + \left(\frac{\pi}{b}\right)^2}. \quad (9-36)$$

Extending the concept from the waveguide to both TE and TM resonant modes of the cavity, equations are changed as described below.

The resonant wavenumber is expressed as

$$k_0 = \sqrt{(m\pi/a)^2 + (n\pi/b)^2 + (l\pi/d)^2}. \quad (9-37)$$

The propagation constant β turns into resonant constant β_0 as

$$\beta_0 = \sqrt{k^2 - k_0^2} = \sqrt{\omega^2 \epsilon \mu - \left(\left(\frac{m\pi}{a}\right)^2 + \left(\frac{n\pi}{b}\right)^2 + \left(\frac{l\pi}{d}\right)^2\right)}. \quad (9-38)$$

Therefore, the resonant frequency f_0 is

$$f_0 = \frac{c}{2\pi\sqrt{\epsilon\mu}} \sqrt{\left(\frac{m\pi}{a}\right)^2 + \left(\frac{n\pi}{b}\right)^2 + \left(\frac{l\pi}{d}\right)^2}. \quad (9-39)$$

The dominant mode of the rectangular cavity corresponding to the lowest cut-off frequency for both TE and TM modes are TE₁₀₁ and TM₁₁₀ when the dimensions meet the requirement of $b < a < d$ along each axis.

9.3.2 Cylindrical cavity [130]

The circular resonator employs a cylindrical coordinate system to simplify the cavity's structure, as the rectangular resonator introduced the cartesian coordinate system. The derivation starts from the circular waveguide with the closed metal wall at both ends, similar to the rectangular cavity. Here, only cavity mode is presented without the waveguide-related equations.

c. TE & TM Mode

The transverse and longitudinal field of TE mode ($E_z = 0$) can be summarized as

$$\begin{aligned}
 E_\rho &= \frac{\omega\mu m}{k_c'^2 \rho} A_{mn} \sin(m\phi) J_m(k_c' \rho) \sin\left(\frac{l\pi z}{d}\right), \\
 E_\phi &= \frac{\omega\mu}{k_c'^2} A_{mn} \cos(m\phi) J_m'(k_c' \rho) \sin\left(\frac{l\pi z}{d}\right), \\
 E_z &= 0, \\
 H_\rho &= -\frac{j l \pi}{k_c'^2 d} A_{mn} \cos(m\phi) J_m'(k_c' \rho) \cos\left(\frac{l\pi z}{d}\right), \\
 H_\phi &= \frac{j m l \pi}{k_c'^2 \rho d} A_{mn} \sin(m\phi) J_m(k_c' \rho) \cos\left(\frac{l\pi z}{d}\right), \\
 H_z &= -j A_{mn} \cos(m\phi) J_m(k_c' \rho) \sin\left(\frac{l\pi z}{d}\right), \\
 m &= 0, 1, 2, \dots // n = 1, 2, 3, \dots // l = 1, 2, 3, \dots
 \end{aligned}
 \tag{9-40}$$

The transverse and longitudinal field of TM mode ($H_z = 0$) can be described as

$$\begin{aligned}
 E_\rho &= -\frac{l\pi}{k_c d} B_{mn} \cos(m\phi) J_m'(k_c \rho) \sin\left(\frac{l\pi z}{d}\right), \\
 E_\phi &= \frac{m l \pi}{k_c^2 \rho d} B_{mn} \sin(m\phi) J_m(k_c \rho) \sin\left(\frac{l\pi z}{d}\right), \\
 E_z &= B_{mn} \cos(m\phi) J_m(k_c \rho) \cos\left(\frac{l\pi z}{d}\right), \\
 H_\rho &= -\frac{j \omega \epsilon m}{k_c^2 \rho} B_{mn} \sin(m\phi) J_m(k_c \rho) \cos\left(\frac{l\pi z}{d}\right), \\
 H_\phi &= -\frac{j \omega \epsilon}{k_c} B_{mn} \cos(m\phi) J_m'(k_c \rho) \cos\left(\frac{l\pi z}{d}\right), \\
 H_z &= 0, \\
 m &= 0, 1, 2, \dots // n = 1, 2, 3, \dots // l = 0, 1, 2, \dots
 \end{aligned}
 \tag{9-41}$$

The cutoff wavenumber for both TE and TM modes are expressed as

$$k_{cTE} = \frac{P'_{mn}}{a},$$

$$k_{cTM} = \frac{P_{mn}}{a},$$

(9-42)

where P'_{mn} , P_{mn} and a dictate the n -th zero of the derivative ($J'_m(x)$) of the Bessel function of the first kind $J_m(x)$, n -th zero of the Bessel function of the first kind ($J_m(x)$), and the radius of the cavity. ϵ , μ and d respectively represent the permittivity, permeability, and the height of the cavity.

A_{mn} , and B_{mn} are constants related to the incident power.

The propagation constant β is,

$$\beta = \sqrt{k^2 - \frac{P'_{mn}}{a}} \text{ for TE mode,}$$

$$\beta = \sqrt{k^2 - \frac{P_{mn}}{a}} \text{ for TM mode, } (k = \omega\sqrt{\mu\epsilon}).$$

(9-43)

Therefore, the cut-off frequency f_c is derived from

$$f_c = \frac{c}{2\pi\sqrt{\epsilon\mu}} \left(\frac{P'_{mn}}{a} \right) \text{ for TE mode,}$$

$$f_c = \frac{c}{2\pi\sqrt{\epsilon\mu}} \left(\frac{P_{mn}}{a} \right) \text{ for TM mode.}$$

(9-44)

Extending the concept from the waveguide to both TE and TM resonant modes of the cavity, equations are changed as described below.

The resonant wavenumber is expressed as,

$$k_0 = \sqrt{(P'_{mn}/a)^2 + (l\pi/d)^2} \text{ for TE mode}$$

$$k_0 = \sqrt{(P_{mn}/a)^2 + (l\pi/d)^2} \text{ for TM mode}$$

(9-45)

Therefore, the resonant frequency f_0 is derived as follows,

$$f_0 = \frac{c}{2\pi\sqrt{\epsilon_r\mu_r}} \sqrt{\left(\frac{P'_{mn}}{a} \right)^2 + \left(\frac{l\pi}{d} \right)^2} \text{ for TE mode,}$$

$$f_0 = \frac{c}{2\pi\sqrt{\epsilon_r\mu_r}} \sqrt{\left(\frac{P_{mn}}{a} \right)^2 + \left(\frac{l\pi}{d} \right)^2} \text{ for TM mode.}$$

(9-46)

The dominant mode of the cylindrical cavity corresponding to the lowest cut-off frequency for both TE and TM modes are TE_{111} and TM_{110} . Fig. 5.6 on page 80 is useful to design the cylindrical cavity since it informs the lower order resonant modes, as well as excitation modes at a given frequency, for a given dimension [130].

9.3.3 Bessel Function

The Bessel function is a generalized sine function that can be used in cylindrical or spherical coordinates to find separable solutions to the Laplace equation and the Helmholtz equation. These functions are particularly important for solving the problems involving wave propagation, for example, electromagnetic waves in a cylindrical waveguide or cavity.

Bessel functions of the first kind, $J_m(x)$, are obtained from the Bessel differential equation:

$$x^2 \frac{d^2 y}{dx^2} + x \frac{dy}{dx} + (x^2 - m^2)y = 0.$$

(9-47)

These solutions, $J_m(x)$, are finite at the origin ($x = 0$), nonsingular, and some examples are described in Fig. 9.3 for $m = 0, 1, 2, 3$. Every zero points of the function gives the values for the EM field calculation of the TE_{mn} or TM_{mn} mode.

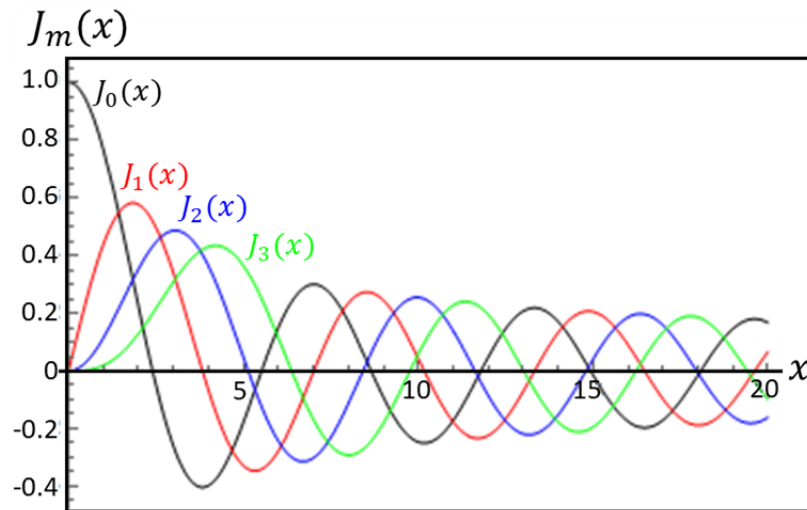


Fig. 9.3: Bessel function of the first order $J_m(x)$, $m = 0, 1, 2, 3$.

Table 9.1: Bessel function of the first kind $J_m(x)$ and its derivative $J'_m(x)$.

| Zeros P_{mn} ($J_m(P_{mn}) = 0, n = 1, 2, 3 \dots$) | | | | | | Zeros P'_{mn} of derivative ($J'_m(P'_{mn}) = 0, n = 1, 2, 3 \dots$) | | | | | |
|---|---------|---------|---------|---------|---------|--|---------|---------|---------|---------|---------|
| | n = 1 | n = 2 | n = 3 | n = 4 | n = 5 | | n = 1 | n = 2 | n = 3 | n = 4 | n = 5 |
| m = 0 | 2.4048 | 5.5201 | 8.6537 | 11.7951 | 14.931 | m = 0 | 3.8317 | 7.0156 | 10.1735 | 13.3237 | 16.4706 |
| m = 1 | 3.8317 | 7.0156 | 10.1743 | 13.3237 | 16.4706 | m = 1 | 1.8412 | 5.3314 | 8.5363 | 11.706 | 14.8636 |
| m = 2 | 5.1356 | 8.4172 | 11.6198 | 14.796 | 17.9598 | m = 2 | 3.0542 | 6.7061 | 9.9695 | 13.1704 | 16.3475 |
| m = 3 | 6.3802 | 9.761 | 13.0152 | 16.2235 | 19.4094 | m = 3 | 4.2012 | 8.0152 | 11.3459 | 14.5858 | 17.7887 |
| m = 4 | 7.5883 | 11.0647 | 14.3725 | 17.616 | 20.8269 | m = 4 | 5.3176 | 9.2824 | 12.6819 | 15.9641 | 19.196 |
| m = 5 | 8.7715 | 12.3386 | 15.7002 | 18.9801 | 22.2178 | m = 5 | 6.4156 | 10.5199 | 13.9872 | 17.3128 | 20.5755 |
| m = 6 | 9.9361 | 13.5893 | 17.0038 | 20.3208 | 23.5861 | m = 6 | 7.5013 | 11.7349 | 15.2682 | 18.6374 | 21.9317 |
| m = 7 | 11.0864 | 14.8213 | 18.2876 | 21.6415 | 24.9349 | m = 7 | 8.5778 | 12.9324 | 16.5294 | 19.9419 | 23.2681 |
| m = 8 | 12.2251 | 16.0378 | 19.5545 | 22.9452 | 26.2668 | m = 8 | 9.6474 | 14.1155 | 17.774 | 21.2291 | 24.5872 |
| m = 9 | 13.3543 | 17.2412 | 20.807 | 24.2339 | 27.5837 | m = 9 | 10.7114 | 15.2867 | 19.0046 | 22.5014 | 25.8913 |
| m = 10 | 14.4755 | 18.4335 | 22.047 | 25.5094 | 28.8874 | m = 10 | 11.7709 | 16.4479 | 20.223 | 23.7607 | 27.182 |

Table 9.1 describes the zeros of the Bessel function of the first kind, $J_m(x)$, and its derivative, $J'_m(x)$, respectively. These values can be utilized for resolving the EM field equations of the cylindrical cavity in Chapter 5.3. Here, P_{mn} is the n -th zero of the Bessel function of order m in case of TM modes, or the n -th zero of the derivative of the Bessel function of order m , P'_{mn} in case of TE modes,

9.4 Microwave Numerical Solution

9.4.1 FDTD (Finite Differential Time Domain)[31]

The concept of FDTD has been introduced firstly by K. S. Yee [185] to solve the electromagnetic scattering based on the Maxwell curl equation in space as well as time. In particular, the FDTD is specialized for time domain calculation with 3D central differential approximation. The energy propagates through the mesh, and the leapfrog method by time is prime differentiates among the FDTD and other methodologies.

The central numerical derivatives are used for the finite difference approximation based on (9-48)

$$\left. \frac{\partial f}{\partial x} \right|_{x_0} = \frac{f(x_0 + \Delta x) - f(x_0 - \Delta x)}{2\Delta x} + O[(\Delta x)^2]. \quad (9-48)$$

The function of both space and time is discretized according to Yee's definition

$$f^n[i, j, k] = f(i\delta, j\delta, k\delta, n\delta t), \quad (9-49)$$

where $\delta = \delta x = \delta y = \delta z$ is the space increment along the x, y, and z-axis, on the other hand, δt denotes the incremental time step. i, j, k , and n are integers. Using (9-48) of space and time derivatives that are second-order accurate in δ and δt , respectively,

$$\begin{aligned} \frac{\partial f^n(i, j, k)}{\partial x} &= \frac{f^n\left(i + \frac{1}{2}, j, k\right) - f^n\left(i - \frac{1}{2}, j, k\right)}{\delta} + O(\delta^2) \\ \frac{\partial f^n(i, j, k)}{\partial t} &= \frac{f^{n+\frac{1}{2}}(i, j, k) - f^{n-\frac{1}{2}}(i, j, k)}{\delta t} + O(\delta t^2). \end{aligned} \quad (9-50)$$

As (9-50) described, the electric-magnetic field components are calculated at an alternate half-time step. The new value of field distribution at any meshes is estimated from the previous value and another field vector at adjacent positions of the previous value.

For the convergence of the numerical analysis with reasonable accuracy, δ should follow the rule of (9-51) corresponding to the Courant condition

$$\delta t \leq \frac{1}{v_{max}} \left(\frac{1}{\partial x^2} + \frac{1}{\partial y^2} + \frac{1}{\partial z^2} \right)^{-1/2}, \quad (9-51)$$

where v_{max} dictates the maximum wave phase velocity in the model.

It represents that the energy in free space was not violating the light speed. In other words, the wave analysis is not going over to the neighboring mesh before the completion of spatial calculation at the previous mesh.

9.4.2 FEM (Finite Element Method)[31]

The FEM method is a representative numerical simulation method applied not only for electromagnetics but also for heat transfer, fluid dynamics, and strength/stiffness analysis. In particular, the use of subdivided mesh formation to express complex geometries and inhomogeneous materials has been very advantageous. An adaptively refined mesh regime can help to define specialized domains with reasonable computer resources. This method discretized the subdomain from the entire problem for ease of calculation and combined all the results for solving the system-based problems.

The first method of the FEM numerical solution adopts the nodal elements of the understructure meshes to find the electromagnetic solution out. However, it is not suitable for getting the field solution for the interfaces where the different materials are in contact with each other due to the continuity of the spatial variable.

The edge-based method that can only consider tangential field components across the interface between different substances emerged to improve feasibility. The element, which consists of different orders and rules for obtaining acceptable results (e.g., convergence), depends on the relationship between the number of orders and wavelength.

(First-order: at least 10 elements per wavelength // Second-order: at least 5 elements per wavelength)

Analytical solvers can also be classified into three methodologies: time domain, frequency domain, and eigenvalue analysis, and details are covered in Chapter 9.4.3, "CST Simulation."

9.4.3 CST Simulation

The CST (Computer Simulation Technology) Studio Suite® is a powerful and user-friendly 3D electromagnetic analysis software package for designing, analyzing, and optimizing electromagnetic components and systems.

The solver and excitation port used to validate both the resonance frequency and electric field distribution of the new resonator are introduced here.

a. Transient solver

This solver is generally called a Time-domain solver based on the FIT (Finite Integration Technique) method proposed by Weiland in 1976 [186]. The time-domain FIT is equivalent to FDTD on Cartesian grids.

It discretized a set of Maxwell equations on a time-grid space to solve the various electromagnetic problems ranging from the static field to high-frequency applications in the time-domain or frequency-domain. The calculation is conducted step by step in time through Maxwell's Grid equation and Leap-Frog scheme. In short, the former substitutes the time derivatives by the central differences to output an explicit update formulation of the loss-free case. The calculation variables are given by electric voltages and magnetic fluxes placed alternately in time as a well-known leap-frog scheme. For instance, the magnetic flux at $t = (n + 1) \Delta t$ is computed from the magnetic flux at the previous time step $t = n \Delta t$, and from the electric voltage at half a time step before, at $t = (n + 1/2) \Delta t$ as shown in Fig. 9.4.

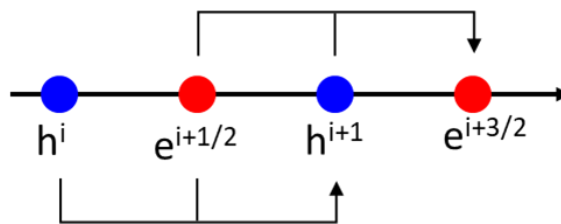


Fig. 9.4: Leap-frog scheme of transient solver.

To avoid any stability problem, the time step should satisfy the Courant-Friedrichs-Levy (CFL)-criterion as

$$\Delta t \leq \frac{\sqrt{\epsilon\mu}}{\sqrt{\left(\frac{1}{\Delta x}\right)^2 + \left(\frac{1}{\Delta y}\right)^2 + \left(\frac{1}{\Delta z}\right)^2}}.$$

(9-52)

It prohibits energy in free space violating the speed of light, already described in (9-51).

This solver is beneficial for obtaining the simulation results in the broad frequency range because it only needs a single computation run. The Fast Fourier Transform (FFT) allows it to show the frequency response. Specifically, this solver is efficient in acquiring a solution for the large dimension or open boundaries and the high-frequency application such as connectors, transmission lines, and antennas.

b. Frequency-domain solver

This solver is suitable for electromagnetic simulations of small sizes or narrow bands, especially when the size of the structure is much smaller than the shortest wavelength. Another application is for the calculation of arbitrary periodic boundaries. A unique feature of this solver is the ability to support hexahedral and tetrahedral grids together, allowing for a more realistic definition of surfaces or boundaries of structures. As a result, it can increase accuracy and speed. The frequency-domain solver also contains the calculation of the S-parameter and Z-matrix similar to the transient solver and is more proper for the highly resonant structure like filters.

c. Eigenmode solver

The primary purpose is to compute the structure's eigenmodes and the corresponding eigenvalues.

This solver calculates a finite number of modal field distributions in closed devices. Since the modes contain all available information related to the system intrinsically, it does not consider the excitation port and the definition of the monitors.

There are two methods available for users: advanced Krylov Subspace (AKS) and Jacoby Davidson Method (JDM), built on different mathematical foundations. The former is suitable for many calculation modes due to the processing speed (usually more than 5), and the latter shows a robust and accurate solution but is more time-consuming.

d. Waveguide port

A typical waveguide port that can stimulate and absorb the energy is employed for representing the coaxial cable. This mode is advantageous in the reflection aspect since it moves out of the defined structure towards the boundary and does not interact again with the trapped wave in the resonator. The excitation mode is automatically defined as a TEM mode, a fundamental mode of the coax, meaning the electric field flows from

the central conductor to the outer conductor. Therefore, this port is helpful, especially for the near-field simulation to obtain an accurate S-parameter.

Port size setting is one of the most important factors to consider in simulation. However, a size covering the entire coaxial cable cross-section is sufficient to acquire an adequate result.

References

- [1] "ASTM F2792 - 12a Standard Terminology for Additive Manufacturing Technologies' (Withdrawn 2015)." <https://compass.astm.org/Standards/WITHDRAWN/F2792.htm> (accessed Oct. 02, 2019).
- [2] N. Travitzky, A. Bonet, B. Dermeik, T. Fey, I. Filbert-Demut, L. Schlier, T. Schlordt, and P. Greil, "Additive Manufacturing of Ceramic-Based Materials," *Adv. Eng. Mater.*, vol. 16, no. 6, pp. 729–754, 2014, doi: 10.1002/adem.201400097.
- [3] "Additive Manufacturing of Ceramics: Issues, Potentialities, and Opportunities - Zocca - 2015 - Journal of the American Ceramic Society - Wiley Online Library." <https://ceramics.onlinelibrary.wiley.com/doi/full/10.1111/jace.13700> (accessed Mar. 19, 2022).
- [4] S. C. Ligon, R. Liska, J. Stampfl, M. Gurr, and R. Mülhaupt, "Polymers for 3D Printing and Customized Additive Manufacturing," *Chem. Rev.*, vol. 117, no. 15, pp. 10212–10290, Aug. 2017, doi: 10.1021/acs.chemrev.7b00074.
- [5] F. P. W. Melchels, M. A. N. Domingos, T. J. Klein, J. Malda, P. J. Bartolo, and D. W. Huttmacher, "Additive manufacturing of tissues and organs," *Prog. Polym. Sci.*, vol. 37, no. 8, pp. 1079–1104, Aug. 2012, doi: 10.1016/j.progpolymsci.2011.11.007.
- [6] W. E. Frazier, "Metal Additive Manufacturing: A Review," *J. Mater. Eng. Perform.*, vol. 23, no. 6, pp. 1917–1928, Jun. 2014, doi: 10.1007/s11665-014-0958-z.
- [7] Y. Zhai, D. A. Lados, and J. L. LaGoy, "Additive Manufacturing: Making Imagination the Major Limitation," *JOM*, vol. 66, no. 5, pp. 808–816, May 2014, doi: 10.1007/s11837-014-0886-2.
- [8] R. A. Sobieszek, "Sculpture as the Sum of its Profiles: François Willème and Photosculpture in France, 1859–1868," *Art Bull.*, vol. 62, no. 4, pp. 617–630, Dec. 1980, doi: 10.1080/00043079.1980.10787818.
- [9] "Manufacture of contour relief-maps," US473901A, May 03, 1892 Accessed: Mar. 19, 2022. [Online]. Available: <https://patents.google.com/patent/US473901A/en>
- [10] B. Ralph, "Method of making decorative articles," US1533300A, Apr. 14, 1925 Accessed: Mar. 19, 2022. [Online]. Available: <https://patents.google.com/patent/US1533300A/en>
- [11] T. Wohlers and T. Gornet, "History of additive manufacturing," p. 34, 2014.
- [12] J. J. Lewandowski and M. Seifi, "Metal Additive Manufacturing: A Review of Mechanical Properties," *Annu. Rev. Mater. Res.*, vol. 46, no. 1, pp. 151–186, 2016, doi: 10.1146/annurev-matsci-070115-032024.
- [13] "Figure 1: ASTM F2792-12A [9] standard terminology for additive...", *ResearchGate*. https://www.researchgate.net/figure/ASTM-F2792-12A-9-standard-terminology-for-additive-manufacturing-processes-with_fig2_284359253 (accessed Oct. 02, 2019).
- [14] J.-Y. Lee, J. An, and C. K. Chua, "Fundamentals and applications of 3D printing for novel materials," *Appl. Mater. Today*, vol. 7, pp. 120–133, Jun. 2017, doi: 10.1016/j.apmt.2017.02.004.
- [15] D. L. Bourell, "Perspectives on Additive Manufacturing," *Annu. Rev. Mater. Res.*, vol. 46, no. 1, pp. 1–18, Jul. 2016, doi: 10.1146/annurev-matsci-070115-031606.
- [16] L. Hirt, A. Reiser, R. Spolenak, and T. Zambelli, "Additive Manufacturing of Metal Structures at the Micrometer Scale," *Adv. Mater.*, vol. 29, no. 17, p. 1604211, 2017, doi: 10.1002/adma.201604211.
- [17] D. Behera, S. Chizari, L. A. Shaw, M. Porter, R. Hensleigh, Z. Xu, X. Zheng, L. G. Connolly, N. K. Roy, R. M. Panas, S. K. Saha, X. (Rayne) Zheng, J. B. Hopkins, S.-C. Chen, and M. A. Cullinan, "Current challenges and potential directions towards precision microscale additive manufacturing – Part IV: Future perspectives," *Precis. Eng.*, vol. 68, pp. 197–205, Mar. 2021, doi: 10.1016/j.precisioneng.2020.12.014.
- [18] "Rapid manufacturing of metallic objects | Emerald Insight." <https://www.emerald.com/insight/content/doi/10.1108/13552541211231644/full/html?fullSc=1> (accessed Mar. 30, 2022).
- [19] R. D. Farahani, K. Chizari, and D. Therriault, "Three-dimensional printing of freeform helical microstructures: a review," *Nanoscale*, vol. 6, no. 18, pp. 10470–10485, 2014, doi: 10.1039/C4NR02041C.

- [20] D. Ding, Z. Pan, D. Cuiuri, and H. Li, "Wire-feed additive manufacturing of metal components: technologies, developments and future interests," *Int. J. Adv. Manuf. Technol.*, vol. 81, no. 1, pp. 465–481, Oct. 2015, doi: 10.1007/s00170-015-7077-3.
- [21] S. H. Mok, G. Bi, J. Folkes, and I. Pashby, "Deposition of Ti–6Al–4V using a high power diode laser and wire, Part I: Investigation on the process characteristics," *Surf. Coat. Technol.*, vol. 202, no. 16, pp. 3933–3939, May 2008, doi: 10.1016/j.surfcoat.2008.02.008.
- [22] J. P. Kruth, "Material Ingress Manufacturing by Rapid Prototyping Techniques," *CIRP Ann.*, vol. 40, no. 2, pp. 603–614, Jan. 1991, doi: 10.1016/S0007-8506(07)61136-6.
- [23] L. J. Kumar and C. G. Krishnadas Nair, "Current Trends of Additive Manufacturing in the Aerospace Industry," in *Advances in 3D Printing & Additive Manufacturing Technologies*, D. I. Wimpenny, P. M. Pandey, and L. J. Kumar, Eds. Singapore: Springer, 2017, pp. 39–54. doi: 10.1007/978-981-10-0812-2_4.
- [24] M. Javaid and A. Haleem, "Additive manufacturing applications in medical cases: A literature based review," *Alex. J. Med.*, vol. 54, no. 4, Art. no. 4, 2018, doi: 10.4314/bafm.v54i4.
- [25] M. Vaezi, H. Seitz, and S. Yang, "A review on 3D micro-additive manufacturing technologies," *Int. J. Adv. Manuf. Technol.*, vol. 67, no. 5, pp. 1721–1754, Jul. 2013, doi: 10.1007/s00170-012-4605-2.
- [26] J. Gockel, L. Sheridan, B. Koerper, and B. Whip, "The influence of additive manufacturing processing parameters on surface roughness and fatigue life," *Int. J. Fatigue*, vol. 124, pp. 380–388, Jul. 2019, doi: 10.1016/j.ijfatigue.2019.03.025.
- [27] J. Gardan, "Additive manufacturing technologies: State of the art and trends," in *Additive Manufacturing Handbook*, CRC Press, 2017.
- [28] B. Dutta and F. H. (Sam) Froes, "The Additive Manufacturing (AM) of titanium alloys," *Met. Powder Rep.*, vol. 72, no. 2, pp. 96–106, Mar. 2017, doi: 10.1016/j.mprp.2016.12.062.
- [29] E. Atzeni and A. Salmi, "Economics of additive manufacturing for end-usable metal parts," *Int. J. Adv. Manuf. Technol.*, vol. 62, no. 9–12, pp. 1147–1155, Oct. 2012, doi: 10.1007/s00170-011-3878-1.
- [30] L. Meng, W. Zhang, D. Quan, G. Shi, L. Tang, Y. Hou, P. Breitzkopf, J. Zhu, and T. Gao, "From Topology Optimization Design to Additive Manufacturing: Today's Success and Tomorrow's Roadmap," *Arch. Comput. Methods Eng.*, vol. 27, no. 3, pp. 805–830, Jul. 2020, doi: 10.1007/s11831-019-09331-1.
- [31] T. V. C. T. Chan, "Understanding microwave heating cavities /," 2000.
- [32] P. A. Haas, J. M. Begovich, A. D. Ryon, and J. S. Vavruska, "Chemical flowsheet conditions for preparing urania spheres by internal gelation," Oak Ridge National Lab., ORNL/TM--6850, 1979. Accessed: Jul. 14, 2020. [Online]. Available: http://inis.iaea.org/Search/search.aspx?orig_q=RN:11499263
- [33] G. Ledergerber, "Improvements of the internal gelation process," *Trans. Am. Nucl. Soc.*, vol. 40 pp. 55–57, 1982, Accessed: Jul. 14, 2020. [Online]. Available: http://inis.iaea.org/Search/search.aspx?orig_q=RN:14788217
- [34] G. Ledergerber, "Internal gelation using microwaves," 1985, Accessed: Jul. 15, 2020. [Online]. Available: http://inis.iaea.org/Search/search.aspx?orig_q=RN:17019599
- [35] S. Yamagishi, "A new internal gelation process for fuel microsphere preparation without cooling initial solutions," *J. Nucl. Mater.*, vol. 254, no. 1, pp. 14–21, Mar. 1998, doi: 10.1016/S0022-3115(97)00351-6.
- [36] S. Yamagishi, T. Ogawa, and A. Hasegawa, "Development of a rapid gelation apparatus with microwave heating," Japan Atomic Energy Research Inst., JAERI-TECH--94-010, 1994. Accessed: Jul. 14, 2020. [Online]. Available: http://inis.iaea.org/Search/search.aspx?orig_q=RN:26001860
- [37] S. Yamagishi, T. Ogawa, and A. Hasegawa, "Performance test of a vertically-directed electric-field cavity resonator made for the rapid gelation apparatus with microwave heating," Japan Atomic Energy Research Inst., JAERI-TECH--96-026, 1996. Accessed: Jul. 15, 2020. [Online]. Available: http://inis.iaea.org/Search/search.aspx?orig_q=RN:27072833
- [38] R. L. N. Beatty and K. J. Notz, "Gel-sphere-pac fuel for thermal reactors: assessment of fabrication technology and irradiation performance," Oak Ridge National Lab., TN (USA), ORNL-5469, Nov. 1979. doi: 10.2172/5863150.
- [39] A. Rosin, A. Schmidt, T. Gerdes, J. Somers, and M. Willert-Porada, "Microwave Assisted Internal Gelation of Droplets - A Case Study," in *Proceedings of the 10th International Conference on Microwave and High Frequency Heating*, 2005.

- [40] Y. Yong, M. T. Nguyen, H. Tsukamoto, M. Matsubara, Y.-C. Liao, and T. Yonezawa, "Effect of decomposition and organic residues on resistivity of copper films fabricated via low-temperature sintering of complex particle mixed dispersions," *Sci. Rep.*, vol. 7, no. 1, p. 45150, Mar. 2017, doi: 10.1038/srep45150.
- [41] Y. Choi, K. Seong, and Y. Piao, "Metal–Organic Decomposition Ink for Printed Electronics," *Adv. Mater. Interfaces*, vol. 6, no. 20, p. 1901002, 2019, doi: 10.1002/admi.201901002.
- [42] J. L. Collins and A. Chi, "Determination of Ideal Broth Formulations Needed to Prepare Hydrous Cerium Oxide Microspheres via the Internal Gelation Process," ORNL/TM-2009/007, 947141, Feb. 2009. doi: 10.2172/947141.
- [43] F. W. van der Bruggen, J. B. W. Kanij, A. J. Noothout, M. E. A. Hermans, and O. Votocek, "A U(VI)-PROCESS FOR MICROSPHERE PRODUCTION.," Keuring van Electrotechnische Materialen, N. V., Arnhem (Netherlands); Ceskoslovenska Akademie Ved, Rez. Ustav Jaderneho Vyzkumu, CONF-700502-, Oct. 1970. Accessed: Jul. 15, 2020. [Online]. Available: <https://www.osti.gov/biblio/4141085-vi-process-microsphere-production>
- [44] J. B. W. Kanij, A. J. Noothout, and O. Votocek, "The KEMA U(VI)-process for the production of UO₂ microspheres," 1974, Accessed: Jul. 15, 2020. [Online]. Available: http://inis.iaea.org/Search/search.aspx?orig_q=RN:5132968
- [45] P. A. Haas, K. J. Notz, and R. D. Spence, "Application of gel microsphere processes to preparation of Sphere-Pac nuclear fuel," Oak Ridge National Lab., TN (USA), CONF-780545-2, Jan. 1978. Accessed: Jul. 15, 2020. [Online]. Available: <https://www.osti.gov/biblio/6748784>
- [46] Y. HIROSE, "Vibration Compacted UO₂ Fuel,(III) Effects of Random Wave Vibration on Compacted Density," *J. Nucl. Sci. Technol.*, vol. 6, no. 7, pp. 351–358, Jul. 1969, doi: 10.1080/18811248.1969.9732906.
- [47] M. Pouchon, G. Ledergerber, F. Ingold, and K. Bakker, "Sphere-pac and vipac fuel," *Compr. Nucl. Mater.*, vol. 3, pp. 275–312, Dec. 2012, doi: 10.1016/b978-0-08-056033-5.00059-8.
- [48] A. S. Icenhour, "Sphere-Pac Evaluation for Transmutation," ORNL/TM-2005/41, 885954, May 2005. doi: 10.2172/885954.
- [49] J. L. Collins, M. H. Lloyd, and R. L. Fellows, "Effects of process variables on reaction mechanisms responsible for ADUN hydrolysis, precipitation, and gelation in the internal gelation gel-sphere process," ORNL/TM--8818, 707319, Apr. 1984. doi: 10.2172/707319.
- [50] Y. Rosen, R. Marrach, V. Gutkin, and S. Magdassi, "Thin Copper Flakes for Conductive Inks Prepared by Decomposition of Copper Formate and Ultrafine Wet Milling," *Adv. Mater. Technol.*, vol. 4, no. 1, p. 1800426, 2019, doi: 10.1002/admt.201800426.
- [51] N. A. Luechinger, E. K. Athanassiou, and W. J. Stark, "Graphene-stabilized copper nanoparticles as an air-stable substitute for silver and gold in low-cost ink-jet printable electronics," *Nanotechnology*, vol. 19, no. 44, p. 445201, Sep. 2008, doi: 10.1088/0957-4484/19/44/445201.
- [52] M. Joo, B. Lee, S. Jeong, and M. Lee, "Laser sintering of Cu paste film printed on polyimide substrate," *Appl. Surf. Sci.*, vol. 258, no. 1, pp. 521–524, Oct. 2011, doi: 10.1016/j.apsusc.2011.08.076.
- [53] H. Min, B. Lee, S. Jeong, and M. Lee, "Fabrication of 10μm-scale conductive Cu patterns by selective laser sintering of Cu complex ink," *Opt. Laser Technol.*, vol. 88, pp. 128–133, Feb. 2017, doi: 10.1016/j.optlastec.2016.09.021.
- [54] Y. S. Rosen, Y. Lidor, R. Balter, A. Szeskin, A. Awadallah, Y. Shacham-Diamand, and S. Magdassi, "Copper interconnections and antennas fabricated by hot-pressing printed copper formate," *Flex. Print. Electron.*, vol. 2, no. 3, p. 035007, Sep. 2017, doi: 10.1088/2058-8585/aa89bb.
- [55] D.-H. Shin, S. Woo, H. Yem, M. Cha, S. Cho, M. Kang, S. Jeong, Y. Kim, K. Kang, and Y. Piao, "A Self-Reducible and Alcohol-Soluble Copper-Based Metal–Organic Decomposition Ink for Printed Electronics," *ACS Appl. Mater. Interfaces*, vol. 6, no. 5, pp. 3312–3319, Mar. 2014, doi: 10.1021/am4036306.
- [56] A. Keller and F. Körösy, "Volatile Cuprous and Silver Salts of Fatty Acids," *Nature*, vol. 162, no. 4119, pp. 580–582, Oct. 1948, doi: 10.1038/162580a0.
- [57] M. A. Pouchon, "Aqueous Additive Production Method for the Fabrication of Ceramic and/or Metallic Bodies," Mar. 01, 2018 Accessed: Jul. 17, 2020. [Online]. Available: <https://patentscope.wipo.int/search/en/detail.jsf?docId=WO2018036813>

- [58] S. YAMAGISHI and Y. TAKAHASHI, "Sol-Gel Method Using Carbon Tetrachloride as Drop-Formation Medium for Producing Large ThO₂-Base Microspheres," *J. Nucl. Sci. Technol.*, vol. 22, no. 12, pp. 995–1000, Dec. 1985, doi: 10.1080/18811248.1985.9735755.
- [59] P. A. Hass, "Formation of liquid drops with uniform and controlled diameters at rates of 103 to 105 drops per minute," *AIChE J.*, vol. 21, no. 2, pp. 383–385, 1975, doi: 10.1002/aic.690210221.
- [60] S. Monsheimer, M. Grebe, and F.-E. Baumann, "Process for producing three-dimensional objects by means of microwave radiation," US7708929B2, May 04, 2010 Accessed: Oct. 02, 2019. [Online]. Available: [https://patents.google.com/patent/US7708929/en?q=\]+Sylvia+Monsheimer+et+al.%2c+%E2%80%9CProcess+for+producing+three-dimensional+objects+by+means+of++++microwave+radiation%2c%E2%80%9D+US7708929B2%2c+2010](https://patents.google.com/patent/US7708929/en?q=]+Sylvia+Monsheimer+et+al.%2c+%E2%80%9CProcess+for+producing+three-dimensional+objects+by+means+of++++microwave+radiation%2c%E2%80%9D+US7708929B2%2c+2010).
- [61] E. Jerby, Y. Meir, A. Salzberg, E. Aharoni, A. Levy, J. P. Torralba, and B. Cavallini, "Incremental metal-powder solidification by localized microwave-heating and its potential for additive manufacturing," *Addit. Manuf.*, vol. 6, pp. 53–66, Apr. 2015, doi: 10.1016/j.addma.2015.03.002.
- [62] M. Cabanes-Sempere, C. Cozzo, S. Vaucher, J. M. Catalá-Civera, and M. A. Pouchon, "Innovative production of nuclear fuel by microwave internal gelation: Heat transfer model of falling droplets," *Prog. Nucl. Energy*, vol. 57, pp. 111–116, May 2012, doi: 10.1016/j.pnucene.2011.12.011.
- [63] M. Cabanes-Sempere, J. M. Catalá-Civera, F. L. Peñaranda-Foix, C. Cozzo, S. Vaucher, and M. A. Pouchon, "Characterization method of dielectric properties of free falling drops in a microwave processing cavity and its application in microwave internal gelation," *Meas. Sci. Technol.*, vol. 24, no. 9, p. 095009, Aug. 2013, doi: 10.1088/0957-0233/24/9/095009.
- [64] M. Cabanes-Sempere, C. Cozzo, J. M. Catalá-Civera, F. L. Peñaranda-Foix, K. Ishizaki, S. Vaucher, and M. A. Pouchon, "Characterization of free falling drops inside a microwave cavity," in *2012 IEEE/MTT-S International Microwave Symposium Digest*, Jun. 2012, pp. 1–3. doi: 10.1109/MWSYM.2012.6259757.
- [65] F. SAVART, "Wemoire sur la constitution des veines liquids lancees par des orifices circulaires en mince paroi," *Ann Chim*, vol. 53, pp. 337–386, 1833.
- [66] "Review of stability of liquid jets and the influence of nozzle design - ScienceDirect." <https://www.sciencedirect.com/science/article/pii/S0300946774800213> (accessed Mar. 08, 2022).
- [67] J. A. F. Plateau, *Statique expérimentale et théorique des liquides soumis aux seules forces moléculaires*. Gauthier-Villars, 1873.
- [68] Lord Rayleigh, "On The Instability Of Jets," *Proc. Lond. Math. Soc.*, vol. s1-10, no. 1, pp. 4–13, 1878, doi: 10.1112/plms/s1-10.1.4.
- [69] C. WEBER, "Disintegration of Liquid Jets," *Z Angew Math Mech*, vol. 1, pp. 136–159, 1931.
- [70] B. Bonhoeffer, A. Kwade, and M. Juhnke, "Impact of Formulation Properties and Process Parameters on the Dispensing and Depositioning of Drug Nanosuspensions Using Micro-Valve Technology," *J. Pharm. Sci.*, vol. 106, no. 4, pp. 1102–1110, Apr. 2017, doi: 10.1016/j.xphs.2016.12.019.
- [71] B. Derby, "Inkjet Printing of Functional and Structural Materials: Fluid Property Requirements, Feature Stability, and Resolution," *Annu. Rev. Mater. Res.*, vol. 40, no. 1, pp. 395–414, Jun. 2010, doi: 10.1146/annurev-matsci-070909-104502.
- [72] N. Reis and B. Derby, "Ink Jet Deposition of Ceramic Suspensions: Modeling and Experiments of Droplet Formation," *MRS Online Proc. Libr. OPL*, vol. 625, ed 2000, doi: 10.1557/PROC-625-117.
- [73] C. Heinzen, A. Berger, and I. Marison, "Use of Vibration Technology for Jet Break-Up for Encapsulation of Cells and Liquids in Monodisperse Microcapsules," in *Fundamentals of Cell Immobilisation Biotechnology*, V. Nedović and R. Willaert, Eds. Dordrecht: Springer Netherlands, 2004, pp. 257–275. doi: 10.1007/978-94-017-1638-3_14.
- [74] C. Baumgarten, *Mixture Formation in Internal Combustion Engines*. Springer Science & Business Media, 2006.
- [75] E.-S. Chan, B.-B. Lee, P. Ravindra, and D. Poncelet, "Prediction models for shape and size of calcium alginate macrobeads produced through extrusion–dripping method," *J. Colloid Interface Sci.*, vol. 338, no. 1, pp. 63–72, Oct. 2009, doi: 10.1016/j.jcis.2009.05.027.
- [76] H. Teng, C. M. Kinoshita, and S. M. Masutani, "Prediction of droplet size from the breakup of cylindrical liquid jets," *Int. J. Multiph. Flow*, vol. 21, no. 1, pp. 129–136, Jan. 1995, doi: 10.1016/0301-9322(94)00053-M.

- [77] H. Brandenberger and F. Widmer, "A new multinozzle encapsulation/immobilisation system to produce uniform beads of alginate," *J. Biotechnol.*, vol. 63, no. 1, pp. 73–80, Jul. 1998, doi: 10.1016/S0168-1656(98)00077-7.
- [78] J. M. Schneider and C. D. Hendricks, "Source of Uniform-Sized Liquid Droplets," *Rev. Sci. Instrum.*, vol. 35, no. 10, pp. 1349–1350, Oct. 1964, doi: 10.1063/1.1718742.
- [79] H. Brandenberger, D. Nüssli, V. Piëch, and F. Widmer, "Monodisperse particle production: A method to prevent drop coalescence using electrostatic forces," *J. Electrostat.*, vol. 45, no. 3, pp. 227–238, Jan. 1999, doi: 10.1016/S0304-3886(98)00052-7.
- [80] M. Whelehan and I. W. Marison, "Microencapsulation using vibrating technology," *J. Microencapsul.*, vol. 28, no. 8, pp. 669–688, Dec. 2011, doi: 10.3109/02652048.2011.586068.
- [81] A. C. Merrington and E. G. Richardson, "The break-up of liquid jets," *Proc. Phys. Soc.*, vol. 59, no. 1, pp. 1–13, Jan. 1947, doi: 10.1088/0959-5309/59/1/302.
- [82] M. Kuschel and M. Sommerfeld, "Investigation of droplet collisions for solutions with different solids content," *Exp. Fluids*, vol. 54, no. 2, p. 1440, Jan. 2013, doi: 10.1007/s00348-012-1440-z.
- [83] H. Aziz, N. M. Farhan, and H. Vahedi Tafreshi, "Effects of fiber wettability and size on droplet detachment residue," *Exp. Fluids*, vol. 59, no. 7, p. 122, Jul. 2018, doi: 10.1007/s00348-018-2579-z.
- [84] Q. Li, J. Wang, S. Yan, J. Gong, and Q. Ma, "A zonal hybrid approach coupling FNPT with OpenFOAM for modelling wave-structure interactions with action of current," *Ocean Syst. Eng.*, vol. 8, no. 4, pp. 381–407, Dec. 2018, doi: 10.12989/OSE.2018.8.4.381.
- [85] "Fundamentals of Heat and Mass Transfer, 8th Edition | Wiley," *Wiley.com*. <https://www.wiley.com/en-us/Fundamentals+of+Heat+and+Mass+Transfer%2C+8th+Edition-p-9781119353881> (accessed Mar. 21, 2022).
- [86] A. Shama, M. A. Pouchon, and I. Clifford, "Simulation of the microfluidic mixing and the droplet generation for 3D printing of nuclear fuels," *Addit. Manuf.*, vol. 26, pp. 1–14, Mar. 2019, doi: 10.1016/j.addma.2018.12.011.
- [87] H. Jin, Y. Liu, H. Li, and Q. Fu, "Numerical analysis of the flow field in a sloshing tank with a horizontal perforated plate," *J. Ocean Univ. China*, vol. 16, pp. 575–584, Aug. 2017, doi: 10.1007/s11802-017-3369-6.
- [88] Z. Z. Hu, D. Greaves, and A. Raby, "Numerical wave tank study of extreme waves and wave-structure interaction using OpenFoam[®]," *Ocean Eng.*, vol. 126, pp. 329–342, Nov. 2016, doi: 10.1016/j.oceaneng.2016.09.017.
- [89] "CFD: PIMPLE Algorithm - Using SimScale / Solid Mechanics / FEA," *SimScale CAE Forum*, Nov. 06, 2020. <https://www.simscale.com/forum/t/cfd-pimple-algorithm/81418> (accessed Mar. 21, 2022).
- [90] G. M. Whitesides, "The origins and the future of microfluidics," *Nature*, vol. 442, no. 7101, Art. no. 7101, Jul. 2006, doi: 10.1038/nature05058.
- [91] L. Dai, X. Zhao, J. Guo, S. Feng, Y. Fu, Y. Kang, and J. Guo, "Microfluidics-based microwave sensor," *Sens. Actuators Phys.*, vol. 309, p. 111910, Jul. 2020, doi: 10.1016/j.sna.2020.111910.
- [92] Hewlett Packard, "Basics of measuring the dielectric properties of materials," *Lit. Number 5091-3300E*, 1992.
- [93] A. C. Metaxas and R. J. Meredith, *Industrial Microwave Heating*. IET, 1983.
- [94] A. Andryieuski, S. M. Kuznetsova, S. V. Zhukovsky, Y. S. Kivshar, and A. V. Lavrinenko, "Water: Promising Opportunities For Tunable All-dielectric Electromagnetic Metamaterials," *Sci. Rep.*, vol. 5, no. 1, p. 13535, Oct. 2015, doi: 10.1038/srep13535.
- [95] A. P. Gregory and R. N. Clarke, "Tables of the Complex Permittivity of Dielectric Reference Liquids at Frequencies up to 5 GHz," p. 94.
- [96] "Permittivity of Pure Water, at Standard Atmospheric Pressure, over the Frequency Range 0–25THz and the Temperature Range 0–100°C: Journal of Physical and Chemical Reference Data: Vol 36, No 1." <https://aip.scitation.org/doi/10.1063/1.2360986> (accessed Jun. 13, 2022).
- [97] M. Y. Onimisi and J. T. Ikyumbur, "Comparative Analysis of Dielectric Constant and Loss Factor of Pure Butan-1-ol and Ethanol," *Am. J. Condens. Matter Phys.*, p. 7, 2015.
- [98] D. K. Misra, "A Quasi-Static Analysis of Open-Ended Coaxial Lines (Short Paper)," *IEEE Trans. Microw. Theory Tech.*, vol. 35, no. 10, pp. 925–928, Oct. 1987, doi: 10.1109/TMTT.1987.1133782.

- [99] J. P. Grant, R. N. Clarke, G. T. Symm, and N. M. Spyrou, "A critical study of the open-ended coaxial line sensor technique for RF and microwave complex permittivity measurements," *J. Phys. [E]*, vol. 22, no. 9, pp. 757–770, Sep. 1989, doi: 10.1088/0022-3735/22/9/015.
- [100] L. S. Anderson, G. B. Gajda, and S. S. Stuchly, "Analysis of an open-ended coaxial line sensor in layered dielectrics," *IEEE Trans. Instrum. Meas.*, vol. IM-35, no. 1, pp. 13–18, Mar. 1986, doi: 10.1109/TIM.1986.6499049.
- [101] J. Baker-Jarvis, M. D. Janezic, P. D. Domich, and R. G. Geyer, "Analysis of an open-ended coaxial probe with lift-off for nondestructive testing," *IEEE Trans. Instrum. Meas.*, vol. 43, no. 5, pp. 711–718, Oct. 1994, doi: 10.1109/19.328897.
- [102] S. Fan, K. Staebell, and D. Misra, "Static analysis of an open-ended coaxial line terminated by layered media," *IEEE Trans. Instrum. Meas.*, vol. 39, no. 2, pp. 435–437, Apr. 1990, doi: 10.1109/19.52531.
- [103] A. J. Canós Marín, B. García-Baños, J. M. Catalá-Civera, F. L. Peñaranda-Foix, and J. D. Gutiérrez-Cano, "Improvement in the Accuracy of Dielectric Measurement of Open-Ended Coaxial Resonators by an Enhanced De-Embedding of the Coupling Network," *IEEE Trans. Microw. Theory Tech.*, vol. 61, no. 12, pp. 4636–4645, Dec. 2013, doi: 10.1109/TMTT.2013.2285359.
- [104] W. Skierucha, R. Walczak, and A. Wilczek, "Comparison of Open-Ended Coax and TDR sensors for the measurement of soil dielectric permittivity in microwave frequencies," *Int. Agrophysics*, vol. 18, no. 4, pp. 355–362.
- [105] R. Zají, L. Oppl, and J. Vrba, "Broadband Measurement of Complex Permittivity Using Reflection Method and Coaxial Probes," no. 1, p. 6, 2008.
- [106] C. Zhu, R. E. Gerald, Y. Chen, and J. Huang, "Probing the Theoretical Ultimate Limit of Coaxial Cable Sensing: Measuring Nanometer-Scale Displacements," *IEEE Trans. Microw. Theory Tech.*, vol. 68, no. 2, pp. 816–823, Feb. 2020, doi: 10.1109/TMTT.2019.2951099.
- [107] C. Zhu, R. E. Gerald, and J. Huang, "Highly sensitive open-ended coaxial cable-based microwave resonator for humidity sensing," *Sens. Actuators Phys.*, vol. 314, p. 112244, Oct. 2020, doi: 10.1016/j.sna.2020.112244.
- [108] M. A. Stuchly and S. S. Stuchly, "Coaxial Line Reflection Methods for Measuring Dielectric Properties of Biological Substances at Radio and Microwave Frequencies-A Review," *IEEE Trans. Instrum. Meas.*, vol. 29, no. 3, pp. 176–183, Sep. 1980, doi: 10.1109/TIM.1980.4314902.
- [109] Yumpu.com, "Agilent 85070E Dielectric Probe Kit 200 MHz to 50 GHz," *yumpu.com*. <https://www.yumpu.com/en/document/view/50052423/agilent-85070e-dielectric-probe-kit-200-mhz-to-50-ghz> (accessed Mar. 14, 2022).
- [110] W. Skierucha and A. Wilczek, "A FDR Sensor for Measuring Complex Soil Dielectric Permittivity in the 10–500 MHz Frequency Range," *Sensors*, Jan. 2010.
- [111] N. I. Sheen and I. M. Woodhead, "An Open-ended Coaxial Probe for Broad-band Permittivity Measurement of Agricultural Products," *J. Agric. Eng. Res.*, vol. 74, no. 2, pp. 193–202, Oct. 1999, doi: 10.1006/jaer.1999.0444.
- [112] T. W. Athey, M. A. Stuchly, and S. S. Stuchly, "Measurement of Radio Frequency Permittivity of Biological Tissues with an Open-Ended Coaxial Line: Part I," *IEEE Trans. Microw. Theory Tech.*, vol. 30, no. 1, pp. 82–86, Jan. 1982, doi: 10.1109/TMTT.1982.1131021.
- [113] S. A. Komarov, A. S. Komarov, D. G. Barber, M. J. L. Lemes, and S. Rysgaard, "Open-Ended Coaxial Probe Technique for Dielectric Spectroscopy of Artificially Grown Sea Ice," *IEEE Trans. Geosci. Remote Sens.*, vol. 54, no. 8, pp. 4941–4951, Aug. 2016, doi: 10.1109/TGRS.2016.2553110.
- [114] J. Bao, M. L. Swicord, and C. C. Davis, "Microwave dielectric characterization of binary mixtures of water, methanol, and ethanol," *J. Chem. Phys.*, vol. 104, no. 12, pp. 4441–4450, Mar. 1996, doi: 10.1063/1.471197.
- [115] Yumpu.com, "Agilent 85070E Dielectric Probe Kit - Agilent Network Analyzer ...," *yumpu.com*. <https://www.yumpu.com/en/document/view/40005494/agilent-85070e-dielectric-probe-kit-agilent-network-analyzer-> (accessed Feb. 11, 2022).
- [116] T. Chen, S. Li, and H. Sun, "Metamaterials Application in Sensing," *Sensors*, vol. 12, no. 3, Art. no. 3, Mar. 2012, doi: 10.3390/s120302742.
- [117] A. Petrin, *Wave Propagation*. BoD – Books on Demand, 2011.

- [118] A. K. Horestani, C. Fumeaux, S. F. Al-Sarawi, and D. Abbott, "Displacement Sensor Based on Diamond-Shaped Tapered Split Ring Resonator," *IEEE Sens. J.*, vol. 13, no. 4, pp. 1153–1160, Apr. 2013, doi: 10.1109/JSEN.2012.2231065.
- [119] J. Naqui and F. Marti'n, "Transmission Lines Loaded With Bisymmetric Resonators and Their Application to Angular Displacement and Velocity Sensors," *IEEE Trans. Microw. Theory Tech.*, vol. 61, no. 12, pp. 4700–4713, Dec. 2013, doi: 10.1109/TMTT.2013.2285356.
- [120] A. K. Horestani, J. Naqui, Z. Shaterian, D. Abbott, C. Fumeaux, and F. Marti'n, "Two-dimensional alignment and displacement sensor based on movable broadside-coupled split ring resonators," *Sens. Actuators Phys.*, vol. 210, pp. 18–24, Apr. 2014, doi: 10.1016/j.sna.2014.01.030.
- [121] A. K. Horestani, D. Abbott, and C. Fumeaux, "Rotation Sensor Based on Horn-Shaped Split Ring Resonator," *IEEE Sens. J.*, vol. 13, no. 8, pp. 3014–3015, Aug. 2013, doi: 10.1109/JSEN.2013.2264804.
- [122] R. Melik, E. Unal, N. K. Perkgoz, C. Puttlitz, and H. V. Demir, "Metamaterial-based wireless strain sensors," *Appl. Phys. Lett.*, vol. 95, no. 1, p. 011106, Jul. 2009, doi: 10.1063/1.3162336.
- [123] R. Melik, E. Unal, N. Kosku Perkgoz, C. Puttlitz, and H. V. Demir, "Flexible metamaterials for wireless strain sensing," *Appl. Phys. Lett.*, vol. 95, no. 18, p. 181105, Nov. 2009, doi: 10.1063/1.3250175.
- [124] R. Melik, E. Unal, N. K. Perkgoz, B. Santoni, D. Kamstock, C. Puttlitz, and H. V. Demir, "Nested Metamaterials for Wireless Strain Sensing," *IEEE J. Sel. Top. Quantum Electron.*, vol. 16, no. 2, pp. 450–458, Mar. 2010, doi: 10.1109/JSTQE.2009.2033391.
- [125] J. B. Pendry, A. J. Holden, D. J. Robbins, and W. J. Stewart, "Magnetism from conductors and enhanced nonlinear phenomena," *IEEE Trans. Microw. Theory Tech.*, vol. 47, no. 11, pp. 2075–2084, Nov. 1999, doi: 10.1109/22.798002.
- [126] H. Kairm, D. Delfin, M. A. I. Shuvo, L. A. Chavez, C. R. Garcia, J. H. Barton, S. M. Gaytan, M. A. Cadena, R. C. Rumpf, R. B. Wicker, Y. Lin, and A. Choudhuri, "Concept and Model of a Metamaterial-Based Passive Wireless Temperature Sensor for Harsh Environment Applications," *IEEE Sens. J.*, vol. 15, no. 3, pp. 1445–1452, Mar. 2015, doi: 10.1109/JSEN.2014.2363095.
- [127] F. Bilotti, A. Toscano, and L. Vegni, "Design of Spiral and Multiple Split-Ring Resonators for the Realization of Miniaturized Metamaterial Samples," *IEEE Trans. Antennas Propag.*, vol. 55, no. 8, pp. 2258–2267, Aug. 2007, doi: 10.1109/TAP.2007.901950.
- [128] J. D. Baena, J. Bonache, F. Martin, R. M. Sillero, F. Falcone, T. Lopetegui, M. A. G. Laso, J. Garcia-Garcia, I. Gil, M. F. Portillo, and M. Sorolla, "Equivalent-circuit models for split-ring resonators and complementary split-ring resonators coupled to planar transmission lines," *IEEE Trans. Microw. Theory Tech.*, vol. 53, no. 4, pp. 1451–1461, Apr. 2005, doi: 10.1109/TMTT.2005.845211.
- [129] W. Withayachumnankul, K. Jaruwongrungsee, A. Tuantranont, C. Fumeaux, and D. Abbott, "Metamaterial-based microfluidic sensor for dielectric characterization," *Sens. Actuators Phys.*, vol. 189, pp. 233–237, Jan. 2013, doi: 10.1016/j.sna.2012.10.027.
- [130] "Microwave Engineering, 4th Edition | Wiley," *Wiley.com*. <https://www.wiley.com/en-mx/Microwave+Engineering%2C+4th+Edition-p-9780470631553> (accessed Feb. 11, 2022).
- [131] A. W. Kraszewski and S. O. Nelson, "Observations on resonant cavity perturbation by dielectric objects," *IEEE Trans. Microw. Theory Tech.*, vol. 40, no. 1, pp. 151–155, Jan. 1992, doi: 10.1109/22.108334.
- [132] A. W. Kraszewski, S. O. Nelson, and T.-S. You, "Use of a microwave cavity for sensing dielectric properties of arbitrarily shaped biological objects," *IEEE Trans. Microw. Theory Tech.*, vol. 38, no. 7, pp. 858–863, Jul. 1990, doi: 10.1109/22.55777.
- [133] J. Sheen, "Comparisons of microwave dielectric property measurements by transmission/reflection techniques and resonance techniques," *Meas. Sci. Technol.*, vol. 20, no. 4, p. 042001, Jan. 2009, doi: 10.1088/0957-0233/20/4/042001.
- [134] A. Kumar and G. Singh, "MEASUREMENT OF DIELECTRIC CONSTANT AND LOSS FACTOR OF THE DIELECTRIC MATERIAL AT MICROWAVE FREQUENCIES," *Prog. Electromagn. Res.*, vol. 69, pp. 47–54, 2007, doi: 10.2528/PIER06111204.
- [135] H. A. Bethe, J. Schwinger, United States, Office of Scientific Research and Development, National Defense Research Committee, Massachusetts Institute of Technology, and Radiation Laboratory, *Perturbation theory for cavities*. Cambridge, Mass.: Massachusetts Institute of Technology, Radiation Laboratory, 1943.

- [136] L. Chen, C. K. Ong, and B. T. G. Tan, "Amendment of cavity perturbation method for permittivity measurement of extremely low-loss dielectrics," *IEEE Trans. Instrum. Meas.*, vol. 48, no. 6, pp. 1031–1037, Dec. 1999, doi: 10.1109/19.816109.
- [137] J. Sheen, "Measurements of microwave dielectric properties by an amended cavity perturbation technique," *Measurement*, vol. 42, no. 1, pp. 57–61, Jan. 2009, doi: 10.1016/j.measurement.2008.03.017.
- [138] R. G. Carter, "Accuracy of microwave cavity perturbation measurements," *IEEE Trans. Microw. Theory Tech.*, vol. 49, no. 5, pp. 918–923, May 2001, doi: 10.1109/22.920149.
- [139] C. D. Field and F. R. Fricke, "Theory and applications of quarter-wave resonators: A prelude to their use for attenuating noise entering buildings through ventilation openings," *Appl. Acoust.*, vol. 53, no. 1, pp. 117–132, Jan. 1998, doi: 10.1016/S0003-682X(97)00035-2.
- [140] B. I. Bleaney and B. Bleaney, *Electricity and Magnetism, Volume 1*, Third Edition. Oxford, New York: Oxford University Press, 2013.
- [141] G. Q. Jiang, W. H. Wong, E. Y. Raskovich, W. G. Clark, W. A. Hines, and J. Sanny, "Measurement of the microwave dielectric constant for low-loss samples with finite thickness using open-ended coaxial-line probes," *Rev. Sci. Instrum.*, vol. 64, no. 6, pp. 1622–1626, Jun. 1993, doi: 10.1063/1.1144036.
- [142] P. De Langhe, L. Martens, and D. De Zutter, "Design rules for an experimental setup using an open-ended coaxial probe based on theoretical modelling," *IEEE Trans. Instrum. Meas.*, vol. 43, no. 6, pp. 810–817, Dec. 1994, doi: 10.1109/19.368062.
- [143] D. Kajfez and E. J. Hwan, "Q-Factor Measurement with Network Analyzer," *IEEE Trans. Microw. Theory Tech.*, vol. 32, no. 7, pp. 666–670, Jul. 1984, doi: 10.1109/TMTT.1984.1132751.
- [144] D. Kajfez, "Q factor measurements, analog and digital1."
- [145] S. A. Bell, "A beginner's guide to uncertainty of measurement.," Mar. 2001. <https://eprintspublications.npl.co.uk/1568/> (accessed Feb. 11, 2022).
- [146] W. Withayachumnankul, K. Jaruwongrungssee, A. Tuantranont, C. Fumeaux, and D. Abbott, "Metamaterial-based microfluidic sensor for dielectric characterization," *Sens. Actuators Phys.*, vol. 189, pp. 233–237, Jan. 2013, doi: 10.1016/j.sna.2012.10.027.
- [147] E. L. Chuma, Y. Iano, G. Fontgalland, and L. L. B. Roger, "Microwave Sensor for Liquid Dielectric Characterization Based on Metamaterial Complementary Split Ring Resonator," *IEEE Sens. J.*, vol. 18, no. 24, pp. 9978–9983, Dec. 2018, doi: 10.1109/JSEN.2018.2872859.
- [148] T. J. R. Yalkowsky, Samuel H, "Solubilization of drugs by cosolvents." *Techniques of solubilization of drugs* 12, 91-134, 1981.
- [149] W. H. Sutton, *Key issues in microwave process technology*. United States: American Ceramic Society, 1993.
- [150] K. E. E. Wilhelm, "Process for altering the energy content of dipolar substances," US2089966A, Aug. 17, 1937 Accessed: Jun. 19, 2022. [Online]. Available: <https://patents.google.com/patent/US2089966A/en>
- [151] "Ultra short wave oscillation," US2096459A, Oct. 19, 1937 Accessed: Jun. 19, 2022. [Online]. Available: <https://patents.google.com/patent/US2096459/en?q=e.e+kassner+1937+dipolar+substance>
- [152] W. White, "Early History of Industrial Electronics," *Proc. IRE*, vol. 50, no. 5, pp. 1129–1135, May 1962, doi: 10.1109/JRPROC.1962.288018.
- [153] W. M. Roberds, "Problems in the Design of High-Frequency Heating Equipment," *Proc. IRE*, vol. 34, no. 7, pp. 489–500, Jul. 1946, doi: 10.1109/JRPROC.1946.230253.
- [154] T. M. Shaw and J. A. Galvin, "High-Frequency-Heating Characteristics of Vegetable Tissues Determined from Electrical-Conductivity Measurements," *Proc. IRE*, vol. 37, no. 1, pp. 83–86, Jan. 1949, doi: 10.1109/JRPROC.1949.233290.
- [155] A. R. von Hippel, Ed., *Dielectric Materials and Applications*. Cambridge, MA, USA: MIT Press, 1952.
- [156] J. Iglesias and W. B. Westphal, "SUPPLEMENTARY DIELECTRIC-CONSTANT AND LOSS MEASUREMENTS ON HIGH-TEMPERATURE MATERIALS," MASSACHUSETTS INST OF TECH CAMBRIDGE LAB FOR INSULATION RESEARCH, Jan. 1967. Accessed: Jun. 19, 2022. [Online]. Available: <https://apps.dtic.mil/sti/citations/AD0650230>
- [157] J. A. Menéndez, A. Arenillas, B. Fidalgo, Y. Fernández, L. Zubizarreta, E. G. Calvo, and J. M. Bermúdez, "Microwave heating processes involving carbon materials," *Fuel Process. Technol.*, vol. 91, no. 1, pp. 1–8, Jan. 2010, doi: 10.1016/j.fuproc.2009.08.021.

- [158] *Microwaves in Organic Synthesis*, 1st ed. John Wiley & Sons, Ltd, 2012. doi: 10.1002/9783527651313.
- [159] R. Roy, D. Agrawal, J. Cheng, and S. Gedevanishvili, "Full sintering of powdered-metal bodies in a microwave field," *Nature*, vol. 399, no. 6737, Art. no. 6737, Jun. 1999, doi: 10.1038/21390.
- [160] D. K. Agrawal, "Microwave processing of ceramics," *Curr. Opin. Solid State Mater. Sci.*, vol. 3, no. 5, pp. 480–485, Oct. 1998, doi: 10.1016/S1359-0286(98)80011-9.
- [161] A. Chatterjee, T. Basak, and K. G. Ayappa, "Analysis of microwave sintering of ceramics," *AIChE J.*, vol. 44, no. 10, pp. 2302–2311, 1998, doi: 10.1002/aic.690441019.
- [162] M. Chen, E. J. Siochi, T. C. Ward, and J. E. McGrath, "Basic ideas of microwave processing of polymers," *Polym. Eng. Sci.*, vol. 33, no. 17, pp. 1092–1109, 1993, doi: 10.1002/pen.760331703.
- [163] D. E. Clark, "Microwave Processing of Materials," p. 34.
- [164] "Microwave-Enhanced Reaction Rates for Nanoparticle Synthesis | Journal of the American Chemical Society." <https://pubs.acs.org/doi/full/10.1021/ja052463g> (accessed Jun. 19, 2022).
- [165] I. Bilecka and M. Niederberger, "Microwave chemistry for inorganic nanomaterials synthesis," *Nanoscale*, vol. 2, no. 8, pp. 1358–1374, 2010, doi: 10.1039/B9NR00377K.
- [166] E. Siores and D. Do Rego, "Microwave applications in materials joining," *J. Mater. Process. Technol.*, vol. 48, no. 1, pp. 619–625, Jan. 1995, doi: 10.1016/0924-0136(94)01701-2.
- [167] S. Chandrasekaran, T. Basak, and S. Ramanathan, "Experimental and theoretical investigation on microwave melting of metals," *J. Mater. Process. Technol.*, vol. 211, no. 3, pp. 482–487, Mar. 2011, doi: 10.1016/j.jmatprotec.2010.11.001.
- [168] M. Al-Harashseh and S. W. Kingman, "Microwave-assisted leaching—a review," *Hydrometallurgy*, vol. 73, no. 3, pp. 189–203, Jun. 2004, doi: 10.1016/j.hydromet.2003.10.006.
- [169] A. R. V. Hippel, *Dielectrics and Waves*. Wiley, 1954.
- [170] F. Caspers, "RF Engineering Basic Concepts: The Smith Chart," p. 23.
- [171] A. J. Canos, J. M. Catala-Civera, F. L. Penaranda-Foix, and Edl. Reyes-Davo, "A novel technique for deembedding the unloaded resonance frequency from measurements of microwave cavities," *IEEE Trans. Microw. Theory Tech.*, vol. 54, no. 8, pp. 3407–3416, Aug. 2006, doi: 10.1109/TMTT.2006.877833.
- [172] R. E. Collin, "Foundations for Microwave Engineering," p. 945.
- [173] M. Cabanes Sempere, "Innovative production of nuclear fuel by microwave internal gelation.," Universitat Politècnica de València, Valencia (Spain), 2013. doi: 10.4995/Thesis/10251/31641.
- [174] R. W. E, "Evaporation from Drops, Parts I & II," *Chem Eng Prog*, vol. 48, pp. 141–146, 1952.
- [175] W. H. McAdams, *Heat transmission*. New York: McGraw-Hill, 1954.
- [176] "Aerosol Technology: Properties, Behavior, and Measurement of Airborne Particles, 2nd Edition | Wiley," *Wiley.com*. <https://www.wiley.com/en-us/Aerosol+Technology%3A+Properties%2C+Behavior%2C+and+Measurement+of+Airborne+Particles%2C+2nd+Edition-p-9780471194101> (accessed May 11, 2022).
- [177] R. E. Bolz, *CRC Handbook of Tables for Applied Engineering Science*. CRC Press, 1973.
- [178] "Heat Transfer von Gregory Nellis. eBooks | Orell Füssli." <https://www.orellfuessli.ch/shop/home/artikeldetails/A1031765086> (accessed May 11, 2022).
- [179] R. Williamson and E. D. Threadgill, "A Simulation for the Dynamics of Evaporating Spray Droplets in Agricultural Spraying," 1974, doi: 10.13031/2013.36835.
- [180] J. P. Zarling, *Heat and Mass Transfer from Freely Falling Drops at Low Temperatures*. The Laboratory, 1980.
- [181] C. E. Lapple and C. B. Shepherd, "CALCULATION OF PARTICLE TRAJECTORIES," *Ind. Eng. Chem.*, vol. 32, no. 5, pp. 605–617, May 1940, doi: 10.1021/ie50365a007.
- [182] K. H. Chen and G. J. Trezek, "The Effect of Heat Transfer Coefficient, Local Wet Bulb Temperature and Droplet Size Distribution Function on the Thermal Performance of Sprays," *J. Heat Transf.*, vol. 99, no. 3, pp. 381–385, Aug. 1977, doi: 10.1115/1.3450706.
- [183] A. R. Dehghani-Sanij, S. R. Dehghani, G. F. Naterer, and Y. S. Muzychka, "Sea spray icing phenomena on marine vessels and offshore structures: Review and formulation," *Ocean Eng.*, vol. 132, pp. 25–39, Mar. 2017, doi: 10.1016/j.oceaneng.2017.01.016.
- [184] D. R. Lide, *CRC Handbook of Chemistry and Physics, 85th Edition*. CRC Press, 2004.

- [185] Kane Yee, "Numerical solution of initial boundary value problems involving maxwell's equations in isotropic media," *IEEE Trans. Antennas Propag.*, vol. 14, no. 3, pp. 302–307, May 1966, doi: 10.1109/TAP.1966.1138693.
- [186] T. Weiland, "A discretization model for the solution of Maxwell's equations for six-component fields," *Arch. Elektron. Uebertragungstechnik*, vol. 31, pp. 116–120, Apr. 1977.

Curriculum Vitae

PERSONAL INFORMATION

- Name Kwanghoon Choi
- Birthday 5th February 1984
- Citizenship South Korea

EMPLOYMENT HISTORY

- 2011 – 2018 Hyundai Motors Research engineer
- 2018 – 2022 Paul Scherrer Institut Researcher Ph.D student

EDUCATION

- 2018 – 2022 Ph.D in Physics, Swiss Federal Institute of Technology Lausanne (EPFL)
- 2009 – 2011 MSc in Mechanical Engineering, Kyunghee University
- 2003 – 2011 BEng in Mechanical engineering, Kyunghee University

PUBLICATIONS

- Kwanghoon Choi, Manuel A. Pouchon, Sébastien Vaucher, et al., The X-band Coaxial Microwave Sensor for the Water-based liquid mixture of Nanoliter-scale volumes. (to be published)
- Kwanghoon Choi, Manuel A. Pouchon, Sébastien Vaucher, et al., The X-band Coaxial Microwave Heating resonator for a microfluidic system. (to be published)

PATENTS

- APPARATUS OF DIVIDING WORKING CHAMBER OF 3D PRINTER (US20180126458A1)
- SEPERATOR FOR FUEL CELL AND METHOD FOR MANUFACTURING THE SAME (US20170141408A1)
- SURFACE TREATMENT METHOD FOR COATING LAYER (US9169550B2)
- COATING LAYER WITH LOW-FRICTION FOR VEHICLE COMPONENT AND METHOD FOR PRODUCING THE SAME (US9061479B2)
- COATING METHOD OF SEPARATOR FOR FUEL CELL AND SEPARATOR FOR FUEL CELL (US20170033374A1)
- METHOD FOR COATING TiAgMoN LAYER (KR101583882B1)
- POLLUTION LEVEL MEASURING METHOD OF PVD COATER (KR101356166B1)
- COATING METHOD OF SEPERATOR FOR FUEL CELL AND SEPERATOR FOR FUEL CELL (US20170141409A1)

- POROUS POLYMER RESIN LAYER AND METHOD FOR MANUFACTURING THE SAME (US20160280877A1)
- SURFACE TREATMENT METHOD WITH A SUPERIOR MASS PRODUCTIVITY AND LOW FRICTION CHARACTERISTICS (US20170107607A1)
- METHOD FOR MEASURING COEFFICIENT OF FRICTION FOR SPECIMEN (US20160161396A1)
- THERMAL INSULATION COATING COMPOSITION AND THERMAL INSULATION COATING LAYER (US20150285140A1)
- TiAgN COATING LAYER, TiAgN COATING METHOD AND TiAgN COATING APPARATUS (US20140170441A1)
- LOW FRICTION COATING LAYER, LOW FRICTION COATING METHOD AND LOW FRICTION COATING APPARATUS (US20140170053A1)
- MULTI COATING LAYER AND METHOD FOR PRODUCING THE SAME (US20150285140A1)
- METHOD FOR PRODUCING COATING LAYER WITH LOW-FRICTION (US20130136896A1)
- MULTI-LAYER COMPOSITES HAVING THERMAL INSULATION PROPERTY (KR101684508B1)
- METHOD AND APPARATUS FOR CONTROLLING WINDSHIELD GLASS WITH FORWARD VISIBILITY IN CASE OF RAIN (KR101684158B1)
- COATING MATERIAL FOR SLIDING PART OF VEHICLE AND COATING METHOD THEREOF (KR101673712B1)
- COATING METHOD FOR ENGINE MOVING PARTS (KR101664615B1)
- LIQUID DROPLET SURFACE FRICTION FORCE MEASURING SYSTEM AND METHOD USING AFM (KR101662523B1)

PRESENTATION

- “Inflight Drying Process of Micro-droplet to Improve the 3D Printing Resolution”, Armasuisse seminar, Armasuisse, Thun, Switzerland, Mar, 2021.
- “Droplet Based Powder Focusing for the 3D Printing”, NES Ph.D Day, Paul Sherrer Institute, Villigen, Switzerland, May, 2019/2021/2022
- “Powder Focusing for Beam Induced Laser 3D Printing”, SFA-AM Annual Review Meeting, EPFL, Neuchâtel, Switzerland, Jan, 2020/2021
- “Microwave drying of powder charged droplets”, SFA-AM Workshop, PSI, Villigen, Switzerland, May, 2019